STRAIN INDUCED MARTENSITE AND ITS REVERSION IN 304 STAINLESS STEEL

A Thesis submitted for the degree

of

DOCTOR OF PHILOSOPHY (ENGINEERING)

By

Pratik Kumar Mallick

Department of Metallurgy and Materials Engineering
Indian Institute of Engineering Science and Technology, Shibpur
Howrah – 711103, West Bengal
India
December 2017

Indian Institute of Engineering Science and Technology, Shibpur

Howrah – 711103, West Bengal, India

CERTIFICATE

This is to certify that the thesis entitled, **“Strain Induced Martensite and its Reversion in 304 Stainless Steel”** being submitted by Pratik Kumar Mallick (Registration No: PhD/R/2011/0040) to Indian Institute of Engineering Science and Technology, Shibpur, Howrah, India for the award of Doctor of Philosophy in Engineering is a record of bonafide research work carried out by him under our supervision and guidance. To the best of our knowledge, the results presented in this thesis have not been submitted by him elsewhere for the award of any other degree or diploma.

We hereby forward the thesis for fulfilling the requirements for the award of the degree of Doctor of Philosophy in accordance with the regulations of the Institute.

Dr. Swarup Kumar Ghosh
Professor
Department of Metallurgy and Materials Engineering
Indian Institute of Engineering Science and Technology, Shibpur, Howrah - 711103
West Bengal, India

Dr. Partha Protim Chattopadhyay
Director, NIFFT, Hatia, Ranchi - 834003 and
Professor (on lien),
Department of Metallurgy and Materials Engineering
Indian Institute of Engineering Science and Technology, Shibpur, Howrah-711103
West Bengal, India

ACKNOWLEDGEMENTS

While working on my thesis, I interacted with many professionals and researchers in the metallurgical field. My thesis would be incomplete without acknowledging their contributions. First and foremost, I would like to express my deep sense of gratitude to my PhD supervisors, Dr. Swarup Kumar Ghosh and Dr. Partha Protim Chattopadhyay for suggesting me to join the PhD program with an interesting field of cryogenic treatment of austenitic stainless steel. In addition to that, I would also mention that this PhD work would not have been possible without my employer's permission. Thanks to my present and previous seniors in M/s Usha Martin Limited, Jamshedpur.

Dr. Swarup Kumar Ghosh suggested the different characterisation techniques such as XRD, TEM, EBSD, DSC, Fractography etc. as and when required for the study. He kept himself always accessible whenever I required, despite his busy schedule and other priorities. He participated not only in the discussion on the subject matter, but also introduced to necessary support activities crucial for this work. His concern to improve my research skills has pressed me to learn the academic research methods and procedures. He has also enriched me with the insights about international publications and due to his constant encouragement; I could communicate and publish six papers in international journals from the present research work.

I was introduced to the cryogenic treatments on austenitic stainless steel by Dr. Partha Protim Chattopadhyay. His introduction was not only crisp and clear but motivating and inspiring as well. Every discussion with him was insightful and enriched my knowledge on the topic and in general; to a great extent, inspired me to learn more. His focus on the fundamentals of the subject and research guidance was the driving force that kept me on the track. He is such a person, who always gave importance in being human rather than a mere researcher. I have always looked upon him in case of any sort of crisis and he could resolve them with his immaculate sense and style. I feel indebted and profoundly acknowledge all support with a deep sense of gratitude.

I was lucky to have incredible colleagues at my research place IIEST, Shibpur and without their constant support and encouragement; this task would not have been completed. I would specifically mention the contributions of Mr. Nisith Kumar Tewary, my fellow Research

Scholar, whose extensive support related to characterisation of the TEM micrographs and X-ray diffraction results made this journey possible.

I would specially mention the name of Prof. Sumit Ghosh from the department of Metallurgy and Materials Engineering in IIEST, Shibpur, who has constantly encouraged me and stood beside me right from my graduation days. He provided the insight on post graduation studies and laid the foundation towards Master’s as well as PhD degree. I would also mention the contributions made by my batch mate Mr. Kingshuk Das during my Masters. He has always been a true friend and source of inspiration. I must mention Prof. Sanjay Sadhukhan for his time to time encouragement from my graduation days.

I consider myself privileged to be associated with Dr. Sudhanshu Chakraborty, with whom I have worked with in my early professional life at M/s Usha Martin Limited and during this association learned how to apply metallurgical fundamentals in industrial application effectively. He has been my role-model as a professional and inspiration behind choosing this Doctoral program.

I would also like to thank Mr. Soham Mukherjee, Mr. Gurudas Mandal, Mr. Dubai Mahata, Dr. Sumit Chabri, Dr. Subhrangshu Chatterjee, Mr. Kumar Nayak, Mr. Sudip Bhattacharjee, Dr. Moloy Kundu, Mr. Salil Dolui and all staff and faculty members of Metallurgy and Materials Engineering Department in IIEST, Shibpur.

I would also thank Ms. Sharmistha Sarkar, Mr. Akshay Das, Mr. Amalendu Das, Mr. Ashok Kumar Gorai and Mr. Prafulla Kaiborto from M/s Usha Martin Limited, Jamshedpur and my Bengal Engineering College juniors Mr. Abhinandan Ganguly, Mr. Amit Kundu, Mr. Piyas Palit, Mr. Chiranjib Das, Mr. Naba Kumar Mahata and Mr. Suman Patra for their time to time help during this journey.

DEDICATION

I dedicate this ***Thesis*** to my "***JETHU***", Late *Mr. Santosh Kumar Mallick*, who has not only been the source of love and affection, he was the symbol of honesty to me. An exceptional, superior human being who lived life with one simple code as emphasised by Swami Vivekananda "*Jibe Prem Kore Jei Jon, Sei Jon Sebiche Ishwar*". It has been a privilege to be associated with him and hear BABUSONA in his voice. Time passed away, but the chanting word will always remain with me. Wherever you are *Jethu*, you are precious to me. I do not miss you. I live with you in my memories.

I also dedicate this ***Thesis*** to my parents *Mrs. Shila Mallick and Mr. Paritosh Mallick.* They have always stayed beside me, believed me and made me capable to reach any destination I have reached today.

I would like to dedicate this ***Thesis*** to the almighty and all of my well wishers, friends and relatives. Without their blessings, it would not have been possible.

Finally, I dedicate this ***Thesis*** to my loving wife *Mrs. Isha Mallick and my little daughter Ms. Pratyusha Mallick* for their continuous encouragement and support.

CONTENTS

LIST OF FIGURES

LIST OF TABLES

SYNOPSIS

Mounting climatic concern has recently drawn special attention towards the development of high specific strength thin gauge steels processed under cold deformation and annealing route. In this effort, austenitic steel has been identified as one of the potential candidates as it can be partially transformed into martensite either by cooling at room temperature or by subjecting it under deformation induced transformation during cold rolling. The austenite-martensite microstructures, during subsequent annealing, result in reversion and/or softening of martensite due to transformation and/or tempering effect. Such ultrafine austenite-martensite microstructures are most conducive to achieve the extraordinary combination of strength and ductility.

304 austenitic steel is one of the potential candidates for high specific strength thin gauge application. The M_d temperature of this steel is below the room temperature and hence, the steel is not amenable to deformation induced transformation at the room temperature during cold deformation under the usual cold rolling schedule. Nevertheless, it is of importance to understand the deformation induced transformation behaviour of 304 austenitic steel and the reversion behaviour of the cold deformed steel in order to assess the microstructural features and the corresponding mechanical properties in cold deformed and annealed steel.

In the present study, 304 stainless steels are subjected to cold deformation at room temperature, 0^{o}C and -196^{o}C with an aim to achieve the deformation induced transformation of austenite. In the case of room temperature, the deformation is found to be predominantly dislocation controlled. Extended stacking faults, ε-martensite (up to 6%) and α′-martensite (28% to 44%) are the dominant strain induced features as compared to the homogeneous dislocation structure along with some amount of α′-martensite (13% to 32%). Lowering of deformation temperature at cryogenic level results in the formation of higher amount of α′-martensite as compared to that at 0°C. Such difference corresponds to the lowering of stacking fault energy (SFE) from 19 mJ/m^2 at 0°C to 9 mJ/m^2 at -196°C.

In view of the fact that that deformation at room temperature results in dislocated austenitic microstructure, reversion annealing treatment has been carried out for the samples deformed at 0^{o}C and -196^{o}C only. In the case of cold deformed samples, the reversion transformation has been found to be enhanced with increasing annealing temperature without significant grain growth up to 800°C. The activation energy value corresponding to the first and second stage of reversion followed by Cr-carbide precipitation has been estimated to be as 77, 130 and 251 kJ/mol, respectively for 30% cold deformed sample at 0°C.

Steel with a higher amount of %Mn results in 1444 MPa UTS after 40% deformation at 0°C against 1225 MPa UTS for same amount deformation at 0°C for steel containing a lower amount of Mn. Whereas, comparatively lower deformation (10-20%) at -196°C leads to higher level of strength (1306-1589 MPa) with 15-9% elongation due to the formation of the higher volume fraction of strain induced martensite (ε/α').

The yield and tensile strength values of the specimen, deformed by 40% at 0^{o}C, increase continuously with the annealing temperature up to 400°C beyond which the values decrease rapidly. The UTS and elongation after annealing at 500^{o}C for 1h were found to be 1210 MPa 25%, respectively. The same attained the values of 814MPa and 49% after annealing at 800^{o}C for 1h. Reversion annealing of 20% cryogenically deformed sample at 725°C for 1 h resulted in a combination of 992 MPa strength and 32% elongation. Annealing treatment at 725°C for 1h is found to be effective to restore the ductility of samples (32-45%) deformed at -196°C, by eliminating the residual stress. The governing mechanism of deformation induced transformation has been identified primarily to $\gamma\rightarrow\varepsilon\rightarrow\alpha'$ for cryogenically deformed sample and $\gamma\rightarrow\alpha'$ for deformation at 0°C. On the other hand, the reversion is governed by two mechanisms; one is shear transformation and the other one is the diffusion controlled transformation. Shear transformation during reversion, generally reveals fine γ grains and high dislocation structure through recovery and recrystallisation. Whereas, diffusionally reversed γ is differentiated by the nucleation of equiaxed austenite grains within the α' matrix and such γ grains gradually grow during annealing.

1

INTRODUCTION

Among the steels designated with the qualifier ‘stainless’, the most popular one is Ni-Cr alloyed austenitic steel that possesses good aesthetic property, superior ductility, cryogenic property and biocompatibility beside its generic corrosion resistance. However, the relatively low tensile strength of stainless steels in comparison with similar structural alloys limits their load bearing applications. Austenitic stainless steels are not amenable to conventional hardening and tempering. While strengthening by grain refinement offers limited success, strengthening effect due to plastic deformation is less explored so far. Strength is achieved due to the formation of α′-martensite in austenite matrix with a decrease in ductility due to work hardening effect. Reversion of α′-martensite to austenite in the course of annealing allows recovering the ductility to large extent.

Cold deformation and annealing have recently been identified as the attractive route for manufacturing thin gauge strip with ultrafine austenite-martensite microstructures. Deformation processing of the austenitic stainless steel results in strain induced transformation following the sequence of $\gamma \rightarrow \varepsilon \rightarrow \alpha'$ transformation [1]. Formation of deformation-induced martensite exerts significant influence on the manufacturing process and, in turn, the target properties of the product. The amount of α′-martensite depends on the deformation methods, amount of plastic strain, strain rate and temperature [2]. Stacking fault energy of austenite, which governs the dominant deformation mechanism, is a function of temperature and composition. For higher stacking fault energy ($>20 \mathrm{mJ/m^2}$), the deformation mode is shifted from ε-martensite formation to deformation twinning and then slip [3]. Plastic deformation of austenite creates the embryo which forms at the intersections of shear bands, e.g., stacking faults, twins, etc. Usually, ε-martensite is formed at the low deformation level (i.e., 5–10%) and at higher strain levels and subsequently, the volume fraction of α′-martensite increases at the expense of ε-martensite [4].

Reversion of deformation induced martensite is essentially governed by two mechanisms, namely diffusion controlled and shear type. During annealing, the heavily deformed regions of austenite undergo recovery and recrystallisation, whereas deformation induced martensite transforms to austenite. The grains of the reverted austenite are refined through the recovery process of the matrix by the formation of dislocation cell and sub-grain, similar to the process in cold worked austenite.

The present study aims to understand the process-microstructure-property correlation concerning the development of thin gauge 304 stainless steel samples for high specific strength application. In view of the M_d temperature of the steel, the samples were subjected to a different amount of deformation at room temperature as well as at 0°C followed by selective reversion annealing treatment to understand the deformation induced martensite formation mechanisms and related changes in the mechanical property. Considering the amount of martensite available at the cold deformed microstructure, samples with 30% and 40% deformation at 0°C, were selected for reversion annealing treatment followed by suitable characterisation. A set of samples was also deformed at -196°C followed by reversion annealing and compared with deformed and reverted samples at 0°C. Effect of pre-strain at room temperature followed by holding at -196°C was also used for comparison purpose. Samples were also subjected to thermo-mechanical controlled processing (TMCP) to understand the effect of grain refinement.

Two types of austenitic stainless steel were used in the present study. Both of them were subjected to 10 to 40% deformation at room temperature as well as at 0°C. Deformation of 10-20% reduction was applied at -196°C in case of one of the steels. The same sample was also subjected to various cryogenic treatment with (20%) or without pre-strain. Reversion annealing treatment at various temperatures ranging from 300 to 800°C for 1 h duration was carried out for selected deformed and cryogenically treated samples. The steel was also subjected to TMCP with finish rolling temperature (FRT) of 700°C, 800°C and 900°C. The deformed and reverted samples were then subjected to suitable characterisation methods through X-ray diffraction, optical, scanning and transmission electron microscopic analysis, electron backscattered diffraction (EBSD), fractographic study, differential scanning calorimetry (DSC) study etc., in order to understand the mechanism of transformation. Mechanical properties of the processed samples were measured through hardness and tensile tests.

The structure of the present study is as following:

The present chapter 1 represents the background, current technological status and highlights of the present work in 304 stainless steel.

Chapter 2 furnishes a detailed review of earlier work encompassing a family of austenitic stainless steel, alloying elements, process and property, process-microstructure-property correlation, the effect of cold deformation and reversion of cold deformed microstructure, areas of specific interest and scope of the present work.

Chapter 3 enumerates the experimental methods adapted for the present study. The chapter presents a brief description of the composition, process schedule, preparation of the experimental samples and different instruments used for understanding of phase transformation, microstructure evolution and properties.

Chapter 4 presents the process schedule for the cold rolling of samples at room temperature and 0°C. Formation of deformation induced martensite has been analysed by conducting X-ray diffraction analysis. The studies on microstructure evolution and its analysis have been presented in terms of optical micrographs as well as scanning and transmission electron microscopy. Mechanical behaviour of the sample has been described with analysis of the results obtained by conducting hardness measurement, tensile test and fractographic analysis of fractured samples.

Chapter 5 presents the results obtained after subjecting the 30% and 40% deformed (0°C) samples to the different reversion annealing treatment schedule. The reversion of deformation induced martensite has been analysed by conducting X-ray diffraction analysis. The reversion behaviour has been examined by conducting differential scanning calorimetric study and estimation of activation energy concerning different phase evolution. The evolution of microstructure has been investigated and analysed by conducting scanning and transmission electron microscopy. Mechanical behaviour has been demonstrated in terms of the results obtained from hardness measurement, tensile testing and fractographic analysis.

Chapter 6 describes the effect of thermo-mechanical controlled processing with varying finish rolling temperature to understand the microstructural evolution and mechanical properties of steel under hot rolling conditions. The thermo-mechanically processed sample has been analysed by conducting X-ray diffraction analysis. The evolution of microstructure has been investigated and analysed by conducting optical microscopy as well as transmission electron microscopy. Mechanical behaviour has been demonstrated in terms of the results obtained from hardness measurement and tensile testing.

Chapter 7 presents the effect of the isothermal holding of samples with or without pre-strain (at room temperature) at cryogenic temperature. The study also includes the effect of the different amount of cold deformation at cryogenic temperature. The phase transformation, microstructural evolution has been investigated by conducting electron backscattered diffraction analysis and scanning as well as transmission electron microscopy. Mechanical behaviour has been demonstrated in terms of the results obtained from tensile testing.

Chapter 8 presents the effect of reversion annealing treatment on samples subjected to cryogenic deformation as well as pre-strain samples. The phase transformation, microstructural evolution has been investigated by conducting scanning as well as transmission electron microscopy. Mechanical behaviour has been demonstrated in terms of the results obtained from tensile testing.

Chapter 9 summarises the specific observations for the present study as furnished in the earlier chapters. Chapter 9 has also mentioned the limitations and gaps left in the present study and in view of that proposes the future scope of work.

2

LITERATURE REVIEW

2.1 Background

Introduction of passivity in ferrous alloy by Faraday around 1836 paved the path way for thedevelopment of a potential class of structural material designated as stainless steel [5]. The attraction for this particular class attained new heights by the discovery of strengthening the alloy with Ni addition and resistant to acid attack withCr addition (> 9 wt.%) by Riley in 1889 and Portevinin 1905, respectively. Austenitic stainless steel was patented in 1912 by Strauss and Krupps. Harry Bearley's experiment in 1912, in which 12.5 wt.% Cr was added to iron (Fe), triggered the commercial production of stainless steels [6]. About in 1914, the medium carbon 14 wt.%. Cr steel was developed as the cutlery material. Subsequently, Monnartz developed the Fe-Cr-Ni steels with the stable austenitic matrix, which was universally designated as 18 wt.% Cr – 8 wt.% Ni steel [7].

Ferritic and austenitic stainless steels found large-scale application for ammonia and HNO_3 plants in America and Europe from 1925. Austenitic stainless steels evolved rapidly to find its use in a wide range of areas such as jet propulsion units, fission, fusion reactor plants, gas turbines, chemical plants, steam power plant, low-temperature technology, food processing industry, biomedicine, petrochemical processing etc. [8].

In the course of plastic deformation, austenite in steel was found to transform into martensite below a characteristic temperature know as M_d temperature (martensite start temperature by deformation). Martensite, so formed, yields higher strength while the toughness was determined by the amount of retained austenite. The formation of deformation induced martensite (DIM) depends on various parameters such as the composition of the material, temperature, amount of deformation (strain), the rate of deformation (strain rate), stress state, pre-strain, stacking fault energy etc. [9-14].

Stacking fault energy (SFE) of austenite, as a function of temperature and composition, governs the dominant deformation mechanism. In austenitic stainless steels, the intersections of shear bands e.g., stacking faults, twins etc. are the potential sites for the formation of embryos of martensite [15-17]. Usually, low deformation levels (i.e. 5-10%) generate ε-martensite and under higher strain levelthe α′-martensite increases at the expense of ε-martensite [18]. The deformation mode is shifted to twinning and then slip from the ε-martensite formation in case of higher stacking fault energy (>20 mJ/m^2) [19]. The amount of α′-martensite changes proportionately with plastic strain (tension) and inversely with compressive strain [15].

The upper limit of the transformation temperature is obtained as [20]:

$$\mathrm{M_{d30}(°C) = 413 - 462(C + N) - 9.2(Si) - 8.1(Mn) - 13.7(Cr) - 9.5(Ni) - 18.5(Mo)} \qquad (2.1)$$

where elements are in wt.%. M_{d30} is the maximum temperature at which austenitic stainless steels produce 50% DIM when subjected to 0.30 true strain. The above equation has been modified [21] by incorporating the effect of grain size (GS) expressed in ASTM grain size number and the modified formula is shown as follows:

$$\mathrm{M_{d30}(°C) = 551 - 462(\%C + \%N) - 9.2(\%Si) - 8.1(\%Mn) - 13.7(\%Cr) -}$$
$$\mathrm{29(\%Ni + \%Cu) - 18.5(\%Mo) - 68(\%Nb) - 1.42(GS - 8)} \qquad (2.2)$$

In the efforts on the enhancement of strength of austenitic steels, the reversion of deformation induced martensite during heating in austenitic steels has drawn special attention [22]. For austenitic stainless steels, significant grain refinement takes place when the deformation induced martensite is subjected to reversion over a temperature range of 450-800°C [22, 23-25]. There are two governing mechanisms for reversion of deformation induced martensite, namely (a) diffusion controlled and (b) shear type. It has been found that in the case of lowering of the martensitic shear reversion temperature by increasing the Gibbs free energy, the transformation between FCC and BCC structure is influenced by the increase in Ni/Cr ratio. Such steels undergo the martensitic reversion in a low-temperature range when Ni/Cr (wt.%) ratio is maintained as high as 0.625 [24]. Thermodynamically, a minimum driving force is required for the shear mechanism to be operative and the lowest possible temperature is 650°C for the 16Cr-10Ni steel [24]. Since the kinetics of reversion is slower in the case of a diffusion controlled process, the longer annealing time is required to complete reversion of deformation induced martensite at low temperatures as compared to higher temperature. Reversion process gets enhanced when the lath martensite is subjected to prior cold working [26]. During reversion annealing, the deformation induced martensite transforms to austenite and the heavily deformed regions of austenite undergo recovery and recrystallisation. At low temperatures, changes in the microstructure of both phases are governed by a diffusion process. Usually above 950°C, reverted austenite grains are induced by high dislocation density owing to operative shear reversion mechanism. Refinement of austenite grains takes place during annealing through the recovery process of the matrix, the formation of dislocation cell and sub-grain, which is similar to the grain refinement mechanism of cold worked austenite.

Grain refinement achieved after reversion of deformation induced martensite to austenite (e.g., $\alpha' \rightarrow \gamma$) contributes significantly toimproving the mechanical property [27, 28]. Reversion mechanism greatly influences grain refinement which improves both strength and toughness in the case of structural steels [24]. Cold rolling followed by recrystallisation is the only way to refine the grains of austenitic stainless steel as it does not respond to phase transformation when subjected to typical annealing temperatures. However, due to high recrystallisation temperature (>900°C) of stainless steels, strengthening by grain refining inherits its limitation. The strengthening effect in the austenite depends in a complex manner on many factors relating to alloy constitution, structure and heat treatment conditions. The high dislocation density of the reversed austenite regions and the presence of stacking faults and twins there in attributes to the strength enhancement of austenite achieved after reversion.

2.2 Family of stainless steels

Several varieties of stainless steels have been evolved in the past, depending upon the composition and properties. However, they are often classified into five different types, named after their microstructures as furnished in Table 2.1 [29].

The austenitic grades have low carbon content (C<0.08 wt.%), with Cr content ranging from 16 to 28 wt.% and the Ni content is in between 3.5 to 32 wt.% [30]. The alloying elements are grouped as ferrite and austenite stabilisers, where Cr acts as ferrite stabiliser and Ni acts as austenite stabiliser.

The fundamental criteria for the selection of stainless steel generally consist of: [31]

i) To survive the service condition with virtually no corrosion.
ii) Adequate resistance against creep and oxidation.
iii) Alloy selection considering the affordability including maintenance over the intended service life.

iv) Stability of strength and ductility (toughness) at ambient and service temperatures.

v) Suitability for intended fabrication and cleaning techniques and procedures.

vi) Resistance to abrasion, erosion etc.

vii) Surface finish and reflectivity.

viii) The magnetic property, thermal conductivity and electrical resistivity.

ix) Sharpness (retention of cutting edge) and rigidity.

Table2.1: Different types of stainless steels [30].

Ferritic	This group of alloys generally containing only chromium, with the balance mostly Fe, are based upon the type 430 composition of 17 wt.% Cr. These alloys are less ductile than the austenitic types and not hardenable by heat treatment.
Austenitic	A family of alloys containing chromium and nickel (and manganese and nitrogen when nickel levels are reduced), generally built around the type 302 chemistry of 18 wt.% Cr, 8 wt.% Ni, and balance mostly Fe. These alloys are not hardenable by heat treatment.
Martensitic	The members of this family of stainless steels may be hardened and tempered just like alloy steels. Their basic building block is type 410 which consists of 12 wt.% Cr, 0.12 wt.% C, and balance mostly Fe.
Duplex	This is a stainless steel alloy group, or family, with two distinct microstructure phases of ferrite and austenite. The duplex alloys have greater resistance to chloride stress corrosion cracking and higher strength than the other austenitic or ferritic [32] grades.
Precipitation hardening	These alloys generally contain Cr and less than 8 wt.% Ni, with other elements in small amounts. As the name implies, they are hardenable by heat treatment.

A comparative analysis of common characteristics among the above mentioned five types of stainless steels is furnished in Table 2.2.

Table 2.2: Comparative analysis of stainless steel characteristics [30, 33].

Ferritic	Martensitic	Austenitic	Duplex	Precipitation hardening
Low content of alloy elements	Higher % of carbon content	Most common and familiar	Austenite + Ferrite	Austenitic, semi austenitic and martensitic
Moderate corrosion resistance	Moderate corrosion resistance	Superior corrosion resistance	Highest corrosion resistance	Moderate corrosion resistance
Lack of toughness in sub-ambient temperature or in thickness greater than 1.5 mm	Hardenable through heat treatment	Hardenable through cold deformation	Very high strength	Highest strength
Magnetic	Magnetic	Non magnetic	Magnetic	Magnetic or non magnetic
Lack of ductility in case required > 30% elongation	Hardness and strength is high	Superior toughness	Superior toughness	Superior toughness
Less expensive	Less expensive	Expensive	Expensive	Expensive
Application: Exhaust pipe in auto industry	Application: Knife blades, shafts and surgical instruments etc.	Application: Kitchen sink, food processing, chemical industry, others	Application: Petrochemical industry etc.	Application: Aerospace and high technology industries etc
Susceptibility to high-temperature embrittling phases when moderately alloyed.	Susceptible to corrosion	Moderately resistant	Susceptible to corrosion at high temperature exposure	Susceptible to corrosion

2.3 Stability of austenite

To achieve the desired stability, the free energy of austenite is lower than that of ferrite with the addition of austenite stabilisers. The driving force for the γ→α transformation increases with undercooling below a characteristic temperature, known as T_0. Figures 2.1(a) and (b) revealthe variation of Gibbs free energy and T_0 temperature withthe nickel additions in 301LN stainless steel respectively as estimated by ThermoCalc (database TCFE 2000, S-version, 2000). It is apparent that increase in Ni content lowers the T_0 temperature, thus driving force for the γ→α transformation gets reduced at a fixed temperature (e.g., room temperature). Further, with the decrease in T_0 temperature, the kinetics of diffusion required to transform to γ→α also reduces. Thus the metastable austenite (γ) state can be trapped if T_0 is low enough along with the combination of lowered driving force and slow kinetics of transformation [34].

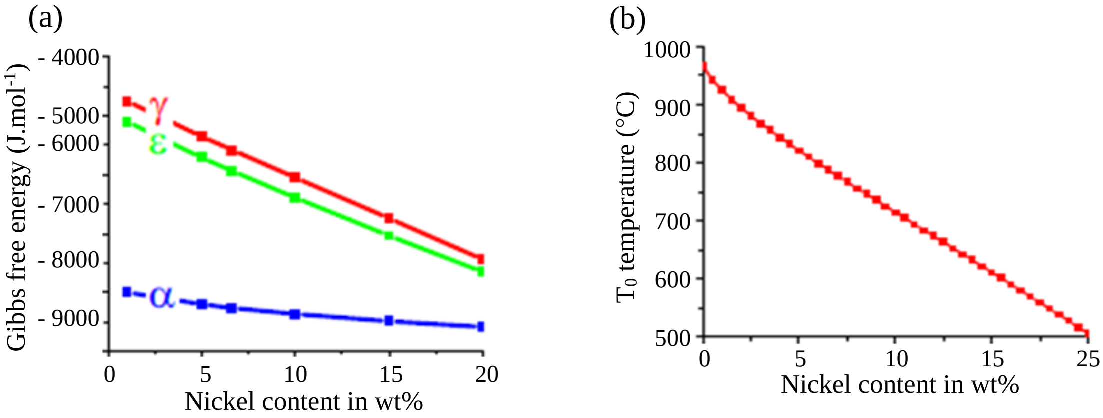

Figure 2.1: Relative stability of phases predicted by Thermo-Calc [35] using the composition corresponding to the 301LN stainless steel at atmospheric pressure (a) Evolution of the Gibbs free energy of FCC (γ), HCP (ε) and BCC (α) phases at room temperature and (b) Evolution of the T_0 temperature with variable nickel content [34].

The appearance of a third phase denoted by ε,having the energy intermediate between BCC (α) and FCC (γ) phases has also been illustrated in Figure 2.1(a), which plays an important role in the respect to the deformation of austenitic stainless steels. The crystal structure of this phase is hexagonal close packed (HCP). There is a close association between ε phase, stacking faults and twins. Typical values of the intrinsic SFE value of FCC materials have been compared in Table 2.3. The intrinsic stacking fault energy of austenitic stainless steels is low in comparison to most metals which liesin between 6 and 60 mJ/m^2 [36] and is strongly influenced by the composition [21, 37, 38]. For example, the SFE is directly proportional to carbon content, whereas nitrogen and silicon show an inverse dependence [21]. It is also to be noted that temperature has astrong effect on SFE in austenitic stainless steels compared to other pure FCC metals [39].

Table 2.3: Experimentally determined stacking fault energies (SFE) of various FCC materials at room temperature.

Material	301LN	316L	304	Ag	Cu	Ni	Al
SFE (mJ/m^2)	14	14	17	22	78	90	166
Reference	[40]	[41]	[37]	[42]	[42]	[37]	[42]

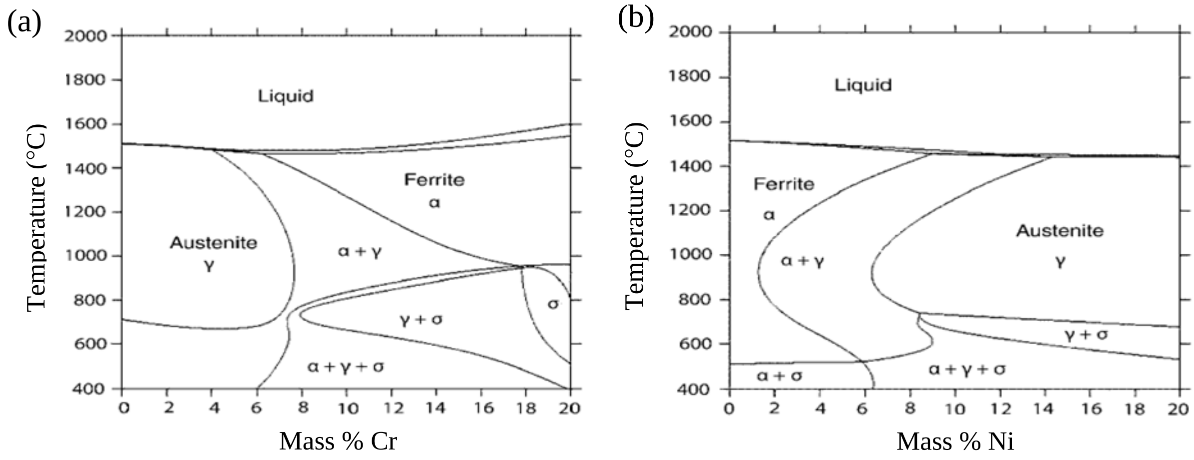

Figure 2.2: (a) Iron-chromium phase diagram at 8wt.% nickel and (b) iron-nickel phase diagram at 18wt.% chromium.

The phase equilibrium, as a function of composition over the entire range of these alloys, is illustrated in Figures 2.2(a) and (b). Martensite produced through deformation or thermal gradient appears in two different forms. The α′ form is having BCC crystal structure and magnetic in nature, whereas ε phase is having HCP crystal structure and nonmagnetic in nature. Stacking fault energy of the alloy determines the formation of ε or α′ phase. In stainless steels, presence of alloying elements in sufficient quantities causes precipitation of second phases in the form of intermetallics, which has been described by σ phase (brittle phase) in above phase diagrams (Figures 2.2(a) and (b)). Stacking fault energy can be calculated by using Eq. 2.3, where it is mostly dependent on chemical composition [38]. Temperature dependence of stacking fault energy is calculated by using Eq. 2.4 [43].

SFE (mJ/m^2) = -53 + 6.2(Ni) + 0.7(Cr) + 3.2(Mn) + 9.3(Mo) (wt.%) (2.3)

$\gamma_{SFE} = \gamma_{SFE}^{RT} + 0.05(T - 293)$,where T is the temperature in Kelvin. (2.4)

An alloy with lower stacking fault energy is favourable for the formation of epsilon martensite (ε). Slip occurs between (111) planes in the FCC structure upon deformation. The structure will look like a series of ABCABC atom arrangements when viewed from (111) planes. ABCA/CAB structure can generate due to slip involving partial dislocations between planes. HCP structure is generated from this so-called stacking fault. This HCP structure (ε phase) can be formed readily in the case of lower stacking fault energies [33]. Another way of looking towards stacking fault can be considered as two partial dislocations with a faulted material between them. These partial dislocations cannot slip past one another readily and thus pile up at crystal imperfections. This piling up of dislocations leads to the increased work hardening rate.

2.4 Deformed microstructure of austenite

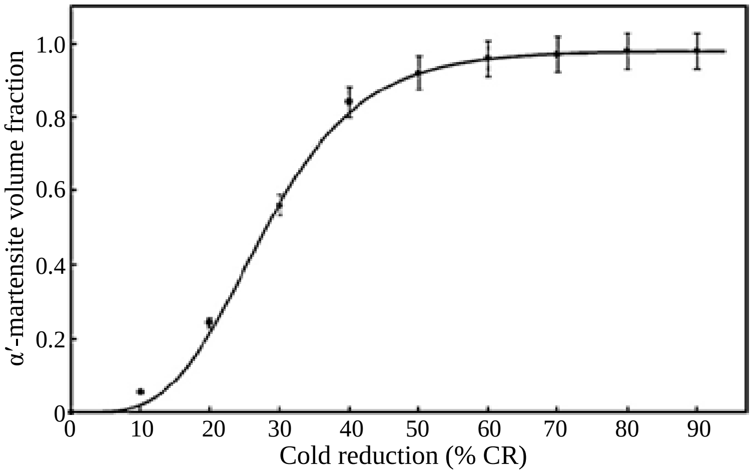

Figure 2.3: Increase in α′-martensite volume fraction with respect to cold deformationfor AISI304L material when deformed at 0°C [44].

Microstructural evolution in austenitic stainless steels during the deformation induced transformation of austenitic into α′-martensite, with the variation of cold deformation is exemplified in Figures 2.3, which shows the sigmoidal variation of the volume fraction of martensite against % reduction during cold rolling at 0°C. This behaviour is attributed to the formation of several nucleation sites (shear band interactions) at the initial stages of deformation. The shear bands can be in the form of ε-martensite, mechanical twins, or dense stacking fault bundles [45, 46]. In higher deformation levels, the α′-martensite content increases with the deformation and below approximately 70% it gets saturated.

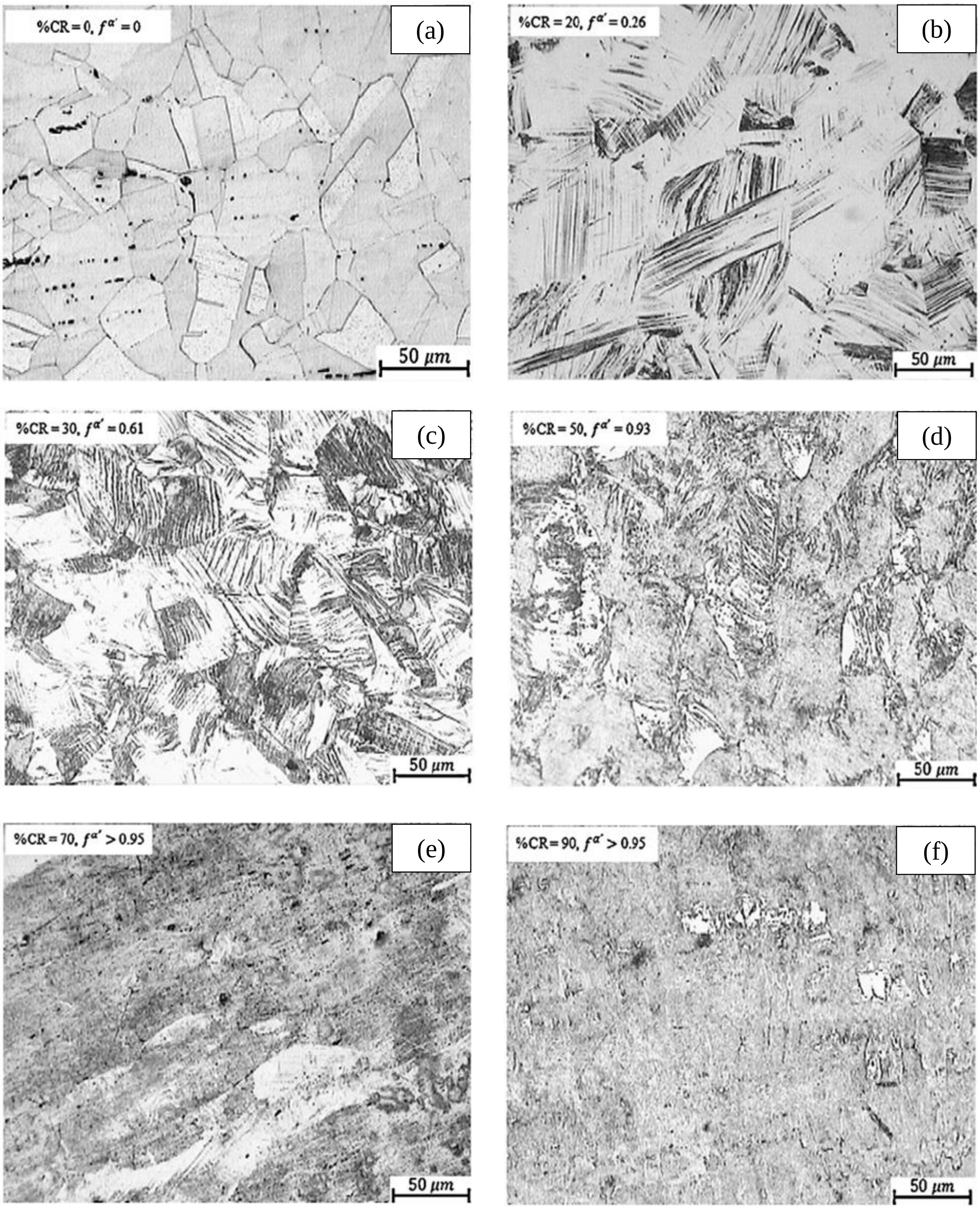

Figure 2.4: Optical micrograph of (a) as-received as well as cold deformed samples at 0°C for (b) 20%, (c) 30%, (d) 50%, (e) 70% and (f) 90% of austenitic stainless steel. Volume fraction

of α′-martensite is mentioned at the top of each micrograph [44].

The optical micrographs corresponding to the variation of cold reduction are shown in Figure 2.4. Figure 2.4(a) reveals the microstructure of solution treated as-received sample, where austenite grains are visible along with the presence of annealing twins. Figure 2.4(b) to (f) show the dark contrast of martensite within the austenite matrix. It also reveals an increase in α′-martensite content with the increase in the amount of deformation. The α′-martensite nuclei are tiny and often located at the shear band intersections. However, relatively bigger α′-martensite particles are visible even at low volume fractions, and with increasing their volume fraction, irregular blocky nature of α′-martensite is visible in the micrograph.

2.5 Effect on the mechanical properties

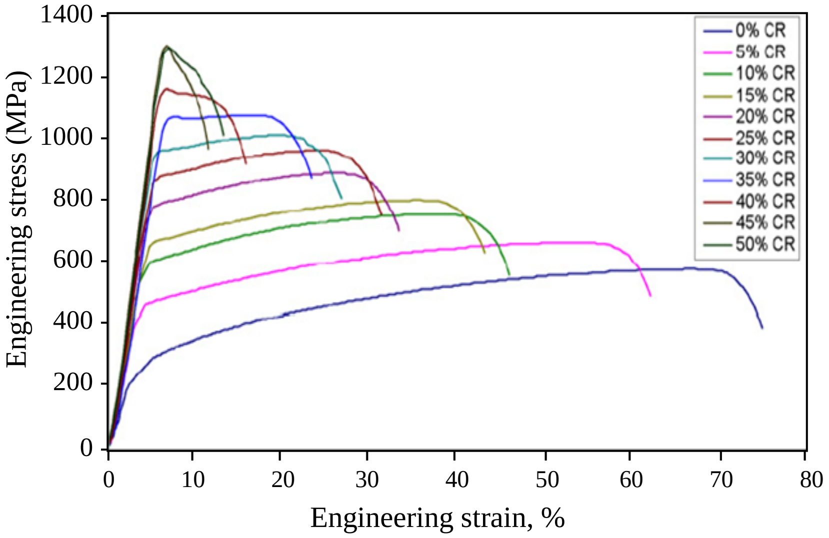

Figure 2.5: Stress-strain curves with respect to the different amount of cold deformations provided at 0°C [47].

Stress-strain variation obtained from the deformed 304 austenitic stainless steel specimens at ambient temperature is illustrated in Figure 2.5 with the reference plot of an undeformed specimen to demonstrate the effect of rolling on the shape of the curve. The role of plastic deformation in the strengthening of this stainless steel is evident from the variation of yield strength, tensile strength and ductility with the amount of cold rolling. The gap between the yield strength and tensile strength curves becomes narrower as the percentage of cold rolling is increased. On the other hand, the ductility of as-received specimen continues to reduce the progress of deformation.

2.6 Mechanisms for deformation induced α′-martensite formation

In austenitic stainless steels, the complex relationship between microstructure, plastic deformation and martensite fraction is attributed to the formation of both ε-martensite and α′-martensite simultaneously during straining and also on the role of formation of ε-martensite in the nucleation of α′-martensite. Earlier studies [15, 48, 49] support the mechanism that the strain induced γ→ε transformation occurs prior to the formation of α′-martensite and conjecture that ε-martensite is important for the nucleation of α′-martensite. The strain induced ε-martensite appears as thin plates, as illustrated in Figure 2.6.

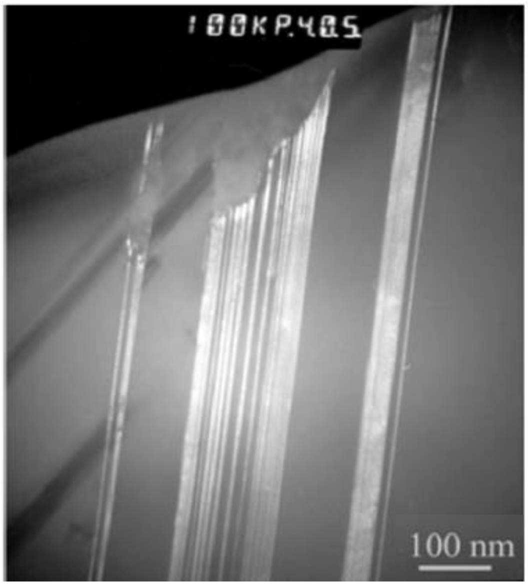

Figure 2.6: Plates of ε-martensite in grade 304L after a 5% tensile strain at -196°C [50].

The structure of ε-martensite is consistent with a stacking fault lying on every second $\{111\}_\gamma$ plane. This results in the Burgers orientation relationship as [51]:

$$\{111\}_\gamma \,//\, \{0001\}_\varepsilon$$

$$\langle 110\rangle_\gamma \,//\, \langle 2110\rangle_\varepsilon$$

which, leads to only four distinguishable variants of ε-martensite out of 12 variants involved in shape deformation [48, 52, 53].

One obvious mechanism involved inthe formation of ε-martensite is the coordinated motion of $a/6\,\langle 112\rangle$ Shockley partial dislocations. The similarity between the structure of ε-plate and a deformation twin is illustrated in Figure 2.7. While a twin can be described as a stacking fault on every adjacent $\{111\}_\gamma$ plane, a plate of ε-martensite requires only one stacking fault on every second plane. This has led to the hypothesis that the formation of ε-martensite is similar to the mechanism of formation of deformation twins [54]. Rémy and Pineau [53, 55] have suggested that there is a continuous transition from the deformation twining to the ε-martensite formation with decreasing stacking fault energy.

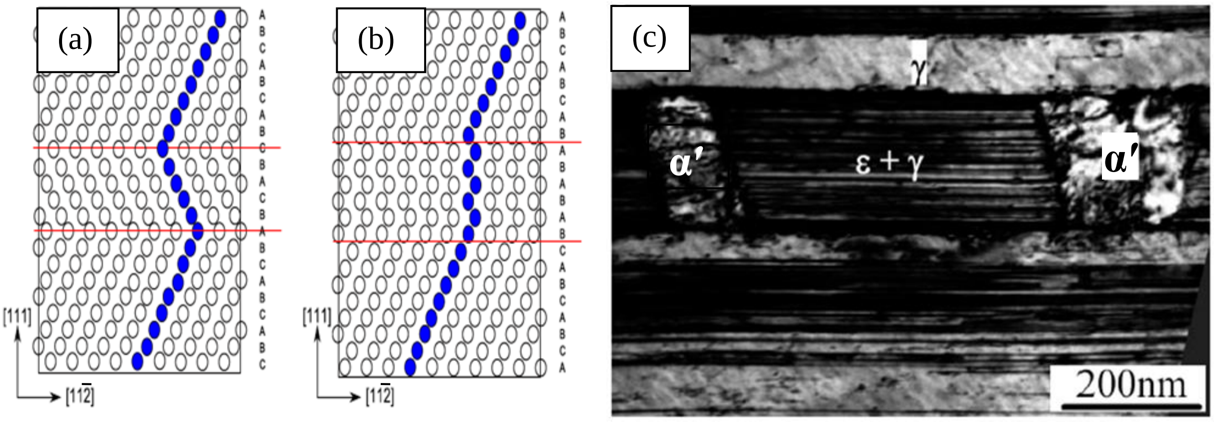

Figure 2.7: Schematic representation of (a) a twin, (b) a thin plate of ε-martensite. The atoms belonging to a {100} plane prior to the transformation are underlined to help visualise their motion and (c) TEM micrograph of the α′-martensite island formed within a ε-band [41].

Despite the apparent similarities, it is important to understand the difference between the formation of ε-martensite and twins in austenitic stainless steel. Earlier, theformation of ε-martensitein Fe-Mn-Al-Si alloy over a range of temperature is attributed to the presence of extrinsic stacking faults. On the other hand, twins form due to the presence of intrinsic stacking faults [56]. This differs from the earlier theory, which has proposed that intrinsic stacking faults are precursors for ε-martensite, while extrinsic stacking faults are precursors for twinning [57, 58]. Plates of ε-martensite are often imperfect and consist of thinner ε-layers with the presence of retained austenite in between [58, 59]. This retained austenite may or may not be twinned [41, 60]. Such ultrafine plate-like packets of stacking faults, in the absence of high-resolution microscopic analysis, is referred in the literature as “shear bands” [46] instead of ε-martensite or deformation twins.

Earlier, two notable mechanisms have been proposed for ε-martensite formation, which is(a) pole mechanism [61] and (b) deviation based mechanism [62]. In all the cases, the formation of ε-martensite is localised in nature which is traced to the existence of extended stacking faults rather than by nucleation at grain or twin boundaries [57, 63-65]. The deviation based mechanism also validates the requirement for overlapping of stacking faults in nucleation of ε-martensite [66]. It has also been suggested that the formation of ε-martensite may obey the Schmid law and in doing so, it occurs when the resolved shear stress on some of the slip system of austenite reaches a critical value. The highest Schmidt factor on the $\{111\}_{\gamma}\langle 1\bar{2}1\rangle_{\gamma}$ slip system of austenitic grains is responsible for theformation of ε-martensite [67]. The same slip system was found to verify the Schmid law for the apparition of mechanical twins [41, 68] in Fe-Mn steels.

For deformation at low levels of strain, the microstructures of austenitic stainless steels are often characterised by the presence of ε-martensite. Figure 2.8(a) illustrates that ε-martensite is always represented by a small fraction of the total volume in microstructure [69]. It is typically found that the volume fraction of ε-martensite significantly exceeds that of α′-martensite after only a few percent plastic strains. In these steels, the α′ phase is comparable to the body centred tetragonal (BCT) crystal structure, which is obtained by quenching of carbon steels [70-73]. However, the interstitial content of austenitic stainless steels being low indicates that the tetragonality of the martensite is nearly zero [74, 75].

Figure 2.8(b) illustrates the formation of α′-martensite at the intersection between ε-martensite. Although the current opinion favours the concept that ε-martensite forms prior to α′ [50], there is no such consensus on whether the ε-martensite appears as an intermediate to α′ [16, 39, 44, 76] or if it is generated to accommodate plastic strains [76, 77]. Apart from nucleation at ε intersections, heterogeneous nucleation of α′ phase takes place on other deformation induced imperfections present in austenite matrix as well as at deformation twins [19, 64, 78-82]. The imperfections acting as the potential nucleation sites are presented in Table 2.4. It has also been observed that the formation of α′ taking place at the intersection between a plate of ε and a deformation twin [18] or an annealing twin [50], or at the intersection of shear bands [83]. Twin boundaries are generally less effective nucleation sites than ε-martensite [50, 84]. Intersecting features are not always a necessary condition for the nucleation of α′-martensite. It can take place within a single ε plate [85, 86].

Grain boundaries as nucleation site are less prominent unless the nickel content is higher than that of traditional austenitic stainless steels [39, 87, 88], or in submicron austenitic grains obtained after severe plastic deformation like equal channel angular pressing (ECAP)

[89]. However, the α′-martensite has also been observed to form directly from a slip in the austenite [76, 90].

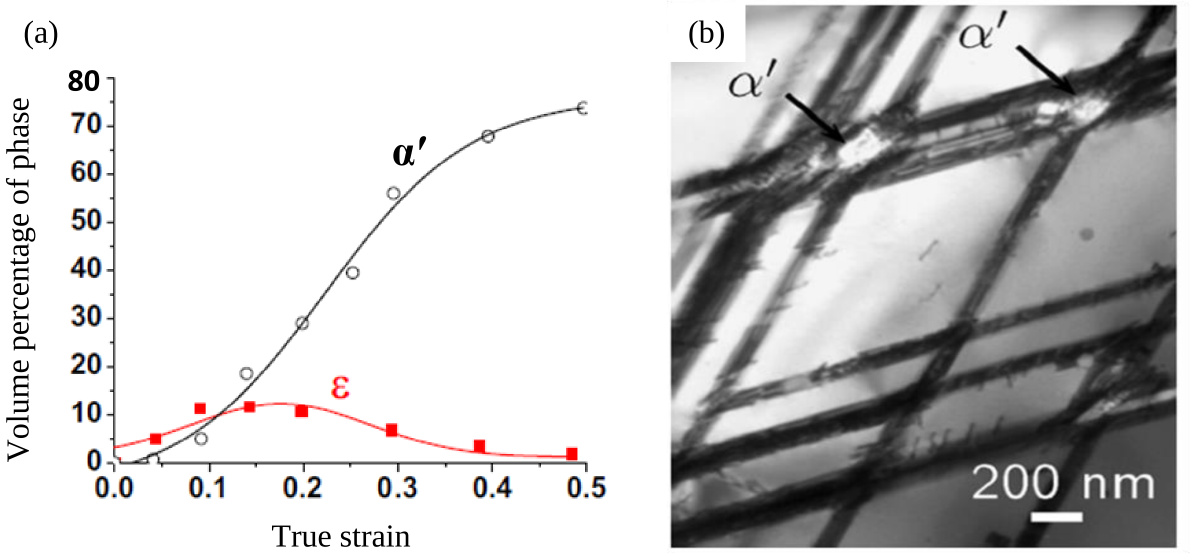

Figure 2.8: (a) Evolution of the volume percentage of ε and α′-martensite formed during room temperature tensile deformation of grade 301 steel. The volume percentage were measured by X-ray diffraction [79] and (b) Nucleation of α′ in grade 316 steel after a 5% tensile strain at -196°C. The dark fault bands are associated with ε-martensite while α′-martensite is highlighted at some, but not all, intersections [50].

Table 2.4: Various nucleation sites for α′-martensite.

Type of nucleation	References
Intersection between two ε plates	[10, 16, 78, 91-93]
Intersection between two deformation twins	[19, 64, 78-82, 94]
Intersection between ε and a deformation twin	[18]
Intersection between ε and an annealing twin boundary	[50, 95]
Nucleation within a single ε plate	[85, 86]
Grain boundary nucleation from γ	[39, 87, 88, 96]
Direct nucleation from γ	[76, 77, 90]

2.7 Techniques for quantification of deformation induced martensite

Quantification of the volume fraction of different phases constituting the microstructure through experimental techniques is important to understand the relationship between deformation and martensitic phase transformation. Phase fractions from X-ray diffraction and neutron diffraction can be estimated from the ratios of the intensities of Bragg peaks (e.g., Dickson's method [97]) or from whole pattern Rietveld fitting [98, 99]. However, such techniques inherit some limitations due to the dependency of diffraction peak intensity upon crystallographic orientation as well the overlap between peaks can influence peak fitting. Various techniques to circumvent such limitations have been proposed [100,101]. Metallographic techniques (optical, scanning electron microscope (SEM), electron backscattered diffraction (EBSD)) have also been attempted to measure the phase volume fraction directly from micrographs [12]. Table 2.5 shows the various techniques for measurement of martensite content. These techniques alsohave their own limitation due to the difficulty of resolving the fine scale phases (particularly ε-martensite) and the poor statistical sampling of the microstructure by these techniques.

Table 2.5: Various techniques for measurement of martensite content [34].

Technique	Probed volume	Advantages	Disadvantages
Magnetic measurements (permeability or force)	Bulk	High accuracy	Magnetic saturation not always reached, Edge effects, Calibration needed
Neutron diffraction	Bulk	High penetration depth (~ 20mm)	Need access to large facility
X-ray diffraction	Surface layer	Fast and relatively easy	Small penetration depth (~ 10μm), Texture effects
Metallography / SEM / EBSD	Surface layer	Spatial information	Phase recognition is not straight forward
Mössbauer	Thin foil	High accuracy	Sensitive to chemistry

2.8 Characterisation through Electron BackscatteredDiffraction (EBSD) method

Electron backscattered diffraction (EBSD) is a microstructural-crystallographic characterisation technique to study any crystalline or polycrystalline material [102]. The technique involves understanding the structure, crystal orientation and phase of materials in Scanning Electron Microscope(SEM). Typically it is used to explore microstructures, revealing texture, defects, grain morphology and deformation and recrystallisation. It is also used to find out crystal orientation of the material located within the incident electron beams interaction volume. Thus by scanning the electron beam in a prescribed fashion (typically in a square or hexagonal grid, correcting for the image foreshortening due to the sample tilt) results in many rich microstructural maps. These maps can spatially describe the crystal orientation of the material under investigation and can be used to examine micro-texture and sample morphology. EBSD is an important technique to characterise materials manufactured through iterative processes. The distribution of grains depending on sizes and grain boundaries based on its misorientation angle can be determined through this effective technique. It can be combined with complementary techniques within the SEM for phase discrimination. Coincident lattice boundaries and its distribution can be identified through this technique. Various statistical tools can be used to measure the average misorientation, grain size and crystallographic texture. From this dataset, numerous maps, charts and plots can be generated. From orientation data, a wealth of information can collect, which in turn help in the understanding of the microstructure and processing history of the investigated specimen. Recent developments include understanding the prior texture of parent phases at elevated temperature, the storage and residual deformation after mechanical testing, the population of various microstructural features, including precipitates and grain boundary character. Traditionally these types of studies have been carried out byX-ray diffraction (XRD), neutron diffraction and/or electron diffraction in a TEM.

2.9 Factors influencing strain induced martensitic transformations in austenitic stainless steel

Table 2.6: Individual parameters affectingstrain induced martensitic transformation enumerated below.

Intrinsic to microstructure		Intrinsic to test conditions	
(a)	Chemical composition	(d)	Test temperature
(b)	Grain size	(e)	Strain rate
(c)	Dislocation density	(f)	Prior strain and strain path

The complex nature of the strain-induced martensitic transformations in austenitic stainless steels is attributed to the dependence with respect to a large number of intrinsic and extrinsic parameters as mentioned in the following Table 2. 6.

Effects of these individual parameters on strain induced martensitic transformation are described below:

(a) Influence of composition

It is well established that transformation of austenite to martensite during deformation contributes significantly to the formability. The extent of transformation is believed to be dependent principally upon alloy chemistry [103], deformation temperature and the extent of plastic strain [9, 15, 20], M_s, M_{d30}, the volume percent of martensite versus temperature, stacking fault energy, and Cr and Ni “equivalents”. Therefore, prediction of formability in stainless steels like 304 type remains difficult and a wide variety of compositional modifications are made to fine tune the formability for specific applications. In such steels, the degree of metastability is to the large extent a function of alloy composition. Leaner alloys such as type 301 will be less stable than those with more alloying, such as type 305 or 316 stainless steel. Therefore, strain induced transformation of austenite to martensite in type 301 will occur at much higher temperatures than in type 316. However, type 304 being in the mid-range of alloying content for austenitic stainless steels (typically designated as 18wt.% Cr and 8wt.% Ni), strain induced transformation behaviour is particularly sensitive to minor changes in chemistry in this range of alloying. One of the key parameters used to characterise the stability of austenite is the M_{d30} temperature. It is the temperature at which true strain value of 0.30 will induce the formation of a 50% volume fraction of α′-martensite.

Quite small variations in chemistry within the type 304 designation can have a substantial effect on the austenite stability and therefore formability. The M_{d30} temperature in 304 austenitic stainless steel may be substantially influenced by three factors such as grain size, Cr concentration and Mn concentration. Statistical analysis did not result in a regression equation having a reliable degree of predictive capability [103].

The effect of individual element effect on the formation of α′-martensite volume fraction has been predicted as illustrated in Figures 2.9(a) to (j). Figures 2.9(k) to (o) indicate the influence of strain rate, temperature, grain size, true stress and true strain, respectively on the formation of DIM in austenitic grade stainless steels, predicted by the model.

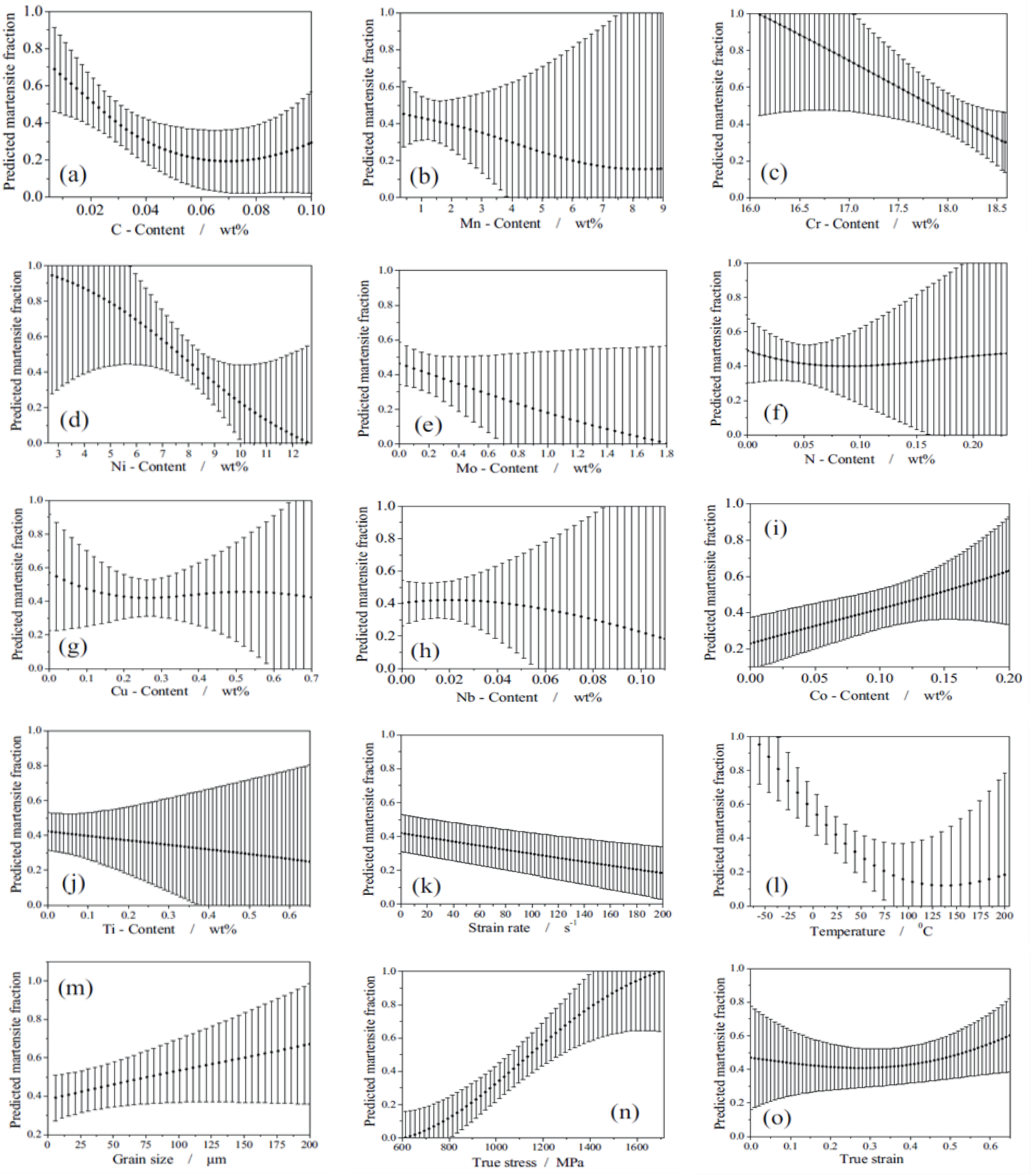

Figure 2.9:Influence of (a) C, (b) Mn, (c) Cr, (d) Ni, (e) Mo, (f) N, (g) Cu, (h) Nb, (i) Co, (j) Ti, (k) strain rate, (l) temperature, (m) grain size, (n) true stress and (o) true strain on the formation of DIM in austenitic grade stainless steels, predicted by the model. Note: the small error bars indicate that the scatter in the database is very small and the large error bars suggest lack of sufficient data in the range examined [104].

(b) Effect of grain size

Grain size refinement leads to the reduction in M_s temperature for both the thermally induced γ→α′ [105] and strain induced γ→ε-martensite [106, 107]. Grain size refinement of austenite can completely suppress the α′-martensite transformation [108, 109]. Similar characteristics are evident in the strain-induced ε-martensite as found in Fe-Mn steels, whereas by reducing the grain size from 40 μm to 10 μm, the γ→ε transformation got suppressed [110] owing to the presence of numerous Σ3 twins in small grains. Such grains act as an obstacle to the growth of the ε-martensite platelets by impeding the motion of the partial dislocation. As an alternate process, the large austenitic grains allow the formation of stacking faults along a large number of planes, which in turn lead to the higher probability of finding nucleation sites (for ε) formed by the overlapping of faults [110]. The effect of grain size on transformation (γ→α′) kinetics and mechanical response in metastable austenitic stainless steels are well documented for the grain size range in between 10 to 200 µm [111], whereas very few experiments have been reported with ultrafine grain sizes in sub-micrometer or in nanometer (average grain size 350 nm) range [89, 112]. Grain size refinement has generally been used to promote stability of γ with respect to the strain-induced formation of both ε [113] and α′-martensite [114, 115]. Direct observations are reported for a reduction in the transformation rate to α′ with respect to decreasing grain size [116-121]. Exceptions have also been reported, whereas in the case of grade 304 austenitic stainless steels, the α′ transformation rate increases with decreasing grain size [122, 123]. Figure 2.10 illustrates examples of the contradicting behaviour of austenitic stainless steels.

Attempt has been made to rationalise the grain size dependence of the γ→α′ transformation mechanism, where the coarse austenite grains of approximately 40 µm size would form α′-martensite at the intersections of shear bands (ε-martensite, deformation twins, stacking faults) and the transformation to martensite occurs gradually with cooling below martensite start temperature [96]. In case of submicron austenitic grains, the grain boundary acts as preferential nucleation sites for α′-martensite formation.

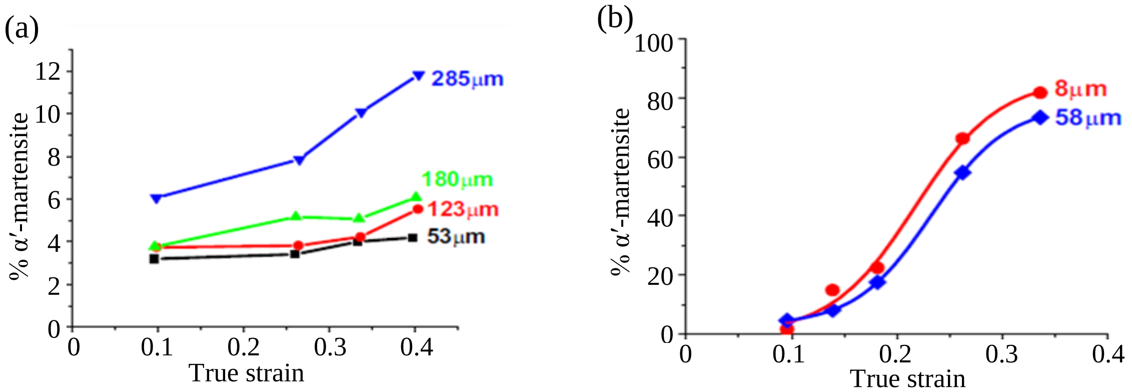

Figure 2.10: Illustration of two different behaviours of the transformation kinetics as a function of grain size. Grade 304 steel deformed in tension (a) at room temperature [119] and (b) at -50°C [123].

(c) Effect of dislocation density

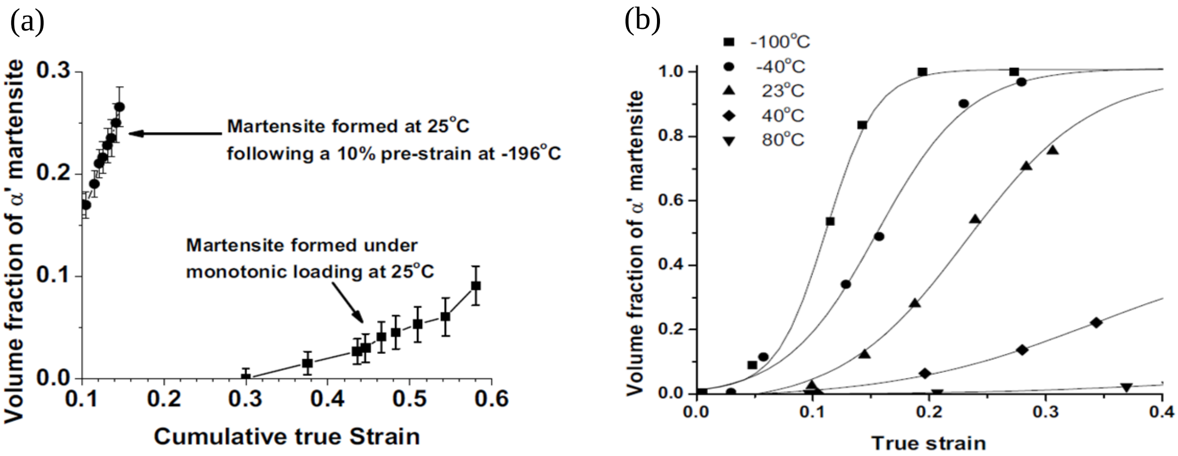

Figure 2.11: (a) Evolution of martensite volume fraction in 316L stainless steel during room-temperature deformation and after straining at -196°C [50] and (b) Effect of deformation temperature on the γ→α′ kinetics of grade 301LN [124].

Initial microstructure has significant importance in the transformation of metastable austenitic stainless steels. Such example is reported for 316L alloy when the steels were subjected to 10% tensile strain at -196°C [50]. The pre-strained material was subsequently allowed to return to room temperature and the tensile deformation continued. Although, the rate of formation of α′-martensite in this alloy was found to be low at room temperature, after pre-straining at -196°C, the transformation rate was found to be extremely high as shown in Figure 2.11. When the situation was reversed by pre-straining at room temperature followed by tensile testing at -196°C, the subsequent formation of α′ at low temperature resulted into the formation of a Lüders-like band which propagated through the material [50]. The amount of α′-martensite within the localisation band was higher than that outside the band as indicated by the observation.

The rate of α′-martensite transformation is therefore found sensitive to the microstructure formed by plastic deformation and thus, to the presence of forest dislocations and other deformation-induced defects. Apart from the microstructural effects, bulk mechanical testing conditions can also have notable effects on the transformation kinetics for metastable austenite. The test temperature is one of the important parameters among them. Figure 2.11 (b) illustrates that in the case of a 301LN stainless steel, the rate of formation of α′ is inversely proportional to temperature. This observation is consistent with a wide range of other alloys [20, 116, 124-127]. The decreasing rate of transformation with increasing temperature is attributed to the reduction in the driving force for transformation from γ→α′ and γ→ε and the associated rise in the stacking fault energy of the austenite, which is linked to the formation of ε-martensite, with increasing temperature. In the case of 304 grade, the increase in temperature from 20°C to 80°C reduces $\Delta G^{\gamma\rightarrow\alpha'}$ by 300 $J.mol^{-1}$ and $\Delta G^{\gamma\rightarrow\varepsilon}$ by 150 $J.mol^{-1}$ while stacking fault energy increases by 4 mJ/m^2 [39]. Most metals exhibit relatively low strain rate sensitivity, but stainless steels are the exception. This rate sensitivity is a direct effect of deformation induced heating of sample which overwhelms the possible intrinsic effects of strain rate on mechanical response even for relatively moderate increases in strain rate.

The heating effect originates from the energy dissipated by the motion of dislocations and the latent heat of the phase transformation. Figure 2.12 shows that increasing the strain rate by one order of magnitude during the tensile test of grade 204M causes an increase of sample temperature at the end of the uniaxial tensile test and therise in temperature is enough for a reduction in the rate of transformation [128-130]. It has also been reported that the increasing strain rate promotes the formation of microscopic shear bands such as ε-martensite [78, 131-133], which is best observed at low strains. Since the effects of self-heating tend to dominate the material response at larger strains, no clear idea can be provided on ε-martensite formation under this condition. The influence of imposed stress and stress state on the formation of thermal martensite are well known, whereas the strain induced martensitic transformations are more complex owing to the path dependence of plastic deformation. It is therefore often difficult to deconvolute the effects arising from the transformation being stress-assisted and/or from the plastic strains generating different nucleation sites depending on the strain path.

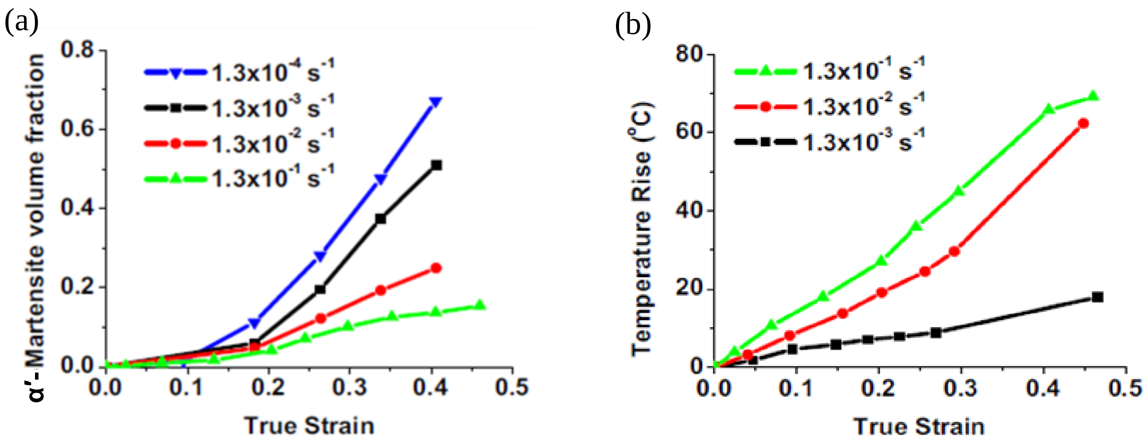

Figure 2.12: Effect of strain rate in grade 204M (a) on the γ→α′ kinetics and (b) on the sample temperature [129].

Determining a definite correlation is difficult due to conflicting results for different modes of mechanical loading compared through transformation kinetics and mechanical response. Comparison between the effects of uniaxial tension and compression reveals that the rate of the γ→α′ transformation was higher in uniaxial tension than either in compression or torsion, which is depicted in Figure 2.13(a) [134,135]. Figure 2.13 (b) shows a variation of α′-martensite volume in tension as well as under compression. Tension, causing an increase in the volume, promotes the γ→α′ transformation and suppresses the formation of ε phase, where as the reverse effect is observed under compressive loading. However, a contradiction to this result also exists where compression resulted in the formation of more α′ than tension, which proves complexity of the transformation mechanism [136, 137].

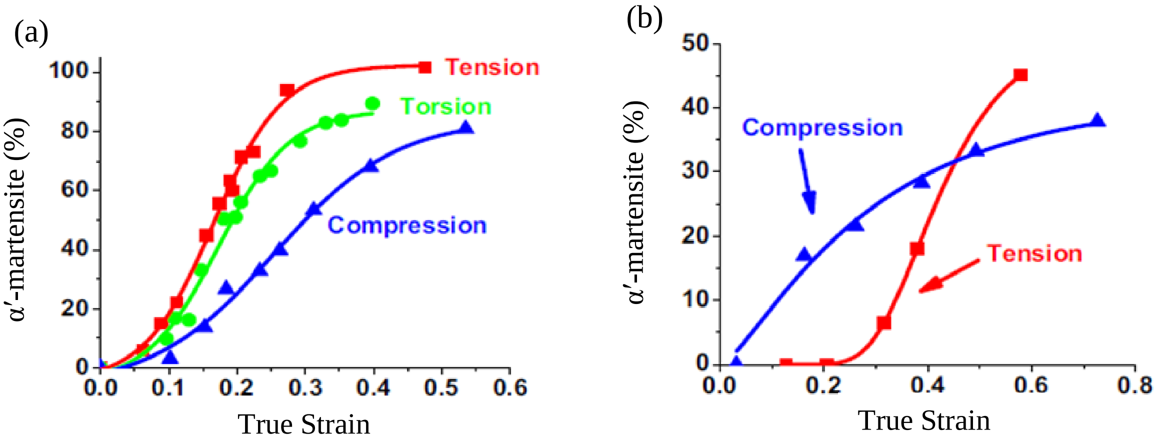

Figure 2.13: (a) Grade 304 deformed at -196°C along 3 different paths, at a constant loading rate. The α′ percentage was measured by X-ray diffraction [134], (b) Difference between tension and compression performed at room temperature on grade 304. This difference is attributed to the deformation induced anisotropy [136].

Figures 2.14(a) and (b) present the relation between the volume fraction of α′-martensite and ε-martensite and the strain corresponding to the three types of loading *viz*., tension, torsion, and compression. A comparison of the curves shows that, depending on the type of loading, the process of the martensitic transformation occurs with different intensities. Tension causes the more intense formation of ε phase than torsion and compression.

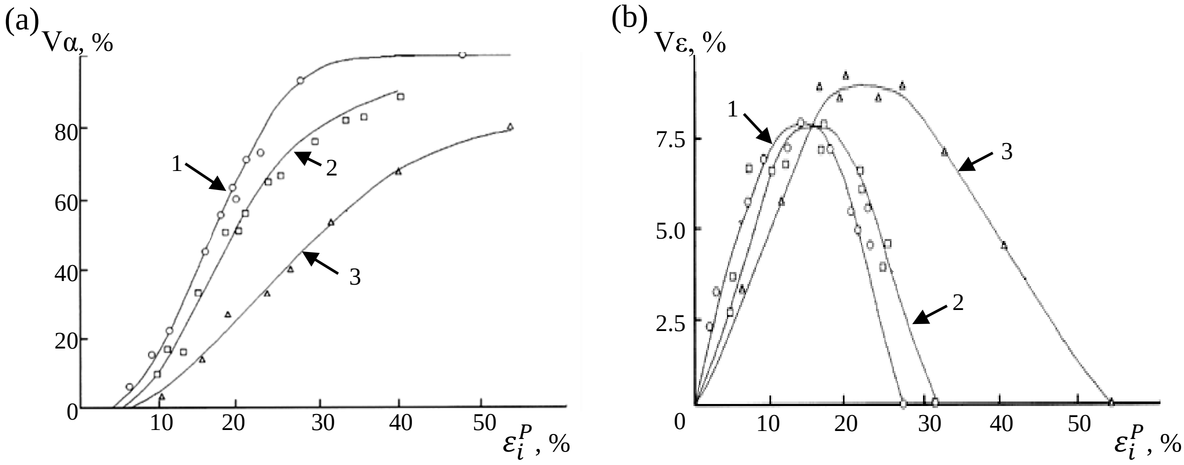

Figure 2.14: The volume percentage of (a) α′ phase and (b) ε phase in 18Cr-10Ni austenitic stainless steels [134] versus the plastic strain intensity under tension (1), torsion (2) and compression (3).

Figures 2.14(a) and (b) illustrate that, the curves in torsion and compression have a smaller slope than in tension and the maximum amount of α′-martensite is reached with higher degrees of straining. The plots also point out that the kinetics of the γ→α′ transformation differs significantly from the kinetics of formation of the α′-martensite as the hexagonal ε-martensite is already formed in the early stages of deformation (traces of ε phase are observed at deformations of 1% approximately), while the γ→α′ transformation do not commence up to 5% deformation. It can be noticed from the plots that, type of loading influences the volume fraction of ε-martensite to a significant extent, especially at large deformations. For all types of loading conditions, the maximum ε phase fraction is approximately the same (8-9%) except the fact that significantly higher range of deformation is required in case of compression than that for tension. The ε phase is absent in the pre-failure state as well as in the failed specimens. Volume change during martensitic transformation is the main reason for the above difference. The tensile loading condition promotes the formation of α′-martensite formation (expansion of volume), whereas during compression reverse effect is observed through the formation of ε-martensite.

At cryogenic temperature, tensile loading significantly increases the strain hardening of the austenite owing to phase transformation and the same is manifested in three stages [134]. First, a rapid increase is caused by work hardening of austenite as well as by the formation of coarse dispersed ε-martensite leading to a hardness value measuring 40% higher than that of austenite. In the second stage, a decrease in strain hardening is noticed owing to a practically imperceptible increase in the volume fraction of ε phase and the finely dispersed α′-martensite, which formed in a small quantity and makes an insignificant contribution to hardening. In the third stage, strong hardening of the steel is witnessed, which occurs primarily as the result of the intense formation of the α′ phase. The features of strain hardening during compression under low temperature are preserved but less pronounced [134].

Differences in the evolution of texture are observed between tension and compression which has been rationalised by using Von Mises equivalent strain [136]. It has been found that under biaxial stress α′ formation starts at lower levels of strain [132]. This observation is found consistent with the finding that the intersection of “shear bands” such as ε-martensite, twins, bundles of stacking faults etc., started at a lower strain along that path [78]. For a higher level of stress triaxiality, the γ→α′ transformation occurs with the increased rate of transformation at crack tips [138]. Under a wide range of stress states, the increased rate of γ→α′ martensitic transformation varies from simple shear to uniaxial tension [124, 134, 139], which is illustrated in Figure 2.15.

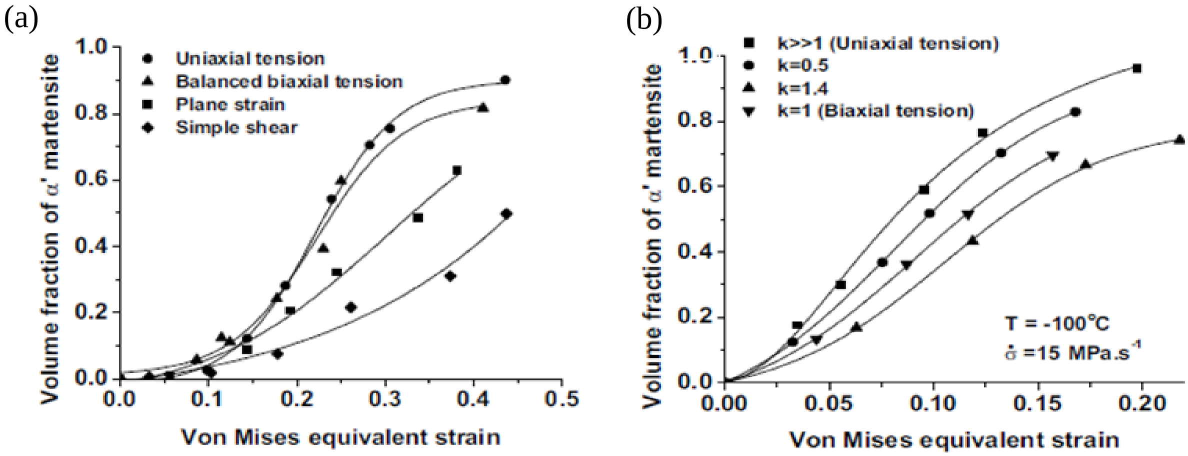

Figure 2.15: Kinetics of two austenitic stainless steels for different loading combinations. (a) Quantification of kinetics by saturation magnetic measurements in grade 301LN steel [124] and (b) 18-10 austenitic stainless steel for various ratios of principal stresses (denoted by k) [134].

(d) Effect of test temperature

When plastic strain is applied to 304 stainless steel sample at low temperature, the stacking fault is formed in it due to its low stacking fault energy. This stacking fault or HCP band intersection region act as the favourable nucleation site for martensite formation. There are other nucleation locations like shear band intersection, isolated shear band, shear band and grain boundary intersection and grain boundary triple points. With the decrease in the temperature, the stacking fault energy decreases and the stacking fault region increases which favour for more number of martensite nucleation. So, the rate of martensite formation is enhanced with a decrease of temperature as shown in Figure 2.16(a). When strain is applied at a low temperature (77K), a considerable amount of martensite is formed after a certain true stain (but before the necking) and the hardening rate also increases with the martensite formation as mentioned in Figure 2.16(b).

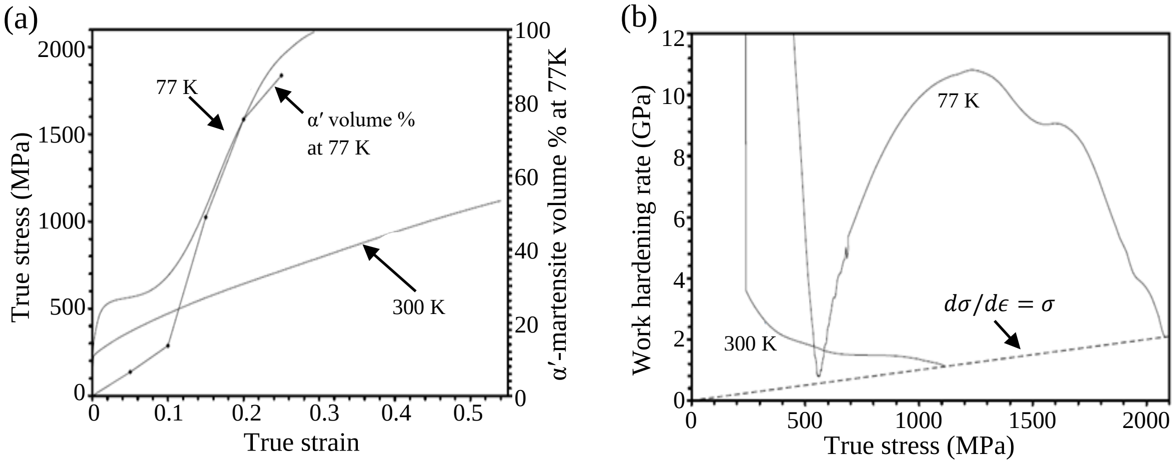

Figure 2.16: (a) True stress and martensite volume percentage with respect to true strain and (b) Work hardening behaviour of 304L stainless steel with respect to true stress.

Figure 2.17(a) shows the volume fraction of martensite with respect to true plastic strain in the range of -80°C to 50°C. For a particular strain value, the extent of transformation decrease with an increase in temperature. The extent of transformation with strain depends on the austenitic stabilising elements (such as an increase in Ni, increase the stability of austenite). However, with the decreasing test temperature (and so increased the rate of martensite transformation with strain), stress-strain curve changes from a smooth parabolic at room temperature to sigmoidal shape at low temperature [9].

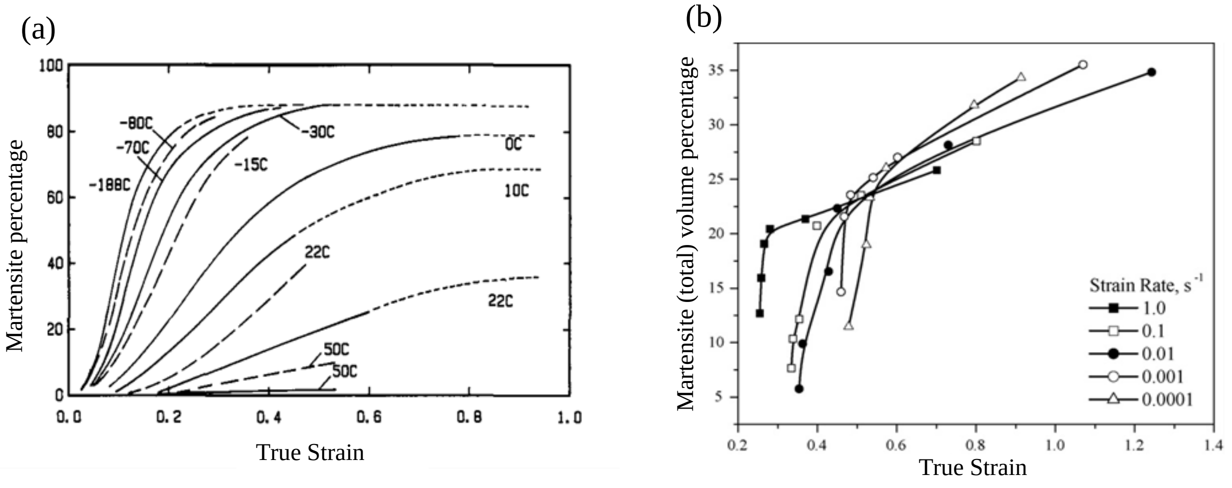

Figure 2.17: (a) Martensite volume percentage formed with respect to true strain corresponding to various temperatures [9] and (b) Volume percentage of deformation induced martensite with a true strain in 304LN stainless steel at various strain rates [10].

(e) Influence of strain rate

In Figure 2.17(b), the martensite volume fraction is plotted against true strain applied to the various values of strain rate. Initially, for the low magnitude of strain, the volume fraction of martensite increases proportionally in a linear fashion, after which the rate of martensite transformation slows down. Comparison of the curves at different strain rates reveals that at higher strain rate, the martensite transformation occurs at low strains than that in slow strain rate condition. When the strain rate is increased, the maximum volume fraction of martensite decreases, since the increased accumulated plastic strain restricts the dislocation movement due to pile up and cause a local rise in temperature, martensitic transformation becomes sluggish [10].

(f) Effect of prior strain and strain path

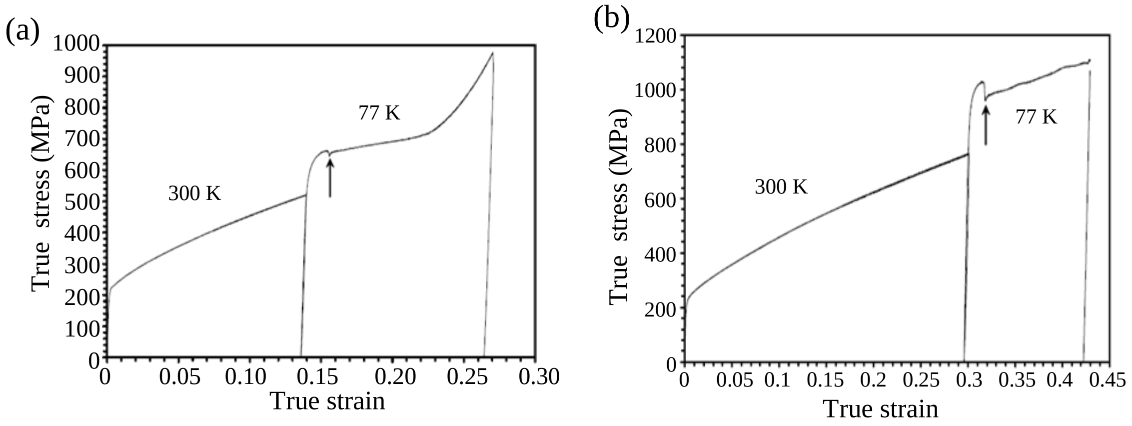

Figure 2.18: Strain localisation occurs in the form of a Lüders front at 77K as a result of a pre-strain at 300 K, indicated by the arrow. (a) 14% pre-strain and (b) 30% pre-strain.

Sometimes prior strain is applied to achieve better spatial distribution. Generally, the martensite formation is restricted in the stacking fault interaction region and is uniformly distributed over the grain. The distribution remains unaffected by the changes of temperature at which strain is applied. The size of the martensite lath is typically less than 300 nm. To get finer martensite distribution prior strain is applied at room temperature. Pre-strain causes high dislocation density, creating a back stress, which prevents the formation of large stacking fault. The result in a large number of stacking fault interaction leads to more number of martensite nuclei.

Figure 2.18 illustrates strain localisation due to the application of prior stain at room temperature. When the driving force is very high, the rate of transformation is also high causing the plastic deformation to be localised in the form of a Lüders front. The martensite formed in this case is finer (~10 nm) than the previous one. It is important to apply calculated prior strain because the excess amount can cause localised necking. The range of prior strain is typically in between 10% to 15%.

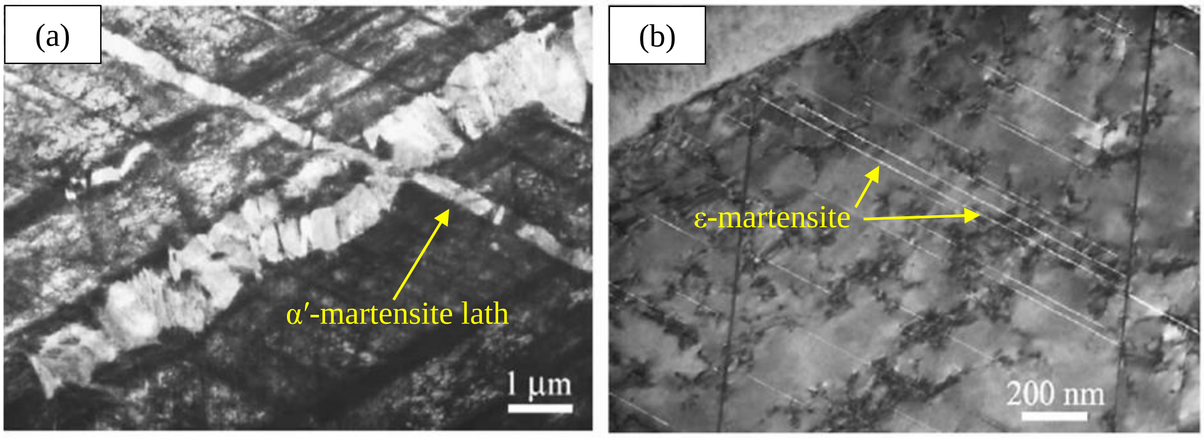

Figure 2.19: TEM micrographs showing the evolution of martensite during transformation front of a sample pre-strained 16% at room temperature, and strained 2% at 77K. (a) α′-martensite and (b) ε-martensite.

Figures 2.19(a) and (b) show the evolution of martensite during the transformation of a sample subjected to 16% pre-strain at room temperature followed by 2% strain at 77K respectively. The TEM micrographs reveal transformed Lüders front and the transformed region tends to be heterogeneous and the Lüders front appears diffused in nature. Some areas have a thin band of ε-martensite, which appear as a thin white line in Figure 2.19(b). Other areas show high density α′-martensite laths (wide white line) as depicted in Figure 2.19(a).

2.10 Response to mechanical property

The understanding of the physical origins of the mechanical response of the austenitic stainless steels remains a complex and challenging subject. The bulk mechanical property of the material strongly varies with the strain induced transformations owing to the evolution of microstructure containing a mixture of α′-martensite, ε-martensite and austenite. This evolution is attributed to the individual volume fraction of phases present in the microstructure and the synergistic effects of the phases. Other complex features like the size and morphology of the martensite phases have its own effect on mechanical properties along with the effect of transformation induced dislocations, which accumulate in austenite due to the formation of α′-martensite.

The yield strength depends on the grain size, which generally follows the Hall-Petch relation [140, 141] for grain sizes ranging from approximately 1µm upwards. Due to variation in grain size measurements, there can be a large dispersion of values given for Hall-Petch slope. Some of the measured values of different stainless steels in comparison to other FCC alloys are enlisted below in Table 2.7.

Table 2.7: Hall-Petch parameters determined at room temperature for various FCC materials.

Material	Friction Stress σ_0 (MPa)	Hall-Petch Slope k_y (MPa.µm$^{1/2}$)	Reference
301LN	252	274	[142]
304	220	492	[143]
316L	200	116	[144]
316L	164	621	[145]
316L(M)	144	580	[146]
Copper	26	110	[147]
Nickel	15	238	[148]

Earlier, it has been mentioned that the grain size influences the work hardening response of austenitic stainless steel by affecting the mechanical property as well as the kinetics for martensitic transformation. Strain dependent Hall-Petch parameter has been introduced in an extended Hall-Petch expression in order to explain the grain size dependence [144, 145, 149, 150]. Dislocation piling up at grain boundaries raises long range stress levels which attribute the grain size dependence of work hardening rate [151]. Accordingly, it has been argued that lower stacking fault energy alloys show higher kinematic hardening and it can be qualitatively agreed against grain size dependent work hardening of FCC alloys [152, 153].

The yield strength of austenitic stainless steel also exhibits high temperature dependence, which has been illustrated in Figure 2.20. This is in contrary to the most FCC metals where the yield stress is found to be weakly dependent on temperature [154, 155].

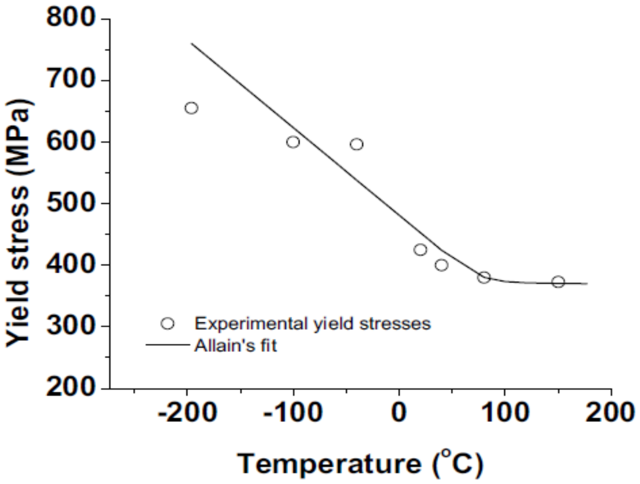

Figure 2.20: Effect of the temperature on the yield stress (determined by 0.2% offset method) of a 301LN stainless steel [156, 157].

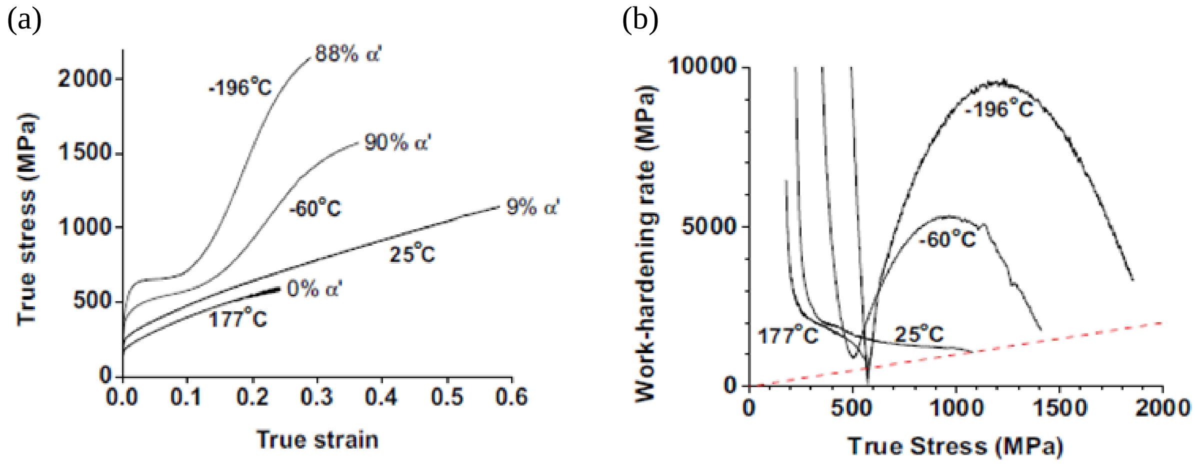

Figure 2.21: (a) and (b) Effect of temperature on tensile curves of a 316L stainless steel [50].

Figure 2.21(a) shows the uniaxial tension stress-strain curve of a 316L austenitic stainless steel grade plotted as the function of test temperature [50], where the curve at 177°C represents the behaviour of a fully austenitic material, as neither α′ nor ε-martensite forms at this temperature. Serrations in the stress-strain curve also appear at higher stresses. In many austenitic stainless steels, these serrations are a common feature, which is associated [68] with dynamic strain ageing. Various explanations for the dynamic strain-ageing in austenitic steels have been proposed [158, 159]. The transformation induced plasticity (TRIP) effect manifests itself in this material at temperatures below 25°C. The effect of the transformation to α′ can be recognised from the inflection in the stress-strain curve and the consequent increase in the rate of work-hardening, at intermediate levels of strain. Effect of the appearance of strain-induced martensite can be more easily seen in a plot of work-hardening rate as presented in Figure 2.21(b).

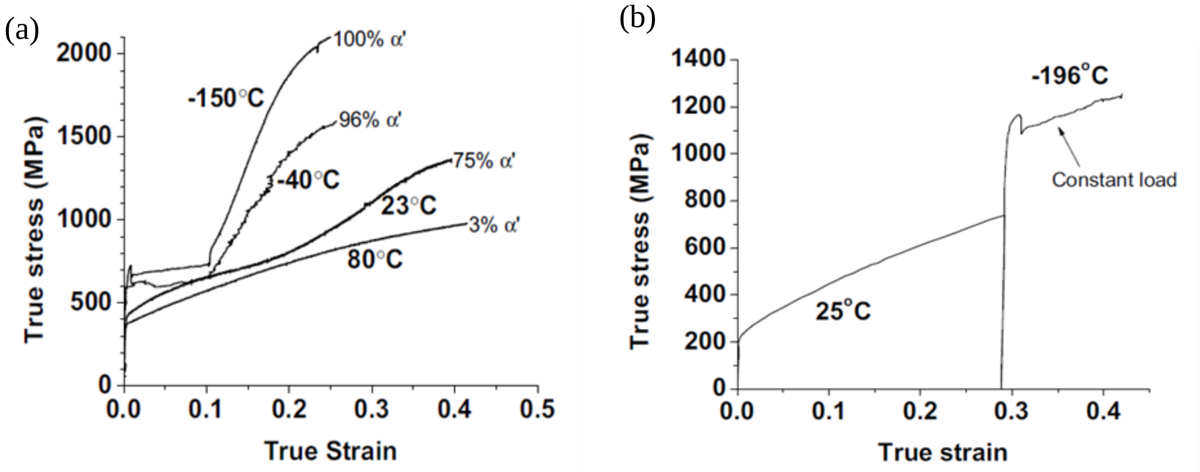

Figure 2.22: (a) Effect of the temperature on the tensile curves of a 301LN stainless steel [156] and (b) Tensile behaviour of 304L pre-strained at 25°C and further deformed at -196°C. The reloading at -196°C was associated with the propagation of a band in which the strain was localised [50].

In 301LN austenitic stainless steel, the evolution of mechanical property with the formation of α′ during straining becomes significant at higher temperatures compared to alloy 316L as a consequence of the lower stability of austenite, which is illustrated in Figure 2.22(a) [160]. The presence of an upper yield point and a lower yield point followed by a long plateau of ~10% strain can be observed from Figure 2.22(a) for temperatures below -40°C. This corresponds to the formation of Lüders like band during deformation.

The α′-martensite was found to form only in the volume swept by the band in which strain localisation takes place. Figure 2.22(b) reflects the stress-strain behaviour of a pre-strained material at a certain temperature and followed by reloading at a lower temperature [50]. Such discontinuous yielding has also been reported in submicron grained 304 or 316 grades. As the temperature was lowered from 25°C to -196°C, the magnitude of the Lüders strain was found to increase [161]. Although the exact explanation to this phenomenon is yet to be found [161], some recent works have suggested the possibility that with decreasing temperature, the strong increase of yield stress may lead to increase of the same above the level necessary to initiate a truly stress assisted martensitic transformation [162].

Stress-strain response of austenitic stainless steel is also affected by the variation in strain path, which can be attributed to the variation of transformation kinetics and variation in texture evolution [136, 163]. Figure 2.23 shows examples of strain path variation. It is often found that the relative position of the stress-strain curves is consistent with the measured kinetics and higher hardening is experienced in the grades which form more α′ at a given equivalent strain [134]. Such comparison is demonstrated in Figure 2.15 and Figure 2.23. After the initial display of similar work hardening, the shear and tension exhibit diversion for an equivalent true strain of 18%. However, the manifestation of difference between the strain paths is observed just after yielding in Figure 2.23(b). The inconsistency in the rate of kinetics can be observed by comparing with Figures 2.15(a) and (b).

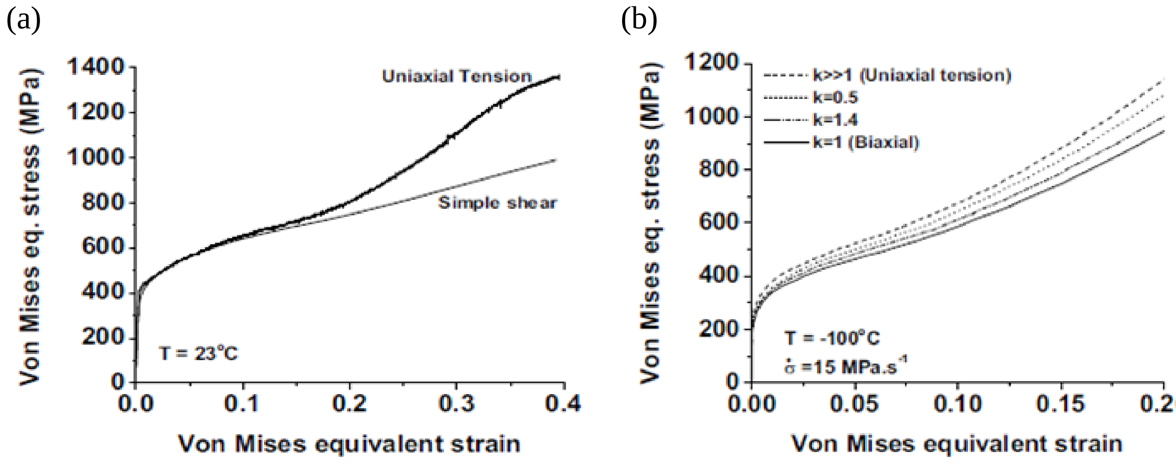

Figure 2.23: Stress-strain curve of two austenitic stainless steels for different loading combinations. (a) 301LN [124] and (b) 18-10 austenitic stainless steel for various ratios of principal stresses (denoted by k) [134].

2.11 Reversion of martensite into austenite during annealing

The transformation of ε-martensite to austenite occurs inside as well as outside ε plates by the discrete shrinking of stacking faults common in both. The recovery of the transformation induced dislocation is the function of annealing temperature where the suitable upper temperature upon annealing is found to be imperative for obtaining a good reversibility in the cyclic transformation from γ→ε→γ.

The reversion of deformation induced martensite is essentially governed either by diffusion controlled or athermal shear type mechanism depending on thecomposition of the material as well as the heating rate during annealing [164]. It has been found that increase in nickel/chromium ratio lowers the martensitic shear reversion temperature by increasing Gibb's free energy change between FCC and BCC structure [24]. Thermodynamically for the shear mechanism to be operative a minimum driving force is required and lowest possible temperature is 650°C as demonstrated in 16Cr-10Ni steel system [24]. During annealing, the heavily deformed austenite regions undergo recovery and recrystallisation, whereas deformation induced martensite transforms to austenite. The reverted austenite grains are further refined through recovery process of the matrix through the formation of dislocation cell and sub-grain.

The reversion technique affects the strength of steel [22], which depends in a complex manner on many factors related to alloy constitution and structure as well as heat treatment, like:

(a) The volume fraction of martensite present prior to reversion determines the volume fraction of reversed austenite produced.

(b) The type of martensite present (like plate or lath; internally twinned or with dislocation sub-structure) affects the defect density and its distribution. Figure 2.24 shows that the reverted austenite contains a high density of tangled dislocations, small twins and stacking faults, which is the characteristic of fine structure [12]. The high dislocation density is partly inherited from the sub-structure of α' crystal and partly from the deformations, associated with the reverse transformation, which further attributes to the high hardness value. This high hardness is also contributed by the carbide precipitates and segregation of carbide and nitride to the dislocations in martensite [12, 22].

(c) The dislocation distribution structure of austenite presents prior to the reversion during the martensite formation or by cold working.

(d) The magnitude of volume contraction during the BCC to FCC conversion, relevant to the generation of vacancies and dislocation sub-structure.

(e) Precipitation in the martensite (carbide and intermetallic compounds) during austenitising may affect the reversion transformation in the terms of dislocation movement and generation, contributing to the strengthening of reverted austenite [22]. There are other factors as well affecting the diffusion like the size of alloying elements, temperature change over which reversion occurs and the austenitising temperature and time.

(f) The recovery and recrystallisation characteristic, depending upon the temperature, time, diffusion coefficient, stacking fault energy, prior grain structure and effects of solute and precipitates.

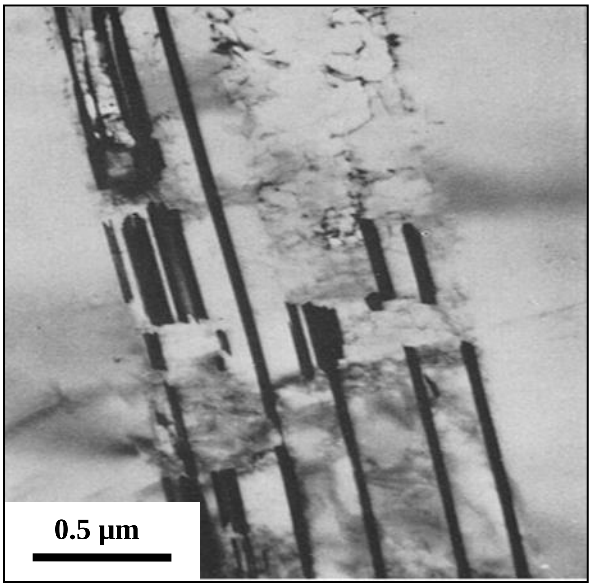

Figure 2.24: Showing the stacking fault and twins within the reversed austenite.

2.12 Microstructure after reversion treatment

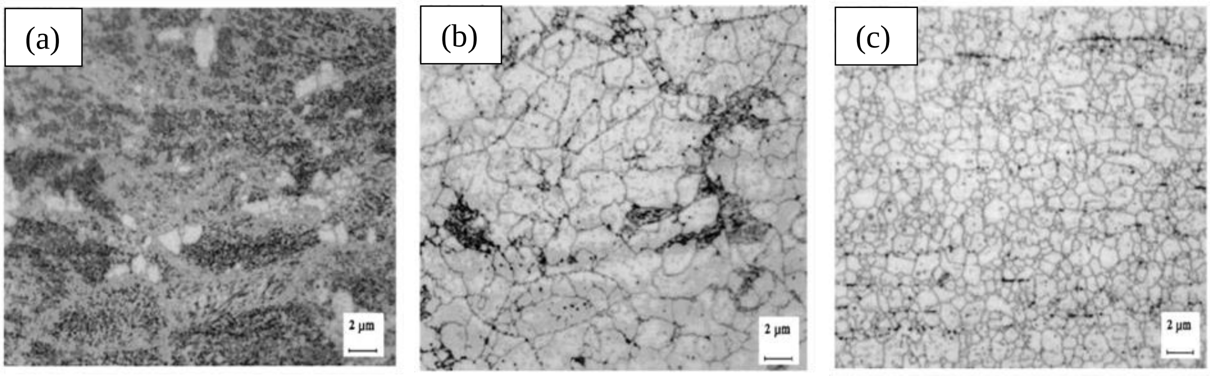

Figure 2.25: Optical micrographs after annealing at 750^{o} C for 1.2 ks for (a) 11-30%, (b) 12-70% and (c) 13-90% deformed samples [165].

Figures 2.25(a) to (c) show the microstructure of deformed sample of 30%, 70% and 90%, respectively after reversion at 750°C for 1.2 ks. In 30% deformed sample, some austenitic grains begin to nucleate. In 70% deformed sample, martensite is almost completely consumed but the grain structure is inhomogeneous. In 90% deformed steel, the microstructure is fully recrystallised and the grain structure is homogeneous [165].

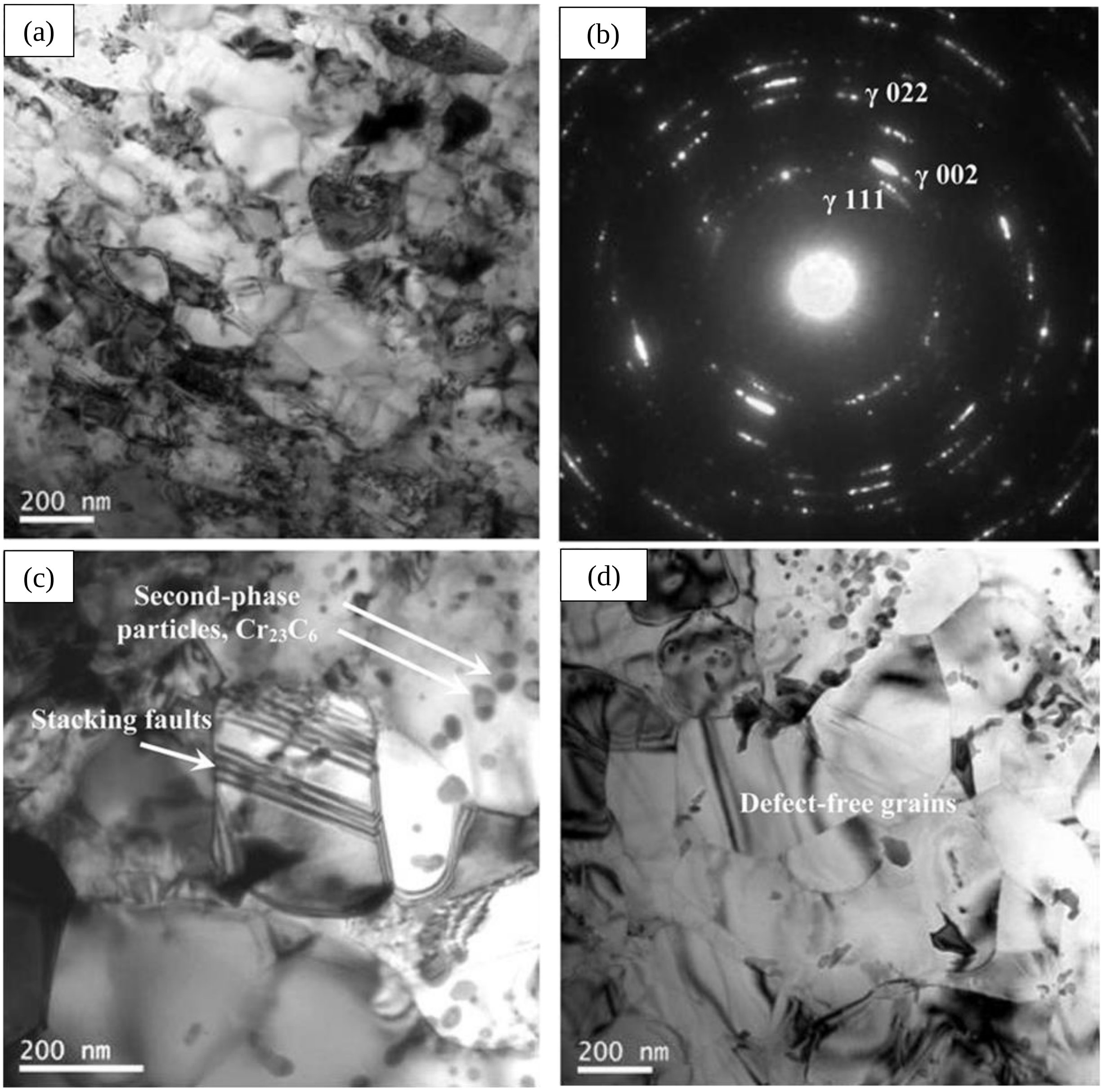

Figure 2.26: TEM micrograph of 301 samples subjected to 52% deformation followed by reversion annealing at 700°C for 100 s [166].

The austenite lath type structure is nearly absent and not properly defined as evident in Figure 2.26(a). The corresponding selected area diffraction pattern closely resembles ring type pattern (Figure 2.26(b)). Areas with lath type austenite grains reveal higher dislocation density. A longer annealing time led to the nucleation of a greater number of fine reverted defect free austenite grains with high angle grain boundaries replacing the austenite laths. The sizes of reverted austenite grains were slightly larger in the range of 200 to 500 nm because of longer annealing times that led to some grain growth. It is also to be noted in this context that, the less frequent presence of stacking faults (marked by white arrows in Figure 2.26(c)) and second phase precipitates (Figures 2.26(c) and (d)). Presence of stacking faults are attributed to lower stacking fault energy of 301 grade austenitic stainless steels (SFE = 15 mJ/m^2) [127]. The second phase particles were identified to be carbides of the type MXC or $M_{23}C_6$ (M = Fe, Cr, Mo) and have been previously observed in 301 austenitic stainless steel [167–169].

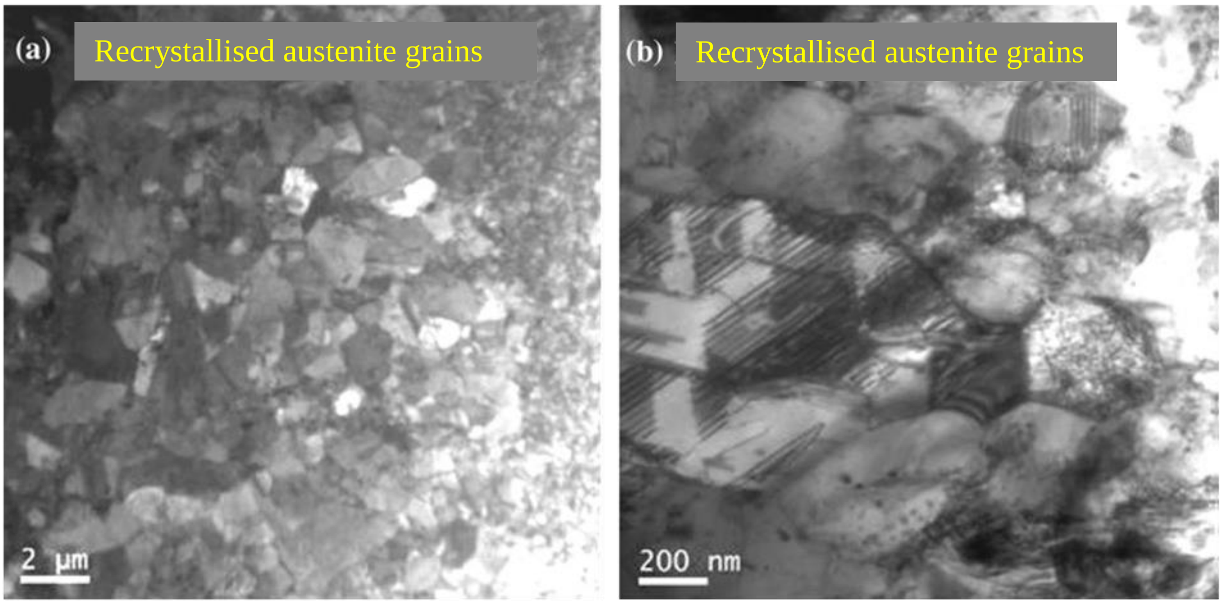

Figure 2.27: TEM micrograph of 301 samples subjected to 52% deformation followed by reversion annealing at 800°C for 10 s [166].

The austenite grains contained stacking faults and high density of defects. The austenite grain size was in the range of 200 to 500 nm and with the increase in annealing temperature from 700°C to 800°C led to the significant grain growth as depicted from micrograph in Figures 2.27(a) and (b). The micrographs also indicate that shear reversion process nears the completion at 800°C and the α′-martensite volume percentage obtained after reversion annealing treatment was less than approximately 10%.

Figures 2.28(a) and (b) show a variation of reverted defect free austenite volume percentage and its grain size range at different annealing conditions. The grain size range is obtained by using Image-J analysis tool on at least 50 transmission electron micrographs with recrystallised microstructure [166]. The reverted austenite lath with high dislocation density, which is yet to get recrystallised has not been considered in this case [166].

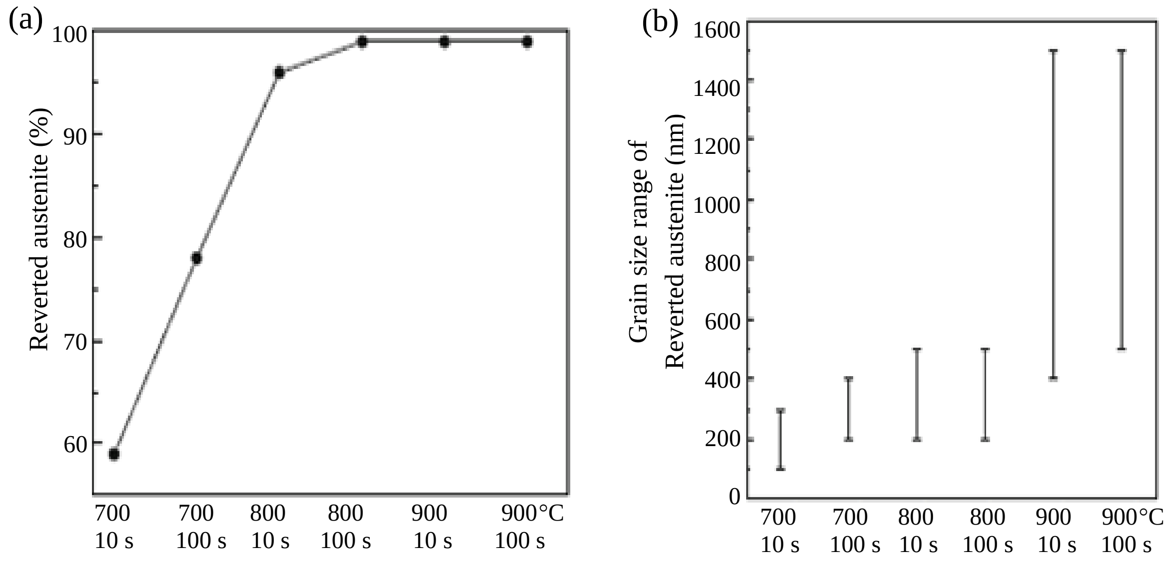

Figure 2.28: (a) Percentage of reverted austenite and (b) Grain size range as a function of annealing condition.

2.13 Effects of reversion annealing time and temperature

Reversion of the strain induced martensites in the austenitic stainless steel occurs at temperatures much lower than the recrystallisation temperature, which may reach temperatures of the order of 750°C. During annealing in between 300°C to 400°C, the α′-martensite content in cold worked austenite increases due to recovery mechanisms. Recrystallisation of the austenitic stainless steel usually occurs at temperatures 100°C higher than martensite reversion temperature [167]. Recrystallisation takes place only in the cold worked retained regions of austenite and not in reverted austenite [170]. It begins on deformation bands in the vicinity of grain boundaries [171]. There is no clear correlation between reversion of martensite and recrystallisation. Recrystallisation temperature in cold worked austenitic stainless steel depends upon composition, heat treatment prior to cold working, temperature and strain rate applied in cold working as well as the heating rate and holding time during annealing [167].

The variation in martensite volume fraction is reduced with the increase in annealing temperature and less time is required in case of higher annealing temperature for AISI 304 stainless steel as depicted in Figure 2.29 [165].

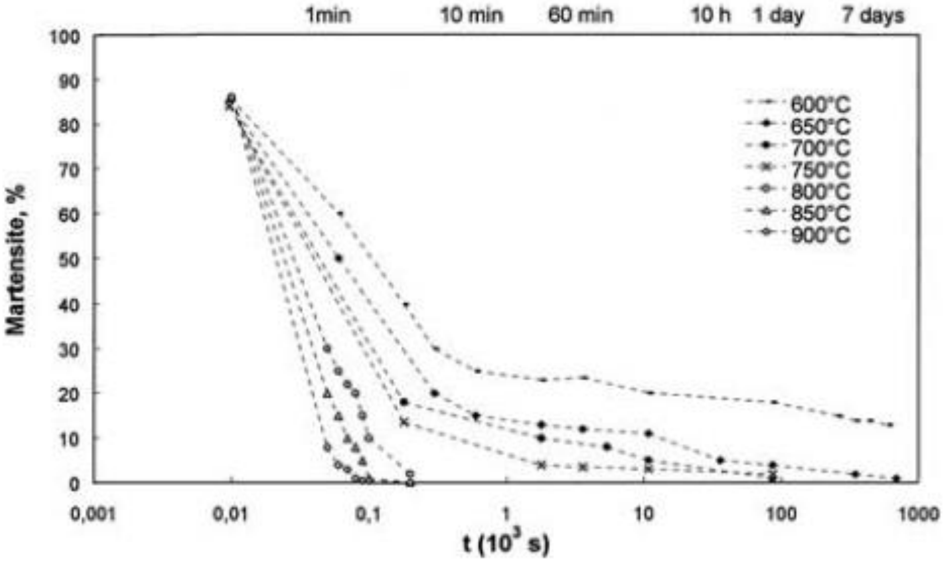

Figure 2.29: Effect of annealing time and temperature on the reversion behaviour of martensite induced by cold deformation [165].

2.14 *Softening during reversion*

The variation in Vickers hardness number (VHN) values is shown with the annealing temperature in Figure 2.30(a), where the hardness value drops down at a temperature close to 550°C owing to reversion of α′-martensite into austenite. Before that, the hardness increases gradually up to 400°C. During plastic deformation of the metals and alloys, a small fraction of energy is stored in the form of defects, mostly as dislocations. This stored energy is the driving force for the recrystallisation and is released during annealing [14].

As in carbon and alloy steels, the martensite transformation can take place simply by cooling, but in the lean austenitic alloys, the temperatures are well below the ambient temperature. The more stable alloys do not transform even with cryogenic treatment. Martensite formed in these alloys is quite stable and does not revert until heated well above the temperatures as depicted in Figure 2.30(b), at which it was formed. The carbon levels of austenitic stainless steels are always relatively low, so strain induced martensite is self tempering and not brittle.

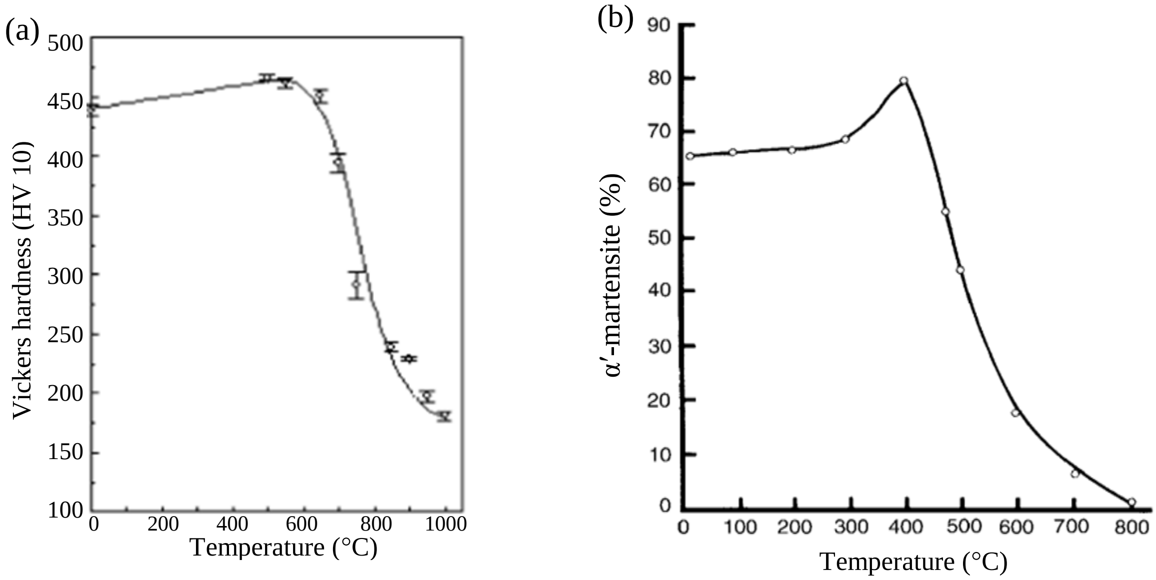

Figure 2.30: Variation of (a) Vickers hardness and (b) α'-martensite phase on reversion annealing temperature.

As the steel has low stacking fault energy, it is reasonable to presume that the recovery has a small contribution to the softening. From Figure 2.30(b), it is also evident, that the 50% martensite reversion occurs at about 550^{o}C, which is much below the recrystallisation temperature indicating that the kinetics is faster than the recrystallisation rate.

Engineering stress-strain plots of 301 austenitic stainless steels annealed at 700-900°C for 10 seconds are presented in Figure 2.31 along with some stress-strain curves for 301LN for comparison. The strength of the cold rolled specimens was considerably high when subjected to a greater amount of deformation sacrificing the total elongation significantly. However, upon reversion, the strength is decreased restoring the ductility and the values of the same depend predominantly on the annealing temperature. At higher temperatures, the improvement of ductility is more. The shape of the stress-strain curves clearly reveals the inflexion in the strain hardening curves generally beyond about 10 to 15% strain (increasing with annealing temperature or holding time), which is an indication of the strain induced martensitic transformation of the reverted austenite. The new martensite should have a very fine size because it was formed from finer austenite grain structure.

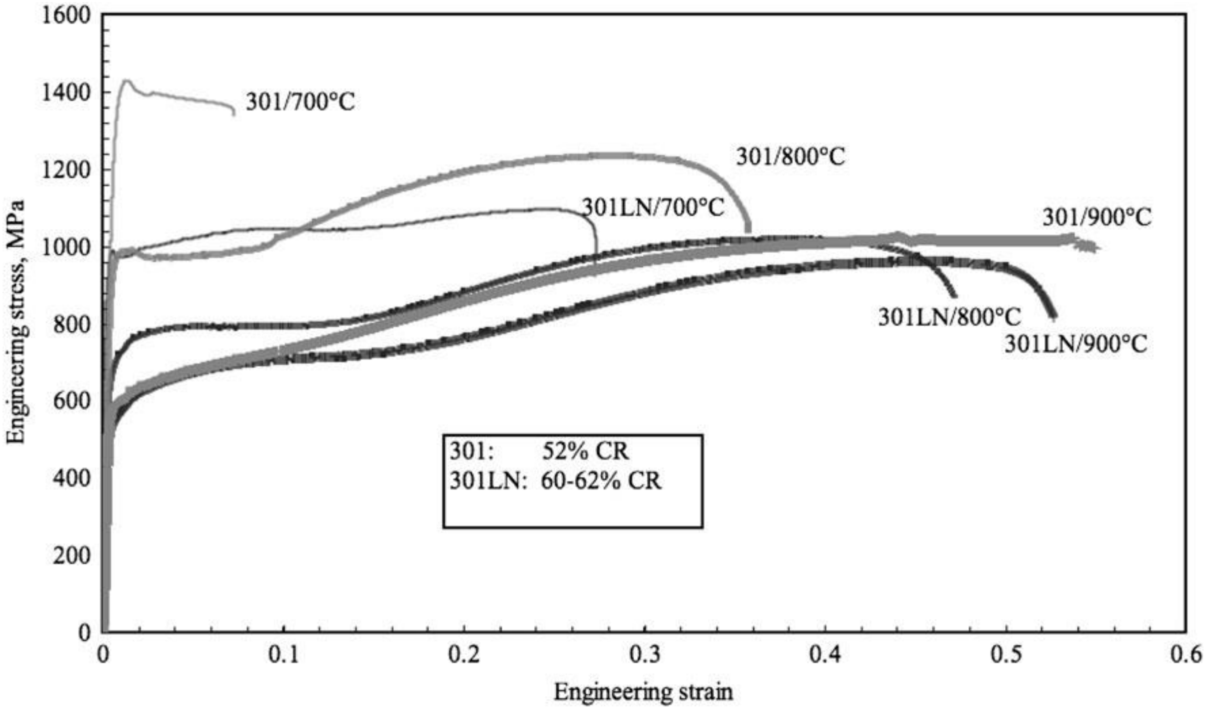

Figure 2.31: Engineering stress-strain plots of 301 and 301LN stainless steels annealed at 700°C to 900°C for 10 s [169].

2.15 Effect of thermo-mechanical controlled processing (TMCP)

In order to achieve superior strength and toughness of steels, grain refinement is one of the most important methods without having an increase in the transition temperature. One of the important and widely used technology in maximising grain refinement is Thermo-mechanical Controlled Processing (TMCP), which is a metallurgical process that combines mechanical or plastic deformation process like compression or forging, rolling etc. with thermal processes like heat-treatment, water quenching, heating and cooling at various rates into a single process [172, 173]. TMCP is thus being utilised as a substitute for heat treatments that require additional material handling and furnace facilities. TMCP involves controlled hot working and micro-alloyed steel compositions. For conducting TMCP, the rough steel section is heated to a temperature regularly used for hot working operations (about 1200°C). The initial hot working (roughing) is carried out in a normal fashion, but the final hot work reduction or 'finishing pass' is carried out at a lower temperature than would be used for older processes. Plastic deformation at this lower temperature promotes fine grain sizes and retards precipitation. This requires heavy rolling equipment capable of deforming the steel at low hot working temperatures. The thermo-mechanical deformation is followed by the cooling, which brings the steel to the transformation temperature range. For some TMCP steels, this last stage of cooling, during which transformation is completed, is accelerated by water cooling, to give a finer grain size.

2.16 Fractographic analysis

In order to understand the kind of fracture (ductile or brittle) during tensile deformation, the fractographic analysis is very important. Fractography analysis is essential in order to determine and establish the cause of failure or origin of cracking by studying the characteristics of a fractured surface [174]. In many cases, fractography requires examination at a finer scale, which is usually carried out in a scanning electron microscope (SEM) to obtain higher resolution. Different types of crack growth (e.g., fatigue, stress corrosion cracking, hydrogen embrittlement, ductile and brittle failure etc.) characteristic features on the well preserved fractured surfaceis used to identify the failure mode. The overall pattern of cracking can be more important than a single crack, however, especially in the case of brittle materials. Common features that may cause crack initiation are inclusions, voids or empty holes in the material, contamination and stress concentrations.

2.17 Applications

The major attraction towards austenitic stainless steels for construction purposes is that their corrosion resistance in atmospheric condition is substantially higher as compared with zinc and copper [175]. A recent study by Wallinder et al. [176] has looked into the release rates of Ni and Cr of 304 and 316 upon exposure to the atmospheric condition. The influences of rain intensity and its pH value have also been studied by these authors [176]. The 304 stainless steel is the popular variety of stainless steel used in the construction of aviation structure and aerospace applications attributed to its reliability, formability and flexibility towards light weight designs. Stainless steels, for aspecial purpose, could be used for concrete reinforcements [177]. However, the high initial cost incurred by the use of Ni may be prohibitive in some cases. Bautista et al. [178] have shown that the less expensive low-Ni stainless steels may be a feasible alternative to traditional stainless steels as concrete reinforcements. Besides reinforcements, stainless steels have also been suggested for use as loading-sustaining structural components.Some of the advantages of stainless steels include fire resistance and better retention of strength and stiffness at elevated temperatures compared with carbon steels [179-182]. Therefore, stainless steel structures are able to retain better structural integrity in the event of a fire accident. Superior plastic deformation behaviour and ability to absorb energy also qualify stainless steels as the attractive structural material [183, 184].

Use of austenitic stainless steel in railcars has increased sustainability in recent times. Durability, corrosion resistance, crash resistance, fire safety, ease of cleaning, minimum maintenance, superior aesthetic property, energy saving light weight designs and 100% recyclability after service life is the important attributes of austenitic stainless steel. It is being used in regional, commuters, underground, metro and light rail train services. For high speed rail cars safety of passengers is provided highest importance, where austenitic stainless steel is preferred owing to its high energy absorption at impact, a greater level of fire resistance and resistance towards corrosion. The presence of α'-martensite and reverted austenite add to its strength as well as wear resistance property.

Stainless steel 304is widely used in all sorts of industrial and domestic applications. In medical device industry, 304is used where high corrosion resistance, good formability, strength, wear resistance, manufacturing precision, reliability, non-magnetic nature, high heat resistance and antibacterial properties for maintenance of proper hygiene are of particular importance. The reassurance that medical devices won't chemically react with bodily tissue, cleaning products used to sterilise and the hard, repetitive wear that many medical devices are subjected to, means that stainless 304 is the perfect material for hospitals, surgeries and paramedic applications etc. Not only does stainless steel 304 offer high strength, it is also extremely workable, with the ability to be deeply drawn into shape without the need for annealing, making 304 perfect for the manufacture of bowls, sinks, pans and a range of different medical vessels and hollow wire. Austenitic stainless steels are extensively used in dairies, food processing and chemical industries, where they are often subjected to the cryogenic environment.

Austenitic stainless steels like AISI304, AISI316, etc., have already been used by the nuclear industry in light water reactors or fast breeder reactors. Besides fission, these stainless steels are also regarded as being potentially suitable for fusion systems. An extensive review of the suitability of using austenitic stainless steels in nuclear reactor systems has been written up by Sahin and Ubeyli [185].

In the present study, an attempt has been made to enhance the strength of AISI304 stainless steels when the same is subjected to judicious cold deformation followed by reversion annealing treatment to restore the ductility. Such steels attain the ability to absorb energy in the event of crash owing to the presence of deformable austenite along with hard martensite in the microstructure. Presence of harder martensitic phase allows the steel to reasonably wear resistant plus usual corrosion resistance, superior aesthetic property and high strength with light weight designs for transportation, which is an important step towards increasing the efficiency of passenger vehicles together with the compatibility to high safety aspects.

2.18 Understanding of existing status and scope of the present study

Cold deformation is known to be the most popular method to impart strength in austenitic stainless steel through the formation of deformation induced martensite (DIM). A variable amount of cold deformation exerts its differential effect on the microstructural evolution and hence, mechanical property. Deformation temperature is also considered to be an important parameter. A variable strain rate also has its own influence during deformation. Hence, it is important to understand the effect of varying amount of cold deformation (cold rolling), at the predetermined sub-ambient temperature of 0ºC, to the microstructure and property of the austenitic stainless steel.

Reversion of DIM into austenite imparts formability and toughness into austenitic stainless steel. The heavily deformed regions of austenite undergo recovery and recrystallisation where as DIM transforms to austenite during reversion. The microstructural changes of both phases are governed by shear as well as diffusional processes. It is important here to find out whether the entire volume fraction of DIM is reverted back to austenite or not; thereby understanding the mechanism of the reversion process. The reversion process of DIM in austenitic stainless steel also accompanies with the austenitic grain refinement. It is also observed that there is no significant amount of grain growth in the material above 850°C which can be attributed to very sluggish recrystallisation rate in austenitic stainless steel owing to carbide precipitation at grain boundary during annealing at a temperature higher than 700°C. Thus, it needs to be essential to study the effect of reversion on the microstructure and mechanical properties of DIM in austenitic stainless steel.

It has also been observed that low carbon heavily alloyed steels similar to austenitic stainless steels have been rarely subjected to thermo-mechanically controlled processing (TMCP) treatment. This has left a scope to study the response of TMCP on 304 austenitic stainless steel, where the enhancement of mechanical property is attributed to the grain refinement.

Characterisation of microstructural constituents in the cryogenically deformed and reverted austenitic stainless steel and their correlation with mechanical property is an attractive area of study from an application point of view. The previous studies have shown in-situ deformation characteristics in cryogenically deformed stainless steels. This inspires to conduct studies ondeformation through cold rolling with inter-pass cooling at -196°C. Moreover, the effect of bringing back the steel to ambient temperature after quenching/holding or deformation at -196°C has not been studied earlier in details. Hence, the effect of deformation as well as holding/quenching at -196°C draws attention in order to provide an insight regarding alternate methods of increasing the combination of strength and toughness in austenitic stainless steel.

Studies on mechanical behaviour, under prolonged holding/quenching without pre-strain at cryogenic conditions, is essential in the context of applications of austenitic stainless steel as a cryogenic container and other applications like biological/biochemical situations.

It is also important to measure the volume fraction of constituent phases of the material when subjected to a differential amount of deformation at a different temperature as well as after reversion annealing treatment under different processing conditions.

The influence of different heating rates and the identification of temperatures concerning various stages of reversion process including Cr-carbide precipitation during reversion annealing treatment of deformed samples through differential calorimetric measurements are of great importance in order to gather insight for microstructural evolution. Such objective is further substantiated by activation energy measurements, which reveals the concerned transformation kinetics. The measured activation energy values indicate whether the transformation kinetics will follow a diffusion controlled route or shear mechanism during reversion of martensite to strain free austenite grains.

Finally, every stainless steel is produced to possess adequate resistance to a corrosive atmosphere. While the work hardening favours the onset of pitting corrosion owing to potential pit nucleation sites at high energy regions, the reversion annealing treatment followed by cold deformation allows the material to regain its corrosion resistance through the generation of strain free austenite grains owing to the removal of residual stress in the matrix. Thus the corrosion resistance property remains unaffected.

3

EXPERIMENTAL DETAILS

3.1 Alloy procurement, its composition and form

The steels used for the study were procured from a standard commercial manufacturing source. Thesteels withtwo types of composition were chosen for the study. One of them was conventional 304 grade austenitic stainless steel with minimum 18 wt.% Cr and 8 wt.% Ni content (Steel A) and the second one was also a variety of grade 304 austenitic stainless steel with a modified composition where part of wt.% Ni has been replaced by wt.% Mn content (Steel B).

Analysis of chemical composition was conducted by using an optical emission spectrometer (ARL 4460) and the results are furnished in Table 3.1. Steel A was subjected to cold deformation at room temperature, 0°C and -196°C followed by the process of reversion annealing for selected samples atvarious time and temperature combinations. Specimens from Steel A were also subjected to thermo-mechanical controlled processing and cryogenic holding with or without pre-strain followed by reversion annealing process. Steel B was subjected to cold deformation at room temperature and 0°C followed by reversion annealing treatment for selected deformed samples at 0°C only. The deformation and reversion schedules for Steel B are identical to that used for Steel A for comparison of mechanical properties between two different compositions.

Table 3.1: Chemical composition (wt.%) of the investigated steels.

Steeltype	C	Mn	Si	Cr	Ni	Mo	Cu	S	P	N	Fe
Steel A	0.06	1.29	0.41	21.85	8.41	0.15	0.45	0.023	0.046	0.052	Bal.
Steel B	0.08	3.30	0.62	19.45	6.00	0.20	0.55	0.017	0.030	0.045	Bal.

The material of both the composition was procured in the form of hot rolled plate. Rectangular pieces of the total weight of about 50 kg and 35 kg were taken out from the parent plates of Steel A and Steel B composition, respectively and used for the study. Small pieces with cross section varying from 11 × 11mm^2 to 20 × 15mm^2 and approximately 100mm length were cut through a band saw from the plate sample. A representative schematic diagram is illustrated in Figure 3.1 for reference.

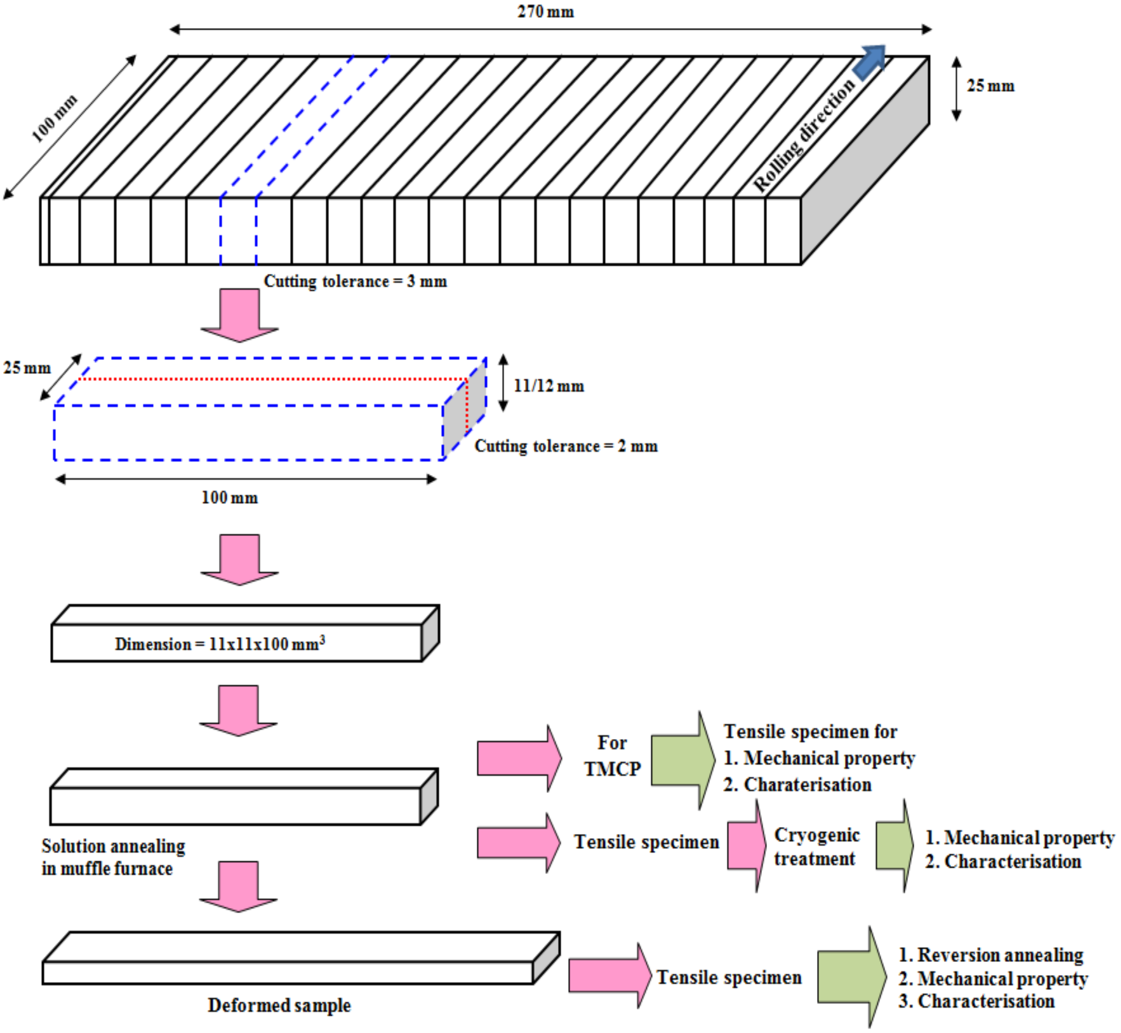

Figure 3.1: Schematic representation of various types of sample cutting by band saw.

Table 3.2: Dimensions of initial sample plate and subsequent cut pieces.

Steel type	Hot rolled plate thickness (mm)	Thickness (mm)	Width (mm)	Length (mm)
Steel A	25	11-12	11-12	100
Steel B	20	20	15	100

The dimensional details of the initial hot rolled plate and further small cut samples are enlisted in Table 3.2.

3.2 Solution treatment and "as-received" sample

All the 100 mm long specimens after cutting out from the hot rolled steel plate were subjected to solution annealing treatment. The soaking temperature for this treatment was kept at 1040°C [186] and the soaking time was 30 to 40 minutes followed by water quenching. The soaking time was selected based on specimen cross-section which was about 11 to 12mm^2. A muffle furnace aided with digital temperature control facility was used for heating and soaking. With this treatment, the material can now be referred as "as-received" sample. The original rolling direction is no longer valid after the solution annealing treatment. The soaking treatment allows the carbides to be in solution followed by the fast cooling through water quenching, which does not allow the carbides to precipitate at the grain boundaries and thus superior corrosion properties can be maintained through this treatment. The "as-received" samples were subjected to various cold deformation schedules at different temperatures, followed by reversion annealing treatment. It was also subjected to thermo-mechanical controlled processing and cryogenic cooling with or without pre-strain. As-received samples were tested for their mechanical properties and also went through several material characterisation techniques for comparison with the processed sample results as and when required for the study.

3.3 Deformation at room temperature and at 0°C

The "as-received" Steel A was divided into a total of 8 batches, where every batch had 15 samples each. These samples were subjected to varying amount of cold deformation (10%, 20%, 30% and 40%) at room temperature as well as at 0°C in order to study the effect of strain (cold rolling) on the formation of deformation induced martensite. Similarly, the "as-received" samples with Steel B were divided into an identical set of samples and subjected to cold rolling with the same amount of deformation levels of 10%, 20%, 30% and 40% at room temperature as well as at 0°C. Each rolling pass during cold rolling as mentioned above was provided 0.50 mm (available rolling mill capacity) reduction in thickness. For rolling at 0°C, all the samples were soaked in the ice-water mixture for at least 20 minutes to acquire uniform temperature in the material to commence the rolling. During rolling, specimens were subjected to inter-pass cooling with theice-water mixture to avoid the effect of adiabatic heating [133, 78]. Similarly, all the samples deformed at room temperature were subjected to inter-pass cooling in normal water at room temperature to avoid the effect of adiabatic heating during rolling. The deformation schedule has been described in Table 3.3.

Table 3.3: Deformation process schedules for the investigated steel specimens.

Steel type	Total number of samples	Number of groups	Number of samples in each group	Thickness reduction (%)	Deformation temperature
Steel A	120	8	15	10, 20, 30, 40	0°C and room temperature
Steel B	120	8	15	10, 20, 30, 40	0°C and room temperature

3.4 Thermo-mechanical controlled processing(TMCP)

Thermo-mechanical controlled processing was carried out with the “as-received” Steel A. Total 18 numbers of samples were divided into 3 groups subjected under TMCP with varying finish rolling temperature (FRT) of 700°C, 800°C and 900°C. The process schedule is furnished below in Figure 3.2 for ready reference.

Controlled hot rolling was carried out in three stages of deformation as shown in Figure 3.2 and tapered reduction pattern was followed to achieve finish thickness of 5 mm from initial 11 mm thickness of the as-received sample. 3 mm, 2 mm and 1 mm thickness reductions were applied during the initial, intermediate and final stage of deformation, which was designated as stage 1, 2 and 3 sequentially. So during 1st stage of deformation, 27% of reduction was provided at 1150 to 1100°C. 2nd stage of reduction involves 25% reduction at 1050 to 1000°C and 3rd stage of deformation involve 17% reduction at a temperature range of 950°C to finish rolling temperature (FRT). All the samples were air cooled after finish rolling.

The temperature of the plates during rolling was monitored by using an infrared pyrometer. The accuracy of the pyrometer was ± 6 °C when the temperature is ≤1000°C and ±6% of the measured value in the temperature range of 1000-1500°C. The margin of the error in temperature measurement on the measuring locations is within ±5 °C.

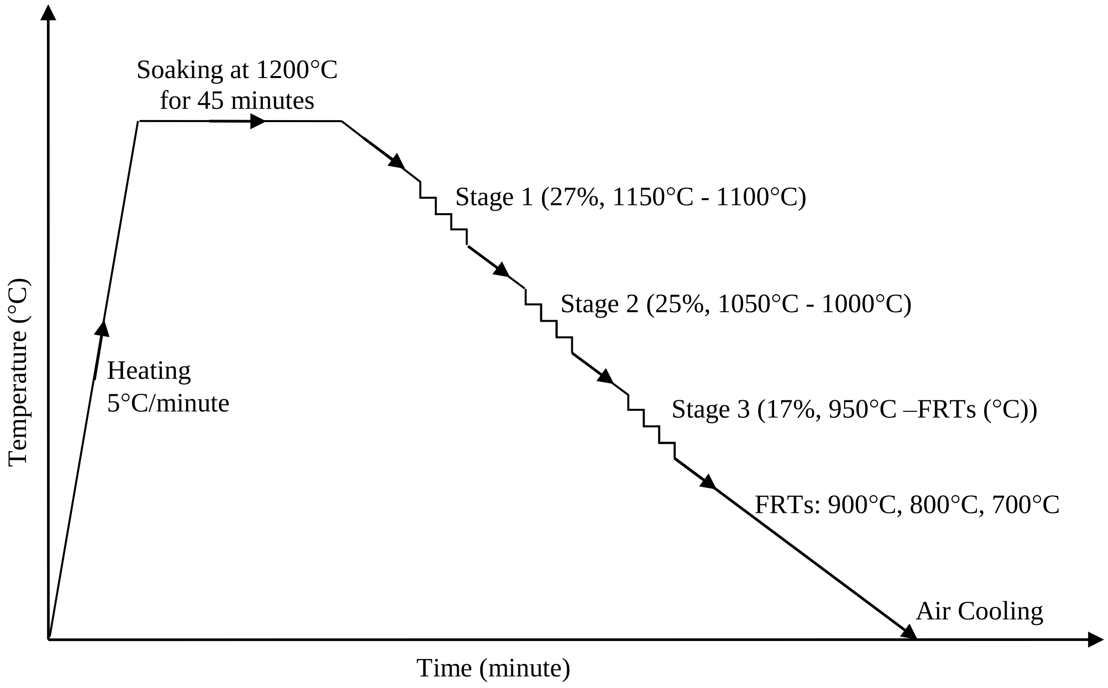

Figure 3.2: Schematic representation of thermo-mechanical controlled processing.

3.5 Cryogenic treatments and deformation

1. Tensile specimens prepared from Steel A (as-received), were subjected to different cryogenic treatments as furnished below.
    a) Soaked at – 196^{o}C for 1h from room temperature without any pre-strain
    b) Soaked at – 196^{o}C for 4h from room temperature without any pre-strain
    c) Soaked at – 196^{o}C for 15h from room temperature without any pre-strain
    d) Soaked at – 196^{o}C for 30h from room temperature without any pre-strain

2. Further, experiments were carried out to understand the effect of pre-strain followed by holding the deformed sample at -196^{o}C for different time duration. For this purpose, tensile samples prepared from as-received material were subjected to 20% deformation through uniaxial loading by computer-controlled Instron-5900R machine. The deformation was only restricted to gauge length area. Then the samples were kept completely immersed in liquid nitrogen for 1h, 4h, 15h and 30h duration.

3. 10% and 20% plastic deformations through rolling at -196°C were provided to total 30 numbers (15 numbers in each category of reduction) of "as-received" samples of Steel A. Before the onset of rolling, all the samples were soaked for at least 20 minutes in liquid nitrogen to acquire the desired temperature in the material. Each rolling pass was provided with 0.50 mm max (available rolling mill capacity) reduction. All deformed samples were also subjected to inter-pass cooling by periodic soaking in liquid nitrogen in order to avoid the effect of adiabatic heating during rolling. Different types of cryogenic treatments given to Steel A sample are enlisted below in Table 3.4.

Table 3.4: Cryogenic deformation and subsequent treatments of the steel specimens.

Sl.No.	Prior condition	Process followed	Type of sample
1.	No pre-strain	1h, 4h, 15h and 30h holding at -196°C	Tensile (Figure 3.3)
2.	20% pre-strain at room temperature	1h, 4h, 15h and 30h holding at -196°C	Tensile (Figure 3.3)
3.	No pre-strain	10% and 20% deformation at -196°C	As-received ($11\times11\times100$ mm^3)

3.6 Reversion annealing treatment

Table 3.5: Reversion annealing schedule after cryogenic deformation/treatment.

Deformation (%) and temperature	Cooling at -196°C	Reversion temperature (°C)	Reversion time (h)	Nature of sample
30% at 0°C (Both Steel A and B)		300, 500, 800 and 725	1	Tensile (Figure 3.3)
40% at 0°C (Both Steel A and B)		300, 500, 800 and 725		
20% Pre-strain at room temperature	Duration of 30 h	725		
10% at -196°C		300, 500 and 725		
20% at -196°C		300, 500 and 725		

Samples of Steel A and Steel B with 30% and 40% deformation at 0°C were subjected to reversion annealing treatment with various combinations of time and temperature and comparison of mechanical properties has been carried out. Steel A samples, subjected to pre-straining followed by cryogenic cooling as well as deformation at -196°C, were also subjected to reversion annealing treatment with various combinations of time and temperature in order to understand the effect of microstructure on the mechanical property. For reversion annealing, a muffle furnace with digital temperature control facility was used. Samples were subjected to air cooling after desired reversion time. The reversion schedule is enlisted in Table 3.5.

3.7 Metallographic analysis

3.7.1 Optical microscopy

For the purpose of metallographic analysis through an optical microscope, samples were cut and mechanically ground using silicon carbide abrasive paper down to mesh number 1200, there after polished with 1 μm diamond paste to a mirror finish followed by etching with aqua regia solution (75% HCl and 25% HNO_3 mixture). During grinding and polishing of the samples, proper care was taken by periodic cooling of the samples with water in order to avoid heating of samples due to friction. Properly etched samples were then employed for analysis under anoptical microscope (Make: Carl Zeiss, Model Axiovert 40MAT) and quantitative image analysis was performed by using Axiovision, version 4.8 software. For measuring the non-metallic inclusion content, adequately polished and unetched samples were examined under anoptical microscope at 100× magnification and the evaluation was carried out through comparison method as per ASTM E45 standard chart.

3.7.2 Scanning electron microscopy and electron backscatter diffraction (EBSD) analysis

Identical sample preparation as well as etching technique as followed for optical microscopy was adopted for Scanning Electron Microscopy(SEM) (HITACHI, S-3400N) which was operated at 15 to 20 kV. Electron backscatter diffraction analysis was carried out for selected samples using another SEM instrument (Make: Zeiss, Model: SUPRA 25). The samples for EBSD analysis were subjected to standard mechanical polishing (down to 0.25 mm grit), followed by electro-polishing in 94% Ethanol + 6% Perchloric acid solution in order to make the samples free from scratches. The corresponding analysis was carried out using HKL software.

3.7.3 Transmission electron microscopy

For transmission electron microscopy, typical 3 mm diameter discs were punched out from thin foils (~80 µm) and subsequently subjected to twin jet electro-polishing using a mixture of the electrolyte of 90% acetic acid and 10% perchloric acid at a temperature of about 10-12°C. The thin electron transparent samples (30-40 µm) were examined in a transmission electron microscope (TEM) (TecnaiG^2) at 200kV operating voltage and selected area electron diffraction (SAED) pattern was captured from the various phases/features for confirmation. The chemical compositions of the precipitates were determined by Energy Dispersive X-ray Spectroscopy (EDS) analysis.

3.8 X-ray diffraction (XRD) study

Small rectangular specimens of 2 mm thickness, 10 to 15 mm width and 20 mm length were cut from the stock after grinding out the rolling surface from the top and bottom portions. The length of the sample is aligned with the rolling direction as illustrated in Figure 3.3.

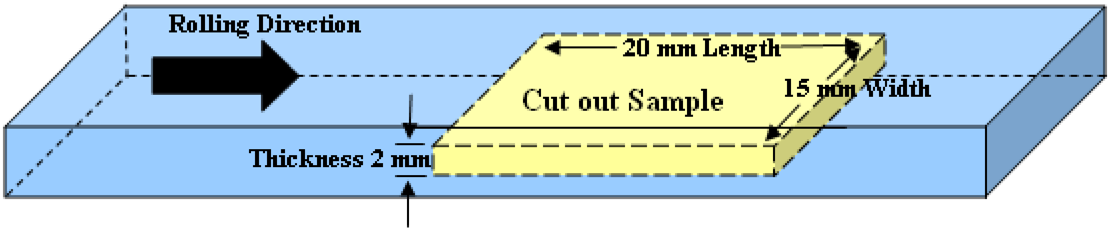

Figure 3.3: Schematic representation of cut out sample for XRD study.

The cut out samples were mechanically ground using silicon carbide abrasive paper down to mesh number 1200, then polished with 1 µm diamond paste followed by chemical polishing with a mixture of hydrochloric acid, nitric acid and distilled water in 1:1:1 proportion to remove any layer damaged by mechanical polishing [12, 187]. The specimen was then examined in a Bruker Diffractometer (D8 Advance) with Cu Kα radiation using 30 kV operating voltage and 40 mA current. The diffracting angle (2θ) was scanned from 40° to 100° to include the three strongest reflections of both austenite and martensite. The scan rate was 0.02° 2θ s^{-1}. The diffraction patterns were recorded and the quantitative estimation of the phases was performed by Rietveld analysis [188] of the X-ray data using commercial software, X’Pert High Score Plus wherever relevant for the present study.

3.9 Differential scanning calorimetry (DSC) study

DSC studies of some selected deformed samples were carried out using a METTLER TA 4000 system using high purity argon atmosphere. Heating runs were carried out at heating rates (ϕ) of 5, 10 and 20°C/min up to a temperature of 700°C which was identified as almost the saturation temperature for the reversion transformation. Activation energy (E) values for the different reactions involved in the reversion process were calculated in terms of the recorded peak temperature T_P for each heating rate using the Kissinger’s formula [189]:

$$\ln(\emptyset/T_P^2) = -E/(RT_P) + constant \qquad (3.1)$$

Where R is the gas constant (8.314 J/mol. K). When $\ln\left(\phi/T_P^2\right)$ is plotted as a function of $1/T_P$, the slope of the straight line obtained provides the value for the activation energy.

3.10 Hardness test

A Brinell-cum-Vickers hardness tester (Model: BV-250 (SPL)) was used to measure the Vickers hardness number (VHN) under 30 kg load for a dwell time of 20 sec. At least six indentations were taken on each sample. For cold deformed, reversion annealed and TMCP samples, hardness values were measured on the rolling planes and the average hardness values were reported.

3.11 Tensile testing

Schematic diagram of the sub-size flat tensile specimen as per ASTM standard (ASTM: Vol. 03.01, E8M-96) is shown in Figure 3.4. Room temperature tensile testing was carried out using a computer controlled Instron-5900R testing machine with a crosshead velocity of 0.5 mm/min. The yield strength (YS), ultimate tensile strength (UTS), percent total elongation (%TEL) were determined from the machine output by using Bluehill 3 software.

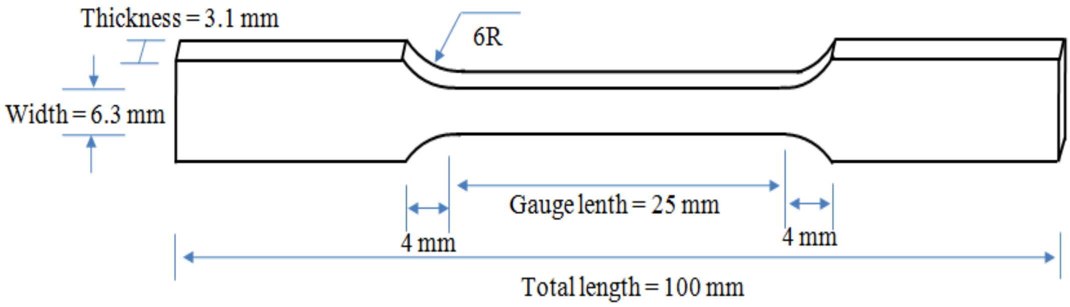

Figure 3.4: Schematic diagram of the sub-size flat tensile specimen as per ASTM standard (ASTM: Vol. 03.01, E8M-96).

3.12 Fracture surface and sub-surface analysis

To understand the micro-mechanism of fracture, tensile fracture surfaces, as well as sub-surfaces just underneath the fracture surfaces, have been studied using SEM. Energy dispersive X-ray spectroscopy (EDS) analysis was also conducted to determine the chemical composition of precipitate/second phase particles.

4

STUDIES ON COLD DEFORMATION AT ROOM TEMPERATURE AND SUB-AMBIENT TEMPERATURE (0°C)

4.1 Introduction

Austenitic stainless steel in as-received condition exhibits low yield strength and ultimate tensile strength with excellent total elongation. The lower level of achievable strength often limits their application for structural and other safety purposes. Judicious plastic deformation has been found to be effective in improving the strength of austenitic stainless steel [164]. The austenitic phase transforms into martensite upon deformation. Therefore martensite has been produced at the expense of austenite, which offers higher strength. This process of cold working does not necessitate additional heat treatment (hardening and tempering). Thus, the approach enhances the versatility and usefulness of the steel for structural and safety applications by the way of improvement of strength with sacrificing its excessive ductility.

The formation of deformation induced martensite (DIM) depends on various parameters such as the chemistry of material, temperature, the rate of deformation (strain rate), strain, stress state, stacking fault energy, pre-strain etc. [9-14]. Stacking fault energy (SFE) of austenite which is a function of temperature and composition governs the dominant deformation mechanism. For higher stacking fault energy (>20 mJ/m^2), the deformation mode is shifted from ε martensite formation to deformation twinning and then slip [19]. Plastic deformation of the austenite creates the proper defect structure which acts as the embryo for the transformation product. In austenitic stainless steels, embryos are formed at the intersections of shear bands, stacking faults, twins etc [15-17]. Usually ε-martensite is formed at the low deformation level (i.e., 5-10%) and at the higher strain levels, the α′-martensite increases at the expense of ε-martensite [18]. The amount of plastic strain (tension) also increases the amount of α′-martensite. In case of biaxial tension, there is a large number of the shear band formed, resulting in a larger volume fraction of α′-martensite than that of the uniaxial tension. The compressive strain decreases the amount of α′-martensite [15]. The morphology of the transformation product is typically lath-like [15-18, 44].

It is also apparent that microstructural design in cold deformed austenitic stainless steel has left large space for further improvement of technology and economy. In this regard, appropriate characterisation is immensely useful to understand the underlying mechanisms of the DIM formation and its mechanical properties. It has been reported that the achievable strength-ductility combination of such steel is governed by the work hardening characteristics of the microstructure. Therefore, it is important to study the work hardening characteristics of such steels over the range of uniform elongation. It is also important to understand the role of individual alloying elements on the microstructure formation under a given schedule.

In view of the above, the present study is primarily focussed on cold deformation of austenitic stainless steels with an aim to improve its mechanical properties through the formation of martensite during cold rolling operation at room temperature and sub-ambient temperature (0°C).

4.2 X-ray diffraction analysis

Figures 4.1 and 4.2 reveal the X-ray diffraction profiles of as-received 304 stainless steel samples along with the samples deformed with 10%, 20%, 30% and 40% thickness reduction at room temperature and at 0°C, respectively. The as-received specimen reveals the presence of austenitic (FCC) phase only, which is depicted by the presence of prominent (111), (200), (220) along with the weaker (311) and (222) peaks. In addition to the aforesaid peaks in austenite phase, the (110) and (211) peaks are also visible from the diffraction profiles for the deformed samples, which indicate the presence of BCC α′-martensite phase generated during the cold deformation process. It is to be noted that the X-ray diffraction pattern does not reveal any peak related to ε-martensite. In this context, it may be mentioned here that the crystal structure of ε-martensite is heavily faulted [190, 62] due to overlapping of stacking faults resulting in low intensity and increased width of the concerned X-ray diffraction peaks. In addition, it is assumed that, either the ε-martensite has not been formed due to the high stacking fault energy, or it has not been detected in X-ray diffraction study due to its minimal presence.

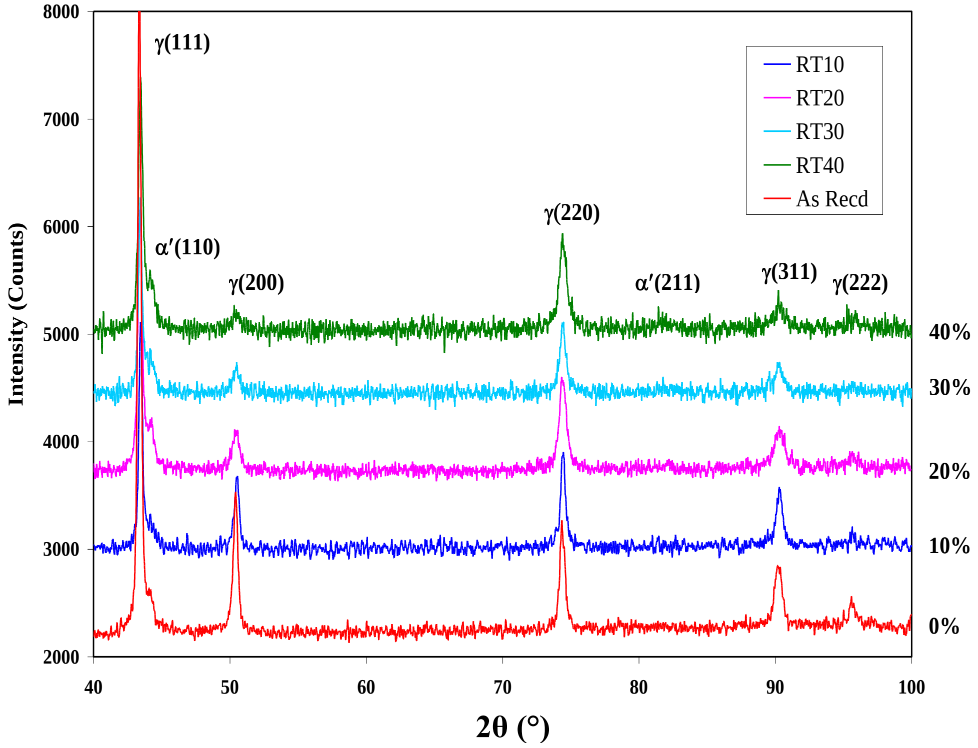

Figure 4.1: X-ray diffraction profiles for stainless steel samples of as-received (0%), 10%, 20%, 30% and 40% deformed specimens at room temperature [Steel A].

The results obtained from the X-ray diffraction conducted in the present study reveal formation of α′-martensite due to the deformation. Moreover, an increased amount of α′-martensite formation is found to occur in the case of deformed samples with a higher amount of reduction, as in 30% and 40% deformed samples in comparison to 10% and 20% deformed sample, which are evident from both the Figures 4.1 as well as 4.2.

A closer look in the X-ray diffraction patterns (Figure 4.1 vis-à-vis Figure 4.2) reflects the presence of higher volume percent of phase with BCC crystal structure for samples deformed at 0°C, in comparison to specimen deformed at room temperature. This is attributed to the formation of additional α′-martensite peak at (200) (Figure 4.2) owing to lower stacking fault energy (19 mJ/m^2) at 0°C. However, the same is found to be absent in Figure 4.1. The volume percentages of austenite and α′-martensite were measured through Rietveld analysis of the corresponding X-ray diffraction profiles. The measured volume fractions of the constituent phases are furnished in Table 4.1. It has been reported earlier that, the quantification of α′-martensite by X-ray diffraction is not reliable below 20% reduction in thickness [191].

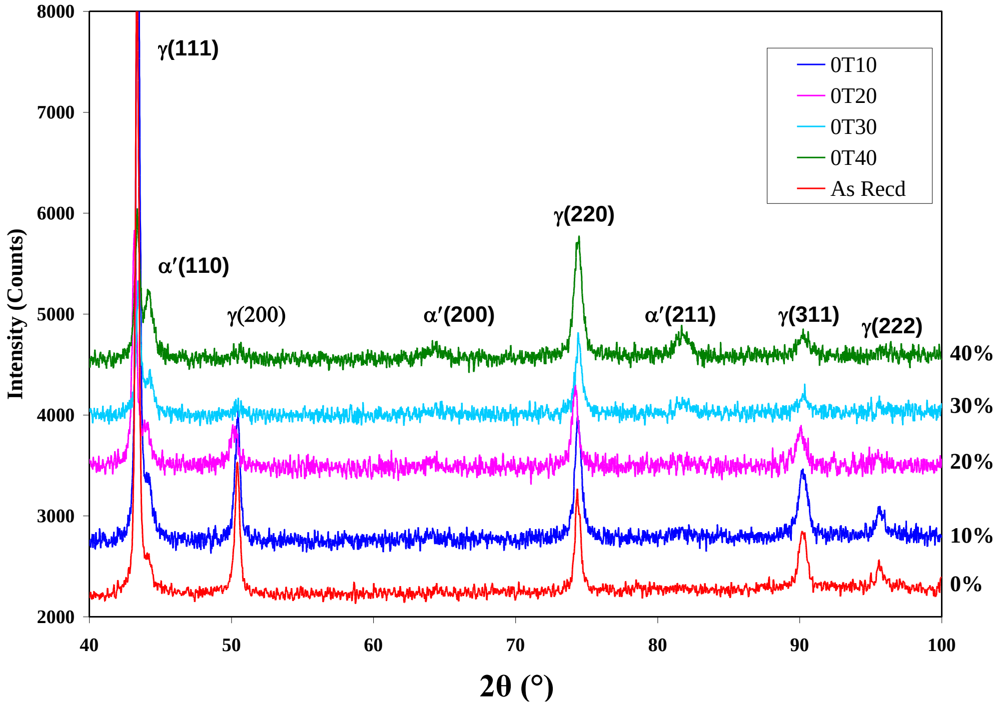

Figure 4.2: X-ray diffraction profiles for stainless steel samples of as received (0%), 10%, 20%, 30% and 40% deformed specimen at 0°C [Steel A].

Table 4.1: Volume percentage of constituent phases calculated from X-ray diffraction profiles.

Different phases	Volume percentage of phases					
	Deformed at room temperature			Deformed at 0°C		
	0%	30%	40%	0%	30%	40%
Austenite (γ) [FCC]	100	81±2	74±2	100	76±2	68±2
α′-martensite [BCC]	0	19±1	26±1	0	24±1	32±1

4.3 *Evolution of microstructure*

4.3.1 Microstructure of as-received samples

Table 4.2: Results of non - metallic inclusion rating for Steel A.

Category	Sulphide (A type)	Alumina (B type)	Silicate (C type)	Oxide (D type)
Thin	1.5	0.5	0	1.0
Heavy	0	0	0	0.5

Table 4.3: Results of non - metallic inclusion rating for Steel B.

Category	Sulphide (A type)	Alumina (B type)	Silicate (C type)	Oxide (D type)
Thin	1.0	0.5	0	1.5
Heavy	0	0	0	0.5

Cleanliness of the as-received steel have been verified through observation of non-metallic inclusion by following ASTM E45, method A and the results are furnished in Table 4.2 and 4.3 for Steel A and Steel B, respectively. It may be mentioned here that both the experimental steels designated as Steel A and Steel B are reasonably clean steel.

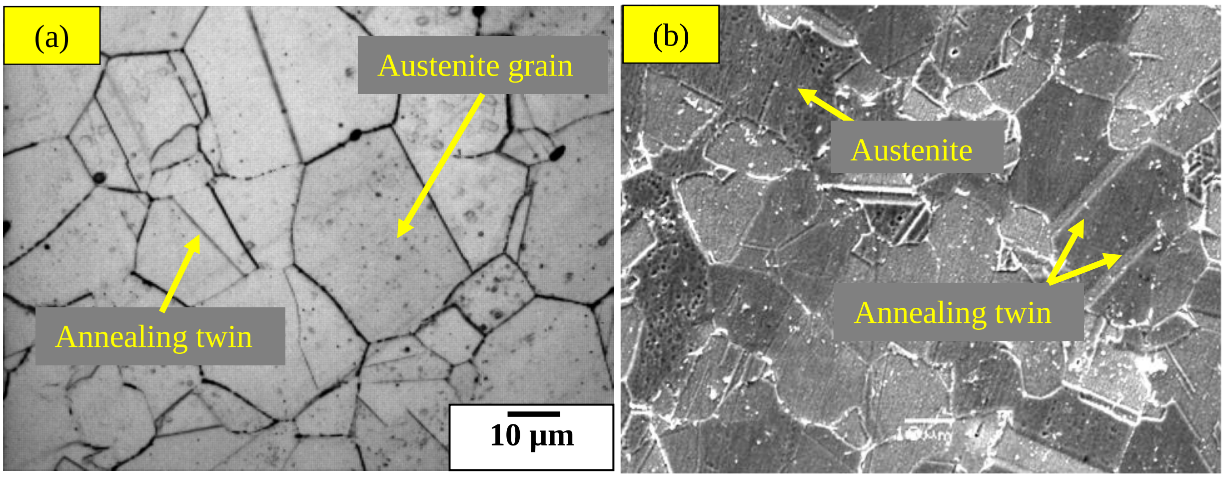

Figure 4.3: (a) Optical micrograph and (b) SEM micrograph of as-received austenitic stainless

steel [Steel A].

Figure 4.3(a) shows the optical micrograph of the as-received specimen which clearly shows the austenitic grains and annealing twins. Figure 4.3(b) shows the SEM micrograph of the typical as-received microstructure. The grain structure is typically austenitic and the average grain size was determined as 25±5µm. No precipitation of chromium carbide can be observed at grain boundary as well as at the triple points as the sensitisation was successfully avoided owing to direct water quenching from 1040°C after holding at that temperature for 40 minutes.

4.3.2 Evolution of microstructure after deformation

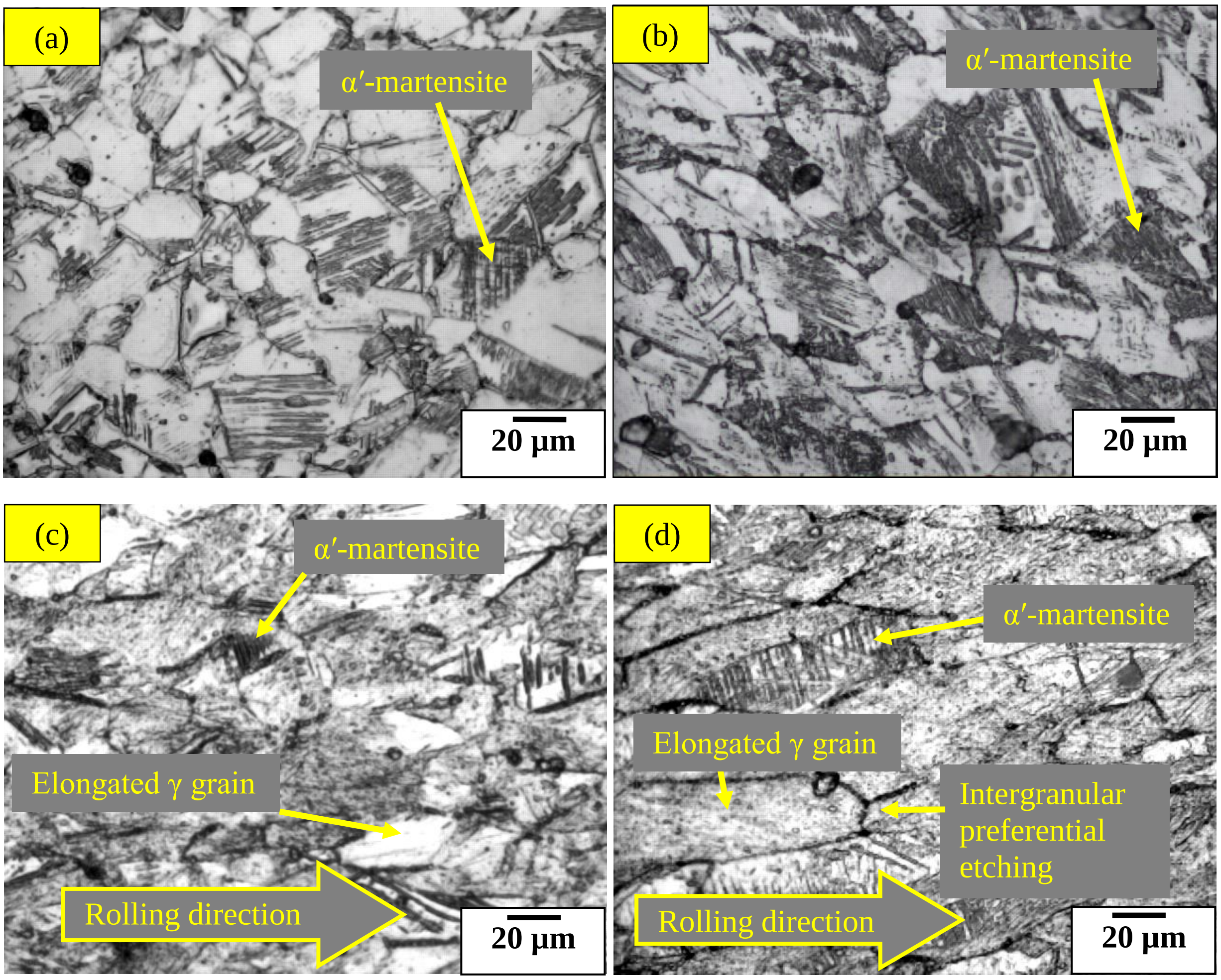

Figure 4.4: Optical micrographs of specimens obtained after deformation at room temperature for (a) 10%, (b) 20%, (c) 30% and (d) 40% thickness reduction [Steel A]. Rolling direction is indicated in Figures (c) and (d).

Figures 4.4(a) to (d) show the optical micrographs of specimens after rolling at room temperature. The micrograph clearly reveals that the martensite (indicated in the figure) is formed due to the deformation. The volume fraction of martensite gradually increases with the amount of deformation. The grains become elongated in the direction of rolling. The similar trend is also observed for the samples subjected to deformation at 0°C as depicted in Figure 4.5(a) to (d).

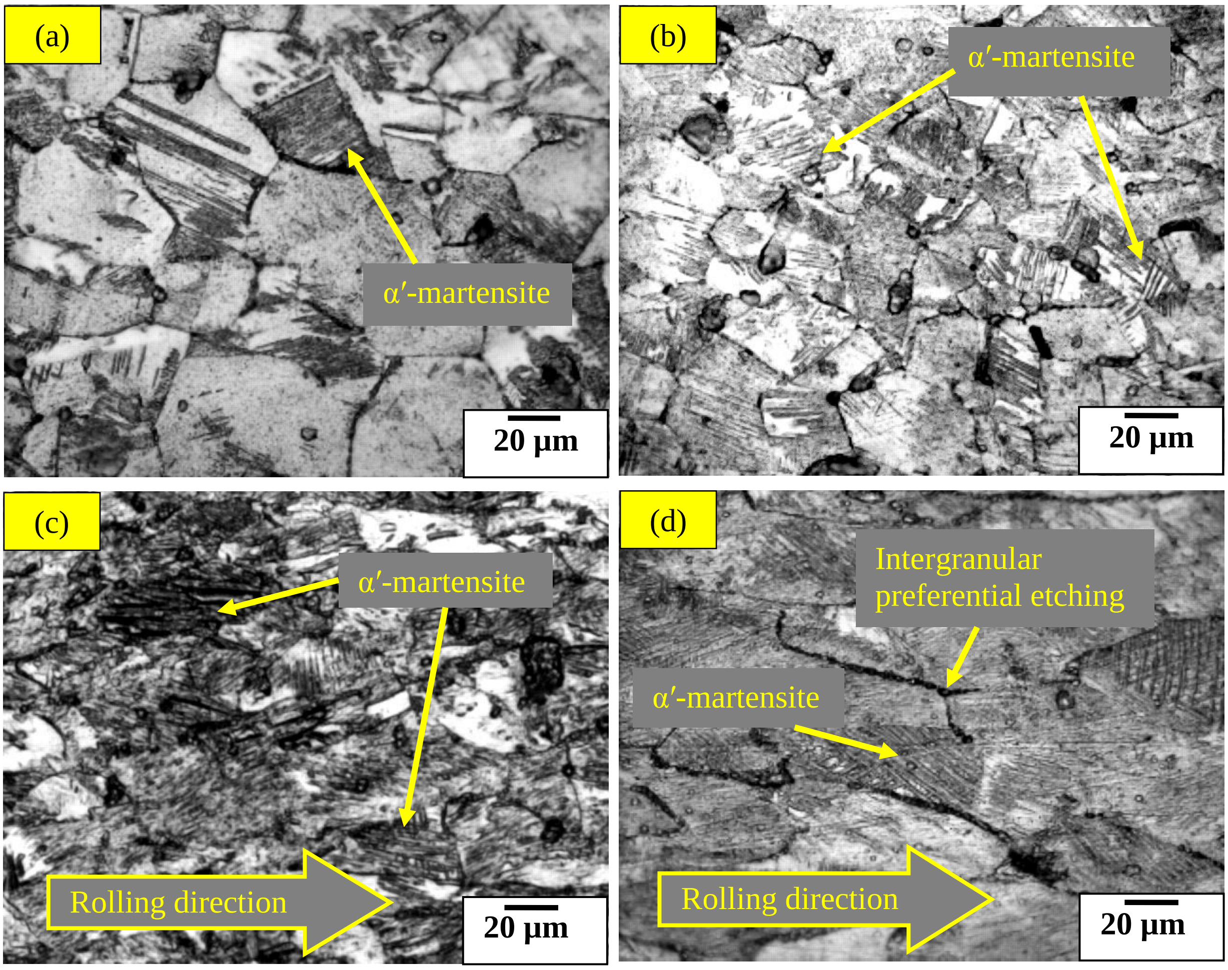

Figure 4.5: Optical micrographs of specimens after deformation at 0°C for (a) 10%, (b) 20%, (c) 30% and (d) 40% thickness reduction [Steel A]. Rolling direction is indicated in Figures (c) and (d).

The deformation by rolling at room temperature as well as at 0°C has triggered the formation of strain induced martensite. It is noticed that the increment of martensite volume fraction is directly proportional to the degree of deformation provided. A careful comparison of the microstructure (Figure 4.4 vis-à-vis Figure 4.5) indicates that samples at 0°C, reveals a higher percentage of martensite for a given amount of deformation. Thus, the microstructural observation corroborates the results of X-ray diffraction.

SEM micrographs for samples (Steel A) subjected to 30-40% cold deformation at 0°C are presented in Figures 4.6(a) and (b). It is evident that the microstructures of the cold rolled steel are characterised by the dispersion of hard martensite in a deformed austenite matrix. In this context, the occurrence of such microstructural constituent can be explained by the estimated SFE for the present steel, which is furnished in Table 4.4. The calculated SFE value for Steel A at room temperature is 20 mJ/m^2 as obtained from previously mentioned Eq. (2.3).

SFE (mJ/m^2) = -53 + 6.2(Ni) + 0.7(Cr) + 3.2(Mn) + 9.3(Mo) (wt.%) (2.3) [38]

$$\gamma_{SFE} = \gamma_{SFE}^{RT} + 0.05\,(T - 293) \quad (2.4)\ [43]$$

Where, T is the temperature in Kelvin.

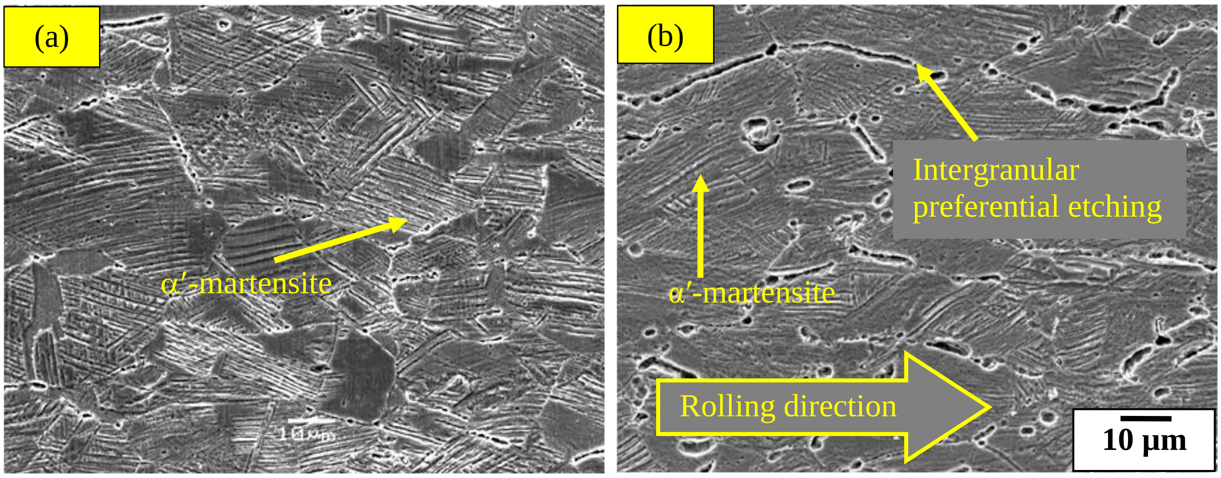

Figure 4.6: SEM micrographs after cold deformation at 0°C for (a) 30% and (b) 40% thickness reduction [Steel A]. Rolling direction is indicated in (b).

Table 4.4: Various degrees of deformation and estimated SFE values at selected temperatures.

Temperature (°C)	Reduction in thickness (%)	Stacking Fault Energy (SFE) using equation (2.3) and (2.4), respectively for room temperature and 0°C (mJ/m^2)	
		Steel A	Steel B
Room temperature (27)	10, 20, 30, 40	20	10
0	10, 20, 30, 40	19	9

Such low SFE value is favourable for the formation of micro-twins [192] and hence, the formation of α′ at the intersections of micro-twins becomes easier. It may be mentioned here that smaller amount of deformation up to 20% reduction in thickness results in a lower density of micro-twins within the austenite matrix, which in turn reduce the chances of the formation of α′-martensite nuclei at the intersection of micro-twins. In the case of 40% cold deformation at 0°C, the density of micro-twins is higher due to a large amount of strain leading to a microstructure consisting of deformed austenite with a higher density of micro-twins and α′-martensite along with a high density of dislocations [187]. In the present study, 40% cold reduction (Figure 4.6(b)) results into the austenite grains, elongated along the rolling direction and the formation of strain induced α′-martensite at the intersections of micro-twins during deformation. The diffused nature [191] of austenite grains in Figure 4.6(b) is apparently the manifestation of localised deformation. The deformation induced martensite morphology is narrower and more elongated than the thermally induced martensite [193]. The micrographs (Figure 4.5(d) and Figure 4.6(b)) further reveal the intergranular preferential etching contrast, which is akin to the intergranular crack at some locations. This is attributed to the accommodation strain during 40% cold reduction at both the deformation temperatures.

Figures 4.7(a) and (b) show the bright field TEM micrographs of samples subjected to 40% deformation at 0°C. The homogeneous dislocation substructures within austenite grains are evident in Figure 4.7(a). The α′-martensite laths with high density dislocations are found in Figure 4.7(b). Selected area electron diffraction (SAED) image at the inset of Figure 4.7(b) confirms the presence of martensite lath. The dislocation substructures are created due to the accommodation of stress due to plastic deformation as well as stress associated with the transformation of γ→α′. The formation of the high density of dislocation and the dislocation-precipitate interaction in the similar austenitic steel after deformation has been demonstrated in earlier studies [187, 191]. Presence of deformation twins (indicated by black arrow) and shear bands (indicated by yellow arrow) illustrated in Figure 4.7(c) and interaction among shear bands is depicted in Figure 4.7(d). These intersections point act as favourable nucleation sites for deformation induced α′-martensite. It may be mentioned here that deformation to large strains results in the formation of α′ phase without the intermediate presence of ε phase. The γ→α′ transformation sequence is followed in this case.

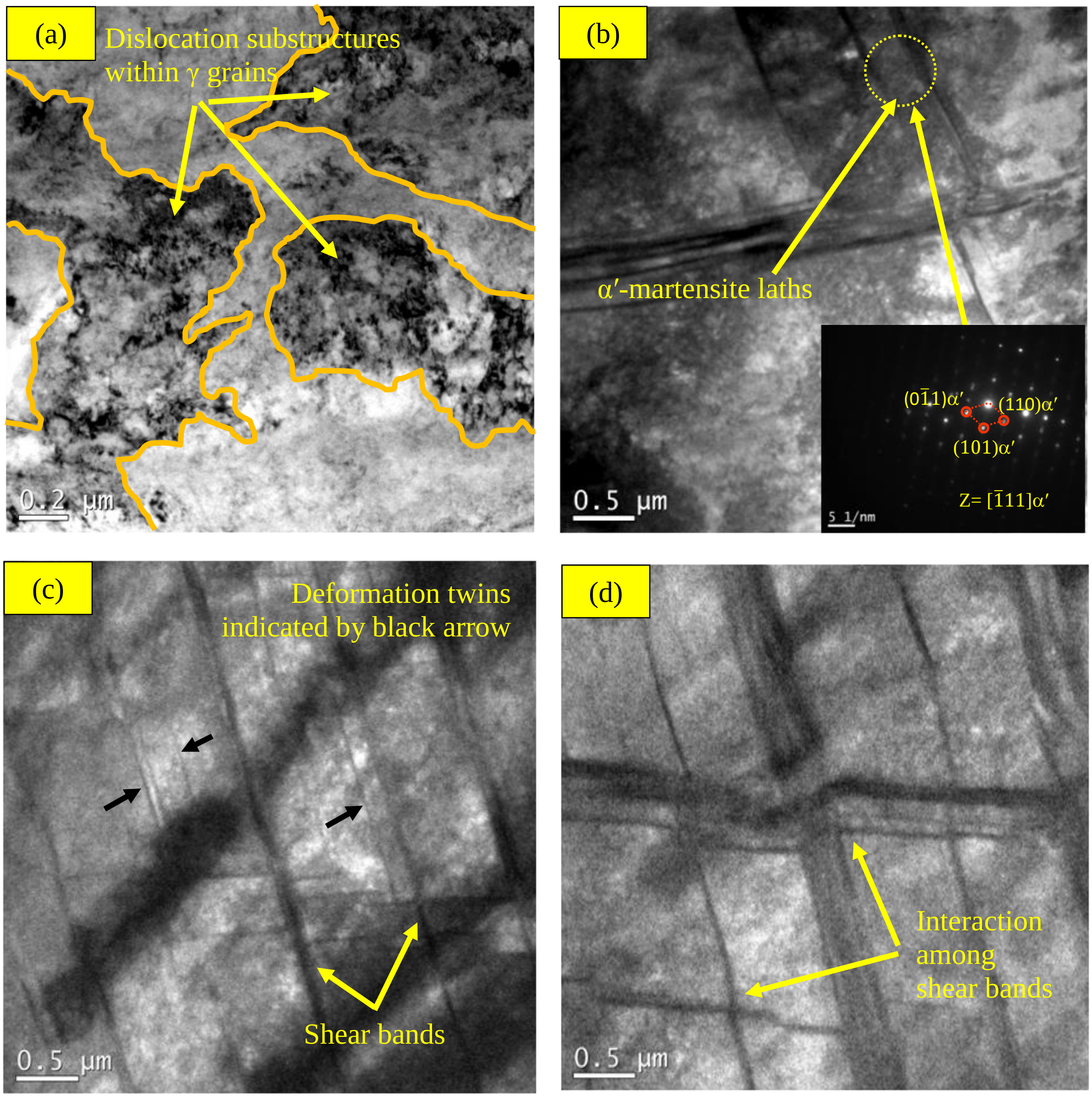

Figure 4.7: TEM bright field micrograph of samples subjected to 40% deformation at 0°C (a) showing dislocation substructures within austenite grains; (b) α′-martensite laths; (c) Presence of shear bands and (d) Intersection of the shear band as well as deformation twins [Steel A].

4.4 Mechanical properties obtained after deformation

Mechanical properties of as-received (0% deformation), as well as deformed samples at room temperature and 0°C, are furnished in Table 4.5. All the samples described here belong to Steel A composition. The as-received specimen reveals lowest hardness value of 149 VHN, while the deformed samples show increasing values of hardness in the ranges of 220-331

VHN and 256-358 VHN for room temperature and 0°C, respectively with the increase in cold deformation from 10 to 40%. The yield strength (YS), ultimate tensile strength (UTS) and percentage total elongation (TEL) values for the as-received sample are 259 MPa, 675 MPa and 90%, respectively. The corresponding stress-strain plot of as-received sample along with stress-strain curves of all deformed samples (10%-40%) has been illustrated in Figures 4.8(a) and (b) in order to understand the progress of mechanical properties during deformation at room temperature as well as at 0°C, respectively against the base material property. The deformed samples at room temperature have recorded YS and UTS values in the range of 724 - 1110 MPa and 927 - 1210 MPa, respectively with consequent lowering of %TEL values from 90% in the as-received sample to 34% - 11% in deformed samples. When the samples were subjected to deformation at 0°C, the tensile properties, YS, UTS and %TEL are witnessed in the range of 703 - 936 MPa, 930 - 1225 MPa and 32% - 13%, respectively.

Table 4.5: Hardness and tensile properties of cold deformed samples [Steel A].

Defor-mation (%)	Deformed at room temperature				Deformed at 0°C			
	Hardness (VHN)	YS (MPa)	UTS (MPa)	TEL (%)	Hardness (VHN)	YS (MPa)	UTS (MPa)	TEL (%)
0%	149±10	259±10	675±14	90±5	149±10	259±10	675±14	90±5
10%	220±12	724±21	927±15	34±3	256±11	703±22	930±12	32±3
20%	234±14	824±24	976±18	30±3	275±14	742±18	981±15	28±3
30%	304±18	759±20	1069±20	24±2	334±15	834±24	1098±19	22±2
40%	331±22	1110±28	1210±21	11±2	358±20	936±20	1225±29	13±2

The rate of work hardening is found similar for both the deformation temperature for the similar amount of deformation. However, the UTS values are slightly higher in case of deformation at 0°C owing to the formation of the higher volume fraction of α′-martensite compared to deformed samples at room temperature. This can be attributed to lowering of stacking fault energy by 1 mJ/m^2 between 0°C and room temperature (27°C) for Steel A composition. The measured values of α′-martensite volume fraction from X-ray diffraction analysis corroborate the same (Table 4.1). The shape of the stress-strain curves in Figures 4.8(a) and (b) are found significantly affected by the presence of α′-martensite. The increment of tensile strength is closely related to the variation in the amount of α′-martensite. Since the comparatively higher amount of deformation (30% and 40%) results in the increased amount of α′-martensite in 304 austenitic stainless steel, it is expected that different amount of deformation induced martensite would cause different strengthening and work hardening behaviour during tensile loading which can be witnessed from Figure 4.8.

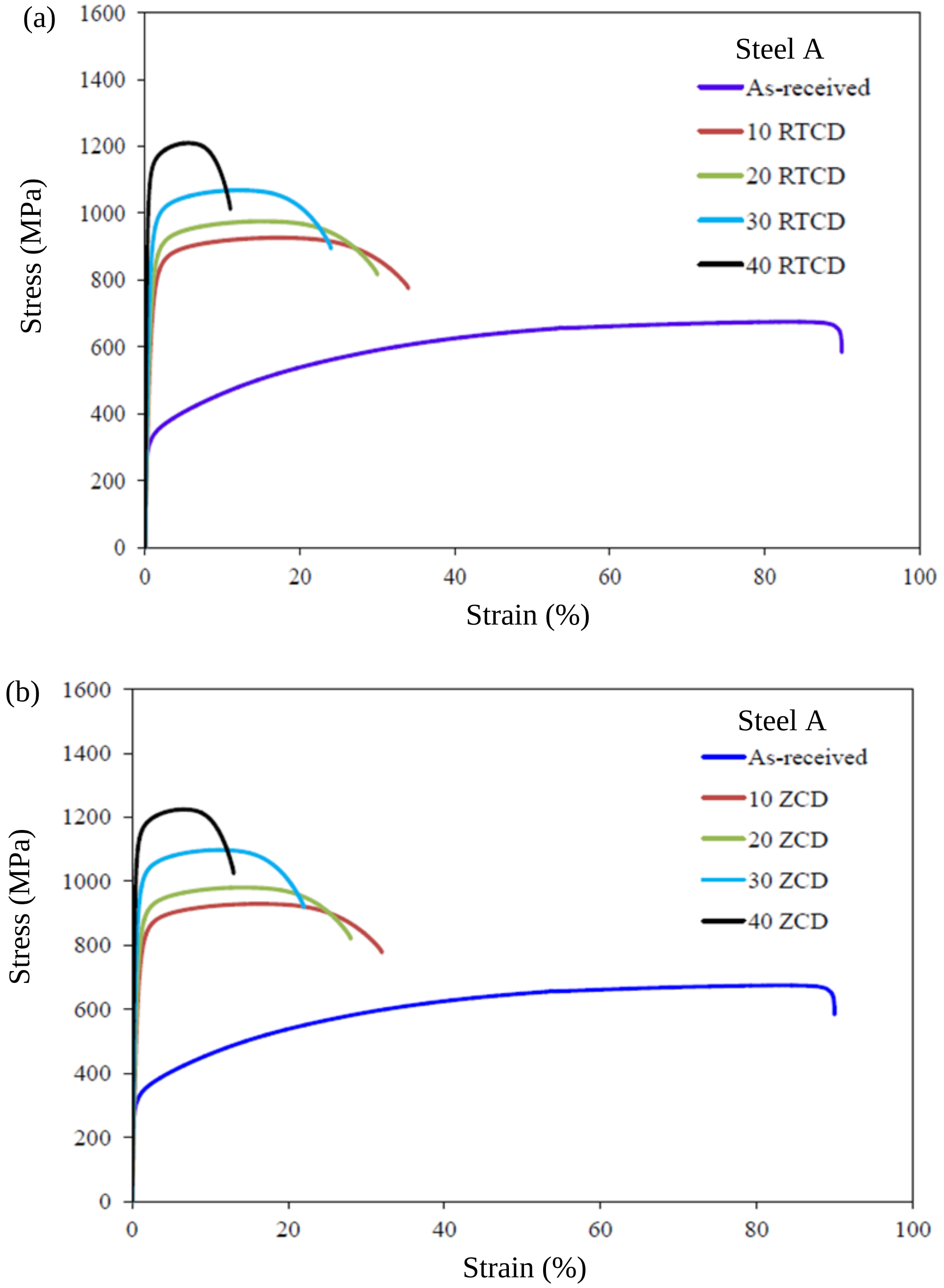

Figure 4.8: (a) Engineering stress-strain curves of as-received (0%), 10%, 20%, 30% and 40% deformed samples of Steel A composition at (a) room temperature and (b) 0°C [Deformation at room temperature = RTCD, Deformation at 0°C = ZCD].

Table 4.6 shows the measured mechanical property of Steel B composition in as-received (0% deformation) as well as deformed conditions. The deformation schedule for Steel B is identical with Steel A to understand the effect of composition variation between two austenitic grades of stainless steel. In as-received condition, Steel B possesses 205 VHN hardness, 378 MPa YS and 680 MPa UTS, which are higher by 56 VHN, 119 MPa and 5 MPa, respectively than those of Steel A. The %TEL in as-received condition is significantly lower in Steel B (26.6%) as compared to (90%) in Steel A sample. It is evident that hardness, YS and UTS values increase and %TEL decrease with the increase of the degree of cold deformation at room temperature as well as at 0°C. Steel B samples when subjected to 30% and 40% deformation yields YS and UTS values of 764 - 1079 MPa and 1125 - 1293 MPa at room temperature. Similarly, for deformation at 0°C yields 961 and 1257 MPa YS and 1259 and 1444 MPa UTS for 30% and 40% deformation, respectively. All these strength values are higher than those of Steel A composition under identical deformation schedule owing to the difference in chemical composition. However, the magnitude of enhancement of hardness, yield strength and tensile strength values is higher in case of Steel B than that of Steel A for 20% - 40% deformation and it appears that the work hardening rate in Steel B increases with the increase in deformation percentage.

Table 4.6: Hardness and tensile properties of cold deformed samples [Steel B].

Defor-mation (%)	Deformed at room temperature				Deformed at 0°C			
	Hardness (VHN)	YS (MPa)	UTS (MPa)	TEL (%)	Hardness (VHN)	YS (MPa)	UTS (MPa)	TEL (%)
0%	205±5	378±10	680±18	26.6±3	205±5	378±10	680±18	26.6±3
10%	306±10	687±14	856±20	13.4±2	313±8	517±11	859±20	13.9±2
20%	393±12	778±18	1028±22	13.3±2	397±10	750±15	1067±22	7.2±1
30%	402±14	764±20	1125±23	8.5±1	447±12	961±20	1259±26	7.7±1
40%	438±18	1079±22	1293±26	6.4±1	478±14	1257±25	1444±32	1.8±0.5

The strength enhancement is accompanied by the loss of percent elongation, which is more in Steel B for deformation at 0°C than at room temperature. TEL for Steel B in as-received condition is 26.6%, which has further lowered down to 13.4% - 6.4% and 13.9% - 1.8% during deformation at room temperature and 0°C, respectively. For 40% deformation at

0°C, the Steel B reveals only 1.8% residual ductility as compared to 6.4% for 40% deformation at room temperature.

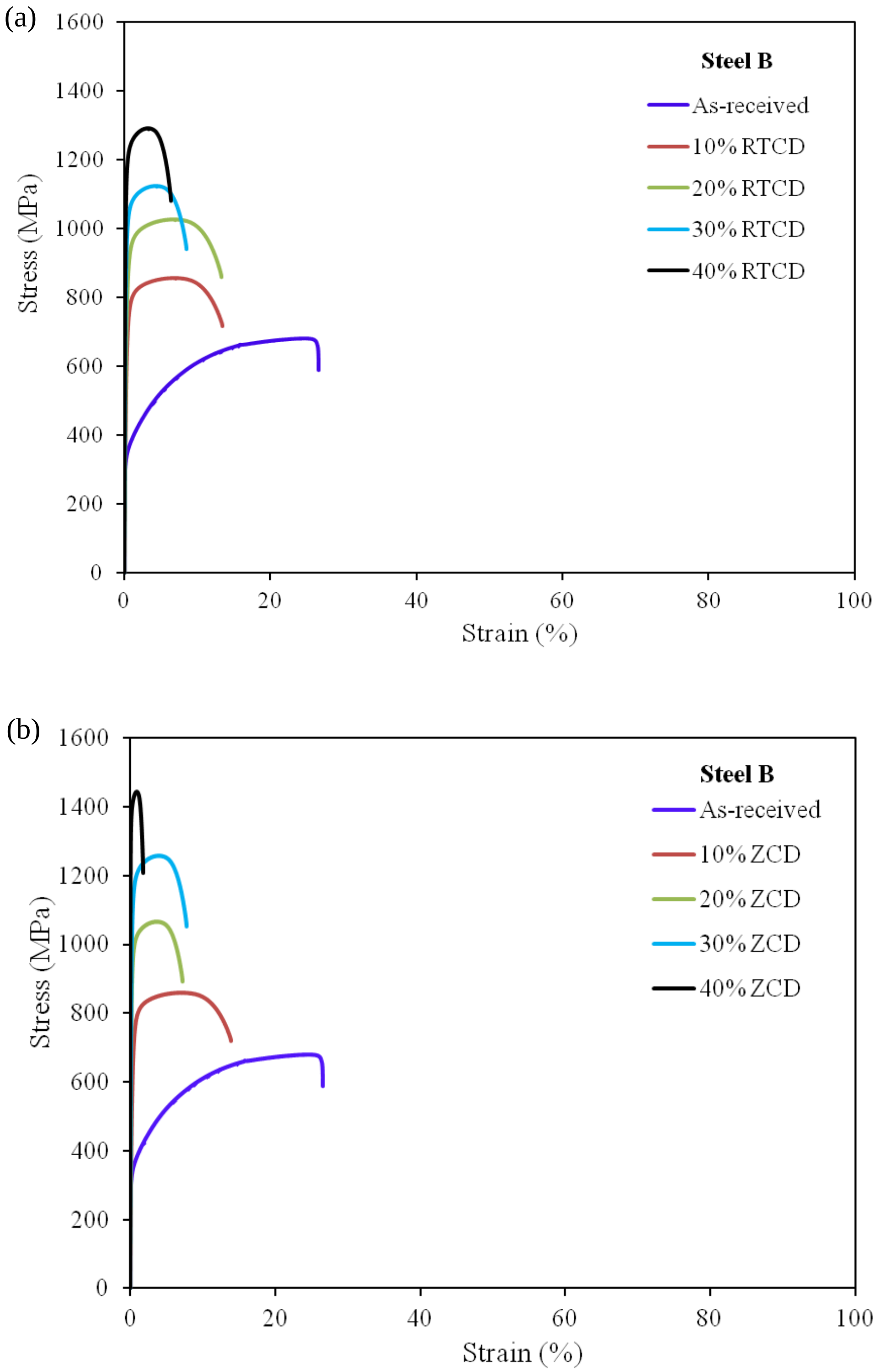

Figure 4.9: Engineering stress-strain curves of as-received (0%) and 10%, 20%, 30% and 40% deformed samples of Steel B composition at (a) room temperature and (b) 0°C [Deformation at room temperature = RTCD, Deformation at 0°C = ZCD].

Figures 4.9(a) and (b) illustrates stress-strain curves of Steel B for the as-received and deformed condition where the deformed samples do not reveal significant area under the curve owing to very less %TEL in deformed samples. It indicates that almost all the remaining austenite during tensile deformation transform to ε/α′-martensite [194]. The product of tensile strength and elongation (UTS × %TEL) has been often utilised as the index of the balance between strength and ductility. From Table 4.6, Figures 4.9(a) and (b), we can understand that, the balance between strength and ductility in case of Steel B material is not encouraging as the UTS × %TEL values for 30% - 40% deformed samples are 9562 - 8275 MPa% and 9694 - 2599 MPa% at room temperature and 0°C, respectively.

The lower strength value along with higher percent elongation of the as-received specimen is an indication of the microstructure (Figure 4.3) apparently free from martensite, carbide precipitates and dislocation sub-structure. On the other hand, higher YS and UTS values as well as drop of percent elongation with increasing deformation are indicative of increasing amount of strain induced α′-martensite formation (Figures 4.6(a) and (b)) in addition to the strain hardening of the highly alloyed austenite [164].

4.5 Comparison of mechanical properties between Steel A and Steel B after deformation at room temperature as well as 0℃

A comparison of Steel A with Steel B (Table 4.5 vis-à-vis Table 4.6) indicates that the magnitude of hardening/strengthening is higher for Steel B than that of Steel A. This behaviour is attributed to the higher Mn content (3.3 wt.%) in steel B as compared to Steel A having lower Mn content (1.29 wt.%).

Figures 4.10(a) to (d) and Figures 4.11(a) to (d) furnish the comparative mechanical properties between two deformation temperatures (room temperature and 0°C) for Steel A and Steel B, respectively. The trend of increment in strength and decrease in ductility between the two deformation temperatures are almost similar for both Steel A and B in case of lower level of deformations up to 20%. The trend lines show a gap for higher deformation amount of 30% and 40% for strength level of both steels and hardness values of Steel B. The reduction trend % total elongation at room temperature and 0°C appears similar for both the steels. From the above comparison, it may be observed that increment in hardness and strength values are higher in case of deformed samples at 0°C than that of room temperature for higher % of deformation (30-40%) in both the steels, whereas the decrease in ductility reveals similar trends irrespective of the deformation temperature for both the steels. The increase in strength in Steel A achieved after 10% cold deformation at 0°C (UTS of 930 MPa with 32% TEL) (Table 4.5 and Figure 4.10(c)) is expected to enhance its reliability in designing durable, light weight and flexible component particularly for aircraft and aerospace industries.

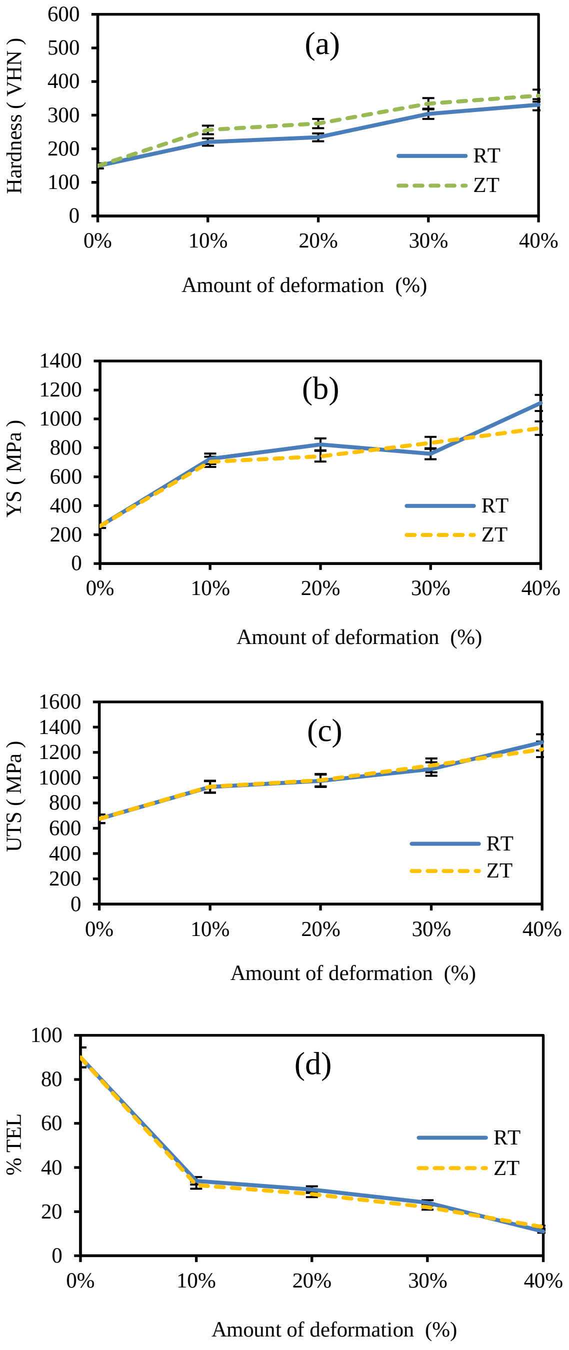

Figure 4.10: Comparison of mechanical properties between two deformation temperatures (RT = Room temperature and ZT = 0°C) for Steel A; (a) Hardness, (b) YS, (c) UTS and (d) %TEL.

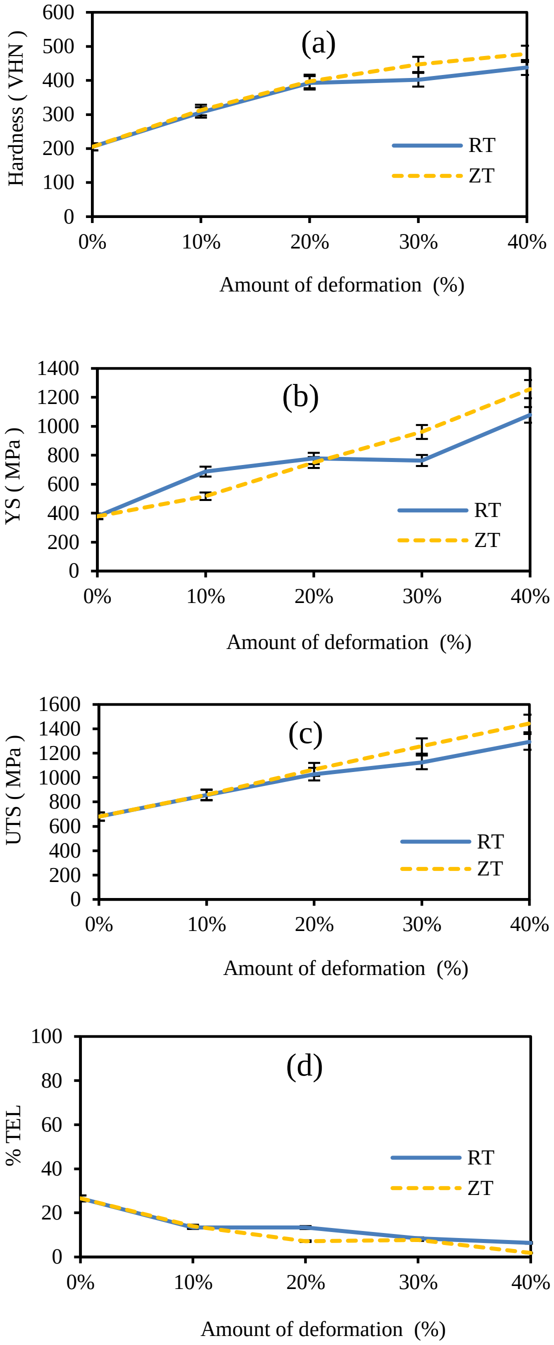

Figure 4.11: Comparison of mechanical properties between two deformation temperatures (RT = Room temperature and ZT = 0°C) for Steel B; (a) Hardness, (b) YS, (c) UTS and (d) %TEL.

Comparison of mechanical property has been carried out between Steel A and Steel B, where some of the Ni content in Steel A has been replaced by Mn (Table 3.1) in Steel B and the same is depicted in Figures 4.12(a) to (d) and Figures 4.13(a) to (d) for deformation at room temperature and 0°C, respectively. At 0°C, Steel B has provided superior values of hardness, YS and UTS for a higher level of deformation (30%-40%). The hardness and strength values for Steel B show a steady increase with increase in the amount of deformation at 0°C, whereas the same for Steel A shows a plateau against 10%-20% deformation level followed by steady increase at a lower rate than Steel B, which can be attributed to better work hardening response of Steel B than Steel A owing to presence of higher amount of Mn. The ductility values of Steel B are always on the lower side than that of Steel A irrespective of the deformation temperature. In as-received condition, Steel B sample exhibits lower %TEL than that of Steel A. This may be attributed to higher rate of work hardening in Steel B in comparison to Steel A during tensile deformation due to the presence of higher wt.% of C and Mn along with lesser wt.% of Ni. This is also manifested by higher yield strength and lower %TEL values in the case of Steel B as compared to Steel A in as-received condition.

It is evident from Figures 4.10(d) to 4.13(d) that, %TEL value, which is the measure of ductility, has been reduced drastically with the onset of deformation induced martensite formation at room temperature or at 0°C. Steel A having TEL value of 90% in as-received condition loses its ductility to the level of 85%-88% (TEL values are 11% and 13% at room temperature and at 0°C, respectively) after 40% reduction in thickness. It may also be noted that, only 10% reduction in thickness triggers nearly 62%-64% drop of ductility (TEL values are 34% and 32% at room temperature and at 0°C, respectively) in the case of Steel A. On the other hand, ductility of Steel B, which is already lower (TEL = 27%) than that of Steel A in as-received condition, further decreases after deformation. In the case of 40% reduction in thickness of Steel B, the TEL value is merely 1.8% at 0°C. However, the drop of elongation in Steel B after 10% thickness reduction (TEL = 14%) is close to 50% which is lower in comparison to the same amount of deformation (10%) in Steel A (64% drop of elongation).

The reason for the overall drop in ductility for both Steel A and B with deformation is that the parent austenite in both types of steel (A and B) is transforming into BCC martensite, thereby contributes to higher strength by sacrificing ductility which varies sigmoidally with deformation temperature [195]. The presence of twins provides a trend towards increasing ductility as the formation of martensite was replaced by twinning at the higher deformation temperatures. It should be noted that the twinning plane is also the habit plane of the strain-induced martensite [196]. The formation of deformation twins is not favoured in materials having stacking fault energy < 20 mJ/m^2 (Table 4.4). In the transition region between well formed strain induced martensite plates and twins, small martensite platelets were observed on slip bands [197]. In this context, it is noted that for austenitic stainless steel, both nickel and carbon increase the stacking fault energy of iron with carbon having a very influential effect [198]. Both of these factors lower the tendency towards twinning, which attribute to the significant reduction in ductility during deformation at room temperature as well as at 0°C.

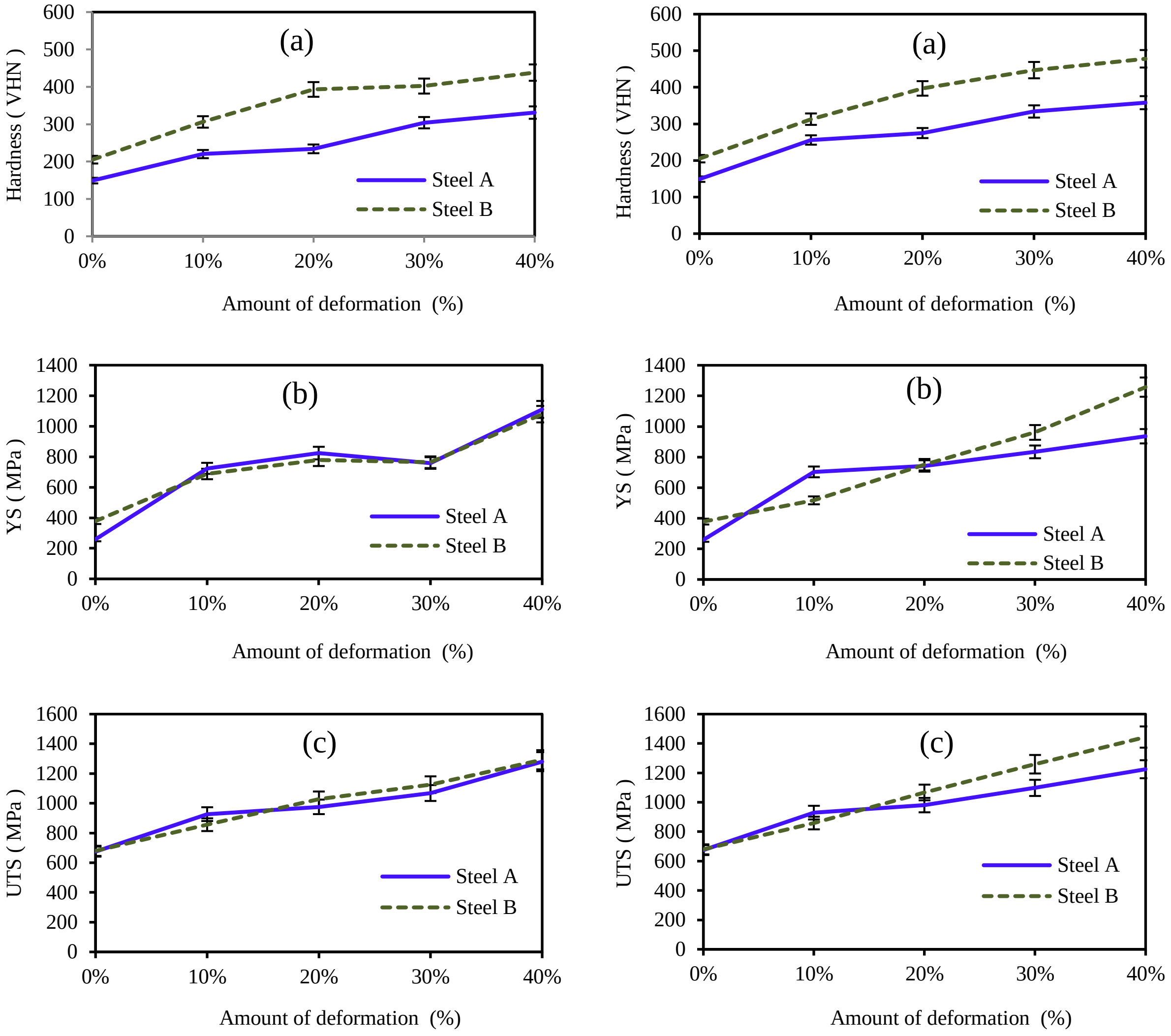

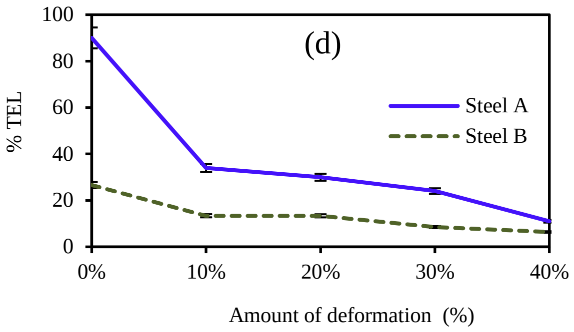

Figure 4.12: Comparison of mechanical properties between Steel A and Steel B deformed at room temperature (RT); (a) Hardness, (b) YS, (c) UTS and (d) %TEL.

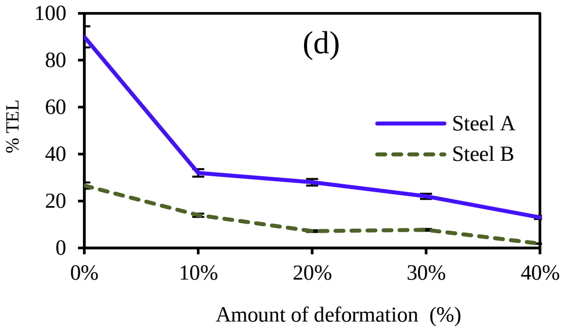

Figure 4.13: Comparison of mechanical properties between Steel A and Steel B deformed at 0°C temperature (ZT); (a) Hardness, (b) YS, (c) UTS and (d) %TEL.

4.6 Fracture surface and sub-surface study

Figures 4.14(a) and (b) show the SEM micrographs of the fracture surface and sub-surface, respectively of the as-received specimen. The fracture behaviour is of predominantly ductile in nature with varying dimple size and depth (Figure 4.14(a)). Higher amount of ductility is reflected through the extremely fine size of dimples. It is apparent from the sub-surface micrograph (Figure 4.14(b)) that frequent nucleation of micro-voids occurs at austenite/martensite interface as well as nucleation and propagation of micro-cracks occur within the martensite. Formation of micro-cracks by fracturing martensite phase (denoted by black arrow) is also evident from the micrograph. In this context, it is noted that the formation of martensite has taken place due to uniaxial strain applied during tensile testing.

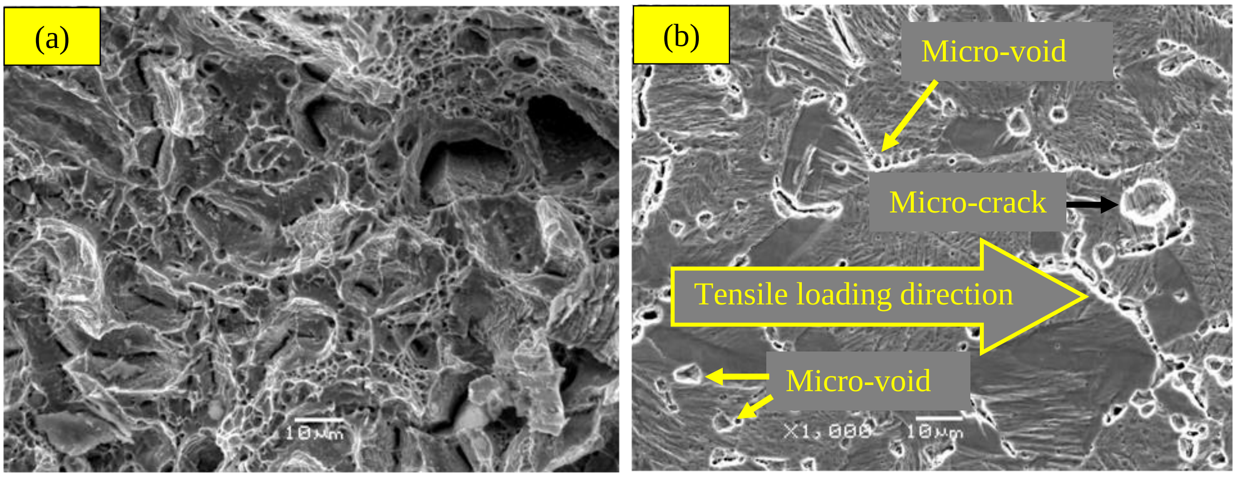

Figure 4.14: SEM micrograph of (a) fracture surface and (b) sub-surface of as-received specimen [Steel A].

Figures 4.15(a) and (b) show SEM micrographs of fracture surface and sub-surface of cold deformed (40%) specimen (Steel A) at 0°C. Figure 4.15(b) shows the presence of crack/void nucleation along the boundary of austenite phase or austenite-martensite interface. The consequent fracture is of predominantly intergranular in nature (Figure 4.15(a)). Figure 4.15(a) indicates brittle nature of the fracture in contrast to ductile fracture of the as-received specimen as shown in Figure 4.14(a). The micro-voids appear to be elongated toward the tensile loading direction for the as-received specimen, while the same appears to be comparatively spherical for deformed specimen (Figure 4.14(b) vis-à-vis Figure 4.15(b)), indicating lower ductility for the deformed sample. The sub-surface micrograph (Figure 4.15(b)) clearly indicates that the micro-voids along the austenite/martensite and/or martensite/martensite interface result into the rapid void coalescence which yields intergranular fracture (Figure 4.15(a)). The fractographic features are in conformation with the corresponding tensile elongation values. The ‘as-received’ specimen records the highest ductility and the 40% deformed specimens reveal the lowest % of total elongation. This is in agreement with the observations of the fracture surface.

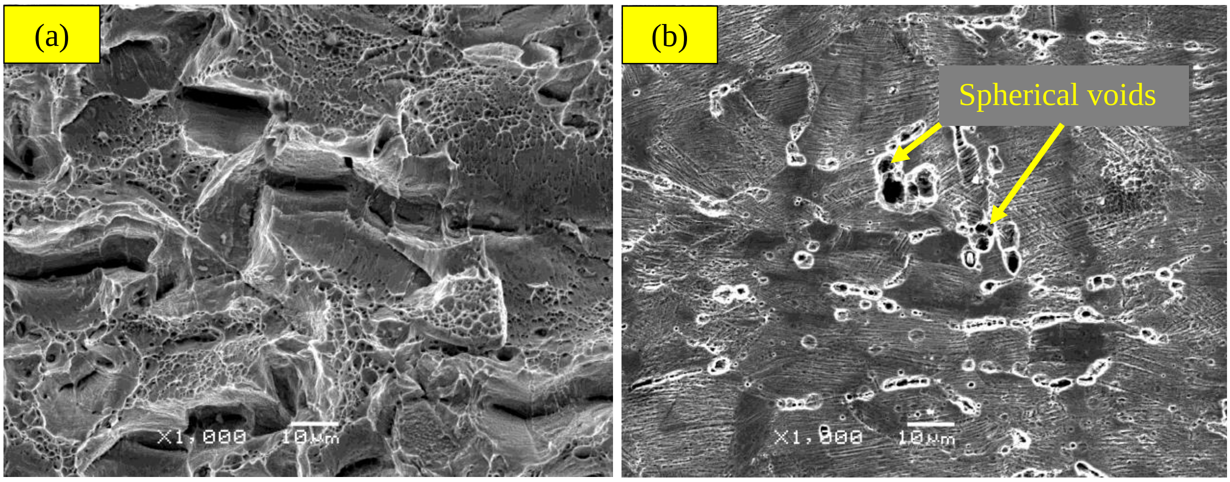

Figure 4.15: SEM micrograph of (a) fracture surface and (b) sub-surface of cold deformed (40%) specimen at 0°C [Steel A].

4.7 Summary

1. The microstructural characterisation reveals the presence of α′-martensite after cold deformation (30-40%), while the as-received specimen shows austenitic microstructure. In the case of 30% and 40% cold deformed samples, 19% and 26% α′-martensite at room temperature and higher amount of i.e., 24% and 32% α′-martensite at 0°C have been obtained from X-ray diffraction analysis.
2. The as-received specimen reveals the lowest strength (675 MPa) with maximum total elongation (90%) among all of the specimens. Hardness, yield strength and tensile strength values increase with the increase of deformation at both room temperature as well as0°C. The achieved values of strength for 10% and 20% deformed sample with adequate elongation (~ 30%) makes the steel amenable for use in high strength structural and safety applications. Higher yield strength and lower ductility in Steel B indicate superior work hardening characteristics under identical processing conditions when compared with Steel A in as-received state.
3. The fracture surface and sub-surface of the as-received and the 40% deformed samples indicate a transition from a predominantly ductile fracture in the as-received specimen to the brittle type of fracture in the deformed sample. The fractographic observation corroborates the results obtained from the tensile testing. The sub-surface micrographs provide the potential sites for the initiation of micro-voids and/or micro-cracks.

5

EFFECT OF REVERSION ANNEALING IN COLD DEFORMED STEELS

5.1 Introduction

The present study aims to investigate the evolution of microstructure in 304 austenitic stainless steel due to reversion annealing of cold deformed samples under different schedules and genesis of corresponding mechanical properties. While strain induced martensite, deformation twins and high dislocated structures comprise the microstructure of the cold deformed samples, reversion annealing of the same results into fine-grained reverted austenite, cell type dislocation sub-structures with some amount of untransformed martensite.

Grain refinement is known to improve both the strength and toughness of structural steels. Grain refining processes are greatly influenced by the reversion mechanism [24]. There are two types of mechanism for the reversion from martensite to austenite: one is diffusional reversion and the other is martensitic shear reversion without diffusional process. In steels which undergo martensitic shear reversion, reversion completes during annealing and reverted austenite contains a high density of dislocations just after reversion. During successive annealing, grain refining proceeds through the process of recrystallisation of reverted austenite. Defects such as dislocations and slip bands are inherited to reverted austenite resulting in grain refining. On the other hand, diffusional reversion proceeds by the growth of austenite nucleated in the martensite lath boundary which contains high dislocation density. Austenitic steels do not undergo phase transformation at typical annealing temperatures and the only way to refine the grain is recrystallisation after cold rolling. However, the strengthening by grain refining is limited due to the high recrystallisation temperature (>900°C) of this stainless steel grade. In austenitic stainless steels, plastic deformation of austenite creates the proper defect structures which act as an embryo for martensite transformation which reverts to recrystallised austenite during annealing in the temperature range of 450-800°C [22, 23, 25]. Therefore, it is of interest to consider the effectiveness of reversion as a mean of strengthening steels. The strengthening effect in the austenite depends in a complex manner on many factors relating to alloy constitution, structure and heat treatment conditions. The increase in strength of austenite achieved by reversion is associated with the high dislocation density of the reverted austenite regions and the presence of stacking faults and twins.

5.2 X-ray diffraction analyses of as-received, cold deformed and reversion annealed samples

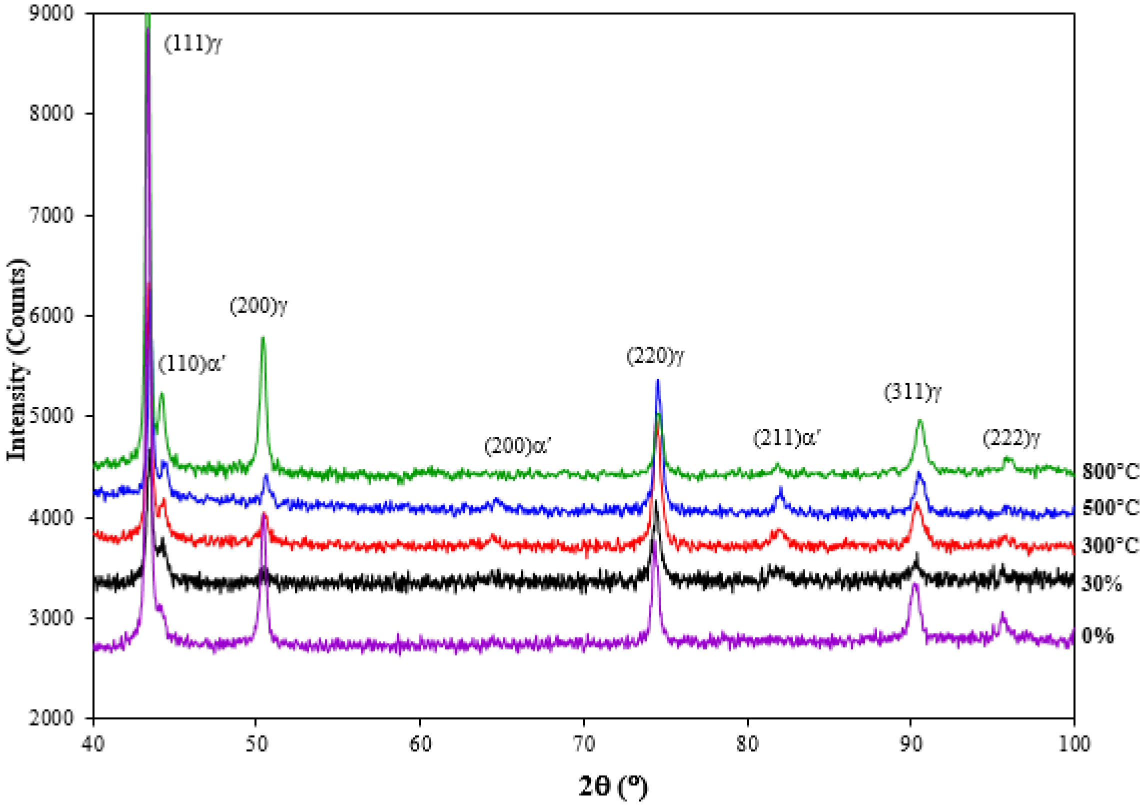

Figure 5.1: X-ray diffraction patterns depicting the formation of strain induced martensite (α′) by cold deformation (30%) and its reversion into austenite (α′→γ) after annealing (300-800°C, 1 h) [Steel A].

Figures 5.1 and 5.2 present the X-ray diffraction profiles of samples subjected to 30% and 40% cold deformation, respectively followed by annealing over the temperature range of 300-800°C for 1 h duration. The X-ray diffraction (XRD) plot of the as-received specimen (0% deformation) has also been appended to the figures to reveal the peaks related to the single phase austenite. In the case of the deformed sample, the (110), (200) and (211) peaks of the BCC α′-martensite phase are clearly revealed along with the (111), (200), (220), (311) and (222) peaks characterising the FCC austenite phase.

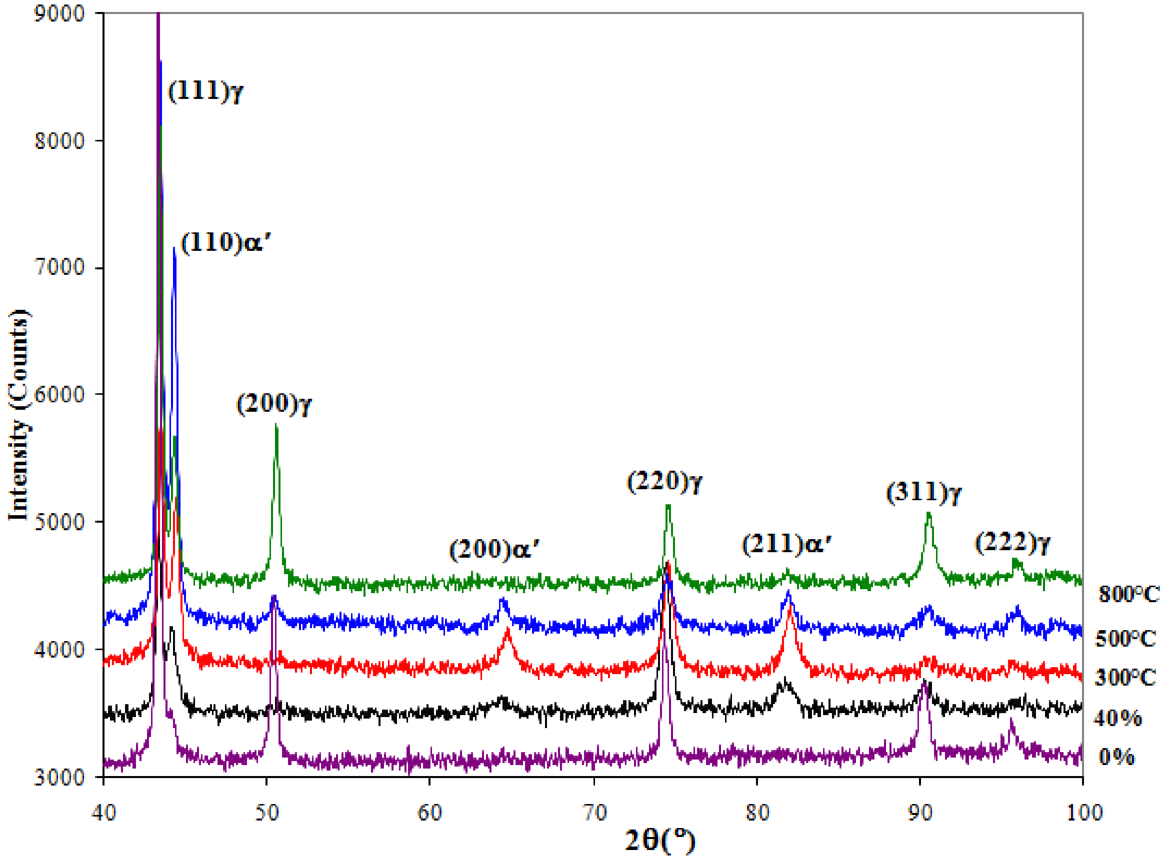

Figure 5.2: X-ray diffraction patterns depicting the formation of strain induced martensite (α′) by cold (40%) deformation and its reversion into austenite (α′→γ) after annealing (300-800°C, 1 h) [Steel A].

The annealing treatment in the temperature range of 300-800°C for 1h duration resulted in the reversion of strain induced martensite. An increase in the annealing temperature from 300 to 800°C evidence more prominent α′→γ transformation. It is also apparent that the peaks related to the α′-martensite become weaker or disappears after the annealing treatments. Earlier, it has been reported that volume fraction of α′-martensite does not change significantly during low temperature ageing (300°C), and the rate of phase transformation increases when the temperature exceeds 450°C [199]. The decrease in α′-martensite volume percentage after annealing at 300°C for 1 h is 3-5% only, as compared to 30% and 40% deformed samples, (refer Table 5.1). It is to be noted that, significant peak broadening can be witnessed in 40% deformed sample with respect to as-received (0% deformation) sample owing to highly stressed structure produced during cold deformation at 0°C. The peak broadening phenomena is associated with decrease in peak intensity, which can be observed from the X-ray diffraction pattern of 40% deformed sample. During subsequent annealing process, the stress in the structure and the residual stress in surrounding matrix get annihilated, resulting into lowering of peak broadening simultaneously with increase in peak intensity. The corresponding X-ray diffraction pattern for reversion at 300°C for 1 h, show an increase in the intensity of α′-martensite at (110), (200) and (211) peaks than those of deformed sample. The increase in peak intensity however, bought no significant change in α′-martensite volume percentage as described earlier. In this context, it is important to mention here that, the volume percentage calculation of constituent phases have been carried out considering all the prominent peaks from the corresponding X-ray diffraction pattern. With further progress in annealing the (200) and (211) peaks corresponding to α′-martensite become weaker and disappear. The measured residual volume percentage of strain induced α′-martensite after annealing at 800°C for 1h is 8% for both the samples. The existence of Cr-carbide could not be identified in the X-ray diffraction result. It implies that the volume percentage of Cr-carbide was inadequate for estimation by the X-ray diffraction.

Table 5.1: Volume percentage of the constituent phases after deformation and annealing.

Initial processing condition	Volume measurements (in %)		Annealing temperature and duration	Volume measurements (in %)	
	After deformation			After reversion	
	FCC (γ)	BCC (α′)		FCC (γ)	BCC (α′)
30% deformation at 0°C	76±2	24±1	300°C, 1h	81±2	19±1
			800°C, 1h	92±2	8±1
40% deformation at 0°C	68±2	32±1	300°C, 1h	71±2	29±1
			800°C, 1h	92±2	8±1

5.3 Evolution of microstructure

5.3.1 SEM micrographs and EDS microanalysis of annealed samples

Figures 5.3(a) and (c) shows photograph for 30% and 40% deformed samples after reversion annealing at 500°C for 1 h, the deformation induced martensite undergoes reversion (i.e., $\alpha' \rightarrow \gamma$) along the martensite/austenite interface as a result of thermal decomposition of strain induced martensite. The reverted austenite grows at the expense of strain induced α′-martensite. It is apparent that individual α′-martensite phase breaks up during reversion, while the other areas of the specimen appear to be unaffected by the heating. The micrograph also reveals "ghost" areas [22] of preferentially etched reversed austenite which corresponds to the original martensitic region. It is important to mention that the intergranular micro cracking has been significantly reduced after annealing due to the release of the residual stresses of 30% as well as 40% cold deformed samples. Figures 5.3(b) and (d) demonstrate that the reversion rate increases with the progress of annealing. The mechanism initiates with the reversion of strain induced martensite to the dislocated austenite lath through diffusion or shear mechanism. Then the newly formed austenite undergoes recovery and recrystallisation. This will lead to the formation of finer (10-15 µm) strain free equiaxed austenite grain. The micrograph also reveals the formation of fine precipitates of brighter contrast along the austenite grain boundary and twin boundaries. The average chemical composition of the brighter precipitate particles obtained from EDS microanalysis is 68.63Fe-22.50Cr-7.41Ni-0.52Si-0.94Mn (wt.%) which indicates the formation of $(Cr, Fe)_{23}C_6$ phase, Table 5.2 [168].

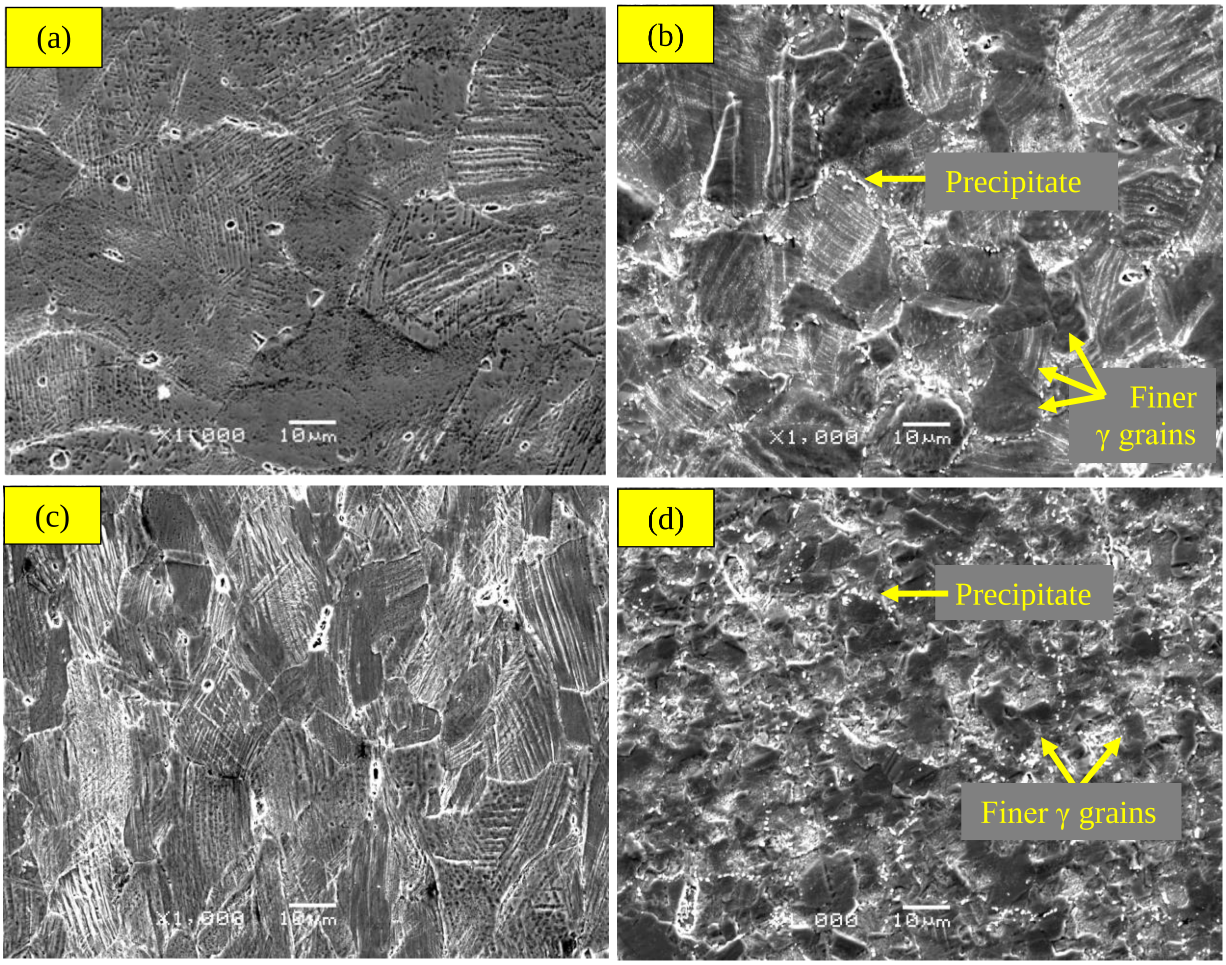

Figure 5.3: SEM micrographs of 30% cold deformed 304 stainless steel specimen subjected to annealing for 1 h. at (a) 500°C and (b) 800°C. 40% cold deformed 304 stainless steel specimen subjected to annealing for 1 h at (c) 500°C and (d) 800°C [Steel A].

Evidence of Cr-carbide precipitation at the grain boundary has been confirmed by conducting the EDS microanalysis of the sample obtained after 30% deformation followed by annealing at 800°C (1h) as shown in Figure 5.4(a). Figures 5.4(b) and (c) show the EDS spectra obtained from the Cr-rich carbide precipitates along the grain boundary and the austenite matrix phase, respectively. Composition analysis (wt.%) of the carbide particles as well as the austenite phase (Table 5.2) indicate that while the carbide particles are rich in Cr and depleted with Ni, austenite is rich in Ni and depleted in Cr.

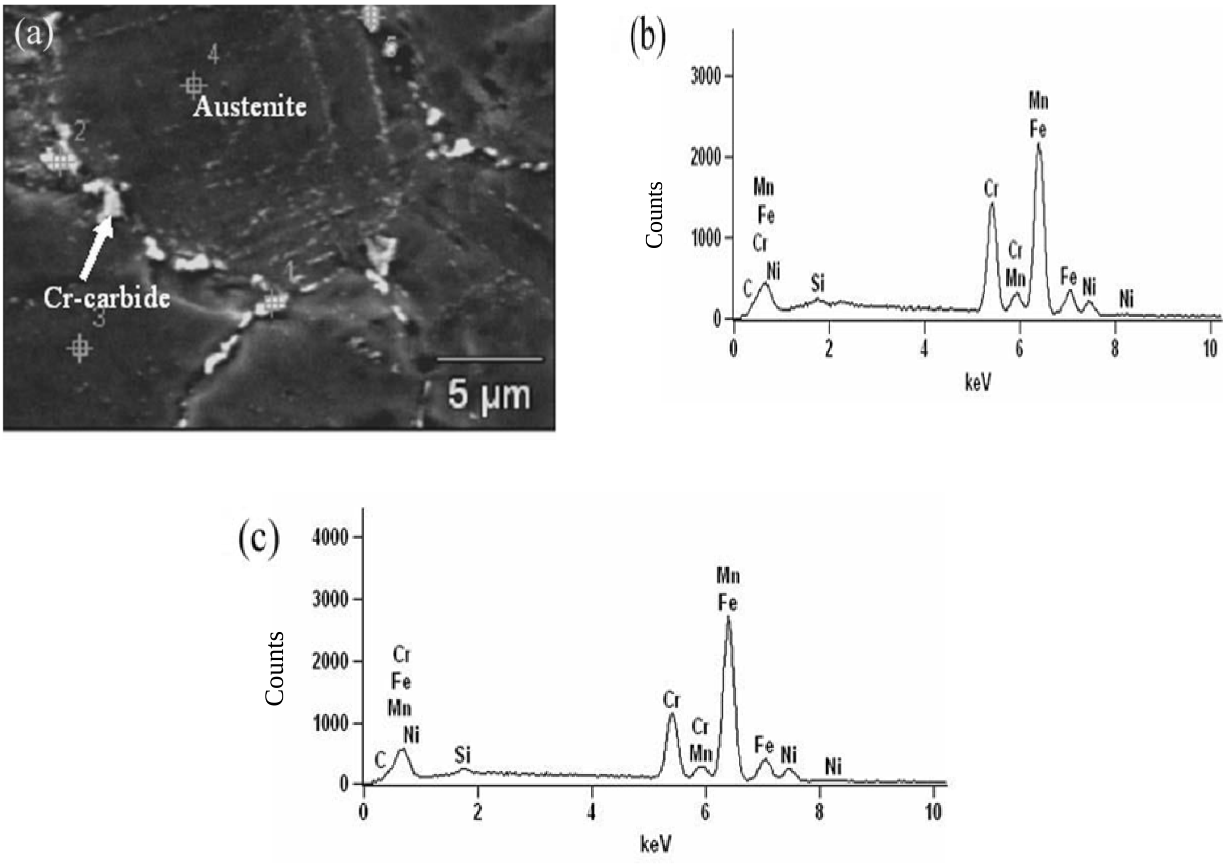

Figure 5.4: (a) SEM micrograph showing Cr-carbide precipitation. (b) & (c) EDS spectrum obtained from precipitate and austenite phase, respectively for the 30% deformed sample subjected to reversion annealing at 800°C for 1 h [Steel A].

Table 5.2: Chemical composition (wt.%) of phases obtained by EDS microanalysis.

Phase	Si	Cr	Mn	Ni	Fe
Cr-carbide	0.53 ± 0.10	24.89 ± 0.39	1.30 ± 0.24	7.27 ± 0.53	66.01 ± 0.74
Austenite	0.67 ± 0.09	18.40 ± 0.34	1.20± 0.22	8.25 ± 0.52	71.48 ± 0.73

5.3.2 TEM micrographs of annealed samples

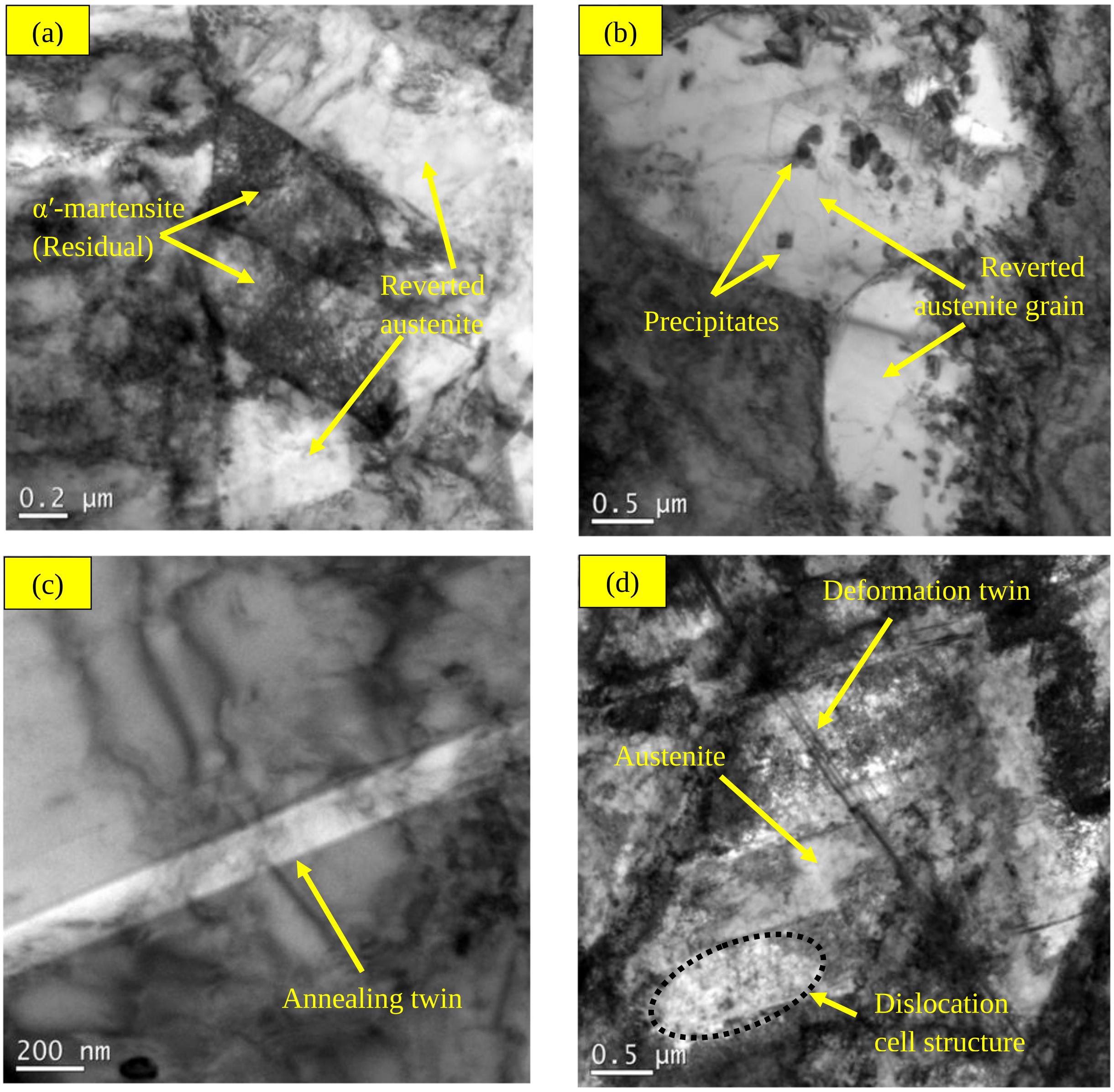

Figure 5.5: TEM micrographs of 40% cold deformed sample at 0°C followed by reversion annealing at 800°C for 1 h [Steel A].

Figure 5.5 reveals micrograph of 40% cold deformed 304 stainless steel specimen subjected to annealing for 1 h at 800°C. Presence of residual deformation induced martensite can be witnessed alongside reverted austenite grains in Figures 5.5(a) and (b). Figure 5.5(b) is also showing the presence of precipitates. Careful examination reveals the presence of fine dislocation substructure within reverted austenite grains. However, the comparison between Figure 5.5(a) and (b) with 5.5(d) shows the presence of higher density of dislocation cell structure in the marked region of Figure 5.5(d), which indicates that stress relieving in reverted austenite grains were almost complete. Presence of deformation twin, as well as annealing twin, is evidenced (Figures 5.5(c) and (d), respectively) from the micrograph of the reverted sample.

5.4 *Mechanical properties after reversion annealing treatment*

Table 5.3: Mechanical properties after annealing at different temperatures for 1 h [Steel A]

Sample condition	30% deformed sample at 0°C				40% deformed sample at 0°C			
	Hardness (VHN)	YS (MPa)	UTS (MPa)	TEL (%)	Hardness (VHN)	YS (MPa)	UTS (MPa)	TEL (%)
As-received	149±10	259±10	675±14	90±5	149±10	259±10	675±14	90±5
Deformed	334±15	834±24	1098±19	22±2	358±20	936±20	1225±29	13±1
Annealed at 300°C	328±15	825±18	1070±20	35±2	355±20	955±21	1242±26	15±2
Annealed at 500°C	320±13	790±18	983±17	40±3	335±18	893±20	1210±22	25±3
Annealed at 725°C	208±10	585±14	810±15	47±4	215±10	617±14	858±15	37±3
Annealed at 800°C	205±10	567±14	795±15	55±4	201±10	581±14	814±17	49±4

Table 5.3 and Figure 5.6(a) along with (b) show the mechanical properties achieved after reversion annealing treatment in comparison to the properties in as-received stage and after cold deformation at 0°C for 30% and 40% reduction in thickness. Figure 5.6 reveals the trends affected by the annealing temperature on hardness, yield strength, ultimate tensile strength and percent elongation of the deformed specimen when held at the annealing temperature for 1 h. The hardness value of the as-received specimen is 149 VHN, which reaches to 358 VHN after 40% cold reduction at 0°C. The increase in hardness value is primarily related to the transformation of austenite to α′-martensite. The yield and tensile strength values of 40% cold deformed specimen increase continuously with the annealing temperature up to 400°C, beyond which the values decrease rapidly. The increment in strength may be attributed to the growth of strain induced martensite due to stress relief of the surrounding matrix [200]. However, as mentioned earlier in section 5.1, the volume percentage of martensite decreases after annealing at 300°C, which improves the ductility. In this context, it is important to note that formation of fine austenite grains takes place through

the shear reversion [201]. The combined effect controls the strength-ductility values of 40% deformed samples after annealing at 300°C for 1 h.

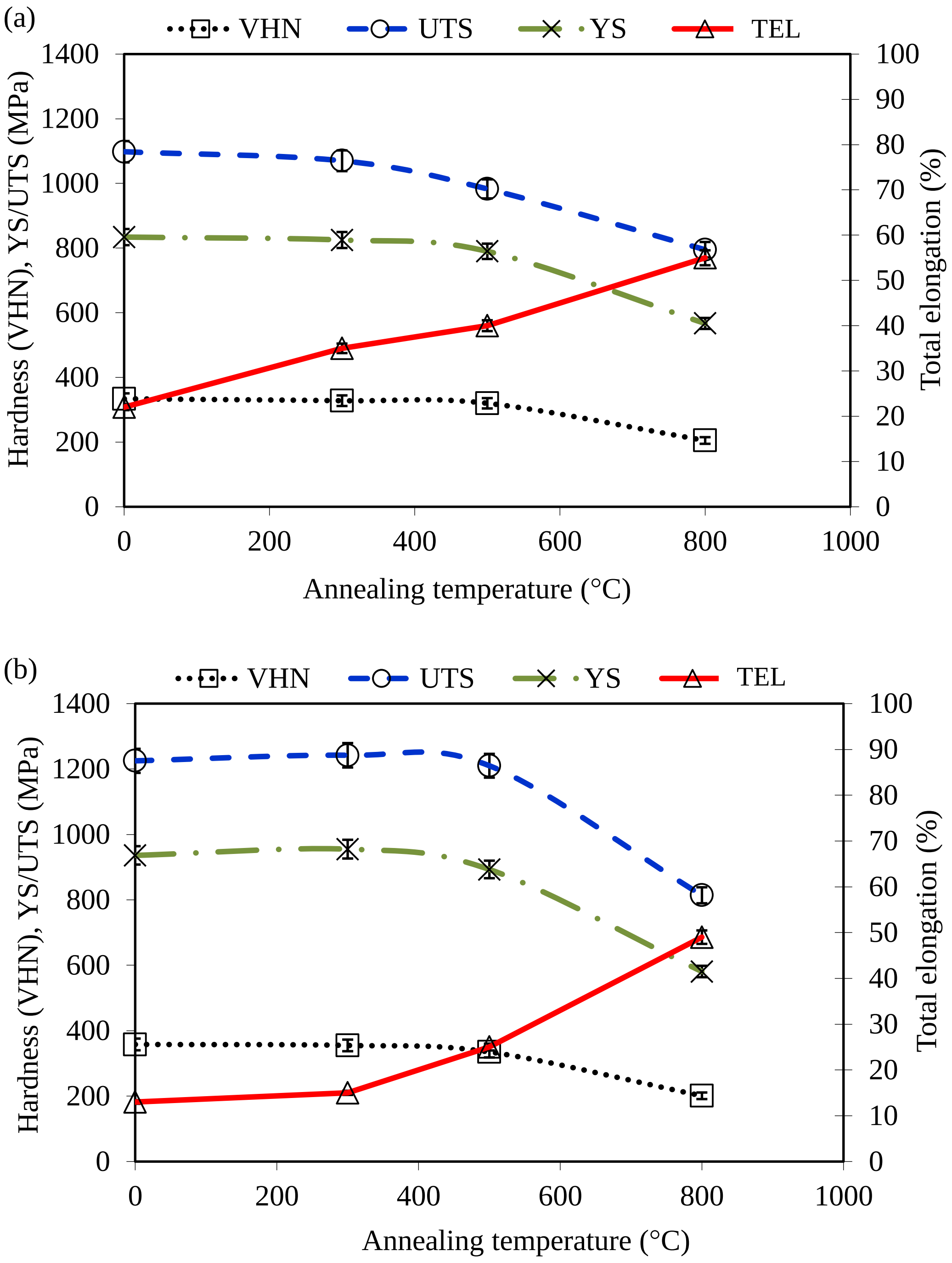

Figure 5.6: Variation of hardness, ultimate tensile strength, yield strength and percent elongation with the annealing temperature (time = 1 h) for (a) 30% deformed sample and (b) 40% deformed sample both of Steel A composition.

Table 5.4: Mechanical properties after annealing at different temperatures for 1 h [Steel B]

Sample condition	30% deformed sample at 0°C				40% deformed sample at 0°C			
	Hardness (VHN)	YS (MPa)	UTS (MPa)	TEL (%)	Hardness (VHN)	YS (MPa)	UTS (MPa)	TEL (%)
As-received	205±12	378±12	680±15	26.6±2	205±12	378±12	680±15	26.6±2
Deformed	447±17	961±19	1259±20	7.7±1	478±18	1257±12	1444±20	1.8±0.5
Annealed at 300°C	452±16	960±20	1273±20	18±2	484±17	1278±12	1478±20	15±1
Annealed at 500°C	421±14	805±18	1189±18	21±2	477±17	1163±12	1467±19	16±1
Annealed at 725°C	235±12	603±15	944±17	26±2	258±13	667±14	992±15	25±2
Annealed at 800°C	215±12	515±14	887±17	26±2	222±12	595±12	1046±16	23±2

Table 5.4 and Figure 5.7(a) along with (b) show mechanical properties of Steel B composition subjected to a similar amount of deformation followed by identical annealing schedule. The properties are characterised by an increase of strength with the consequent lowering of percent elongation. The yield strength has been significantly increased to 1257 MPa, which is more than 3.3 times higher than that of the as-received sample (378 MPa). 40% cold reduction also increases the tensile strength in two orders of magnitude i.e., from 680 MPa (as-received) to 1444 MPa with the drastic reduction of percent elongation from 26% (as-received) to 1.8%. The improvement of strength and drop of elongation by cold deformation is attributed to the strain induced α′-martensite in addition to the ordinary strain hardening of high alloyed austenite [164]. It is important to note that during the course of annealing both tensile strength and percent elongation increase. Usually, an increment of tensile strength results in the decrease of percent elongation. Earlier, it has been reported that tensile strength and percent elongation increase in similar steel when the void nucleation site during the tensile test decreases [202, 203]. Annealing in the temperature range of 300-400°C reduces the void nucleation site during the tensile test; both the tensile strength and percent elongation might increase. The strength value drops down to 1046 MPa with the 23% total elongation after annealing at 800°C. The hardness value of 222 VHN is obtained which is approximately close to the hardness value of the as-received specimen. This combination of the mechanical property is attributed to the annihilation of dislocation density, the formation of finer (10-15 µm) and strain free reverted austenite grain along with the fine precipitates of $(Cr, Fe)_{23}C_6$ phase as depicted in Figure 5.4.

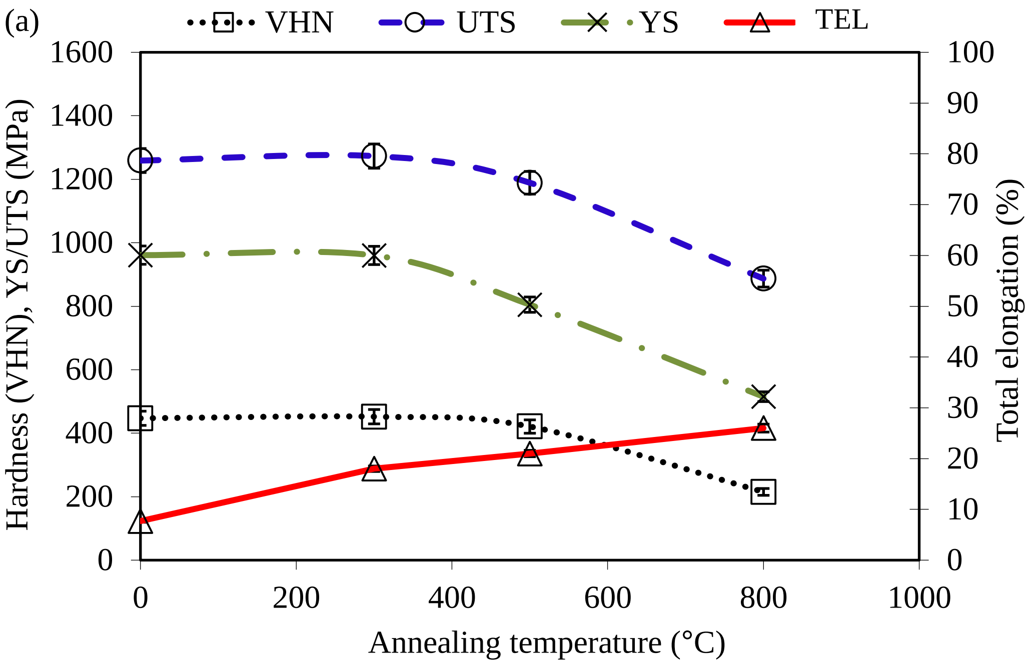

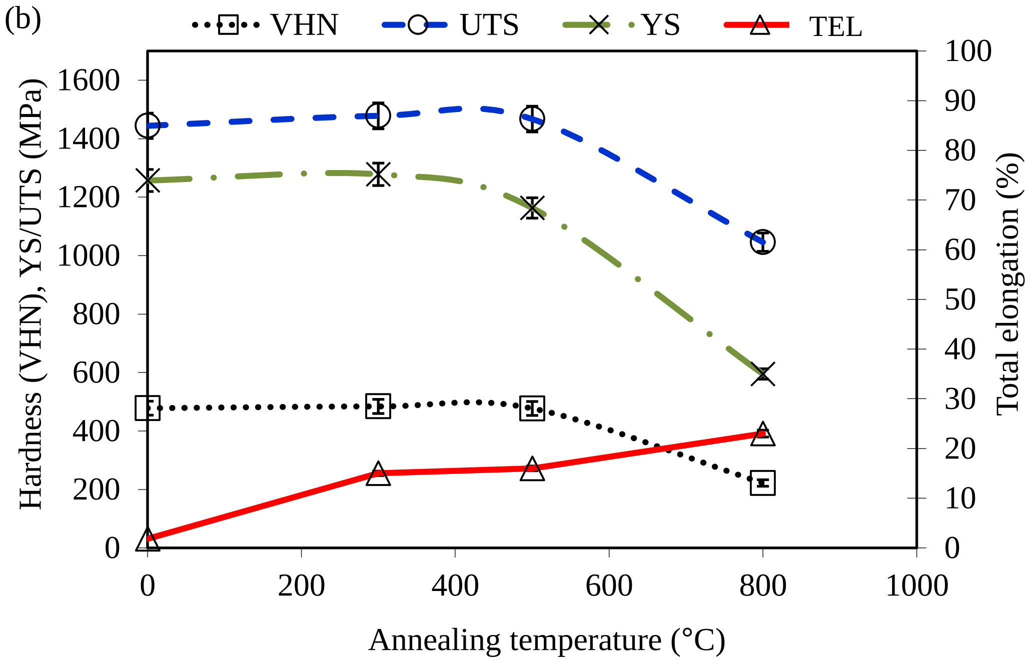

Figure 5.7: Variation of hardness, ultimate tensile strength, yield strength and percent elongation at the annealing temperature (time = 1 h) for (a) 30% deformed sample and (b) 40% deformed sample both of Steel B composition.

5.5 Comparison of mechanical properties of Steel A and Steel B after reversion annealing treatment

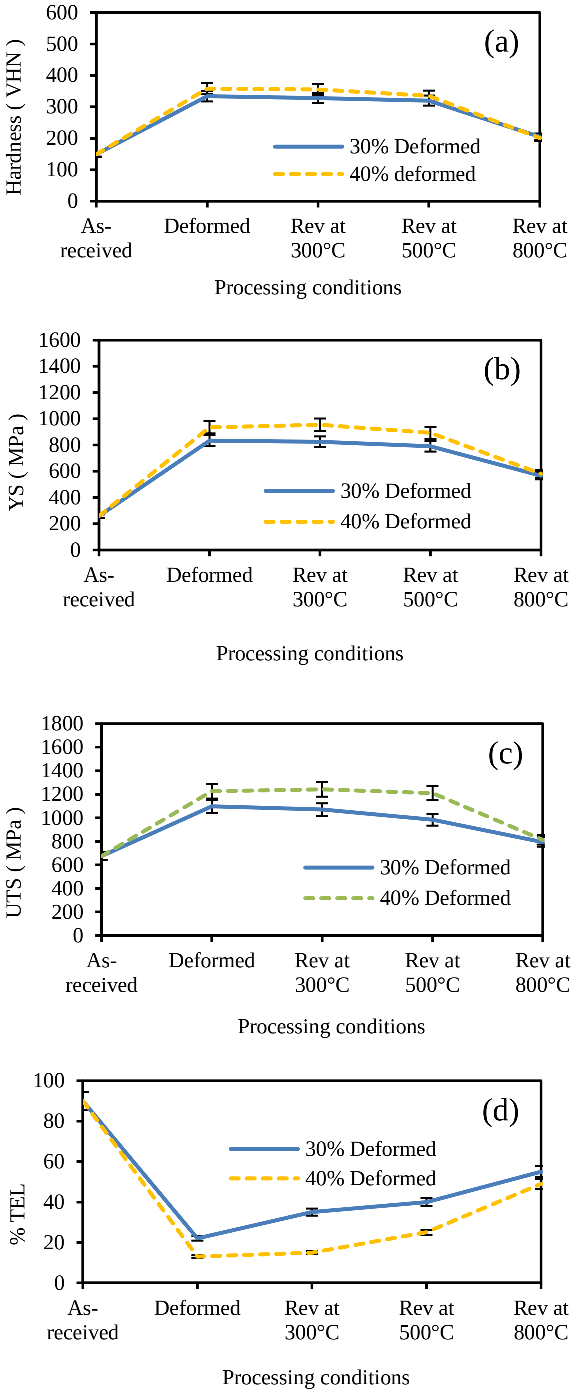

Figure 5.8: Comparison of mechanical properties between 30% and 40% deformation at 0°C for Steel A (a) Hardness, (b) YS, (c) UTS and (d) %TEL.

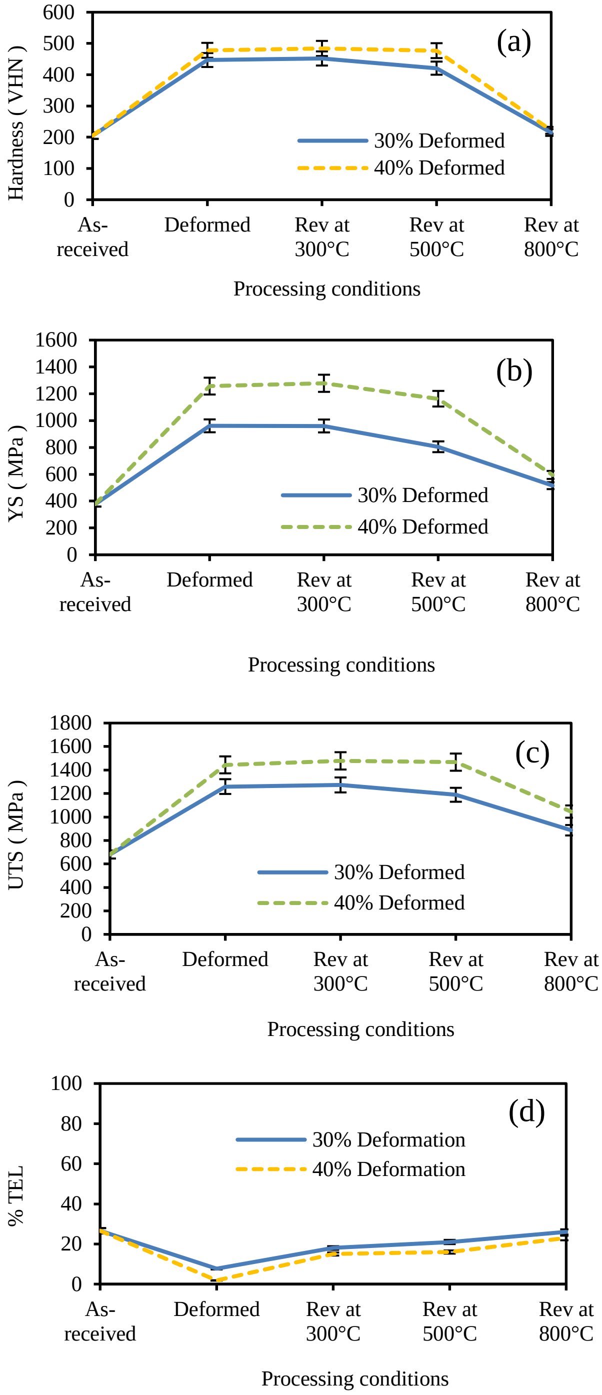

Figure 5.9: Comparison of mechanical properties between 30% and 40% deformation at 0°C for Steel B (a) Hardness, (b) YS, (c) UTS and (d) %TEL.

Figures 5.8(a) to (d) present a comparison of mechanical properties between 30% and 40% deformation at 0°C for hardness, YS, UTS and %TEL values of Steel A. It is evident that deformation (30-40%) results in improvement of hardness, YS and UTS values, whereas reversion leads to decrease those values. On the other hand, %TEL shows the reverse trend. Figures 5.9(a) to (d) indicate the similar trend of mechanical properties for Steel B as depicted in Figures 5.8(a) to (d) for Steel A. It is also evident from the comparison analysis that, hardness, YS and UTS values are always on higher side for 40% deformed sample than that of 30% deformed sample for both Steel A and Steel B. In general, the gap between the two trend lines of 30 and 40% deformed samples are more in case of Steel B than those for Steel A.

The differences in mechanical properties after deformation followed by reversion annealing treatment among Steel A and Steel B for 30% and 40% cold deformed samples has been illustrated in Figures 5.10(a) to (d) and Figures 5.11(a) to (d). Steel B exhibits higher values of hardness and UTS than those of Steel A irrespective of deformation provided and the difference between the trends of two steels is wider in case of 40% deformed samples owing to higher rate of work hardening rate at higher level of deformation in Steel B than Steel A. After reversion annealing both Steel A and Steel B reveal almost similar rate for restoration of ductility in case of 30% deformed samples. For 40% deformation, the increment in ductility with the progress of annealing for Steel A shows initial sluggish enhancement followed by a sharp rise during annealing in the temperature range of 500°C to 800°C. On the other hand, Steel B exhibits an initial sharp rise in %TEL for annealing up to 300°C temperature followed by a slow increment when annealed between 500°C to 800°C for 1 h. From this comparison, it can be understood that, after reversion annealing between 500-800°C for 1 h, Steel A provides better toughness than that of Steel B, which encourages us to conduct further studies on thermo-mechanical controlled processing and cryogenic treatment as well as reversion annealing treatment of the cryogenically treated samples on Steel A composition. Results and discussions of these studies have been made in the subsequent Chapter 6, 7 and 8, respectively.

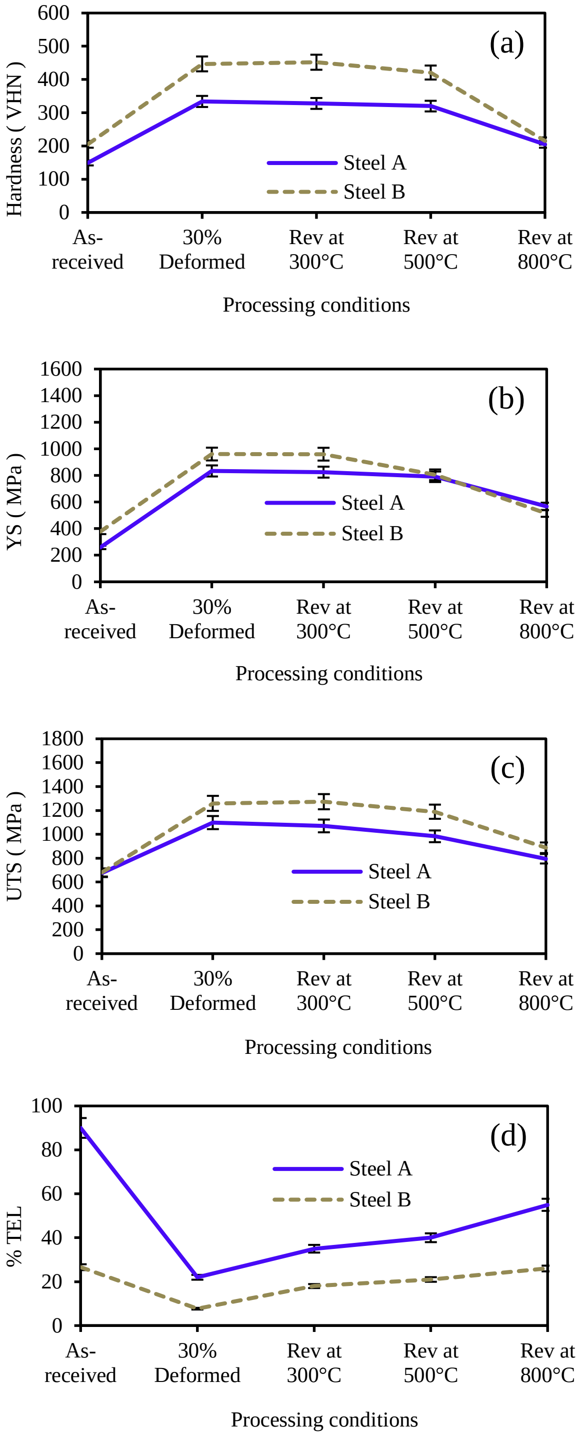

Figure 5.10: Comparison of mechanical properties between Steel A and Steel B for 30% deformation at 0°C, (a) Hardness, (b) YS, (c) UTS and (d) %TEL.

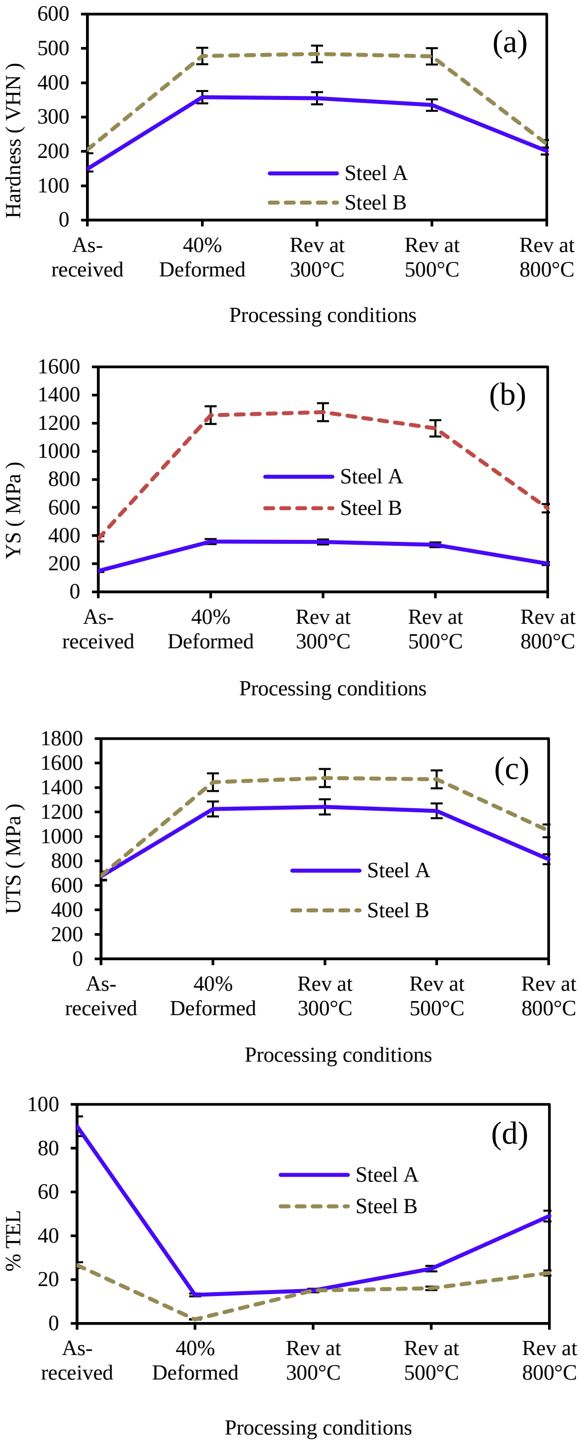

Figure 5.11: Comparison of mechanical properties between Steel A and Steel B for 40% deformation at 0°C, (a) Hardness, (b) YS, (c) UTS and (d) %TEL.

5.6 Differential scanning calorimetric study

In the present study, kinetics of different processes associated with annealing of the cold rolled 304 stainless steels have been studied by differential scanning calorimetry (DSC) technique. Figure 5.12represents the DSC thermograms obtained from the 30% deformed sample at the heating rate of 5, 10 and 20°C/min, respectively. For all the heating rates, Figure 5.12 reveal two endothermic peaks in the temperature ranges of 300-400°C and 450-550°C and one exothermic peak in the temperature range of 600-650°C. For the heating rates of 5 and 10°C/min, additional exothermic peaks appear at 265°C and 316°C, respectively. These peaks may be matched with segregation and clustering of carbon atoms [204]. At higher heating rate (20°C/min), the heat release associated with these exothermic peak overlaps with the heat absorption associated with the subsequent transformation and do not appear distinctly in the thermogram.

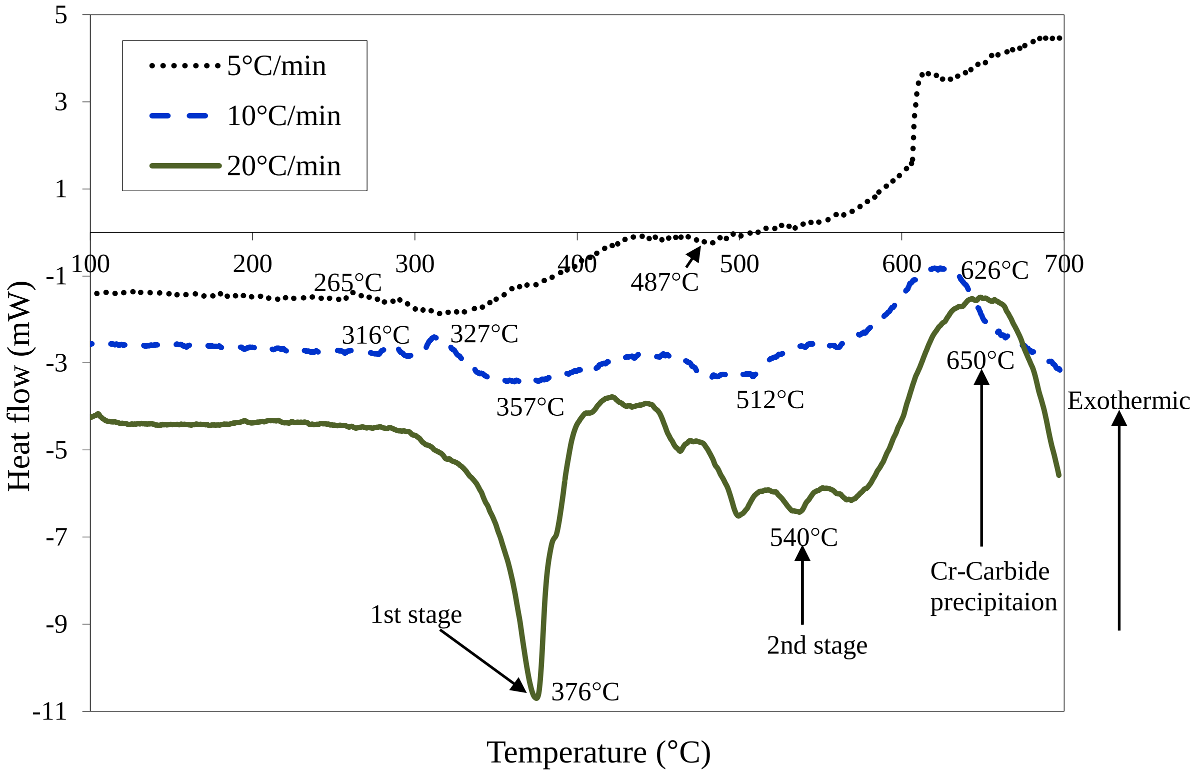

Figure 5.12: DSC curves obtained at various heating rates for 30% cold deformed sample at 0°C [Steel A].

Earlier, it has been identified that the endothermic peaks between 300°C and 400°C are due to the dissolution of martensite and crystal defect occurring at the initial stage of the reverse transformation of DIM in small regions along the austenite/martensite interface [205]. The simultaneous diffusion of Fe and Ni across the austenite/martensite interface seems to stabilise the rest of martensite by interrupting the reverse transformation in the temperature range of 400-450°C. The peaks related to the second stage of reverse transformation appear between 450°C and 550°C. The prominent exothermic peak between 600°C and 650°C indicate the precipitation of chromium carbide. Although, the temperature of ~600°C is apparently low for the precipitation of (Cr, Fe)$_{23}$C$_6$ [168], the prior cold deformation supports the same in the present case.

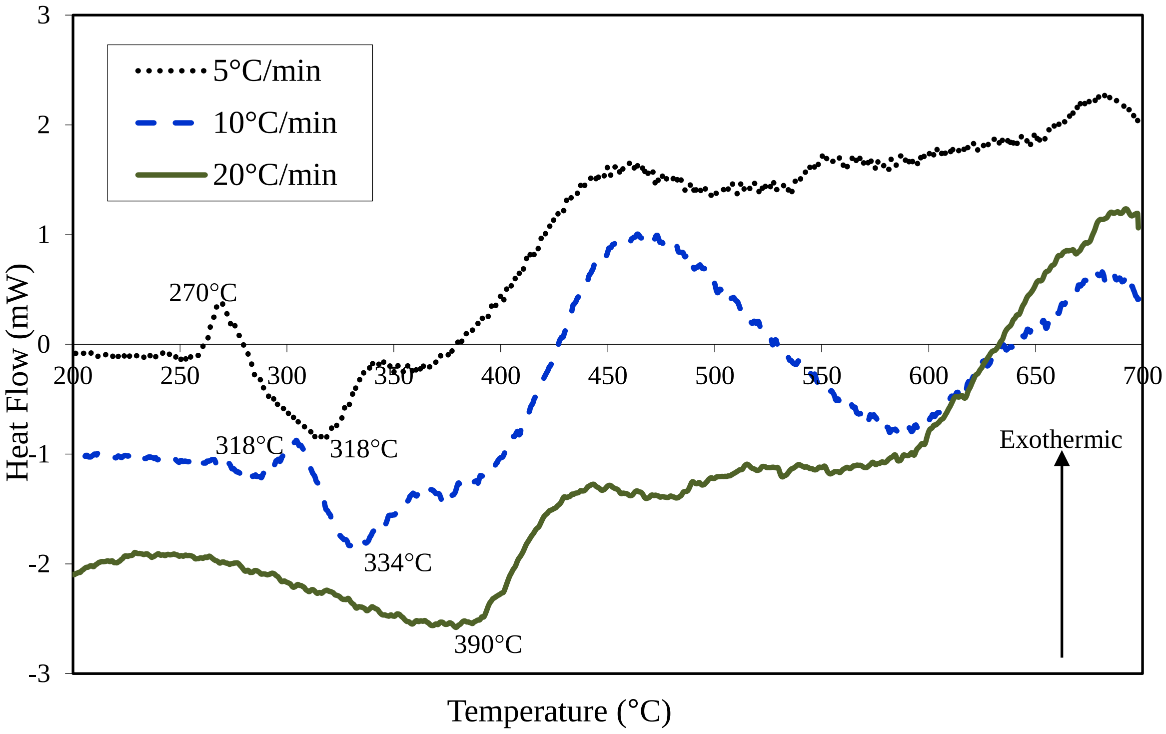

Figure 5.13: DSC plots obtained at 5, 10, and 20°C/min for the samples subjected to 40% cold deformation at 0°C [Steel A].

The enthalpy values (ΔH) of two-stage of martensite reversion and Cr-carbide reactions have been estimated as 36, 38 and 25 J/g respectively from the DSC curve obtained at 20°C/min. The values could not be precisely compared in the absence of literature data. However, some related values like latent heat for the $\gamma \rightarrow \alpha'$ transformation for pure iron at 912°C is 16.36 J/g [206] and heat evolution during martensite formation in Fe-18.5Cr-8.7Ni alloy has been reported as 35 J/g in the literature [207]. The enthalpy value for the Cr-carbide precipitation is lower than that of martensite reversion. Usually, the heat of formation of $Cr_{23}C_6$ is higher than the martensite reversion [14] and the lower value may be attributed to the lower amount of precipitation at 600°C in the present study.

Figure 5.13 shows the DSC thermograms obtained from the 40% deformed sample at the heating rate of 5, 10, and 20°C/min, respectively. For all the heating rates, the plots reveal one endothermic peak in the temperature range of 300–400°C and two exothermic peaks in the temperature range of 400–550°C and 600–700°C. For the heating rates of 5 and 10°C/min, additional exothermic peaks appear at 270°C and 318°C concerning segregation and clustering of carbon atoms [204]. In this context, it is also to be noted that, for heating rate (20°C/min), the heat release associated with these exothermic peaks overlaps with the heat absorption associated with the subsequent transformation and do not appear distinctly in the thermogram.

5.7 Determination of activation energy using Kissinger method

The activation energy (E) values concerned with the DSC peaks were obtained by analysing the Kissinger's plot shown in Figure 5.14. The estimated activation energy values for different samples are presented in Table 5.5. The activation energy value of 77 kJ/mol has been obtained for the first stage of the reversion. This phenomenon may reasonably be attributed to dislocation pinning and clustering [208]. The value is comparable to the activation energy for the formation of Cottrell atmosphere and clustering [209] and activation energy for carbon diffusion in ferrite (80 kJ/mol [208]) in the temperature range of 350-850°C. Slightly lower E value of 67-70 kJ/mol was reported [187] for the migration of interstitially dissolved carbon atoms to dislocations in α′-martensite. Fujita et al. [210] reported that the segregation of solute atoms on the stacking faults known as Suzuki effect can occur in both deformed and annealed 304 stainless steel.

The activation energy for the second stage of reversion is obtained as130 kJ/mol. The value is in between those for diffusion of carbon in α-Fe (80 kJ/mol) and for diffusion of iron along dislocations (i.e., pipe diffusion, 152 kJ/mol [211]). This stage can be considered as the carbon diffusion controlled including the retardation of the same in presence of substitutional elements like Si [212]. The estimated activation energy value is also in agreement with the same for the diffusion of carbon in austenite in the temperature range of 900-1060°C (135 kJ/mol [213]). The slightly higher level of E value, 133-138 kJ/mol has been attributed to the segregation of solute carbon atoms to dislocations and micro-twins in deformed austenite during ageing [187]. Moreover, Morra et al. [204] also have reported the activation energy of 140 kJ/mol for the interface controlled growth in the case of $\gamma \rightarrow \alpha$ transformation in Fe-Mn alloys.

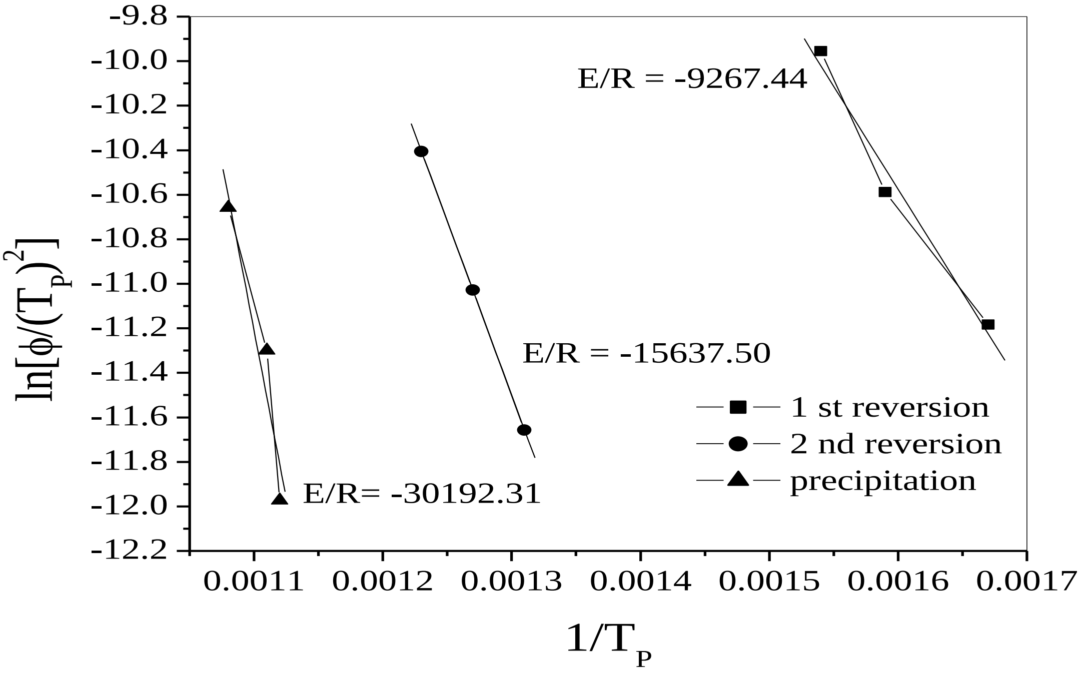

Figure 5.14: Presentation of Kissinger plots and related linear fit obtained at 5, 10 and 20 °C/min [Steel A].

The value of activation energy obtained for the third stage of transformation i.e., in between 600°C and 650°C, is 251 kJ/mol which is associated with the activation energy for volume diffusion of iron (251 kJ/mol [214]) and Cr diffusion in α-Fe in the temperature range of 800-880°C (251±7 kJ/mol [215]). Therefore, the third stage of reversion is related to the precipitation of Cr-carbide at a higher temperature, where the volume diffusion becomes relatively more important. The dominant mechanism concerning the third stage comprises diffusion of carbon and Cr atoms in austenite resulting in precipitation of fine Cr-rich carbides and consequent depletion of carbon and Cr in the surrounding matrix. The reported activation energy values for the aforesaid range of temperature are also in agreement with the estimated values in the present study (Table 5.5).

Table 5.5: Estimated activation energy values and comparison with literature data.

Steel	Activation energy values (kJ/mol) for reversion, precipitation reaction, carbon (c) clustering, transition carbide (ε/η), decomposition of retained austenite (γ_R) and cementite (θ) precipitation								
	Present study			Literature data					
	1st reversion	2nd reversion	Cr-carbide precipitation	Steel/ Condition	C clustering	ε/η	γ_R decomposition	θ	Ref
304 SS (Steel A)	77.05 ±02	130.01 ±05	251.02±10	C-Mn-Si (Tempering)	56	127	202	233	[208]
				C-Mn-Al (Tempering)	58	116	124	245	[208]
				Fe-C (Tempering)	81	118	135	198	[204]
				Fe-Cr-C (Tempering)	89	114	141	-	[204]
				SAE 52100(Tempering)	94	111	144	-	[204]
				Carburized Fe-0.93C (Tempering)	82	129	141	212	[204]
				304 SS (Ageing)	67-70	-	-	-	[187]

The reported values of activation energy for the formation of the transition carbide (ε/η) as furnished in Table 5.5 lies in the range of 111–129 kJ/mol. In the present case, the formation of transition carbides during tempering of martensite is suppressed here by the presence of Si and Cr [204, 208] which is corroborated by the DSC curve (Figure 5.12). Moreover, the influence of Si on suppressing decomposition of austenite into the mixture of ferrite and carbide, typical of the second stage of tempering is manifested by the absence of heat release peak in the DSC curve. Activation energy associated with such transformation is about 124-202 kJ/mol (Table 5.5). The reported activation energy of cementite (θ) precipitation lies in the range of 198-245 kJ/mol which apparently indicates a process controlled by volume diffusion of Fe at a higher temperature [204, 208]. However, the activation energy values should not be considered as absolute values since the Kissinger equation deals with a chemical reaction in a solution, where as transformations are of first order.

5.8 Work hardening behaviourof samples subjected to reversion annealing treatment

The variation of dσ/dε (θ) with ε is widely used to interpret tensile work hardening behaviour [148, 216]; thereby attempted to examine the different stages of work hardening of the investigated steel. The plots of θ versus ε at a strain rate of $3.3\times10^{-4}s^{-1}$ are presented in Figures 5.15(a) to (d) for cold deformed (40%) specimen at 0°C along with those annealed at low (300°C), intermediate (500°C), and high (800°C) temperatures, respectively. All the plots exhibit an initial transient stage (TS) of rapid decrease in θ (stage I) followed by a region of plateau or gradual decrease (stage II). However, Figure 5.15(d) shows the three-stage behaviour, whereas θ decreases with ε due to the onset of dynamic recovery in stage III. It can be mentioned that while the stage II is more pronounced at an intermediate temperature, stage III is evident at higher annealing temperature (800°C). It is noteworthy that these observations are in accordance with the results of similar steels reported earlier [217, 218].

In the TS (stage I), dislocation velocity and mobile dislocation density increase which lead to rapid increase in plastic strain rate immediate after elastic limit [219]. This stage is attributed to the stabilisation of the plastic strain rate with the dislocation source density. In this study, the low value of SFE (i.e., 19mJ/m^2) prevents the cross-slip of dislocations at low strain which results in the occurrence of stage I. While the transition from stage I to stage II at 300°C occurs at the 3.3% strain, the same is found to be as lower values (1.7%) for 500°C. The higher value of transition strain (9.8% and 15% for stage II and stage III) obtained after annealing at 800°C can be attributed to the coarse grain size of steel. The rapid increase in dislocation density in stage II with plastic strain signifies the characteristic feature (i.e., storage of dislocation) [217] of stage II hardening. In Figure 5.15(d), the dominant recovery in stage III is noticeable as a decrease in θ with respect to ε with increasing temperature. The increased rate of dynamic recovery is attributed to early cross-slip and climb of dislocations. The rapid increase of the sub-grain size above $0.5T_m$ due to dynamic recovery [220, 221] leads to the observed decrease in θ.

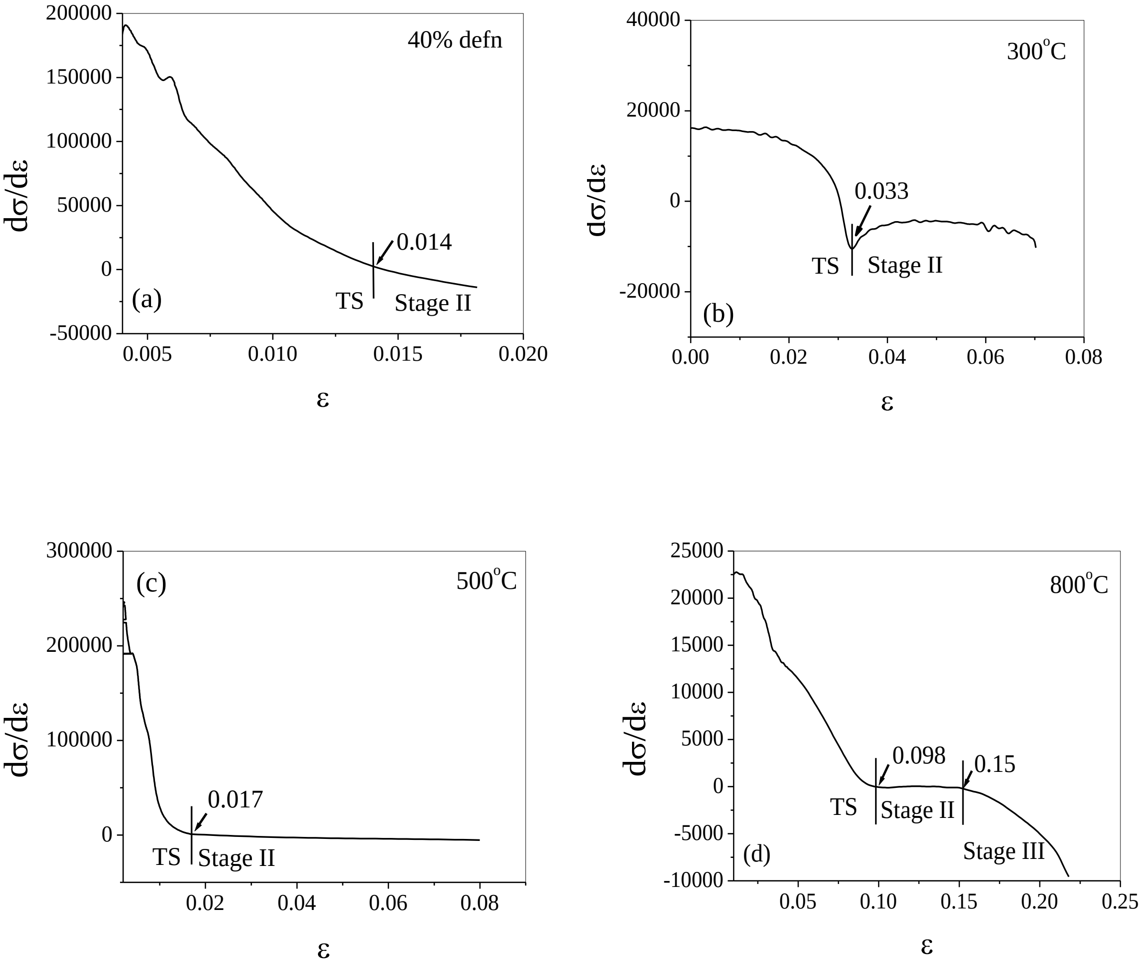

Figure 5.15: Variation in strain hardening rate (dσ/dε) as a function of true strain (ε) at (a) 40% cold deformed sample, (b) 300 °C, (c) 500 °C, and (d) 800°C [Steel A].

5.9 Fractographic investigation of fracture surface and sub-surface

The fractograph of deformed and annealed (300°C, 1 h) specimen as shown in Figure 5.16(a) shows the typical quasi-brittle nature. The fractographic features of the sample are in conformance with the corresponding percent elongation values. The sub-surface micrograph (Figure 5.16(b)) clearly indicates that the micro-voids have essentially nucleated along the austenite/martensite and/or martensite/martensite interface which results in the rapid void coalescence and tensile fracture becomes predominantly intergranular in nature. The micro-voids appear elongated toward the tensile loading direction for as-received specimen while the same appears to be comparatively spherical for cold rolled and annealed (300°C, 1 h) specimen (Figure 4.14(b) vis-à-vis Figure 5.16(b)) indicating the less ductility in the latter one.

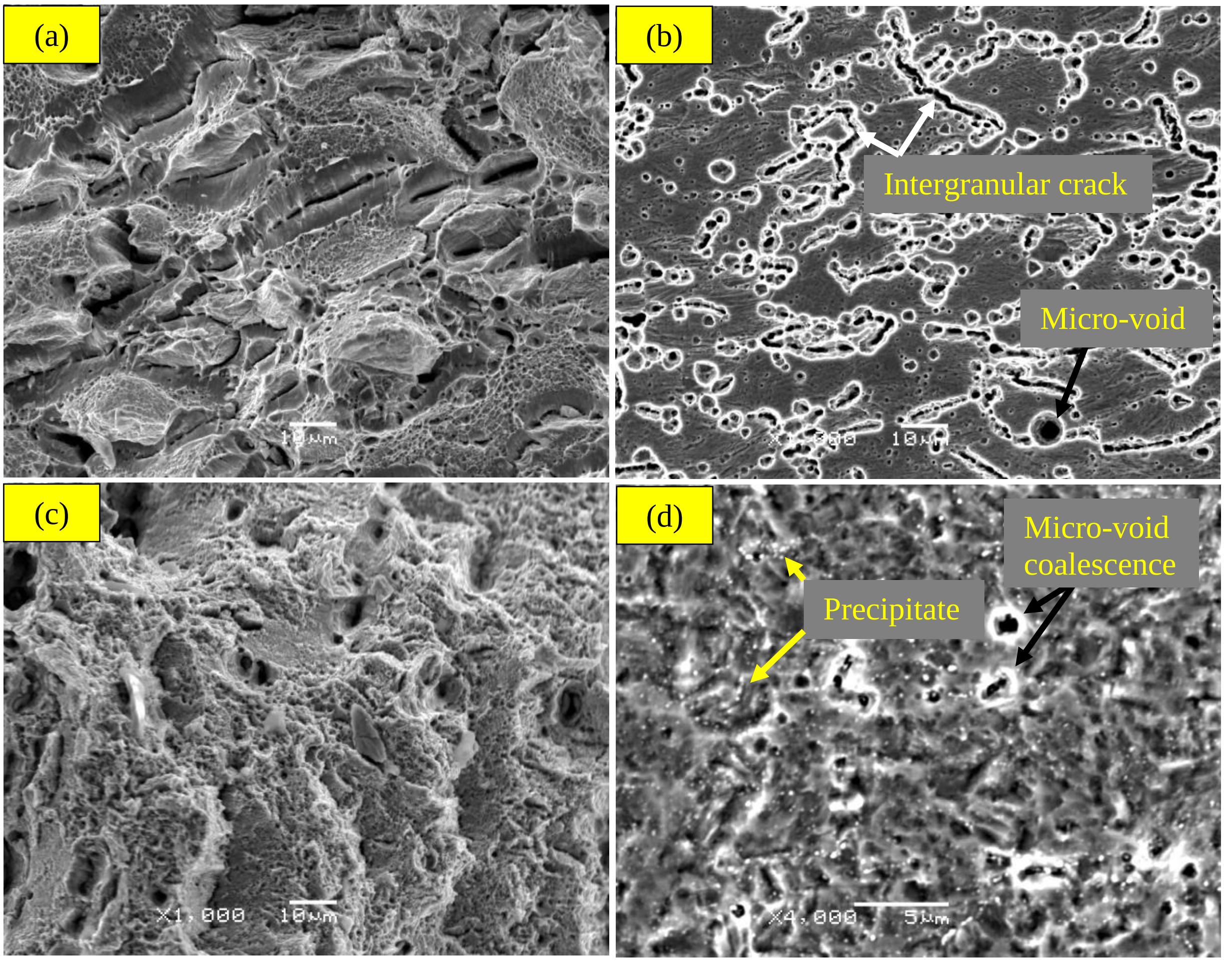

Figure 5.16: SEM micrographs of fracture surface and sub-surface of 40% deformed at 0°C and annealed (a) & (b) at 300°C for 1 h specimen and (c) & (d) at 800°C for 1 h specimen. White and black arrows in (b) indicate the sites of cracks and/or void nucleation, respectively [Steel A].

The fractograph of deformed and annealed (800°C, 1h) specimen as shown in Figure 5.16(c) shows the quasi-brittle nature. The sub-surface micrograph (Figure 5.16(d)) demonstrates that the voids are nucleated from the austenite/martensite interface as well as from the precipitate particle/austenite phase interface (denoted by black arrow). The quasi-brittle fracture behaviour may be attributed to the presence of chromium-rich carbide phase in austenite which offers some resistance to the motion of advancing crack. The fine recrystallised reverted austenite grains (Figure 5.3(d)) are favourable for increased plasticity.

As a consequence, the sample reveals higher percent elongation as compared to that of the former annealed at 300°C (Figure 5.16(b)).

5.10 Summary

1. The present study has identified that, 30-40% cold deformation at 0°C followed by reversion annealing treatment in a temperature range of 500-800°C is conducive conditions for manufacturing high strength 304 austenitic stainless steel under deformation-reversion route.
2. The reversion transformation has been found to be enhanced with increasing annealing temperature without significant grain growth up to 800°C in the presence of finer Cr-carbide precipitation at austenite grain boundaries. The residual α′-martensite volume fraction after reversion at 800°C for 1 h has been estimated through X-ray diffraction analysis to 8% for both 30 and 40% cold deformed sample at 0°C.
3. Temperatures concerning the different stages of the reversion process including the Cr-carbide precipitation, which has been identified in the range of approximately 600-650°C by differential calorimetric measurements. This is useful for controlling the microstructural evolution under the process schedule followed. The activation energy value corresponding to the first and second stage of reversion followed by Cr-carbide precipitation has been estimated to be as 77, 130 and 251 kJ/mol, respectively for 30% cold deformed sample at 0°C. These results are suitably compared with the published results. This allows correlating the occurrence of specific reaction with the different temperature regimes concerning the proposed manufacturing schedule. However, the activation energy values should not be considered as absolute values since the Kissinger equation deals with a chemical reaction in a solution, where as transformations are of first order.
4. The variation of $d\sigma/d\varepsilon$ with ε is used to examine the different stages of work hardening of the 40% cold deformed samples at 0°C followed by reversion annealing. Both tensile strength and percent elongation values increase with increasing annealing temperature up to 450°C and beyond that annealing result in a drop of tensile strength value with the consequent rise in percent elongation. 40% cold deformation and annealing at 500°C for 1 h has resulted in an attractive strength-ductility combination (30.25 GPa%).

5. Fractographic features substantiate tensile results. The corresponding sub-surface examination identifies the micro-mechanism of tensile fracture.

6

EFFECT OF THERMO-MECHANICAL TREATMENT ON MICROSTRUCTURE AND MECHANICAL PROPERTIES

6.1 Introduction

Grain refinement is one of the effective methods employed for enhancing the strength with a favourable ductility of steel [222]. There are several methods which produce fine grain structure like equal channel angular pressing (ECAP) [223], high-pressure torsion (HPT) [224], accumulative roll bonding (ARB) [225] reversion annealing of martensitic structure etc. However, the main problem in these methods is the formation of stain induced martensite, which lowers the ductility [226]. In this connection, it is important to note that reversion of strain induced martensite improves the ductility in the steels processed under aforesaid routes [227]. During reversion, the formation of fine grains and inhomogeneous distribution of these fine grains lead to strain localisation causing improvement in the ductility value [228, 229].Cold rolling, as well as hot rolling, has been employed for achieving grain size refinement. Cold working improves the strength of the material and lowers the ductility by higher forming forces, while hot rolling allows simultaneous recrystallisation, which controls the grain refinement. To avoid high working temperatures and forces, warm rolling ($0.35T_m < T < 0.55T_m$, Where T_m is the melting temperature) is commonly used as the intermediate process [230], which allows recovery but not recrystallisation to get a favourable combination of strength and ductility. Among the available methods, grain refinement by thermo-mechanical treatment has drawn great attention in steel research, because it improves both corrosion and mechanical properties of the stainless steel [231-233]. During thermo-mechanical processes (TMCP), the steel undergoes various metallurgical phenomena such as work hardening, dynamic recovery and dynamic recrystallisation. Among these processes, dynamic recrystallisation [234, 235] is the most important mechanism during thermo-mechanical controlled processing (TMCP) of low stacking fault energy FCC alloys, because it influences the final microstructures and thereby the mechanical properties of the materials [236]. Thermo-mechanical controlled processing (TMCP) and its influence on the microstructure and mechanical properties are well established in low and ultralow carbon steels [237, 238]. However, limited studies have been carried out on this aspect in austenitic stainless steels.

In view of the above, in the present study, 304 austenitic stainless steel has been thermo-mechanically processed with three different finish rolling temperatures (FRT) of 700°C, 800°C and 900°C to study the effect of FRT on microstructure and mechanical properties of the steel. Recrystallisation and grain growth which strongly influence the mechanical properties of steel are known to occur during TMCP. The purpose of the present work is to vary the grain size with altering the finish rolling temperature during TMCP and the presence of different types of microstructural features generally form in austenitic stainless steel which strongly affects the strength-ductility combination of the steel.

6.2 *X-ray diffraction study of thermo-mechanically processed samples*

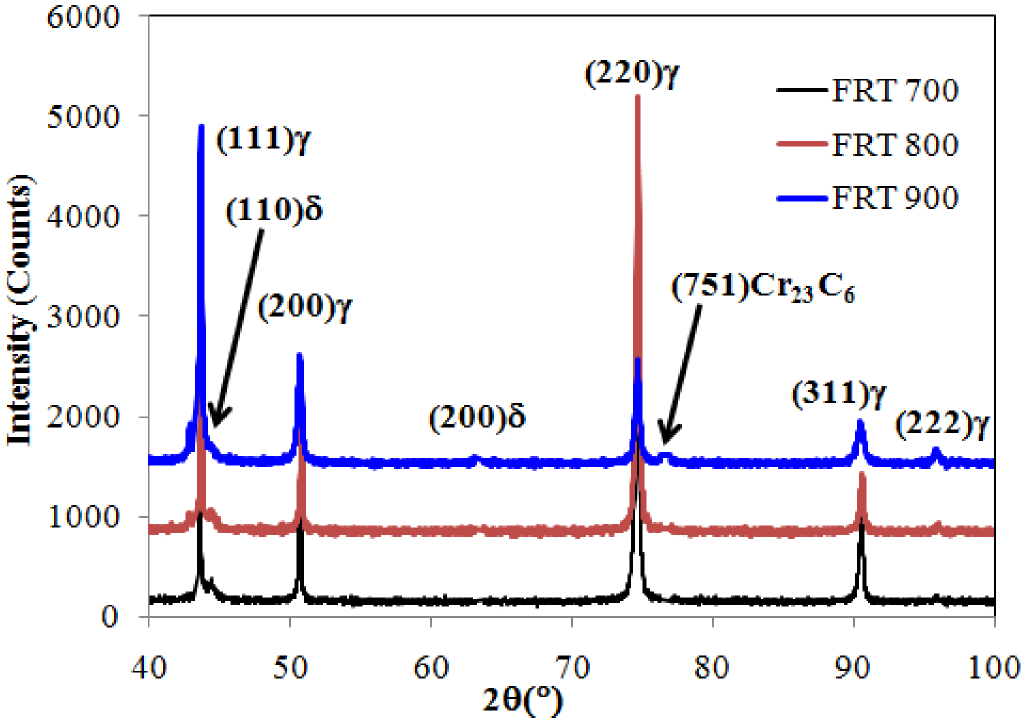

Figure 6.1:X-ray diffraction profiles of three different FRT 700°C, 800°C and 900°C samples.

The constituent phases evolved in the samples processed with three different FRTs (700°C, 800°C and 900°C) were identified by X-ray diffraction study. Figure 3 reveals X-ray diffraction profiles of samples processed with FRTs of 700°C, 800°C and 900°C. The individual diffracting planes, primarily corresponding to FCC-austenite, are labelled in Figure 3. X-ray profiles confirm the presence of (111), (200), (220), (311) and (222) peaks of austenite, which are consistent with the chemical composition of the 304 stainless steel [239]. The maximum intensity is observed for the (111) and (220) peaks and the remaining peaks reveal lower intensity. It can also be seen from Figure 3 that the X-ray profiles reveal very weak intensity peaks of δ ferrite ((110) and (200)) and $M_{23}C_6$ type Cr carbide (i.e., $Cr_{23}C_6$) with a reflection of (751). Earlier, similar types of δ ferrite [240] and $Cr_{23}C_6$ [241] phase were detected in X-ray study. Sadeghpour et. al [242]have reported that such δ-ferrites generally form during higher temperature which is stable at room temperature and these ferrites are unfavourable due to their adverse effects on high temperature workability and corrosion resistance. It is imperative to mention here that, the intensity of the $Cr_{23}C_6$ carbide peak at lower FRTs (800°C and 700°C) is negligible than that of higher FRT (900°C). Hence it can be concluded that the formation of carbides is more likely at the higher finish rolling temperature.

It may also be noted that stain induced martensite peaks have not been observed in this XRD patterns, which can be associated with the low amount of such phases present in the matrix along with the defects present in that structure [243]. Here as the deformation temperature is higher, the formation of strain-induced martensite is not possible because in austenitic stainless steels the temperature below which austenite transforms spontaneously to martensite is lower than 0°C [130]. Therefore, during TMCP martensite formation cannot be ascertained.

6.3 Evolution of microstructure (Optical and TEM micrographs)

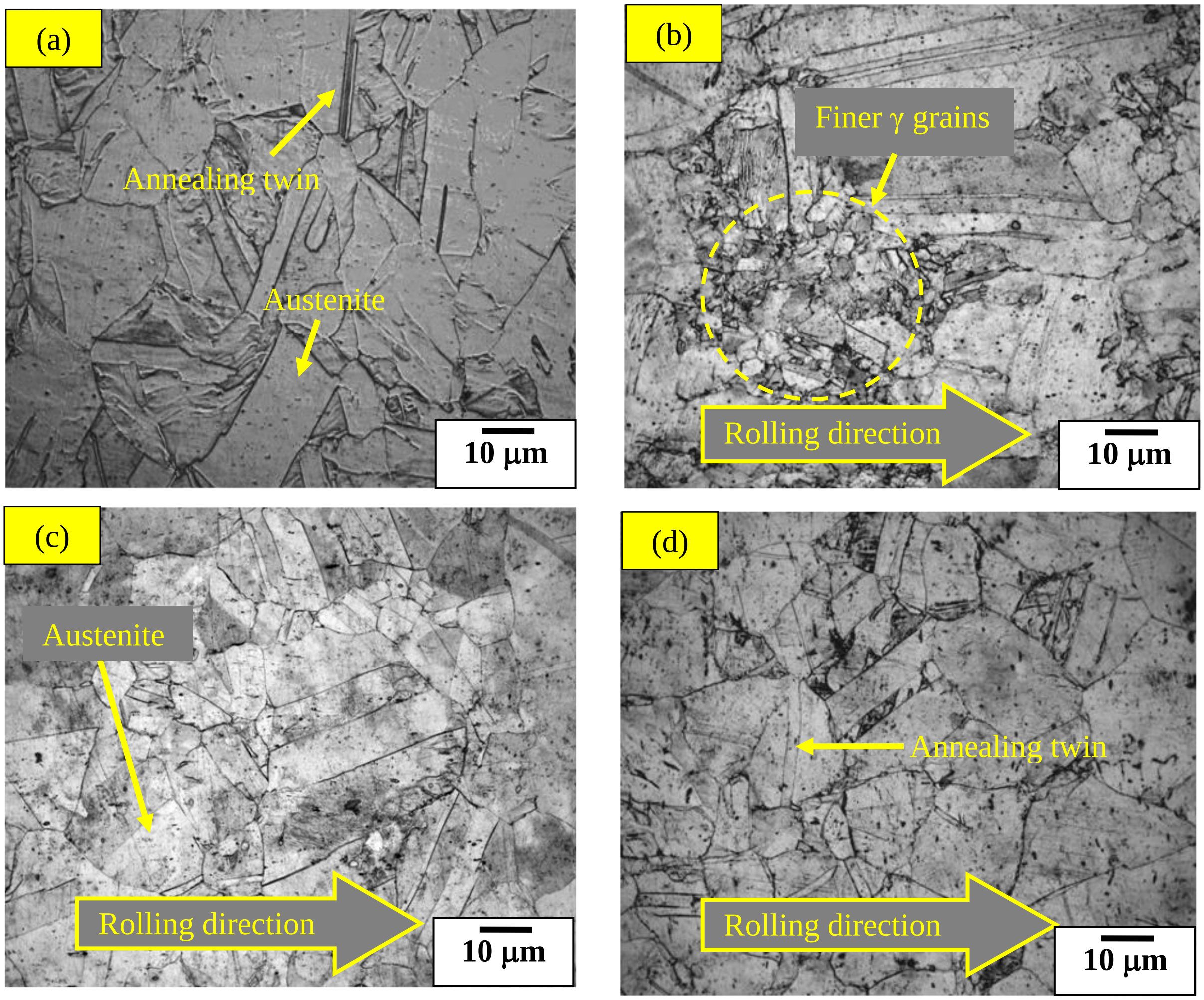

Figure 6.2: Optical micrograph of TMCP samples (a) as-received sample, (b) FRT 700°C, (c) FRT 800°C and (d) FRT 900°C.

Figures 6.2 shows optical microstructures of the as-received as well as samples hot rolled with FRT of 700°C, 800°C and 900°C. Primarily presences of the fully austenitic structure with some amount of annealing twins are evident in these microstructures. Figure 6.2(a) is showing polygonal austenite grain with the average grain size in the range of 20-30μm. Annealing twins are present within the austenite grains, which are blocked by the grain boundaries. This is akin to the earlier published results corresponding to the similar chemical composition [244].

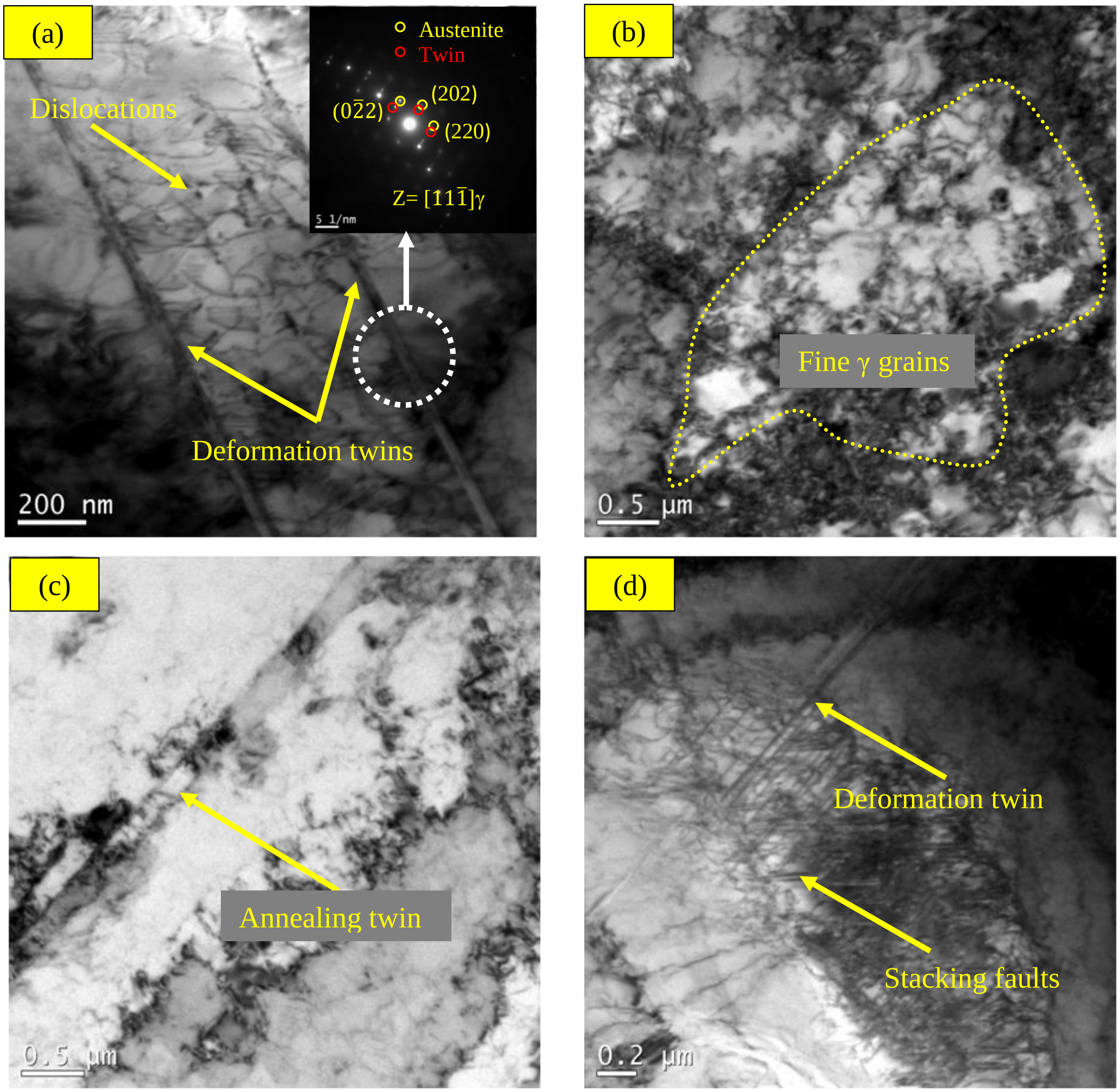

Figure 6.3: Transmission electron micrographs of TMCP samples with FRT 700°C.

Figure 6.2(b) reveals fine austenite grains which are obtained for lower finish rolling temperature of 700°C. It may be seen that the grains are oriented and flattened along the direction of rolling. The grain sizes lie within a range of 1 µm to 30 µm, hence, it is difficult to calculate the average grain size. Some grains are found to have the size at the nanometer level. In this context, it is relevant to mention that, the yield strength value in 304 austenitic stainless steel has been found to vary between 530 MPa to 290 MPa approximately for 2.5 µm to 50 µm grain size range [143, 153]. Therefore, in the present case, it is reasonable to expect that the finer grains are useful to contribute in enhancement of strength, whereas bigger grains may help to improve the ductility in the steel subjected to thermo-mechanical treatment [245]. Annealing twin within the austenite grains is also apparent in Figure 6.2(c) and (d) for FRT of 800°C and 900°C, respectively. The average grain size achieved for FRTs of 800°C and 900°C has been calculated by following the intercept method and found to be 25±3 and 40±5μm, respectively.

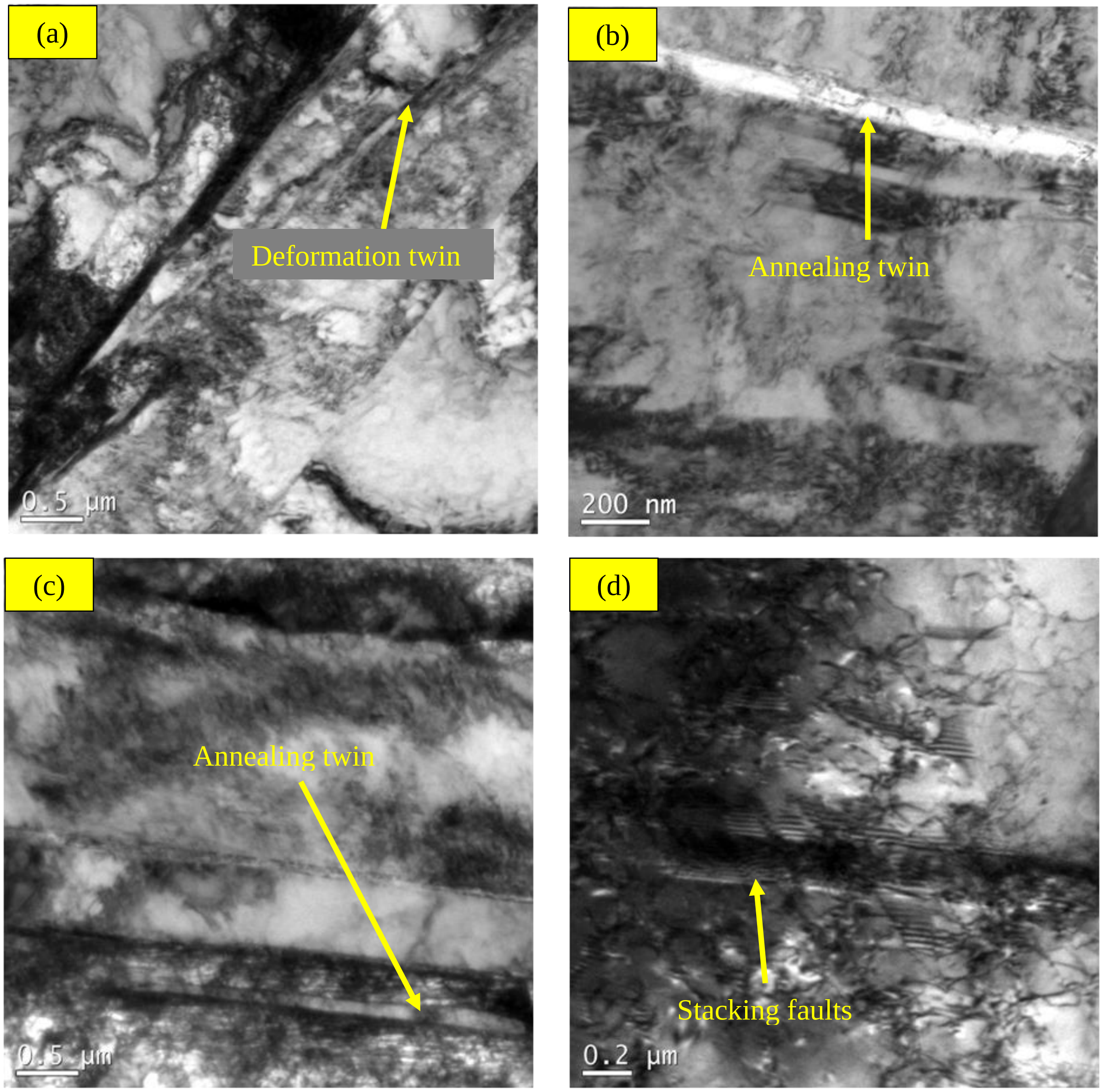

Figure 6.4: Transmission electron micrographs of TMCP samples with FRT of 800°C.

Figure 6.3 shows TEM microstructures obtained for the FRT 700°C. Figure 6.3(a) reveals the deformations twins in the austenite grain which also contains dislocation substructures. Selected area electron diffraction (SAED) and its schematic analysis at the inset of Figure 6.3(a) substantiate the presence of twin. Fine austenite grains along with high dislocation density are also evident in FRT 700°C samples (Figure 6.3(b)). Figure 6.3(c) reveals annealing twins within the austenite grains which is consistent with the observed optical microstructures. It is important to note that the annealing twins are thicker compared to the deformation twins and such annealing twins are formed during hot rolling [246]. Stacking faults and twin interactions are also observed in Figure 6.3(d).

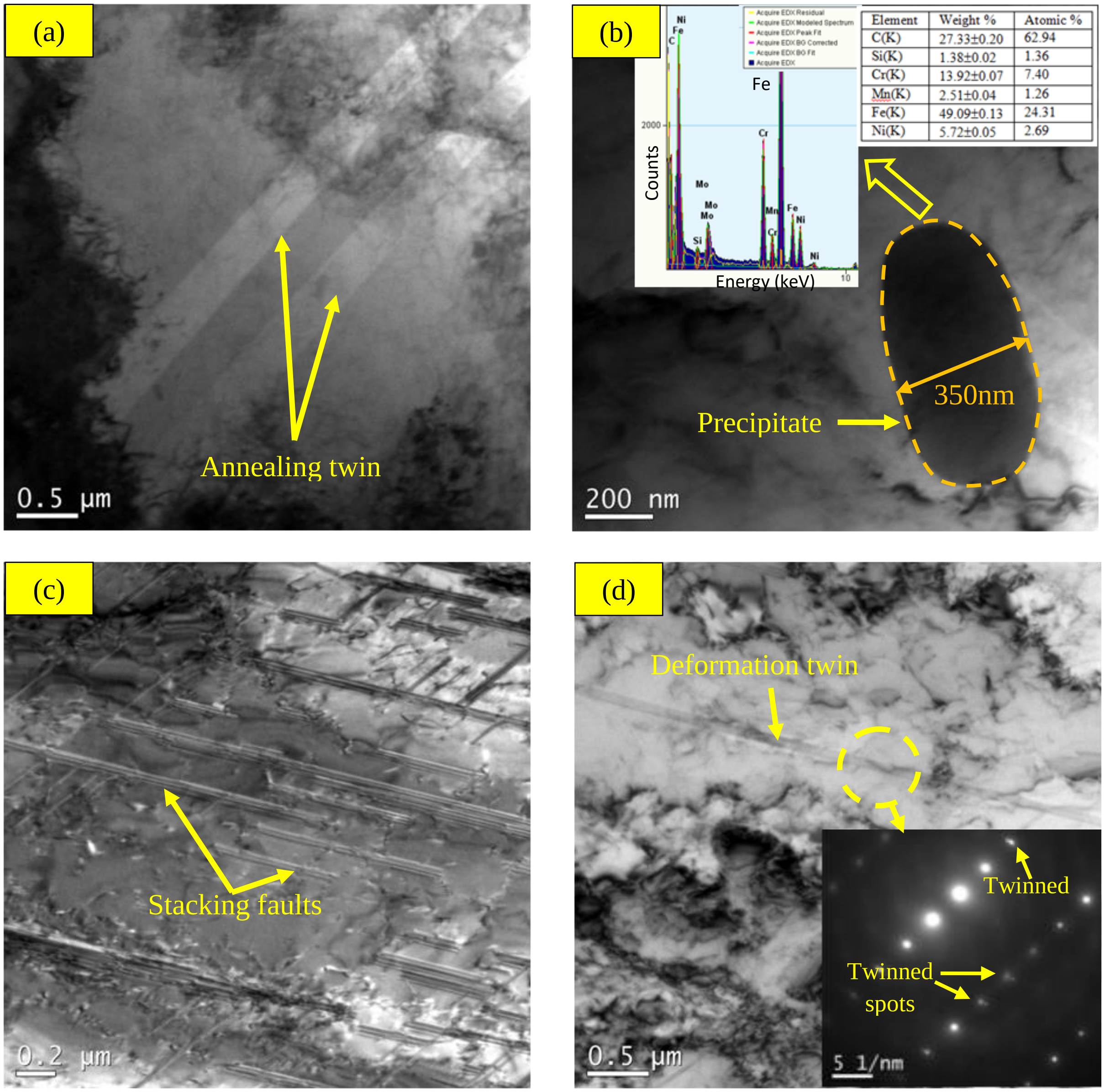

Element	Weight %	Atomic %
C(K)	27.33±0.20	62.94
Si(K)	1.38±0.02	1.36
Cr(K)	13.92±0.07	7.40
Mn(K)	2.51±0.04	1.26
Fe(K)	49.09±0.13	24.31
Ni(K)	5.72±0.05	2.69

Figure 6.5: Transmission electron micrographs of TMCP samples with FRT of 900°C.

TEM microstructures corresponding to the FRT of 800°C are shown in Figures 6.4. Figure 6.4(a) reveals deformation twins within the austenite grains and the same contains high dislocation density. Thicker annealing twins are evident in FRT 800°C sample (Figure 6.4(b)). Figure 6.4(c) reveals annealing twins within the austenite grains with dislocation substructure. Stacking faults and dislocation cell structures are also observed in Figure 6.4(d).

Figure 6.5 reveals the TEM microstructures of samples with the FRT of 900°C. Figure 6.5(a) shows annealing twins in austenite grain and thickness of the annealing twins are ~250 nm. Figure 6.5(b) is showing the presence of precipitate phase having the size of about ~350 nm. The corresponding EDS analysis results in the inset of Figure 6.5(b) shows a higher amount of Cr, Fe and C, indicating these precipitates could be of $M_{23}C_6$ type i.e., $(Cr, Fe)_{23}C_6$ [167] which has been consistent with the present result observed in X-ray study. Figure 6.5(c) reveals an array of stacking fault which is typical for such low SFE steel. In Figure 6.5(d) the deformation twins (≈100 nm) are evident along with some recrystallised grains. The twinned spots (indicated by arrow) are confirmed in the SAED taken from the twinned region as shown in the inset of Figure 6.5(d). It is important to note that the annealing twins are thicker compared to the deformation twins and these annealing twins are formed during hot rolling.

6.4 Mechanical properties of thermo-mechanically processed samples

The variations of hardness and tensile values with different FRTs are given inTable 6.1. Comparison of the mechanical properties of the as-received sample with those of thermo-mechanically treated ones indicates the improvement of both strength and hardness of the specimens after thermo-mechanical treatment. It is seen that among all the samples, the highest yield strength (YS) and ultimate tensile strength (UTS) have been achieved in the case of the sample with FRT of 700°C. The highest elongation has been attained in the sample with FRT of 900°C. Similarly, it is clear that the finer grains have increased the YS (460 MPa) and UTS (925 MPa) values in the sample with FRT of 700°C, whereas maximum elongation of 68% has been revealed in the sample with FRT of 900°C. The increment of YS and UTS in 700°C sample is approximately in agreement with the statement made earlier against discussion of Figure 6.2(a). The sample with FRT of 800°C also reveals a good combination of strength (720 MPa) and ductility (52%). It is imperative to mention here that thermo-mechanical treatment with lower FRT results in lots of ultra fine (Figure 6.3(b)) and fine austenitic grains (Figure 6.2(b)) which influences the mechanical properties of stainless steel. While higher FRT samples show formation of coarse grains (Figure 6.2(d)) lowers the hardness as well as the tensile strength of the samples. It is clearly observed that mechanical properties of the 304 stainless steels are significantly influenced by the application of thermo-mechanical treatment.

Table 6.1: Summary of mechanical properties with different FRT samples.

TMCP condition	Hardness (VHN)	YS (MPa)	UTS (MPa)	Total elongation (%)
As-received	149±10	259±10	675±14	90±5
FRT at 700 °C	210±5	460±7	925±10	34±2
FRT at 800 °C	189±4	368±5	720±8	52±2
FRT at 900 °C	170±3	342±5	698±7	68±3

Mechanical properties of steels strongly depend on their microstructure which is controlled by precipitation, recrystallisation, etc. Grain refinement and uniform distribution of fine second phase are essential to increase the strength and toughness. Thermo-mechanical treatment, which includes heat treatment and deformation, found to be effective for microstructural control and thus it helps in improving mechanical properties of austenitic stainless steels, which cannot be hardened by conventional heat treatment processes. The probable reason for the higher strength and hardness of this steel can be attributed to the presence of dispersed precipitates, mainly $M_{23}C_6$ types within the austenitic matrix of the steel [247]. The presence of deformation twins and annealing twins also refine the austenite grains and improve the tensile strength by strain hardening of the steel [248]. The newly formed twins also decrease the mean free path of the dislocation, thereby increasing the strain hardening of these samples. The maximum and minimum improvements in tensile strength are 37% and 3%, respectively, compared to as-received (hot rolled and solution treated) samples.

6.5 Summary

1. Optical and TEM microstructures of FRT 700°C, 800°C and 900°C samples of 304SS, primarily reveal fully austenitic structure with some amount of annealing twins and the grains are oriented and flattened along the direction of rolling.
2. Fine partially recrystallised austenite grains have been observed at a lower finish rolling temperature of 700°C, where the grain size lies in a range of 1 to 30 μm. Whereas specimen processed at 900°C FRT reveals primarily equiaxed and coarse grains than those observed for 700°C and 800°C FRT.
3. TEM microstructure also reveals the deformation twins which generally form during deformation in low SFE materials. The TEM microstructure also shows the presence of $M_{23}C_6$ ($(Cr, Fe)_{23}C_6$) precipitates in higher FRT of 900°C samples. The presence of $Cr_{23}C_6$ carbide has also been confirmed by the X-ray study.
4. X-ray diffraction analyses do not substantiate the strain induced martensitic transformation during TMCP by showing primarily austenite peaks with low intensity peaks of δ ferrite which are consistent with the chemical composition and processing temperature of the investigated stainless steel.
5. A maximum improvement of tensile strength for 700°C FRT samples is 37% with respect to that of as-received (hot rolled and solution treated) specimen. Maximum elongation value of 68% has been attained in FRT 900°C samples due to the formation of strain-free equiaxed grains ($\approx$ 40 μm).

7

MICROSTRUCTURE AND MECHANICAL PROPERTIES OF CRYOGENICALLY ROLLED/TREATED STEEL

7.1 Introduction

304 austenitic stainless steel (SS) is one of the important engineering alloy characterised by its high ductility and excellent corrosion resistance offered by the high Cr content [249]. However, the low value of strength restricts its application in several structural purposes. 304 stainless steels exhibit austenitic structure at room temperature, which results in a high value of ductility. However, the onset of deformation results in the improvement of strength due to martensite formation and increase in defects structures [47]. Cryogenic and low temperature deformation of 304 stainless steel is of special interest for the industries associated with transportation of the cryogenic material, liquefied natural gas, low temperature technology, ocean technology, food processing, petrochemical processing etc. [250]. Cryogenically or low temperature deformation of austenitic stainless steels exhibits high strength and toughness due to the presence of strain induced martensite, deformation twins, ε-martensite and highly dislocated structures.

It is also important to understand that there is a limited opportunity of compositional modification in stainless steels as the compositions are designed on the basis of specific functional requirements besides the mechanical properties. Therefore, judicious microstructural design in cold deformed austenitic stainless steel is a favourable option for achieving the desired strength-ductility combination. Popularly two approaches are adopted to control the microstructure of the 304 SS by the formation of a different amount of α′ and ε-martensite. Among these two factors, one is SFE and the other is the amount of deformation. It is known that SFE depends on temperature as well as composition [19]. As the composition of 304 SS can’t be altered much due to its specific needs, the SFE can be varied with varying in temperature which considerably affects the deformation microstructure.

In view of the above, the present study aims to understand the influence of low temperature as well as cryogenic temperature deformation on both microstructures as well as mechanical properties in 304 SS by virtue of reduced stacking fault energy with the lowering of temperature. In the present chapter, the as-received austenitic steel samples are subjected to three different processes involving the cryogenic conditions, which are listed below:

(a) Quenching/holding at -196°C for different durations without any pre-strain
(b) 20% pre-strain applied at room temperature followed by quenching/holding at -196°C for different durations
(c) Different amount of deformations provided at -196°C

The above process routes will provide a clear concept or distinguish between the effects of deformation at cryogenic temperature and quenching at that temperature with and without pre-strain. The microstructure and mechanical properties of as-received samples under Steel A composition subjected to cold deformation (10-40%) at 0°C has been used for comparison purpose in order to substantiate the effect of deformation between 0°C and -196°C. Table 7.1 shows the amount of deformation provided at the selected temperatures along with estimated stacking fault energy of Steel A at that temperature.

Table 7.1: Various degrees of deformation and estimated SFE values at selected temperatures.

Temperature (°C)	Reduction in thickness (%)	Stacking Fault Energy (SFE) of Steel A
Room temperature (27)	0	20 (using equation 2.3)
0	10, 20, 30, 40	19 (using equation 2.4)
-196	10 and 20	9 (using equation 2.4)

7.2 Response to cryogenic quenching/holding with or without pre-strain

Tensile testing results of the samples subjected to cryogenic quenching/holding (-196°C) are furnished in Table 7.2. This Table also illustrates the influence of cryogenic holding after application of 20% pre-strain on Steel A composition. Table 7.2 reveals no significant change in the mechanical property after cryogenic quenching/holding from room temperature for the time duration of 0 h to 30 h. The YS and UTS values show aslight increase of 27 and 26 MPa, respectively against as-received properties after 30 h quenching at -196°C, but the same cannot be considered as a notable increment in strength since the austenitic stainless steel also provides similar mechanical property in as-received condition owing to composition variation. On the other side, the pre-strained samples show YS and UTS enhancement of 122 and 109 MPa, respectively owing to the formation of α′-martensite during application of 20% strain at room temperature. However, when these pre-strained samples were subjected to quenching/holding at -196°C between 0 to 30 h time period, further enhancement of mechanical properties is negligible, which indicate the fact that, the thermal gradient arising due to temperature difference between room temperature and -196°C could not influence perceptible change in microstructure which can enhance the mechanical property of austenitic stainless steel.

Table 7.2: Mechanical properties after quenching/holding at -196°C for various durations.

Time duration (h)	Without Pre-strain			With 20% Pre-strain at room temperature		
	YS (MPa)	UTS (MPa)	TEL (%)	YS (MPa)	UTS (MPa)	TEL (%)
0	259±10	675±14	90±5	381±13	784±16	71±3
1	320±12	683±14	54±2	397±12	786±16	62±3
4	290±11	666±13	59±2	383±10	772±15	66±3
15	296±10	673±13	58±2	413±14	794±16	72±4
30	286±10	701±15	58±2	391±12	786±16	68±3

Figure 7.1 illustrates trends at different quenching/holding duration at -196°C, which reflects almost no change in mechanical properties. No indication of enhancement related to mechanical property is noticed from the analysis.

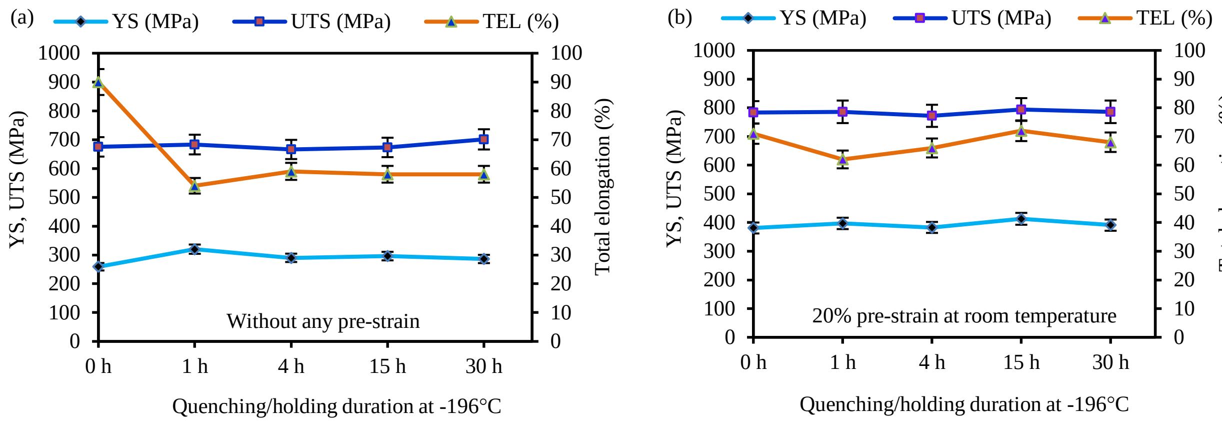

Figure 7.1: Variation of YS, UTS and %TEL at different quenching/holding time at -196°C for austenitic stainless steel samples (a) without any pre-strain and (b) with 20% pre-strain at room temperature.

Figure 7.2 shows the X-ray diffraction pattern for 30 h quenched sample without any pre-strain, where no peak related to α′ or ε-martensite could be observed. Prominent peaks of austenite at (111), (200), (220), (311) and (222) are noticed which is similar to X-ray diffraction pattern of the as-received sample (Figures 4.1 and 4.2). It may be seen that, the base of (111) peak is not symmetrical. This may reasonably be attributed to the formation of small amount of α′-martensite at sample surface owing to accommodation of large quench stress at -196°C. However, it is to be noted that, the α′-martensite is so small that, its volume percentage could not be determined. Therefore, formation of ε or α′-martensite after prolong holding at -196°C is inconclusive from Figure 7.2.

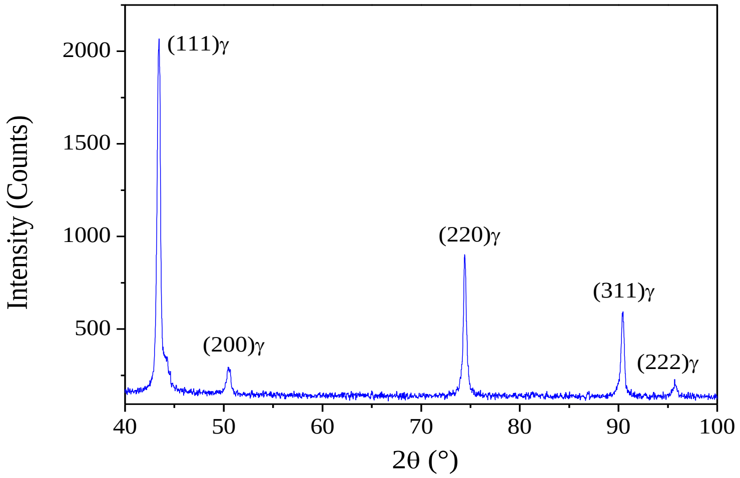

Figure 7.2: X-ray diffraction pattern of 30 h quenched/holding sample at -196°C from room temperature without any pre-strain.

Figures 7.3(a) to (d) reveal optical micrographs of 20% pre-strained samples subjected to quenching/holding at -196°C for different time durations. Micrographs, in general, show the presence of α′-martensite anddeformed austenite grains in all the micrographs. Austenite grains are elongated towards tensile loading direction. However, the micrographs do not show any significant change between them with respect to quenching/holding duration at -196°C. In addition to that, the volume fraction of strengthening constituent phases (i.e. α′/ε-martensite) has not been changed with the increasing quenching/holding time.

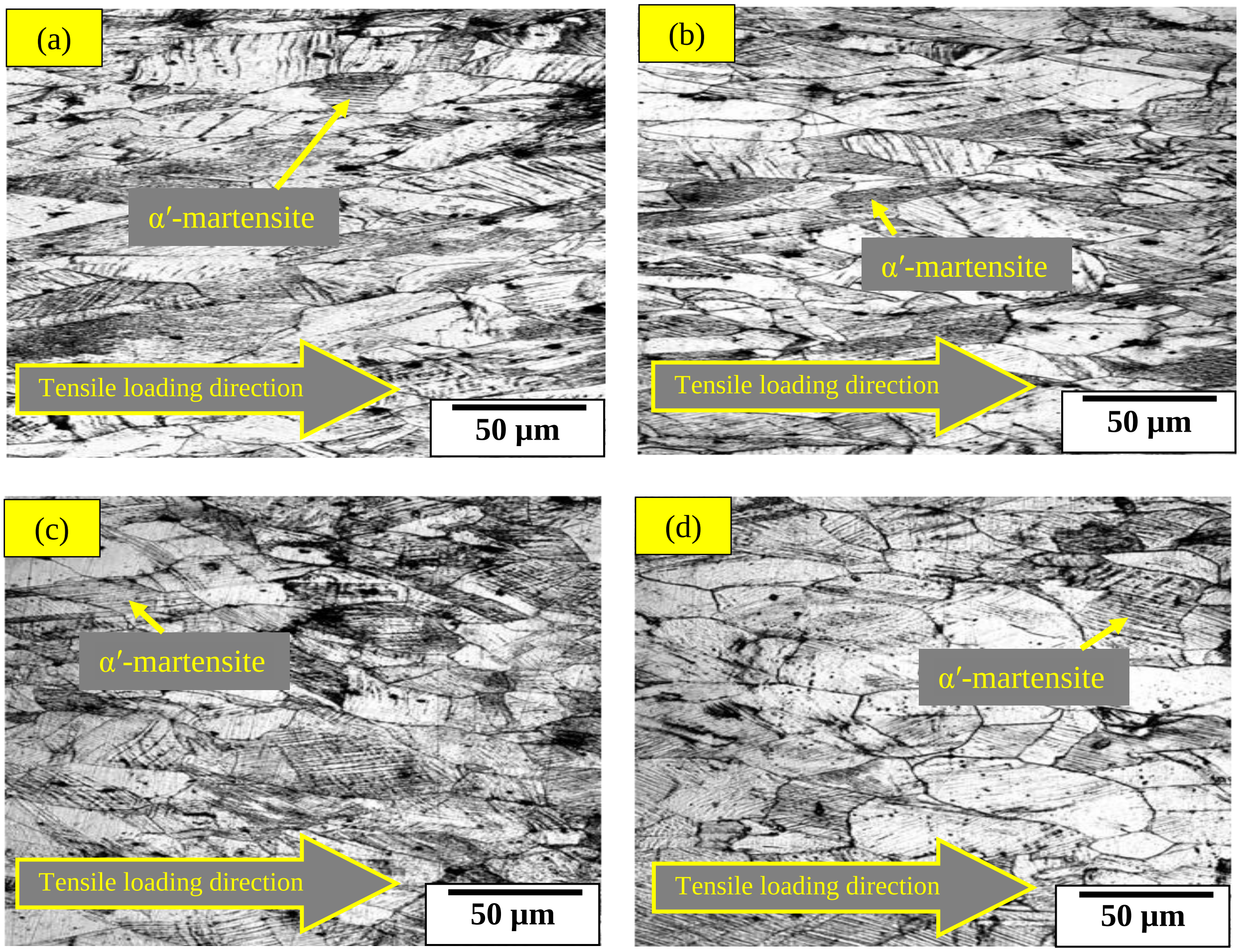

Figure 7.3: Optical micrographs of tensile fracture end of the samples subjected to 20% pre-strain at room temperature followed by cryogenic quenching/holding at -196°C for (a) 1 h, (b) 4 h, (c) 15 h and (d) 30 h.

These experiments help us to understand that the formation of martensite is unlikely to take place for 304 austenitic stainless steel grade (Steel A) through the application of thermal gradient (quenching to -196°C from room temperature). No favourable transformation took place which can impart strength into the material. Sufficient amount of dislocations introduced through 20% pre-strain before quenching/holding at -196°C. But no increase in strength or any microstructural change could be noticed (Figure 7.3), which indicate that it is independent of time also.

7.3 Effect of deformation at cryogenic temperature and comparison with deformation at 0 ℃

Effect of cryogenic deformation at -196°C in comparison to deformation at 0°C and pre-strain followed by cryogenic quenching/holding samples are described below.

7.3.1 X-ray diffraction study

The constituent phases in the microstructures were identified by carrying out the X-ray diffraction study followed by Rietveld analysis using X'Pert High Score Plus software. Figure 4.2 (illustrated in Chapter 4) shows the X-ray diffraction profiles of l0%, 20%, 30% and 40% cold deformed samples at 0°C. The diffraction profile of the as-received 304 stainless steel is also appended to the figure. The XRD pattern of the as-received specimen reveals only the peaks related to the austenite phase (FCC) which is in good agreement with the typical diffraction patterns reported in the cases of 304 stainless steels [251]. The diffraction pattern of the cold-deformed samples reveals (110), (200) and (211) peaks related to the body centred cubic (BCC) α′-martensite phase, in addition to the aforesaid austenite peaks. Such peaks representing α′-martensite do not appear for 10% and 20% deformation at 0°C. Moreover, the XRD pattern does not reveal any perceptible presence of peaks characteristic of the faulted crystal structure of ε-martensite [62, 190, 252]. It is imperative to mention here that at a low level of deformation (up to 20%) at room temperature, quantification of α′-martensite by X-ray diffraction is difficult due to its minimal presence [191]. Therefore, Figure 4.2 indicates that the deformation induced transformation of austenite is primarily manifested by the α′-martensite formation mainly due to higher deformation (above 30%).

Figure 7.4 reveals prominent (110), (200) and (211) peaks corresponding to the α′-martensite formed after 20% reduction at -196°C and the remaining peaks are mainly austenite peaks. It may be noted that, the presence of (101) peak of ε-martensite is clearly revealed after 20% deformation at -196°C, which may be attributed to the lowering of stacking fault energy at -196°C [243]. The reduction of SFE with the lowering of deformation temperature increases the stacking fault region which accelerates the rate of martensite formation.

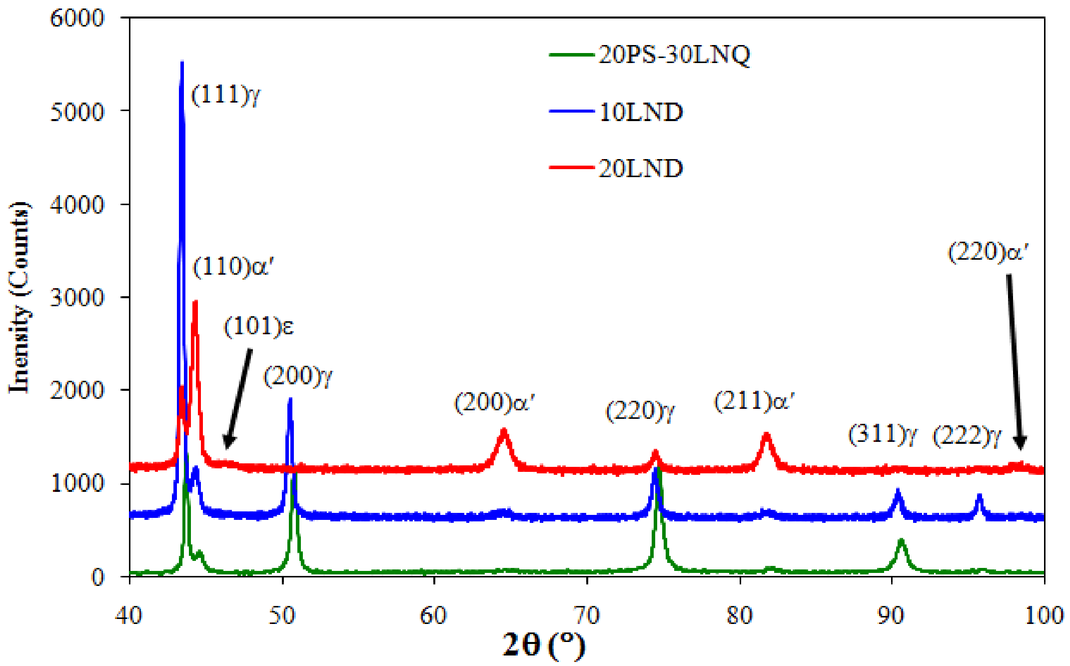

Figure 7.4: X-ray diffraction profiles of 10% and 20% deformed specimens at -196°C and 20% pre-strain followed by 30 h holding in liquid nitrogen.

Table 7.3 shows the volume fraction of austenite (FCC), α′-martensite (BCC) and ε-martensite (HCP) phases as obtained by Rietveld analysis corroborating the occurrence of the higher volume fraction of α′-martensite with increasing amount of cold deformation. The amount of α′-martensite in 10% and 20% deformed samples at -196°C is higher than that of deformation at 0°C. In 40% deformation at 0°C, the amount of α′-martensite is about 32% whereas, for 20% deformation at -196°C, the total volume fraction of α′-martensite and ε-martensite is almost 50%. However, 20% pre-strain triggers lower percentage of α′-martensite (9%) during 30 h of isothermal holding in liquid nitrogen.

Table 7.3: Volume percentage of constituent phases obtained from X-ray diffraction analysis.

Processing conditions		Measured volume of FCC (γ) (in %)	Measured volume of BCC (α′) (in %)	Measured volume of HCP (ε) (in %)
Deformation temperature (°C)	Deformation (%)			
0	10	87±2	13±1	0
0	20	83±2	17±1	0
0	30	76±2	24±1	0
0	40	68±2	32±1	0
-196	10	72±2	28±1	0
-196	20	50±2	44±1	6±1
20% pre-strain at room temperature + 30 h LNQ		91±2	9±1	0
As-received		100	0	0

7.3.2 SEM micrograph of as-received and deformed samples

Figures 7.5(a) to (d) shows the SEM micrographs of the as-received sample and the same after 20-40% cold deformation at 0°C. For the as-received sample, Figure 7.5(a) reveals fully austenitic structure having a grain size of 20 µm along with annealing twins within the austenite grains. Earlier studies have reported the formation of annealing twins during hot rolling and subsequent annealing of 304 stainless steel specimen [253]. Figures 7.5(b) to (d) show twinned austenite grains along with some deformation induced α′-martensite after application of 20-40% cold deformation at 0°C. Deformation has resulted in the formation of α′-martensite at the austenite grain boundaries as well as at the intersections of micro/nano twins formed during deformation. In this regard, the low SFE value (Table 7.1) favours the formation of stacking faults which act as the nuclei for such micro twins and α′-martensite during deformation [254]. The volume fraction of α′-martensite has been estimated as 32% for 40% deformation (Table 7.3).

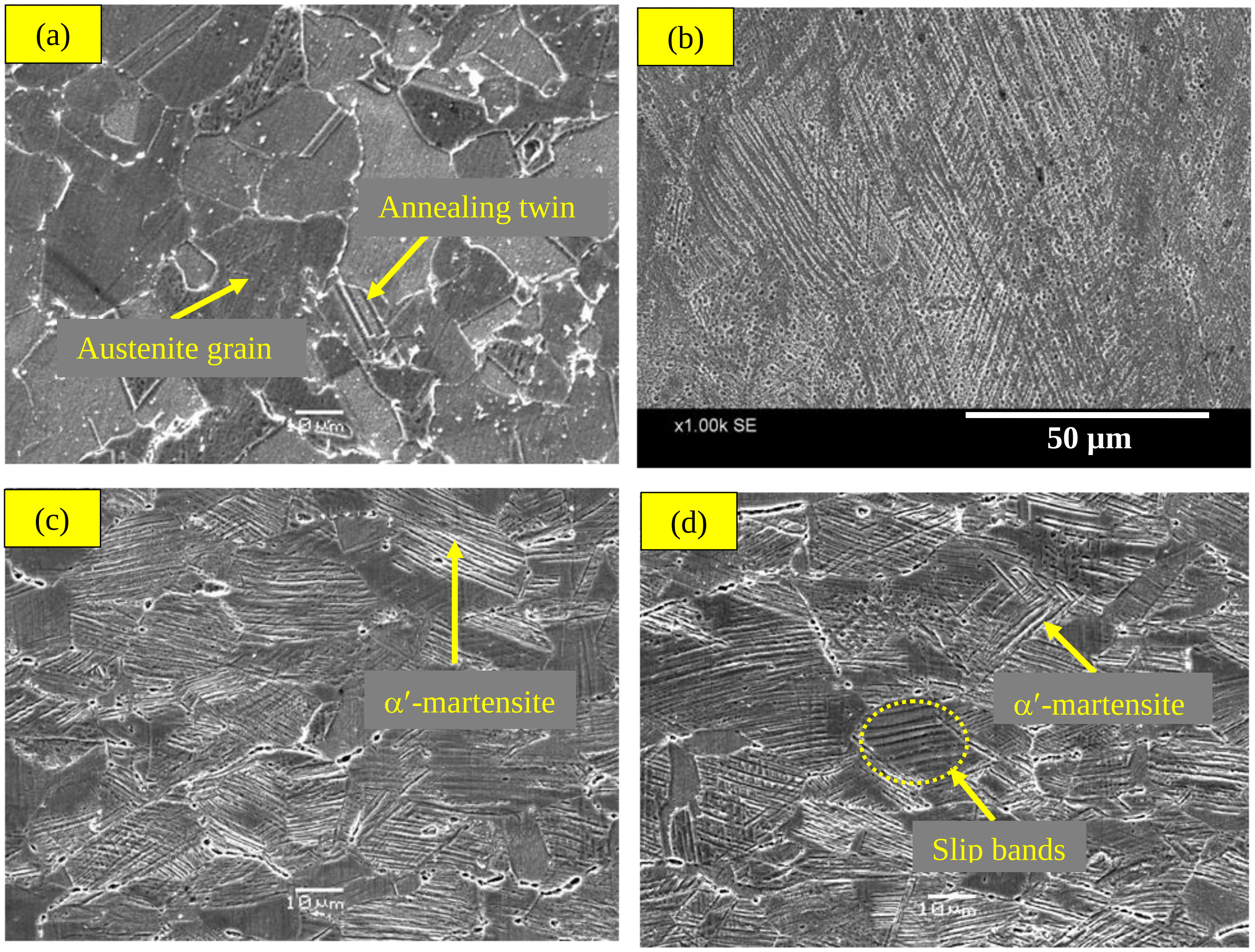

Figure 7.5: SEM micrograph of (a) as-received, (b) 20% cold deformed, (c) 30% cold deformed and (d) 40% cold deformed steel specimens at 0°C.

It is obvious that the volume fraction of α′-martensite is increasing with the increasing amount of deformation at 0°C. The diffused nature of austenite grains observed in Figure 7.5(d) is apparently due to the deformation localisation. The deformation induced martensite (DIM) is finer and more elongated in nature than those of thermally induced martensite [193]. The intergranular micro cracking in Figure 7.5(d) can be related to over-etching in these regions which corroborate the earlier report for 304 SS [239]. After deformation, high density of dislocation and the interaction between dislocation and precipitate in α′-martensite is common in similar austenitic steel [187].

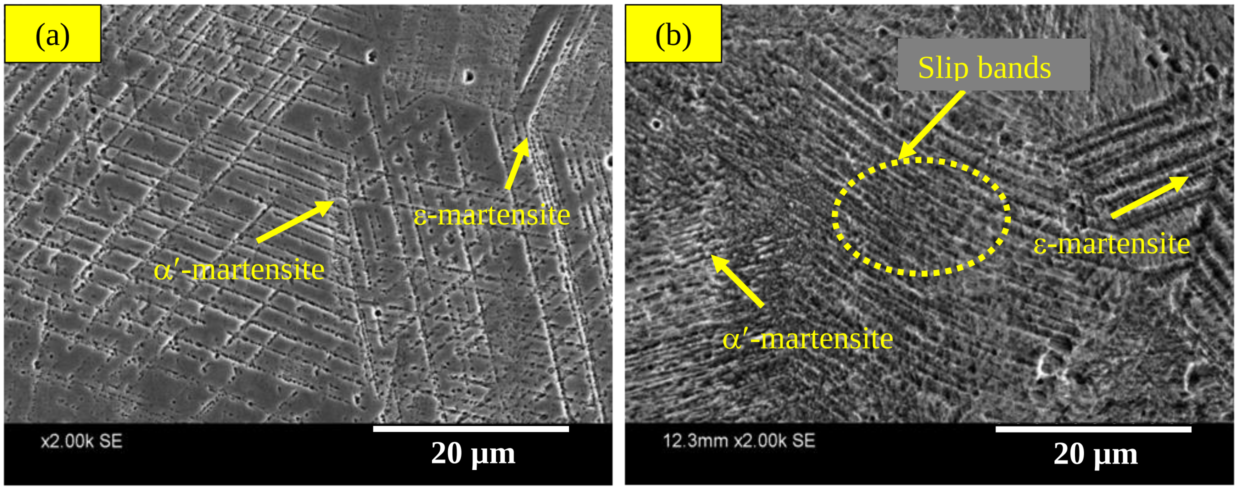

Figure 7.6: SEM micrograph of samples subjected to cold rolling at -196°C for (a) 10% deformation and (b) 20% deformation.

Figures 7.6(a) and (b) demonstrate SEM micrograph of samples subjected to 10% and 20% cold rolling at -196°C, respectively. It is evident that 20% deformed sample at -196°C (Figure 7.6(b)) exhibits higher quantity of α′-martensite in the microstructure than the sample deformed by 10% at -196°C. The presence of ε-martensite is also apparent in the SEM microstructure obtained at lower magnification. The identification of twins, alpha prime and epsilon (Figures 7.5 and 7.6) martensites are only tentative based on the matching with similar features reported earlier in the literature [123, 255]. However, such features like a twin, shear band, α′-martensite or ε-martensite have been confirmed appropriately by conducting TEM analysis along with SAED. A comparison of microstructural evolution due to deformation at 0°C and -196°C, reveals that for deformation at 0°C temperature, the microstructures are non-uniform with high density of slip bands localised in some austenite grains (Figure 7.5), whereas multiple slip band of each slip system can be observed in Figures 7.5(d) and 7.6(b). It is important to note that alignment of the martensite laths (α′) is along the crystallographic slip bands. Slip bands generally lie in the grain without reaching boundaries and it may be continued up to the twin boundaries within the grain and there is no continuity of slip bands through grain boundaries into the neighbouring grains. It is known that after polishing of deformed samples, slip lines may disappear from the surface. According to previous studies [123, 256], slip bands are visible in optical microstructure after polishing. Consequently, it is evident that microstructural evolution in austenitic steels is significantly influenced by the amount and temperature of deformation.

7.3.3 TEM micrograph of deformed samples

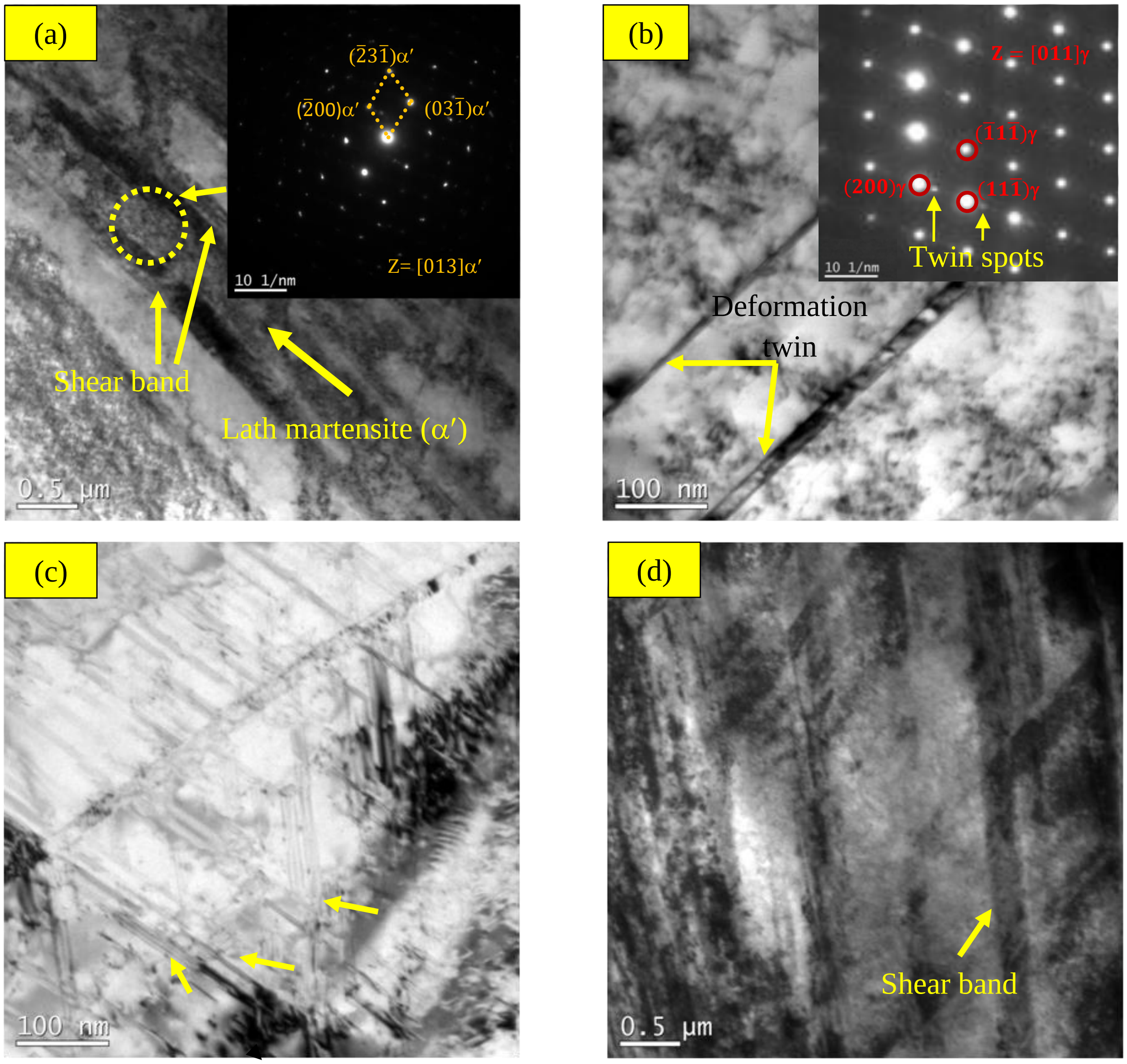

Figure 7.7: TEM bright field micrographs of samples subjected to 40% deformation at 0°C showing (a) austenite and lath martensite with high dislocation density and SAED in inset, taken from the circular area confirms the presence of α′-martensite, (b) twinned austenite grain and SAED at the inset confirms the twin, (c) array of stacking faults and (d) high dislocation with the presence of some shear bands.

In view of the observed features in optical and SEM images, 40% deformed sample was subjected to the TEM study for the confirmation of finer microstructural features. Figures 7.7(a) and (b) reveal the austenite and α′-martensite phases along with the presence of deformation twins in 40% cold deformation at 0°C. Figure 7.7(a) reveals the dislocated structure and lath martensitic regions within the junction of two shear bands. Tian et al. [243] have reported the similar type of features of α′-martensite and shear bands (Figure 7.7(a)) in case of austenitic Fe-Cr-Ni alloys. In this context, it should be mentioned that slip bands are confined in a grain which means that they cannot cross the grain boundary. On the contrary, shear bands can cross existing grain boundary. A similar type of characteristic of shear bands has been reported in the previous literature [10]. Figure 7.7(b) shows nano twin and interaction of dislocation and deformation twin within the austenite grain which is in good conformity with the estimated stacking fault energy (Table 7.1). The SAED image appended at the inset of Figure 7.7(b) confirms the presence of twins in this microstructure. However, the presence of ε-martensite phase is not evident in these two micrographs. Deformation of large strain results in the formation of α′ phase without the intermediate ε phase where the γ→α′ transformation sequence is followed. Figures 7.7(c) and (d) divulge array of stacking faults and high dislocation with the presence of some shear bands, respectively.

The deformation behaviour of 20% isothermally deformed specimen at -196°C is depicted in Figures 7.8(a) to (d). In contrast to the deformation microstructure at 0°C, at low temperature and strain, the formation of extended and overlapping stacking faults are evident in Figures 7.8(a) due to the low stacking fault energy of the austenite at -196°C (9 mJ/m^2 as shown in Table 7.1) [39]. In the cases where the SFE is low, especially at low temperature, formation and overlapping of stacking faults arefrequently found which favours the nucleation of ε-martensite [257]. This is followed by formation of thin bands of the HCP ε-martensite phase (Figure 7.8(b)) which appears to be faulted. SAED and its analysis from the marked region in Figure 7.8(b) indicate Kurdjumov-Sachs relationship [258, 259] between austenite and ε-martensite. Preferred nucleation sites of the α′ phase at intersecting bands [257] of ε-martensite or in a band of ε-martensite with an intersecting slip band are shown in Figure 7.8(c). The laths of α′ phase nucleate and grow within the bands of the ε phase in the sequence of γ→ε→α′. This is consistent with the formation of laths in partially transformed steels [260]. A substantial γ→α′ transformation takes place without the perceptible lath-like morphology as soon as nucleation takes place at the intersections of ε phase with the application of the higher amount of deformation [15].

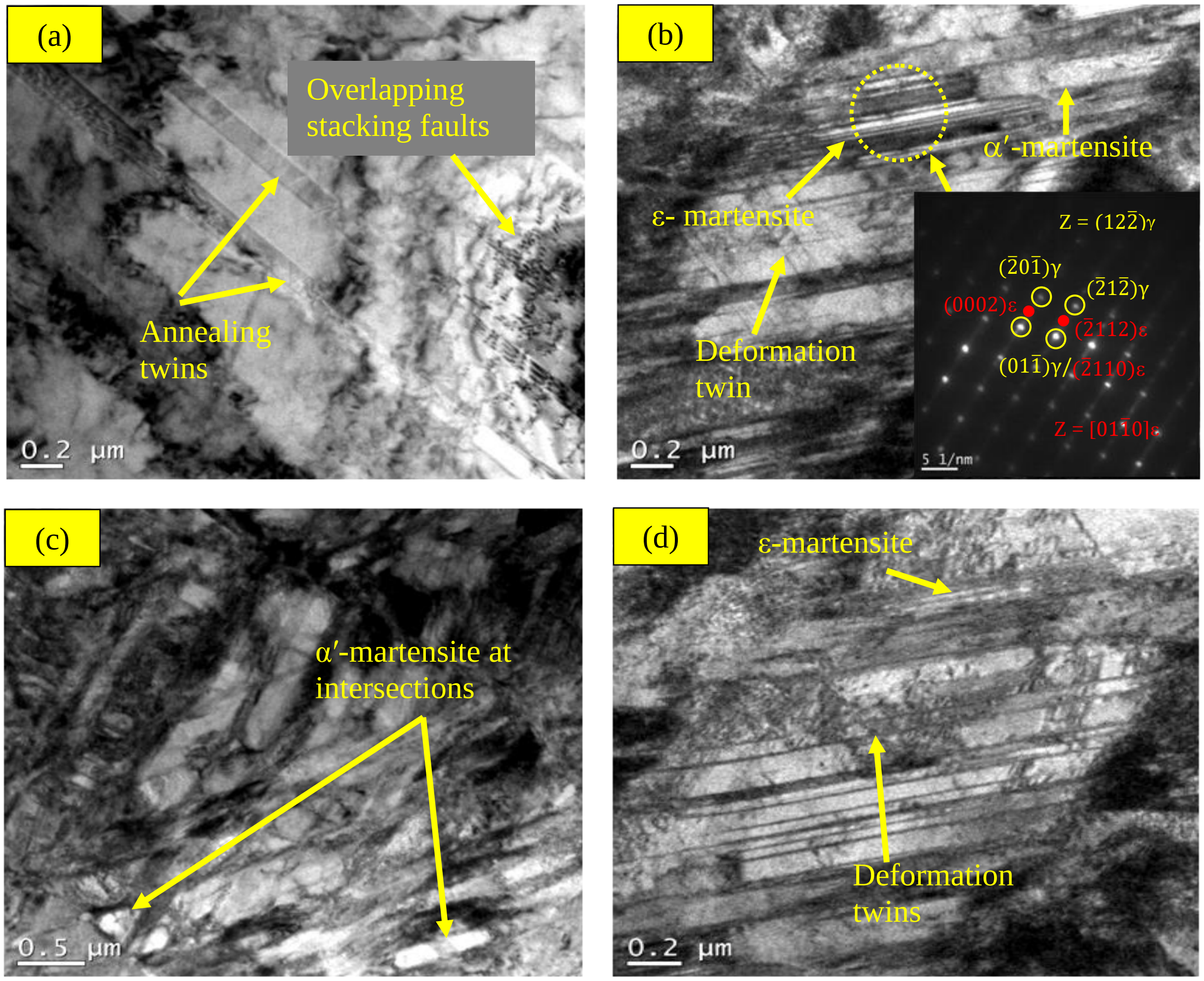

Figure 7.8: TEM bright field micrographs of samples subjected to 20% deformation at -196°C.

In general, grain boundaries were not found to be preferred nucleation sites for the α′ phase except in such locations where the ε phase intersected the grain boundary. Preferential nucleation of α′-martensite occurs heterogeneously on twin boundaries which are intersected by either a band of the ε phase or by a slip band [257]. Earlier, it has been established that the twin boundary appears to contain different layers suggesting that the same may be faulted. The presence of faults is consistent with the previous studies which have reported that ε layers cannot thicken and that the retained austenite between ε layers can only transform to the ε phase by the nucleation of new layers [58]. According to the Olson and Cohen's model of strain induced martensite nucleation [66], it requires two intersecting invariant plane strains for the γ→α′ transformation; an intersecting ε-martensite band can well be postulated as a second invariant plane strain. This could be a logical explanation for the relative effectiveness of twin boundaries as nucleation sites for the α′ phase.

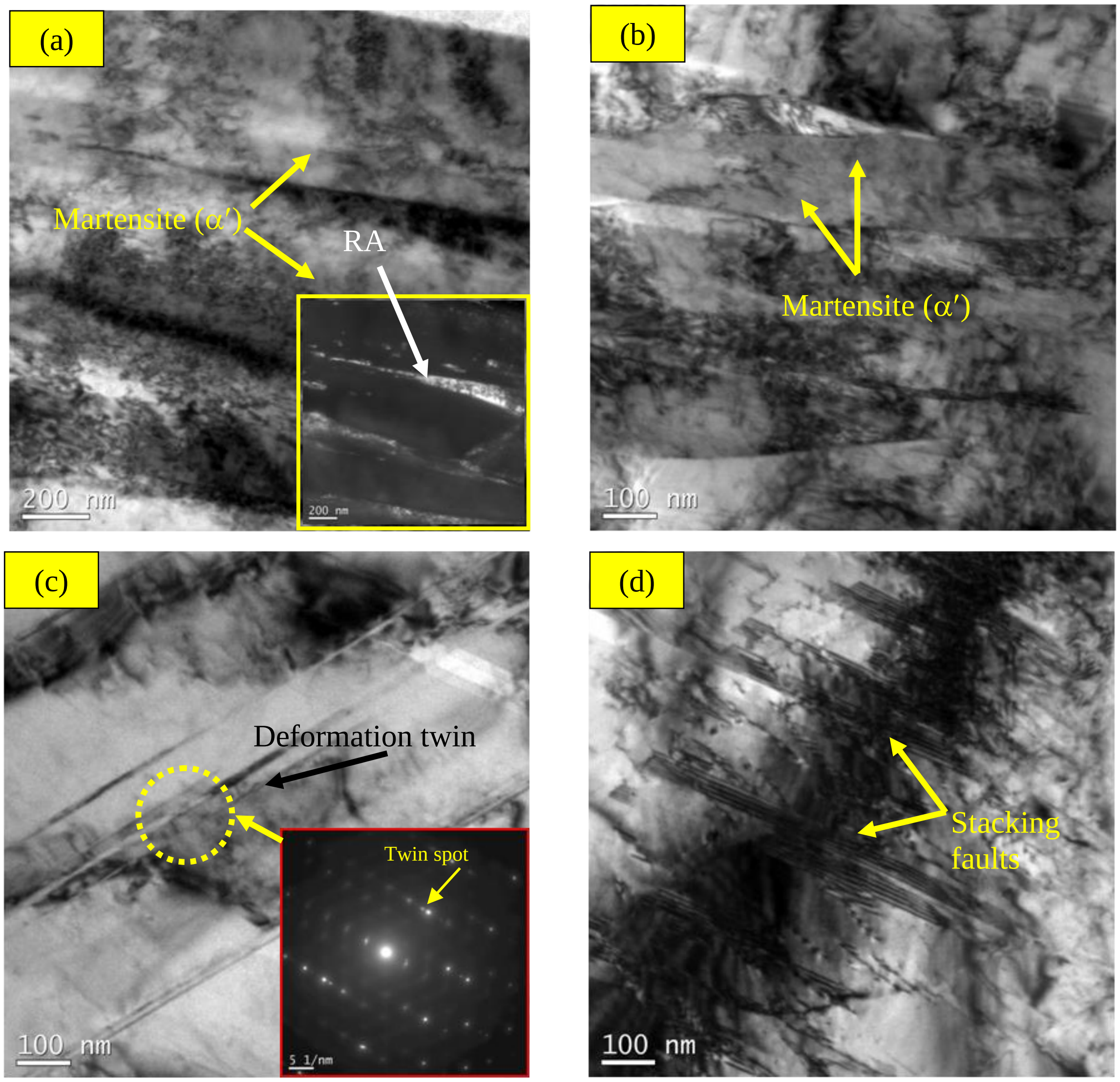

Figure 7.9: TEM bright field micrographs of samples subjected to 20% pre-strain at room temperature followed by 30 h holding at -196°C.

The α′-martensite is apparent in Figures 7.9(a) and (b), whereas deformation twins and an array of stacking faults are observed in Figures 7.9(c) and (d) in the case of TEM bright field micrographs of samples subjected to 20% pre-strain at room temperature followed by 30 h holding at -196°C. Insets of Figures 7.9(a) and (c) are showing untransformed austenite or retained austenite (RA) of white contrast in between two martensite laths and presence of deformation twin, respectively. It is evident in Figures 7.9(a) and (b) that lots of dislocations are present which promotes the nucleation of α′-martensite. It is noteworthy that the transformation of martensite from the parent austenite phase in 304 SS can occur in different mechanisms such as [10]:

a. γ (FCC)→ε (HCP),
b. γ (FCC)→α′ (BCC) and
c. γ (FCC)→ε (HCP)→α′ (BCC).

In view of the above, the TEM study well corroborates the results obtained in X-ray diffraction experiment where the sample subjected to 40% cold deformation at 0°C reveals lower amount of strain induced martensite (32%) along with high dislocation density as compared to the samples deformed by 20% at -196°C which shows 50% martensite along with the presence of ε-martensite. Such high amount of martensite leads to better tensile strength with a loss in ductility. However, in 20% pre-strained samples show a lesser amount of martensite with a higher amount of untransformed austenite results in a favourable combination of strength and ductility.

7.3.4 EBSD analysis of as-received and deformed samples

Figures 7.10(a), (c) and (e) reveal EBSD phase map along with the respective recrystallised fraction formed in as-received, 10% and 20% deformed specimens at -196°C. The EBSD phase maps reveal the cell or sub-grain boundaries as well as finer grains from which the recrystallised fraction is obtained [261]. Mean subgrain size and misorientation angle values are obtained and the total number of subgrains are analysed for each sample, which provides the volume fraction of deformed and substructure from the software.

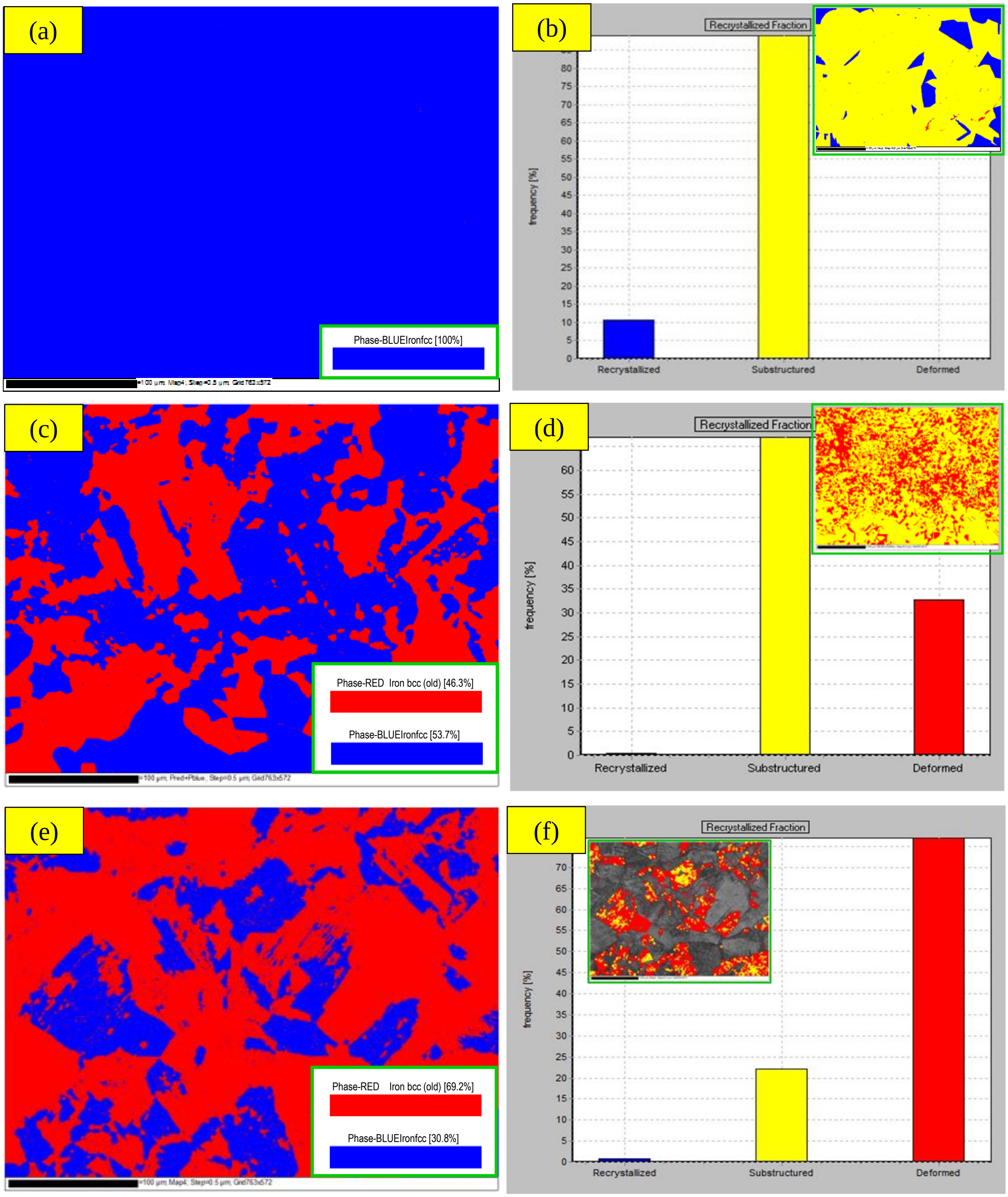

Figure7.10:EBSD phase map of (a) as-received, (c) 10%, (e) 20% deformed specimens at -196°C and corresponding recrystallised fraction along with its map at the inset of (b) as-received, (d) 10% and (f) 20% deformed specimens at -196°C.

The fraction of high angle grain boundaries (HAGB) changes during recrystallisation. Here, the change in HAGB fraction is correlated to the recrystallisation. EBSD mapping methods provide more detailed information for recrystallisation and texture as reported earlier [262]. A recrystallised grain can be identified in a set of plastically deformed grains by the grain orientation spread (GOS) method [263]. Although the recrystallisation fraction measured from the EBSD profiles is less accurate due to slower data acquisition, the exercise serves the purpose of comparative study. The EBSD image as shown in Figure 7.10(a) of the as-received sample shows 100% face centred cubic phase (blue) without any sign of the deformed structure. 10% and 20% cold deformation at -196°C resulted in the formation of deformation induced α′-martensite (red) in the austenite matrix (blue). The presence of α′-martensite (red) in the austenitic matrix (blue) is found in the level of 46.3% and 69.2% for 10% and 20% deformation at -196°C, respectively. The error involved in estimation of volume percentage of martensite from EBSD analysis usually amounts to ~5% [264]. Figures 7.10(b), (d) and (f) are showing corresponding recrystallised fraction along with its map at the inset of as-received, 10% and 20% deformed specimens at -196°C, respectively. Figure 7.10(b) reveals 89% substructure and 11% recrystallised structure. During hot rolling, steel samples have undergone dynamic recovery. However, in the case of such steels with low stacking fault energy, dynamic recovery may be substantially hindered leading to the retained substructures as evident by the coexistence of cell and cell block boundaries as well as twin boundaries. Therefore, the observed substructure formation in the as-received austenitic stainless steel with low SFE may be due to limited dynamic recovery. Figures 7.10(d) and (f) show a higher amount of deformed structure i.e., 76% in case of 20% deformation compared to 33% for 10% deformation, which is in conformance with the microstructure study. Occasionally, it is difficult to characterise some areas of a highly deformed sample in EBSD system which is apparent here for 20% deformed specimens at -196°C (Figure 7.10(f)). This has constrained the indexing of some of the grains, and hence, the fractions were approximately estimated from the indexed part only.

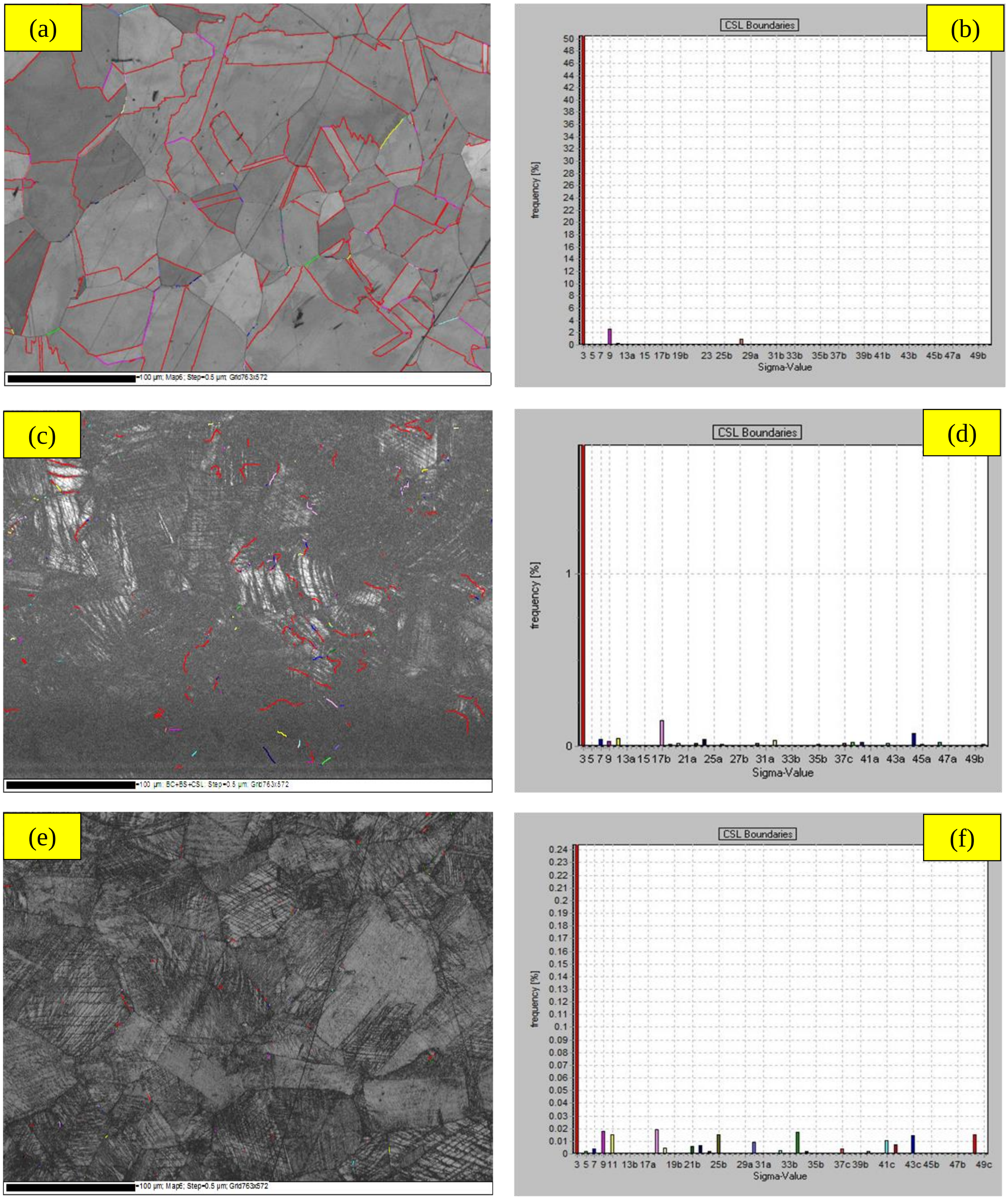

Figure 7.11: Band contrast maps with embedded CSL boundaries of (a) as-received, (c) 10% deformed and (e) 20% deformed specimens at -196°C. (b), (d) and (f) represent the distribution of corresponding CSL boundaries of the respective samples.

In Figure 7.11, band contrast maps with embedded coincidence site lattice (CSL) boundaries are shown for the as-received sample and samples deformed by 10% and 20% at -196°C. EBSD maps show grain boundary regions where twins, dislocation and the triple point of austenite grains are apparent with a higher density of sub-boundaries. The various types of CSL boundaries are revealed in different colours. The annealing twins and its boundaries as seen in the micrographs in Figure 7.11 are notionally referred as substructures and their occurrence has been appended as the histograms in Figure 7.10 and similar histograms presenting the frequency of CSL boundaries are shown in Figure 7.11. The frequency of special boundary (CSL) increases with the progress of recrystallisation, owing to the presence of twin boundaries and recrystallised grain boundaries, which are prominent in the as-received sample as depicted in Figure 7.11(a). The observation is corroborated by the corresponding CSL distribution profile, presenting Σ3 CSL boundaries higher than 50%, as shown in Figure 7.11(b). Red, yellow, green, and magenta boundaries represent different types of CSL boundaries such as Σ3, Σ9 boundaries etc. as depicted in Figure 7.11. In this context, it is important to note that a few grains (Figures 7.11(c) and (e)) are not resolved as they were below the resolution of the EBSD facility used in the present study.

7.3.5 Mechanical properties and correlation with microstructure

The tensile results furnished in Table 7.4, allow one to compare the tensile properties obtained due to the variation of process scheduling. 40% deformation at 0°C yields 1225 MPa UTS which is 550 MPa higher than that of as-received state (675 MPa). On the other hand, 10% and 20% deformation at -196°C exhibit maximum increment to the level of 631 MPa and 914 MPa, respectively over that of the as-received sample. Enhancement of UTS in the case of 20% deformation at -196°C is 135% and the YS is of 92% of UTS value and both are attributed to the formation of α′-martensite, ε-martensite along with deformation twin. In both, the samples, deformed at 0°C and -196°C, the higher dislocation density is found which interacts with newly formed nano-twins and higher strength has achieved with a loss in ductility. As tensile strength increases with the increasing amount of deformation, the ductility has decreased.

Table 7.4: Tensile properties of steel samples under different processing conditions.

Processing conditions	YS (MPa)	UTS (MPa)	YS/UTS ratio	TEL (%)
As-received (AR)	259±10	675±14	0.38	90±5
10% deformation at 0°C (10 ZCD)	703±22	930±12	0.76	32±3
20% deformation at 0°C (20 ZCD)	742±18	981±15	0.75	28±3
30% deformation at 0°C (30 ZCD)	834±24	1098±19	0.76	22±2
40% deformation at 0°C (40 ZCD)	936±23	1225±18	0.76	13±1
10% deformation at -196°C (10 LND)	1061±21	1306±12	0.81	15±1
20% deformation at -196°C (20 LND)	1463±24	1589±17	0.92	9±1
20% pre-strain at room temperature (20 PS)	381±10	784±16	0.49	71±4
20% pre-strain at room temperature + 15 h holding at -196°C (20 PS+15LNQ)	413±14	794±17	0.52	72±4
20% pre-strain at room temperature + 30 h holding at -196°C (20 PS+30LNQ)	391±12	786±19	0.50	68±4

The yield ratio of the deformed samples at 0°C is quite lower as compared to those deformed at -196°C. Furthermore, to recover the ductility, pre-strain along with liquid nitrogen quenching has been carried out. The tensile strength of 784 MPa along with 71% total elongation has been achieved in the case of 20% pre-strained sample. Further soaking at -196°C for 15 h has increased the tensile strength to 794 MPa with comparable ductility achieved in the case of 20% pre-strain. The same sample, after 30 h holding at -196°C, shows UTS of 786 MPa and a similar amount of ductility indicating that no significant change has taken place after prolonged holding at -196°C.

Figure 7.12 reveals comparison of strength properties (UTS and YS) and total elongation of steel samples after various processing conditions as mentioned in Table 7.4. It indicates that the tensile strength is increasing with increasing amount of deformation. However, the tensile strain (total elongation) is found lower with the increase of tensile strength due to the formation of strain-induced martensite, deformation twins and dislocation densities as observed in the microstructural study. The tensile strength, as well as yield strength, is maximum after deformation at -196°C, due to the formation of the higher volume fraction of α′-martensite and twins along with ε-martensite.

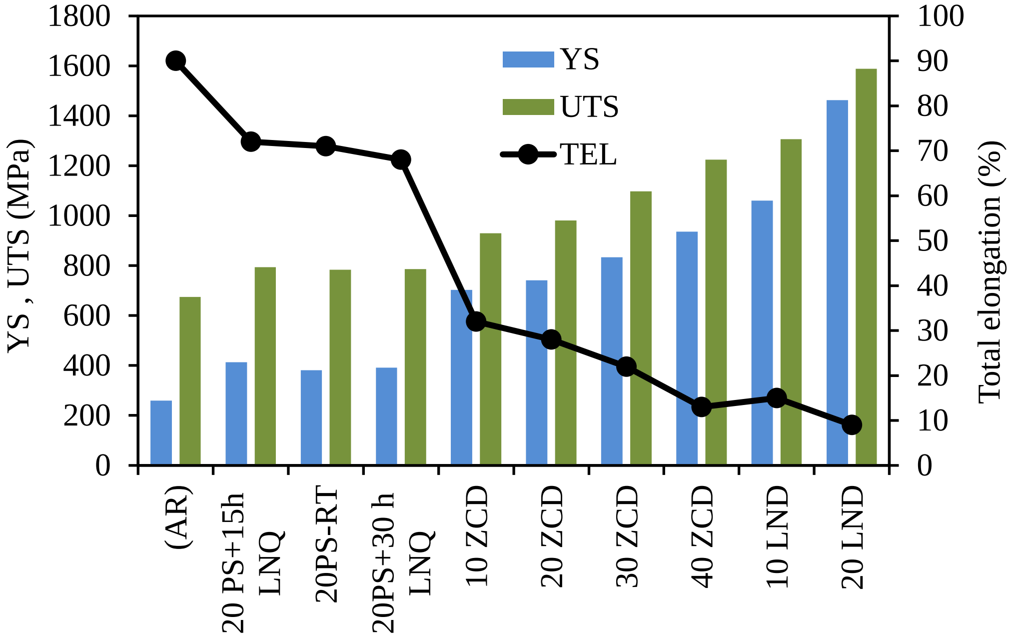

Figure 7.12: Variation in YS and UTS and total elongation (%) with respect to the various processing conditions as mentioned in Table 7.4.

Figure 7.13 reveals variation in volume percentage of austenite and ductility (total elongation) with respect to various processing conditions as presented in Table 7.4. It indicates a decrease in volume percentage of austenite with an increase in the amount of α′-martensite leading to the lower ductility of steel samples. 20% deformation at -196°C exhibits the highest UTS and YS among all the specimens and the corresponding austenite volume percentage is 50% only (Figure 7.12 vis-à-vis Figure 7.13). It may be mentioned that the enhancement of tensile properties corroborates the estimated austenite volume percentage.

The increase in tensile strength with a higher degree of cold rolling may be attributed to the increased dislocation and twin density along with the formation of strain-induced martensite. During cold deformation at -196°C, the metastable austenite has transformed to strain-induced α′-martensite and also ε-martensite. In addition, deformation twins can form in the remaining austenite during this deformation process. Moreover, shear band favours the α′-martensite transformation [265]. Therefore, it is reasonable to presume that the temperature and composition dependent SFE always play a key role in the transformation of austenite during deformation [266]. At -196°C the SFE is 9 mJ/m^2 (Table 7.1) and the transformation to α′-martensite is quite obvious and the microstructure and X-ray results also show that the amount of martensite (α′ and ε) is maximum (~50%) in 20% deformation at -196°C along with low amount of twins (Figure 7.6). However, as the SFE at 0°C is about 19 mJ/m^2, here formation of deformation twin is more favourable rather than the martensitic transformation (Figure 7.5). Although 20% deformed specimen at -196°C is showing highest UTS (~1589 MPa) along with 9% of total elongation, the 10% deformed specimen at -196°C reveals the best combination of tensile properties among the investigated samples (Table 7.4).

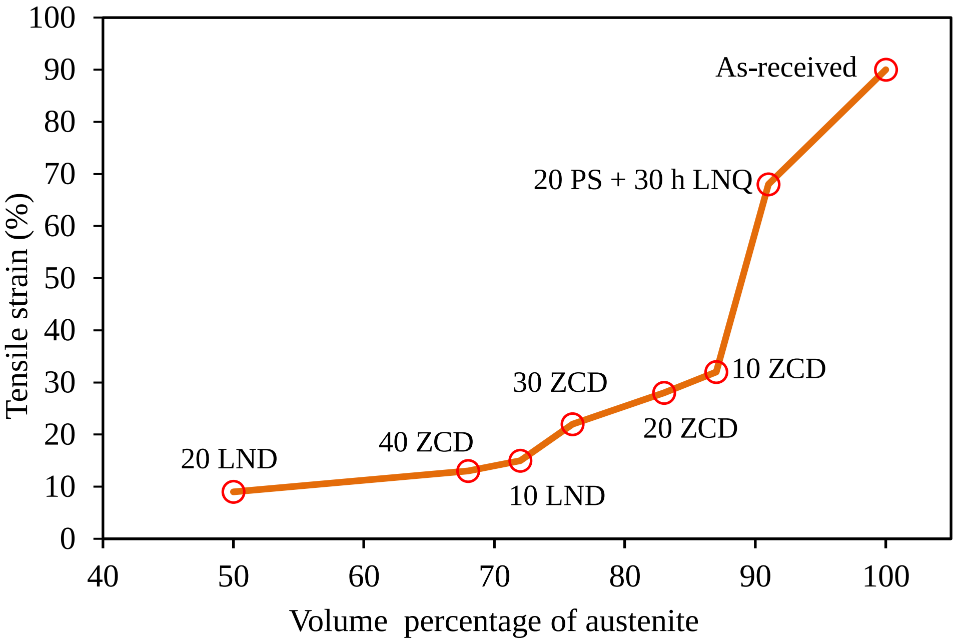

Figure 7.13: Variation in volume percentage of austenite and total elongation with respect to the various processing conditions as mentioned in Table 7.4.

Higher strength in 10% deformed specimen at -196°C than 40% deformed at 0°C is attributed to the ε-martensite formation at near cryogenic temperature in addition to the α′-martensite, which is less probable in the case of 40% deformation at 0°C. This ε-martensite transforms to α′-martensite at the higher deformation of 40%. Though the presence of ε-martensite is expected at low deformation amount of 10% at a lower temperature but the X-ray study does not reveal the prominent peak of ε-martensite at this temperature which may be due to the low penetration depth of X-ray and/or presence of a lower amount of ε-martensite. The interruption of dislocation movement by ε-martensite in 10% deformed specimen at -196°C leads to higher strength in this sample.

In summary, a high amount of martensitic phase constituents (α′ and ε) (50%) lead to maximum strengthening (1589 MPa) (more than two times higher than that of the as-received one) with a significant loss in ductility. The steels having a good percentage of strain-induced martensite (32%) and dislocation density (Figure 7.7) achieved at higher level of deformation (40%) at 0°C indicates brittle behaviour i.e., higher strength and lower ductility, due to nucleation of void or crack from the martensitic region leading to the early damage. On the other hand, a lower amount of martensite (9%) with a higher amount of austenite (91%) demonstrates higher strength with excellent ductility due to progressive strain induced transformation of martensite under the applied strain.

7.4 Summary

Analysis of the aforesaid results allows to summarise the following:

1. The present study has explored the genesis of different deformation induced features and their interactions in austenite, under the given amount of strain and temperature dependent SFE, leading to the strengthening and initiating the mechanical instability. Despite the absence of a quantitative understanding, the microstructural analyses have reliably demonstrated the contribution of the strain induced microstructural features to the encouraging tensile properties conducive to the high strength applications at sub-ambient (0°C) as well as cryogenic (-196°C) temperatures.
2. In the case of deformation at near cryogenic temperature (-196°C), extended stacking faults, ε-martensite (up to 6%) and α′-martensite (28% to 44%) are the dominant strain induced features as compared to the homogeneous dislocation structure along with some amount of α′-martensite (13% to 32%) formed in the case of deformation of austenite at 0°C. Such difference corresponds to the lowering of SFE from 19 mJ/m^2 at 0°C to 9 mJ/m^2 at -196°C.

3. Twins are found as the common strain induced feature in all the samples rolled at 0°C as well as -196°C. However, the formation of deformation twin is more favourable during deformation at 0°C due to the relatively higher value of SFE.
4. The presence of substantial amount of ε-martensite after 20% deformation at -196°C corroborates the overlapping of stacking faults and lower value of SFE of 9 mJ/m^2.
5. The presence of higher volume percentage of α′-martensite (44%) after 20% deformation at -196°C is attributed to the numerous nucleation sites formed at the locations of intersections among ε-martensite and shear bands. On the contrary, 20% deformation at 0°C leads to the formation of a lower amount of α′-martensite (17%) due to the paucity of nucleation sites.
6. 40% cold deformation at 0°C leads to the high strength (1225 MPa) with appreciable (13%) total elongation, whereas comparatively lower deformation (10-20%) at -196°C leads to higher level of strength (1306-1589 MPa) with 15-9% elongation due to the formation of higher volume fraction of strain induced martensite (ε/α′).

8

EFFECT OF AUSTENITE REVERSION ON THE MECHANICAL PROPERTIES OF CRYOGENICALLY DEFORMED STEEL

8.1 Introduction

The reversion annealing treatment of the cryogenically deformed steel is important from the viewpoint of controlling structures and improving mechanical properties. The process of reversion annealing is mainly a function of cold deformation and temperature-time annealing sequence where the loss in ductility during cryogenic or room temperature deformation could be brought back to get a favourable amount of strength-ductility combination [267]. During deformation at zero and cryogenic temperature, the structure generally contains strain induced martensite, twins, stacking faults and high dislocation density grains which result in an attractive tensile strength with low ductility in austenitic stainless steels having low stacking fault energy (SFE) [268]. On the other hand, the purpose of reversion annealing is to increase the ductility without significant loss in strength. The favourable amount of strength-ductility combination can be achieved by the reversion of strain induced martensite is an important way out [269].

After reversion annealing of stainless steel, the structure primarily consists of ultrafine-grained reverted austenite on the predominance of dislocation cell type structure with some amount of untransformed martensite [270]. Such microstructure has been found to play a significant role in altering the mechanical properties of 304 SS. Misra et al. [271] have reported that the transformation of lath type martensite to dislocation cell type martensite during deformation involves refinement of laths which causes high strength in austenitic stainless steel. However, the main difficulty in this deformation process is the loss of ductility. Many researchers [272, 273] have studied the reversion annealing process where severely deformed strain-induced martensite reverts back to austenite by diffusion or shear reversion mechanism which results in improvement in ductility. During reversion annealing process, the reversion of strain induced martensite (α′) to austenite (γ) not only depends on annealing time and temperature but also depends on the morphology of the martensite, dislocation density, different types of defects which acts as a nucleation site for the reverse transformation and may accelerate the transformation [271]. The volume fraction of the reverted austenite and the refinement of grains depend upon the volume fraction of α′ and the amount of deformation. According to Eskandari et al. [274] a decrease in the amount of saturation strain improves the process of grain refinement due to the more crushed martensite provided (martensite contains defects) and these crystal defects in the structure provide more nucleation sites for austenite transformation during reverse annealing.

Table 8.1: List of deformation processes followed by selected reversion annealing treatments.

% Deformation and temperature (°C)	Sample identification	Reversion annealing temperature (°C)	Reversion time (h)
40% at 0°C	40ZCD	300, 725	1
10% at -196°C	10LND	300, 725	
20% at -196°C	20LND	300, 725	
20% Pre-strain, 30 h holding at –196°C	20PS-30LNQ	725	

Significant works have been reported in the earlier literature [24, 275-277] where deformation has been done at room temperature followed by the reversion annealing of austenitic stainless steel. However, reports on cryogenic (-196°C) and low temperature (0°C) deformations of 304 SS are found to be limited in the literature [278-280]. Further, report on the reversion of cryogenic deformation in austenitic steel is also limited. Therefore, cryogenic and low temperature deformation followed by reversion annealing of 304 SS will strengthen the current understanding and provide future directions in obtaining preferred mechanical properties by manipulating the phases achieved after subsequent deformation. The study also helps to get desired properties of 304 SS, which can be of interest for futuristic application of present steel at low and cryogenic temperatures. An attempt has been made to understand and compare the deformed structure and reversion structure at various processing conditions along with the mechanism of reversion process and mechanical properties correlation with microstructure.

The deformed and pre-strained specimens were subjected to reversion annealing treatment in order to restore ductility in the deformed samples by the reversion of strain induced martensite to austenite. Different reversion schedules (300°C and 725°C, 1 h) were selected from Table 3.5 to understand the mechanism at different stages of reversion. The different reversion processes selected along with the concerned deformation schedule are furnished in Table 8.1.

8.2 *Tensile properties of processed samples*

Table 8.2: Mechanical properties of 304 SS samples under different processing condition.

Processing conditions	YS (MPa)	UTS (MPa)	TEL (%)	YS/UTS ratio
As-received (AR)	259±10	675±14	90±5	0.38
40% at 0°C (40ZCD)	936±20	1225±29	13±1	0.76
40ZCD + Rev 300°C-1h	955±21	1242±26	15±2	0.77
40ZCD + Rev 725°C-1h	617±14	858±15	37±3	0.72
10% at -196°C (10LND)	1061±12	1306±17	15±2	0.81
10LND + Rev 300°C-1h	827±9	1104±11	25±1	0.75
10LND + Rev 725°C-1h	628±13	929±7	45±2	0.68
20% at -196°C (20LND)	1463±16	1589±15	9±1	0.92
20LND + Rev 300°C-1h	1488±10	1676±14	8±3	0.88
20LND + Rev 725°C-1h	706±9	992±15	32±3	0.71
20PS-30LNQ	391±12	786±19	68±4	0.50
20PS-30LNQ + Rev 725°C-1h	401±11	753±18	72±2	0.53

The tensile results of the experimental steel samples processed under different conditions are summarised in Table 8.2 and the corresponding engineering stress versus strain curves are shown in Figures 8.1 and 8.2. In Figure 8.1(a), engineering stress-strain curves of 40ZCD, 10LND, 20LND and 20PS-30LNQ samples show a continuous yielding behaviour. 20PS-30LNQ sample exhibits maximum elongation, whereas 20LND sample is showing maximum tensile strength with the lowest elongation. However, after reversion annealing at 300°C for 1 h, the tensile strain of 10LND sample has been increased from 15% to 25% with the decrease in tensile strength. This is indicative of stress relief due to annealing at such low temperature.

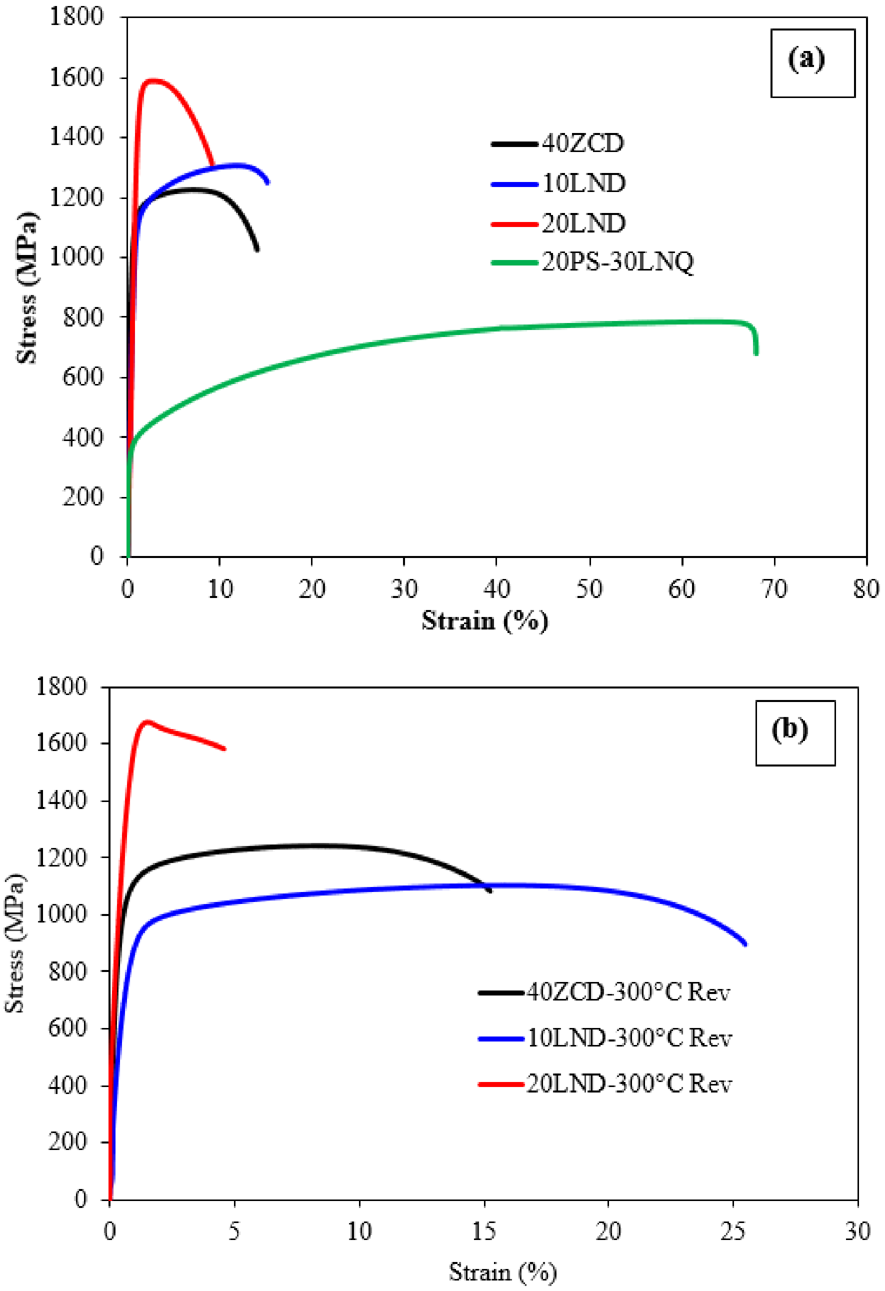

Figure 8.1: Engineering stress-strain curves of (a) 40ZCD, 10LND, 20LND, 20PS-30LNQ specimens and (b) 40ZCD, 10LND, 20LND followed by reversion annealing at 300°C for 1 h.

However, the tensile strength of 40ZCD and 20LND increase whereas the elongation value remains almost same or higher (Figure 8.1(b) and Table 8.2) indicating the advantage of reversion at 300°C. The increment in UTS may be attributed to the growth of strain induced martensite due to stress relief of the surrounding matrix [200]. However, the volume fraction of martensite decreases after annealing at 300°C. The observation allows to conjecture that the tetragonality (c/a ratio) of martensite is increased due to stress relief. In this context, it is important to note that formation of fine austenite grains takes place through shear reversion [201]. The combined effect increases the strength-ductility values of 20LND and 40 ZCD samples after annealing at 300°C for 1 h.

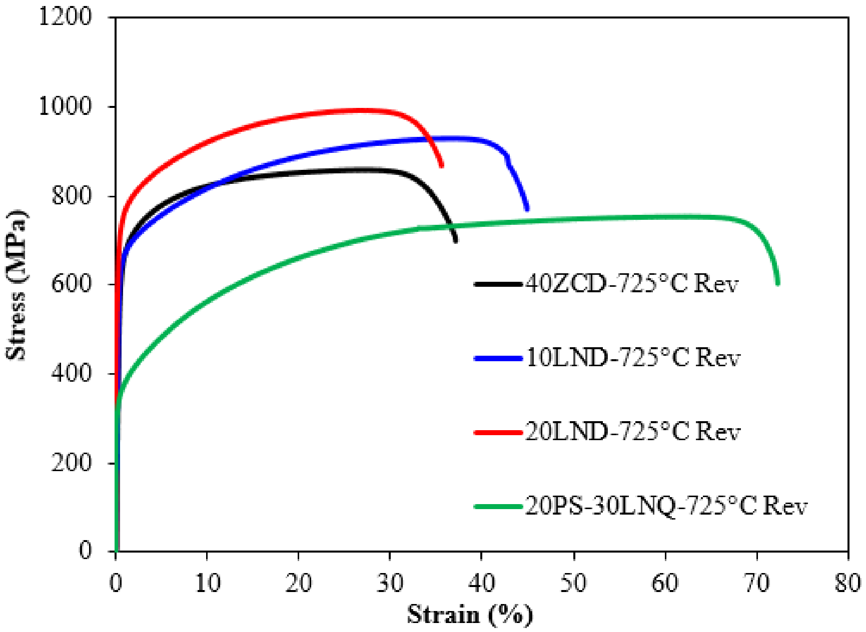

Figure 8.2: Engineering stress-strain curves of 40ZCD, 10LND, 20LND and 20PS-30LNQ specimens followed by reversion annealing at 725°C for 1 h.

After annealing at 725°C for 1 h, all the samples exhibit an increase in elongation with the decrease in tensile strength (Figure 8.2 and Table 8.2). Among the samples annealed at 725°C, the 20PS-30LNQ sample reveals maximum elongation value of 72% along with the tensile strength of 753 MPa, which is found to be higher than that of as-received samples (675 MPa). Reversion of 20LND sample at 725°C, shows the UTS of 992 MPa and 32% total elongation which are corroborated with the resultant effect of recrystallisation and reversion of α′→ γ along with the presence of residue of cryogenic deformation like strain induced martensite, deformation twins, dislocations etc. [281].

Steel samples deformed at -196°C were also subjected to reversion annealing treatment at 500°C for 1 h and tensile test was carried out to measure the YS, UTS and %TEL values and the results are shown in the following Table 8.3.

Table 8.3: Mechanical properties of 304 SS samples after reversion at 500°C for 1 h.

Processing conditions	YS (MPa)	UTS (MPa)	TEL (%)	YS/UTS ratio
10% deformed at -196°C	707±8	924±8	30±3	0.77
20% deformed at -196°C	901±10	1096±12	19±2	0.82

The strength value drops significantly after reversion annealing at 500°C than the deformed sample. However, the %TEL increment for 20% deformed sample was not significant enough. The combinations of strength and ductility achieved after reversion annealing at 500°C are within those values obtained for other two annealing temperatures (300°C and 725°C) discussed earlier in this chapter.

8.3 X-ray diffraction analysis

The constituent phases in the samples after different processing conditions are identified by X-ray diffraction study and the estimated volume fractions are calculated from the respective X-ray profiles by carrying out the Rietveld analysis. Figure 8.3(a) reveals the X-ray diffraction profiles of 40ZCD, 10LND, 20LND and 20PS-30LNQ samples, where the presence of α′-martensite along with the untransformed austenite has been achieved in all the samples. The (101) peak of ε-martensite in the 20LND sample appears with a very low intensity, which is in resemblance to the results published earlier [243]. Other peaks of ε-martensite are not perceptible in the pattern either due to the low penetration depth of X-ray and/or presence of a lower amount of ε-martensite. The diffraction patterns of the sample annealed at 300°C after deformation, as shown in Figure 8.3(b), reveals (110), (200) and (211) peaks related to the body centred cubic (BCC) α′-

martensite phase, in addition with (111), (200), (220), (311) and (222) austenite peaks. However, the XRD pattern does not reveal any other phases in these samples. It is imperative to mention here that decrease in the peak intensity of strain induced martensite is the result of reversion from α′ to γ [282].

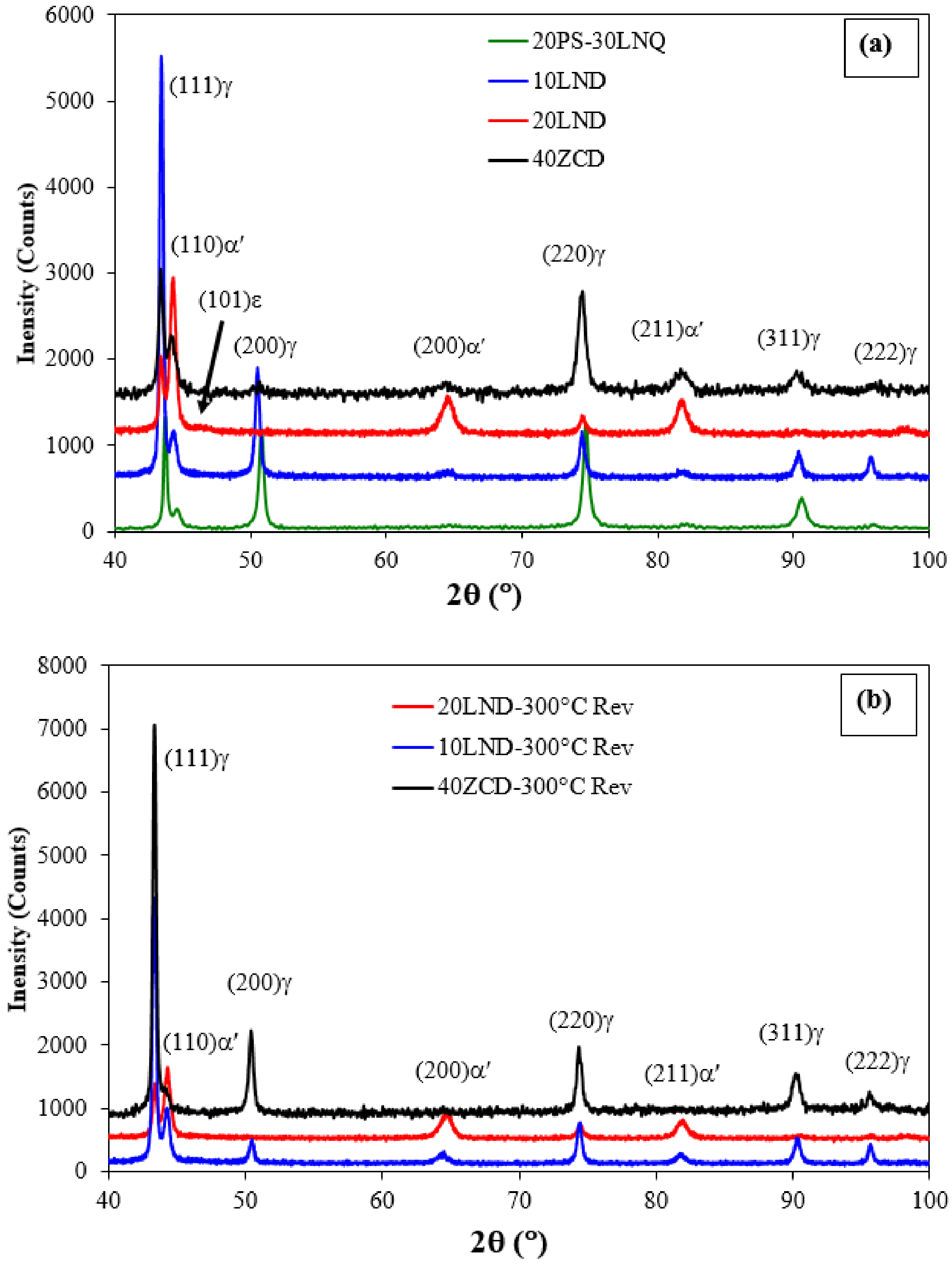

Figure 8.3: X-ray diffraction patterns of (a) 40ZCD, 10LND, 20LND, 20PS-30LNQ specimens and (b) 40ZCD, 10LND, 20LND specimens followed by reversion annealing at 300°C for 1 h.

Figure 8.4 shows the X-ray diffraction profiles of 40ZCD, 10LND, 20LND and 20PS-30LNQ samples subjected to reversion annealing at 725°C for 1 h. A comparison of Figure 7.3(b) with Figure 8.4 indicates that the austenite peaks have gained higher intensities, whereas α′ peaks reveal lower intensities indicating increased reversion of α′-martensite. The X-ray diffraction results allow to estimate the corresponding volume fraction of α′-martensite as 32%, 28%, 44% and 9% (obtained by Rietveld analysis) for 40ZCD, 10LND, 20LND and 20PS-30LNQ samples, respectively, as shown in Table 8.4. Similarly, the volume fractions of the reverted austenite have been estimated from X-ray analysis as 91%, 89%, 85% and 95% after reversion at 725°C (Table 8.4) of 40ZCD, 10LND, 20LND and 20PS-30LNQ samples, respectively.

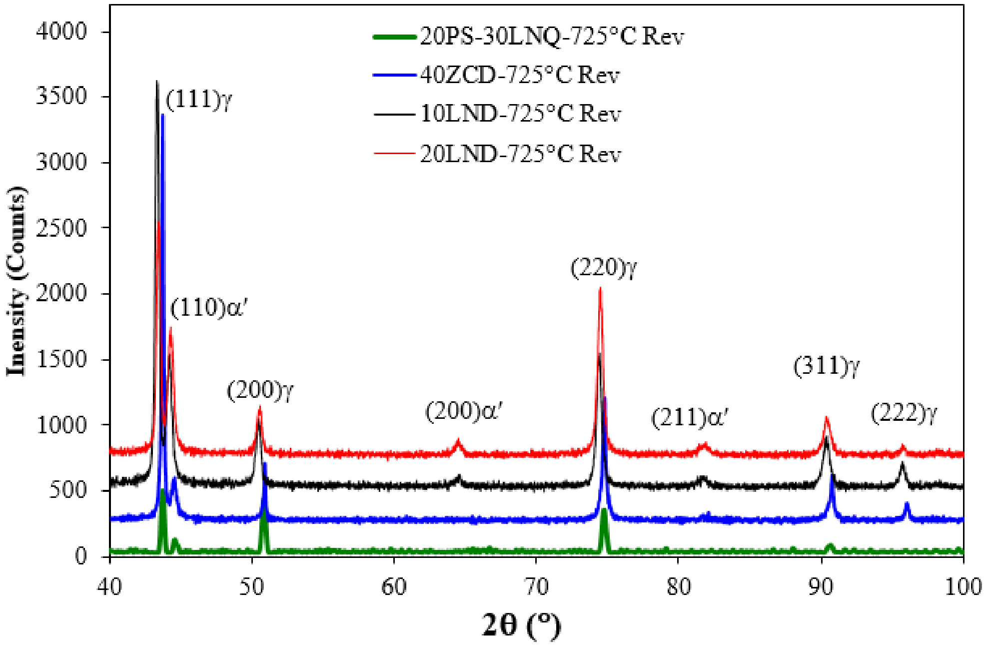

Figure 8.4: X-ray diffraction patterns of 40 ZCD, 10 LND, 20 LND and 20PS-30LNQ specimens followed by reversion annealing at 725°C for 1 h.

8.4 *Characterisation of microstructure*

Figures 8.5(a) to (d) show the optical, SEM and TEM microstructures of as-received hot rolled and solution treated 304 SS samples. The fully austenitic structure with the signature of annealing twins is evident in these microstructures. Figures 8.5(a) and (b) show the polygonal austenite grains with a grain size of about 20-30 μm.

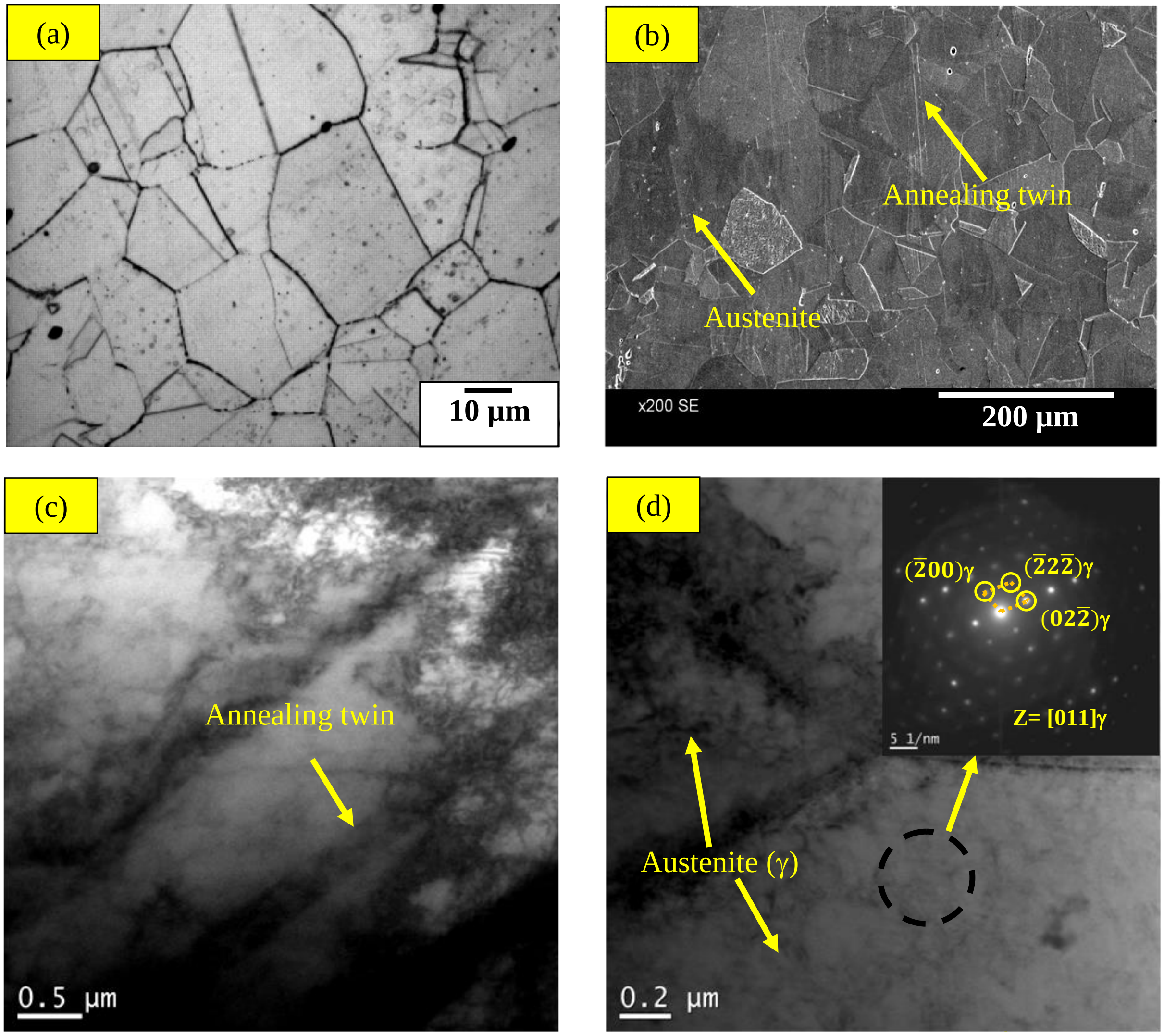

Figure 8.5: (a) Optical micrograph, (b) SEM micrograph, (c) & (d) TEM bright field micrographs of as-received 304 austenitic stainless steel specimen.

The presence of annealing twins which are blocked by the grain boundaries is in good agreement with the earlier results on the 304 SS [244]. TEM micrographs as shown in Figures 8.5(c) and (d) depict the presence of annealing twins with dislocated austenitic structure. Figure 8.5(d) shows a triple point of austenite grains in the hot rolled and solution treated 304 SS sample. The inset in Figure 8.5(d) shows the analysis of SAED taken from the circular area marked in this figure which evidences the austenite phase.

Table 8.4: Measured volume percentage of constituent phases (obtained by Rietveld analysis).

Initial processing condition	Volume measurements (in %)		Annealing temperature and duration	Volume measurements (in %)	
	After deformation			After reversion	
	FCC (γ)	BCC (α′)		FCC (γ)	BCC (α′)
40% deformation at 0°C	68±2	32±1	300°C, 1h	71±2	29±1
			725°C, 1h	91±2	9±1
10% deformation at -196°C	72±2	28±1	300°C, 1h	76±2	24±1
			725°C, 1h	89±2	11±1
20% deformation at -196°C	50±2	44±1(+6±1ε -Martensite)	300°C, 1h	59±2	41±1
			725°C, 1h	85±2	15±1
20% pre-strain at room temperature followed by quenching at -196°C for 30 h	91±2	9±1	725°C, 1h	95±2	5±1

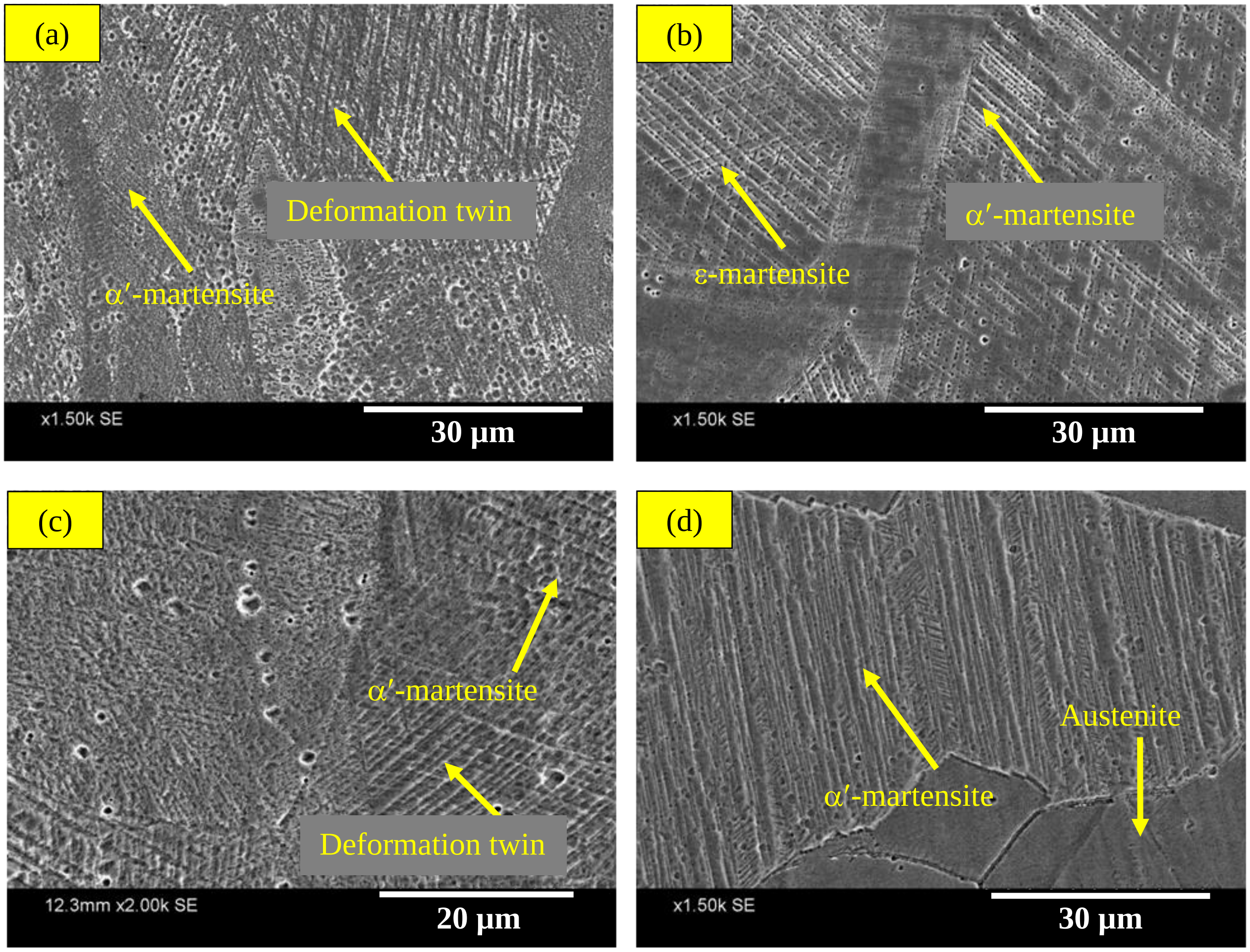

Figure 8.6: SEM micrographs of (a) 40ZCD, (b) 10LND, (c) 20LND and (d) 20PS-30LNQ samples.

The SEM micrographs of 40ZCD, 10LND, 20LND and 20PS-30LNQ samples are shown in Figures 8.6(a) to (d), respectively. Figures 8.7(a) to (c) show the SEM micrographs of 40ZCD, 10LND and 20LND samples followed by reversion annealing at 300°C for 1 h. At this reversion temperature, the onset of the reversion structures is evidenced in Figures 8.7(a) and (c), where some amount of reverted austenite grains are visible. The deformation induced martensite and deformation twins are still present in these microstructures. Such microstructural features are also consistent with the earlier report [283].

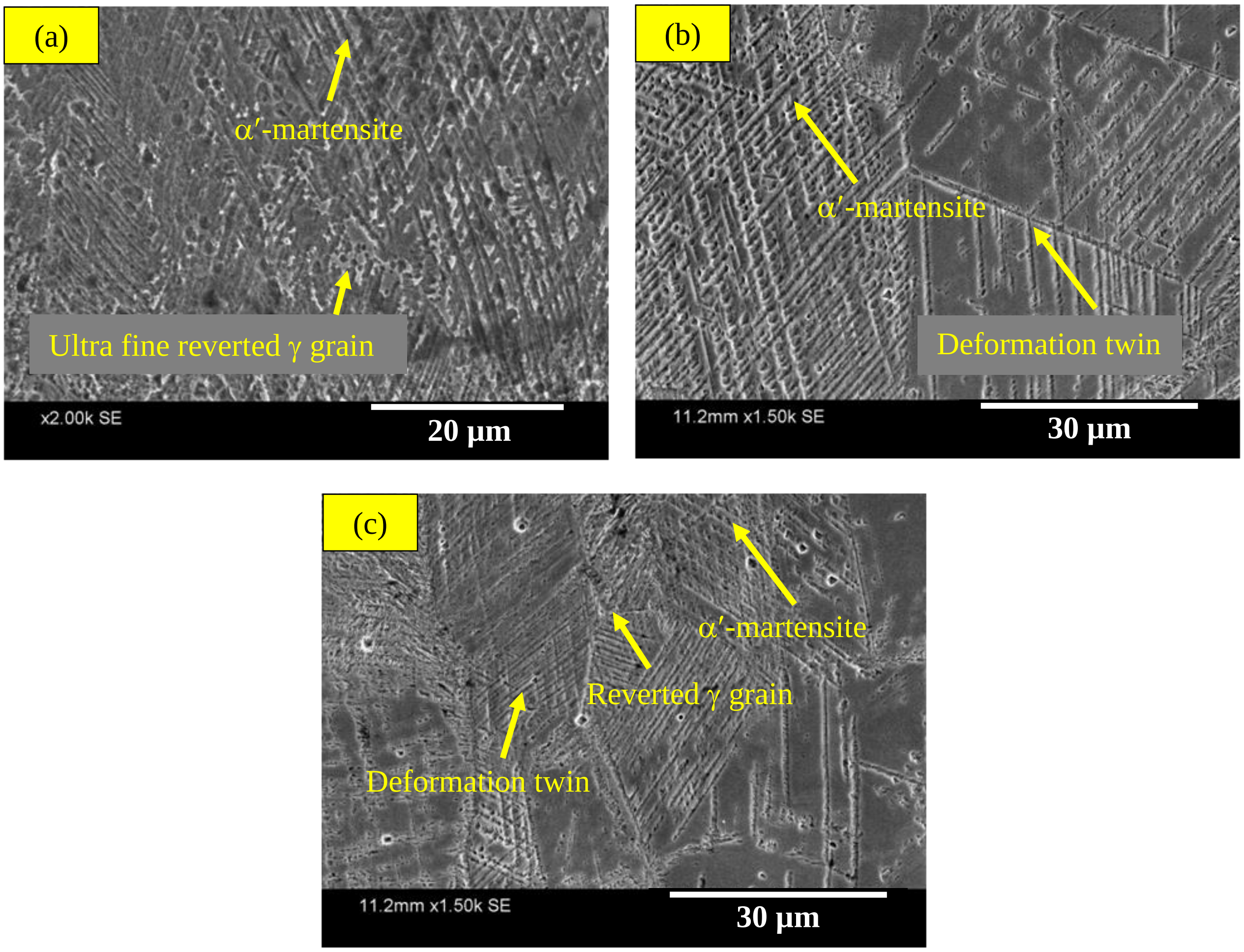

Figure 8.7: SEM micrographs of (a) 40ZCD, (b) 10LND and (c) 20LND samples followed by reversion annealing at 300°C for 1 h.

Figures 8.8(a) to (d) reveal the SEM micrographs of 40ZCD, 10LND, 20LND and 20PS-30LNQ samples followed by reversion annealing at 725°C for 1 h. These microstructures primarily reveal the reverted austenite grains and recrystallised fine grains with the presence of untransformed α′-martensite. The reduction in the amount of strain induced martensite is in good agreement with the reversion process reported earlier for X-ray diffraction analyses.

Figures 8.9 to 8.12 show the TEM images of 40ZCD, 10LND, 20LND and 20PS-30LNQ samples and the corresponding reversion structure after annealing for 1 h. The micrograph of 40% cold rolled at 0°C, as shown in Figure 8.9(a), shows highly dislocated grain with strain induced martensite (α′). Whereas, 10% and 20% samples (10LND and 20LND) deformed at -196°C reveal deformation twin and α′-martensite. The 20LND sample shows the presence of ε-martensite. The presence of deformation twins is as expected in the present steel with low SFE. In the case of deformation at -196°C, it is evident that the 20% deformed sample (Figure 8.9(c)) exhibits a higher amount of α′-martensite than the 10% deformed sample.

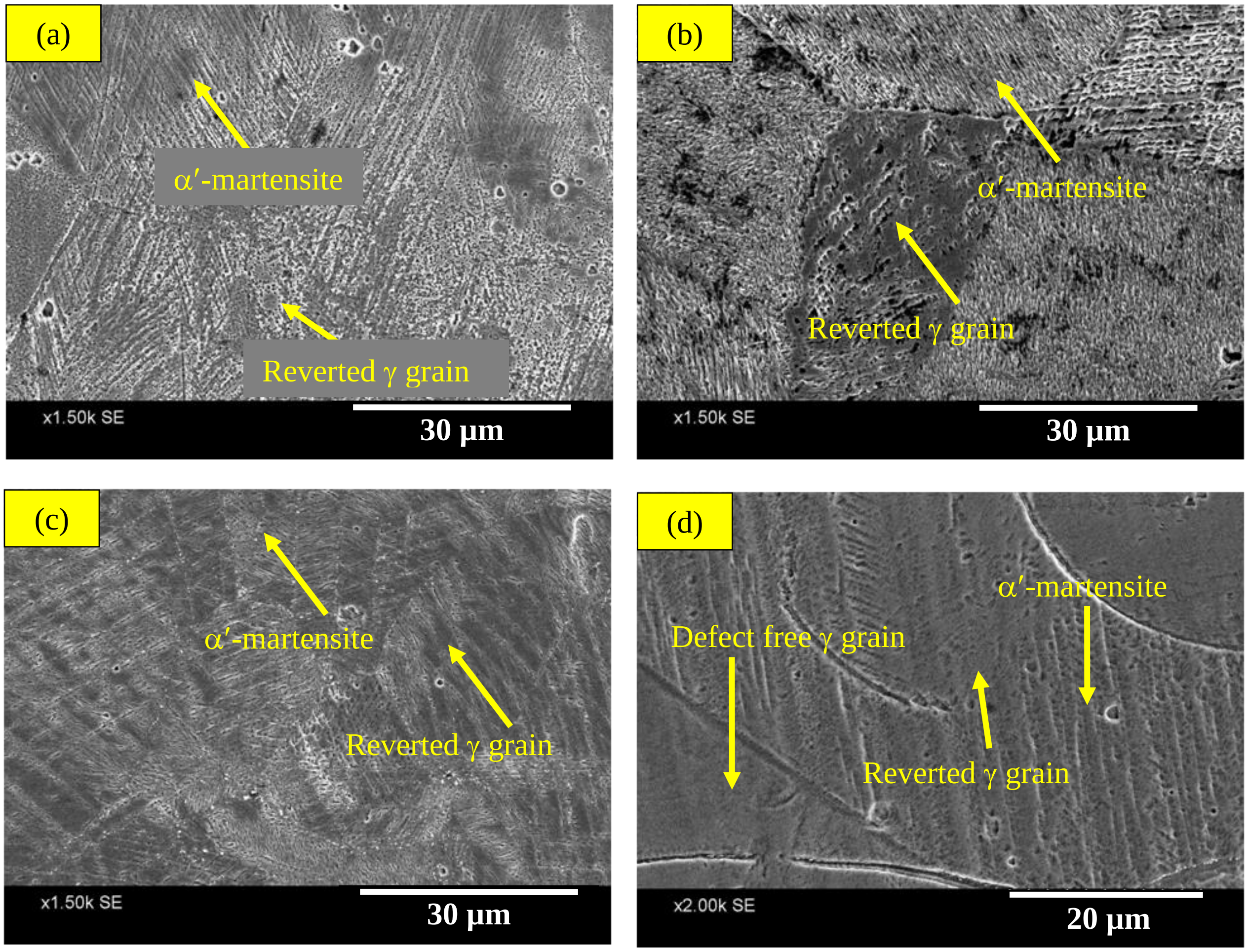

Figure 8.8: SEM micrographs of (a) 40ZCD, (b) 10LND, (c) 20LND and (d) 20PS-30LNQ samples followed by reversion annealing at 725°C for 1 h.

It is evident that cluster of the α′-martensite laths are observed in one particular orientation which is generally termed as martensite packet (Figures 8.9(b) and (c)). With the increase in percentage cold deformation, the lath size decreases with the formation of dislocated laths as is seen in Figures 8.9(a) and (c). With deformation at low temperature, the crystallographic distortion occurs and it leads to the formation of the shear band. Such shear bands act as the potential nucleation site for α′-martensite formation [257]. Further increase in deformation promotes the transformation of martensite morphology from lath-type to dislocation cell type [271]. 20PS-30LNQ samples show a significant amount of stacking faults (SFs) and deformation twins along with the reduced amount of α′-martensite (Figure 8.9(d)) compared to the deformed samples.

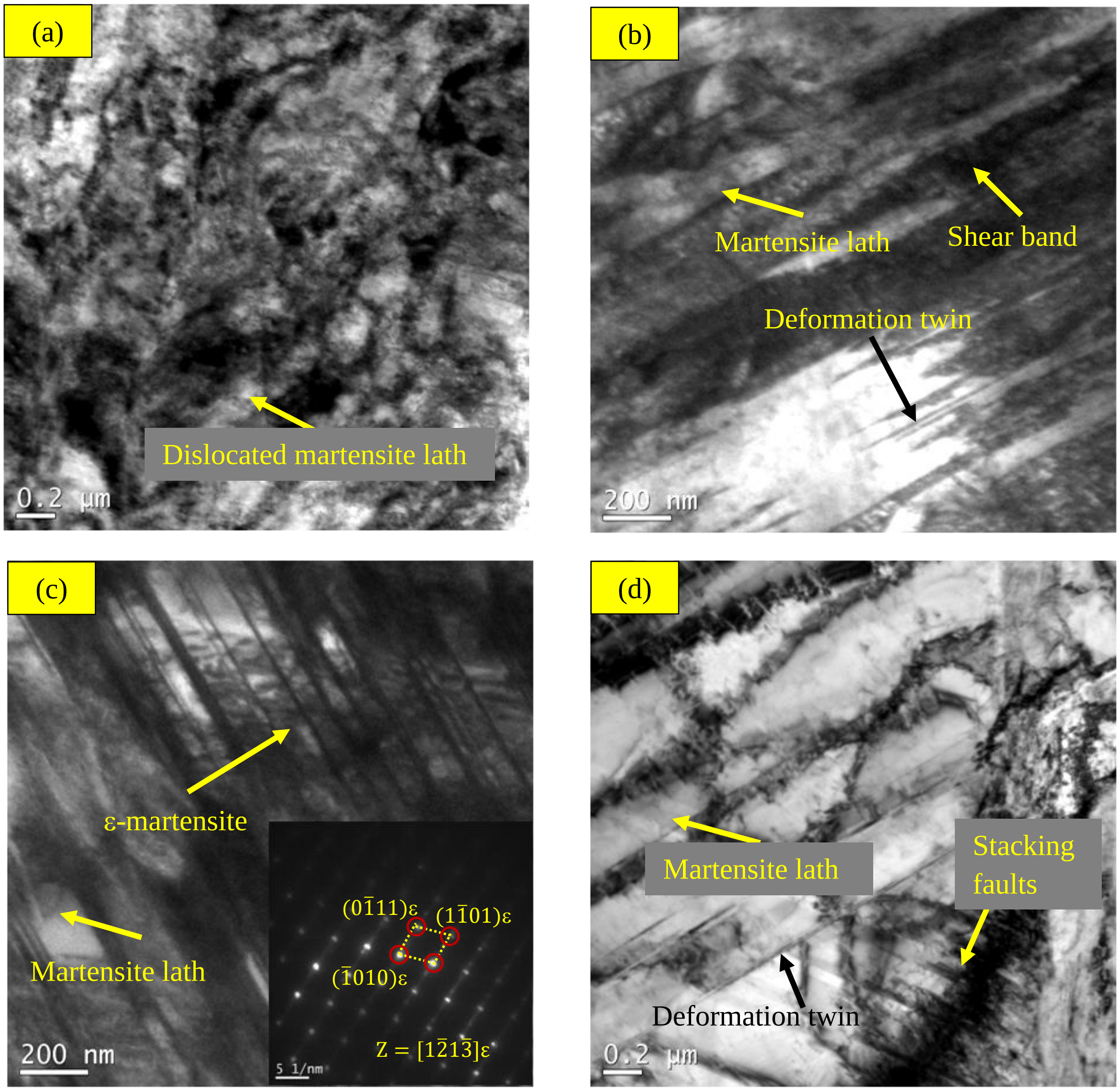

Figure 8.9: TEM bright field micrographs of (a) 40ZCD, (b) 10LND, (c) 20LND and (d) 20PS-30LNQ samples.

Figures 8.10(a) and (b) reveal the dislocation cell structures in a 40ZCD specimen subjected to reversion at 300°C. The deformation twins and α′-martensite are still present in the microstructure after reversion at low temperature. SAED image of the sample is presented as the inset of Figure 8.10(b) as the confirmation of the presence of twin. The reverted austenite grains are not clearly visible in these microstructures. However, precipitate, annealing twins and reverted austenite are evident in Figures 8.10(c) and (d) after reversion of 40ZCD samples at 725°C for 1 h. The signature of α′-martensite is also observed in these microstructures.

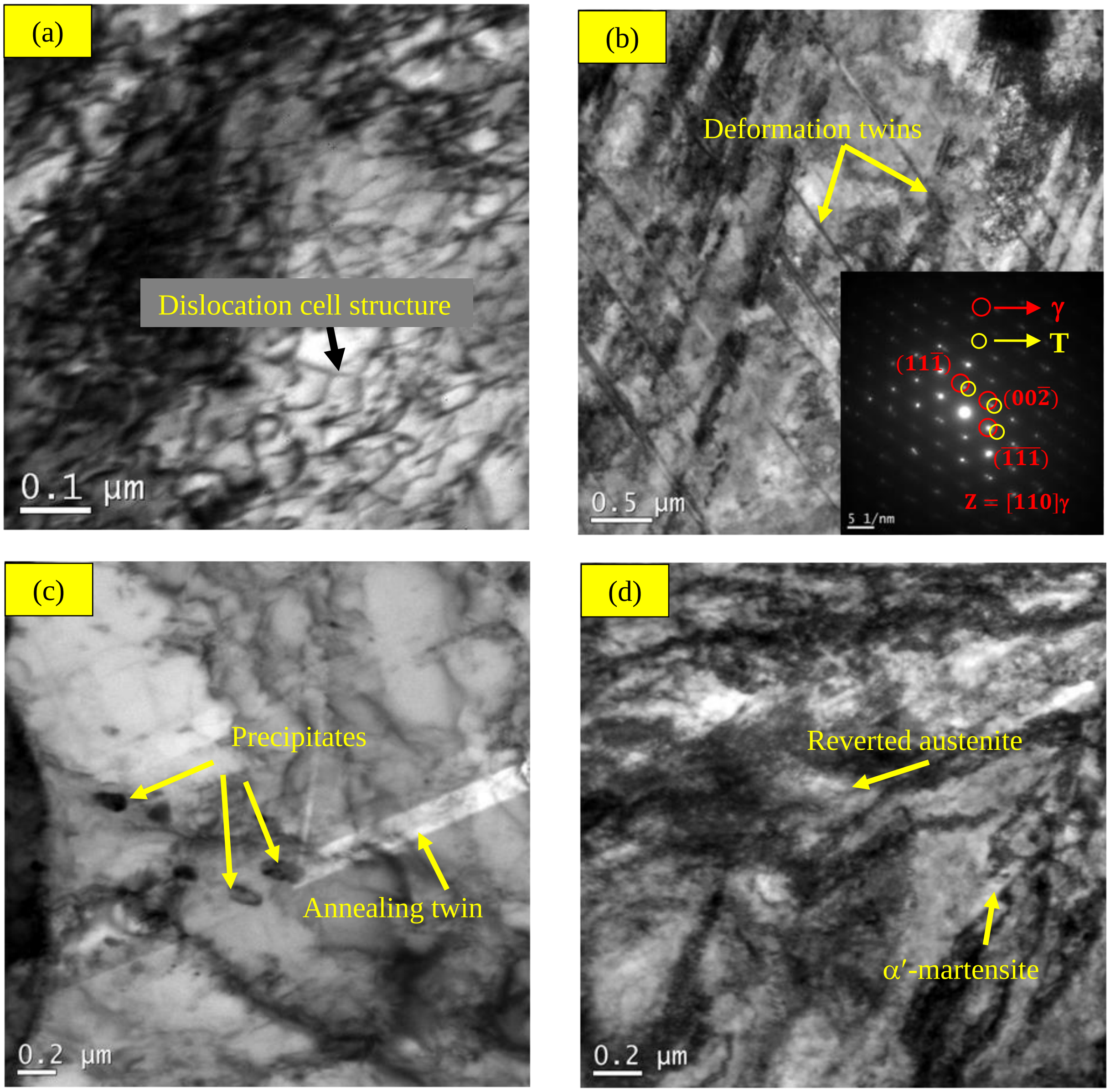

Figure 8.10: TEM micrograph of 40% cold deformed steel specimens at 0°C (a) and (b) after reversion at 300°C and (c) and (d) after reversion at 725°C for the duration of 1 h. Inset in (b) is showing twin spots in austenite.

Figures 8.11(a) and (b) reveal the lath structure of α′-martensite, deformation twins and SFs in the 10LND specimen subjected to deformation followed by reversion at 300°C. Retained austenite of bright contrast at the interlath position of α′-martensite is evident in a dark field image shown in the inset of Figure 8.11(a).

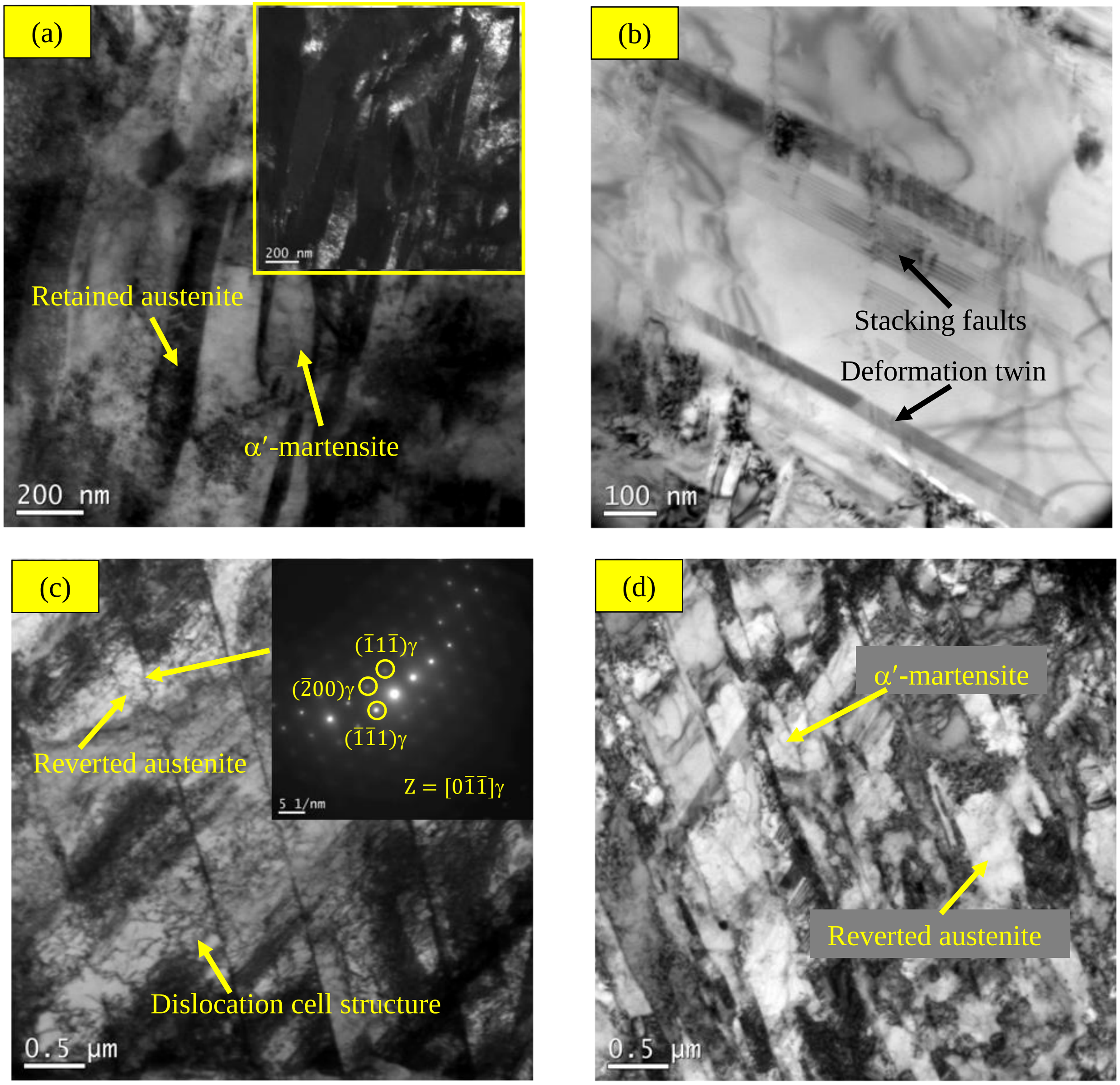

Figure 8.11: TEM micrograph of 10% cold deformed steel specimens at -196°C (a) and (b) after reversion at 300°C and (c) and (d) after reversion at 725°C for 1 h.

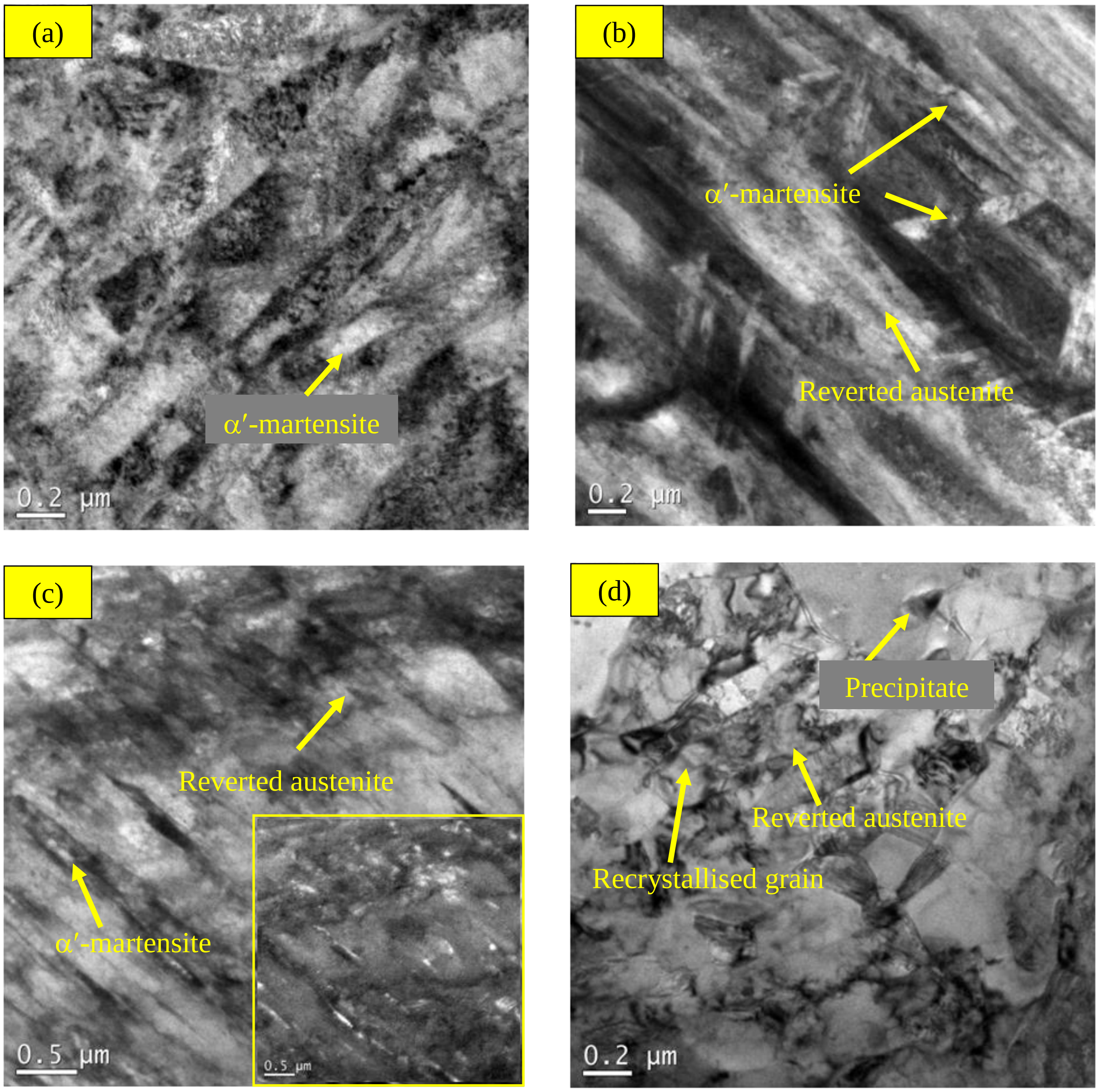

Figure 8.12: TEM micrograph of 20% cold deformed steel specimens at -196°C (a) and (b) after reversion at 300°C and (c) and (d) after reversion at 725°C for 1 h.

The greater amount of reverted austenite is evident in Figures 8.11(c) and (d) after reversion of 10LND samples at 725°C for 1 h than that of 300°C (Figure 8.11(a)). The SAED and its analysis are shown in the inset of Figure 8.11(c) those confirm the presence of reverted austenite. The signature of α′-martensite is also observed in these microstructures. It is relevant to mention here that the structure of martensite is clearly lath type after conducting cryogenic rolling (Figures

8.9(b) and (c)), whereas the blocky type martensites are known as the potential nucleation site for reversion to austenite [284]. It implicates that most of the blocky α′-martensite has been reverted to austenite after annealing at 725°C for a prolonged duration of 1 h and forms a lamellar structure of reverted austenite as evident in Figure 8.11(d).

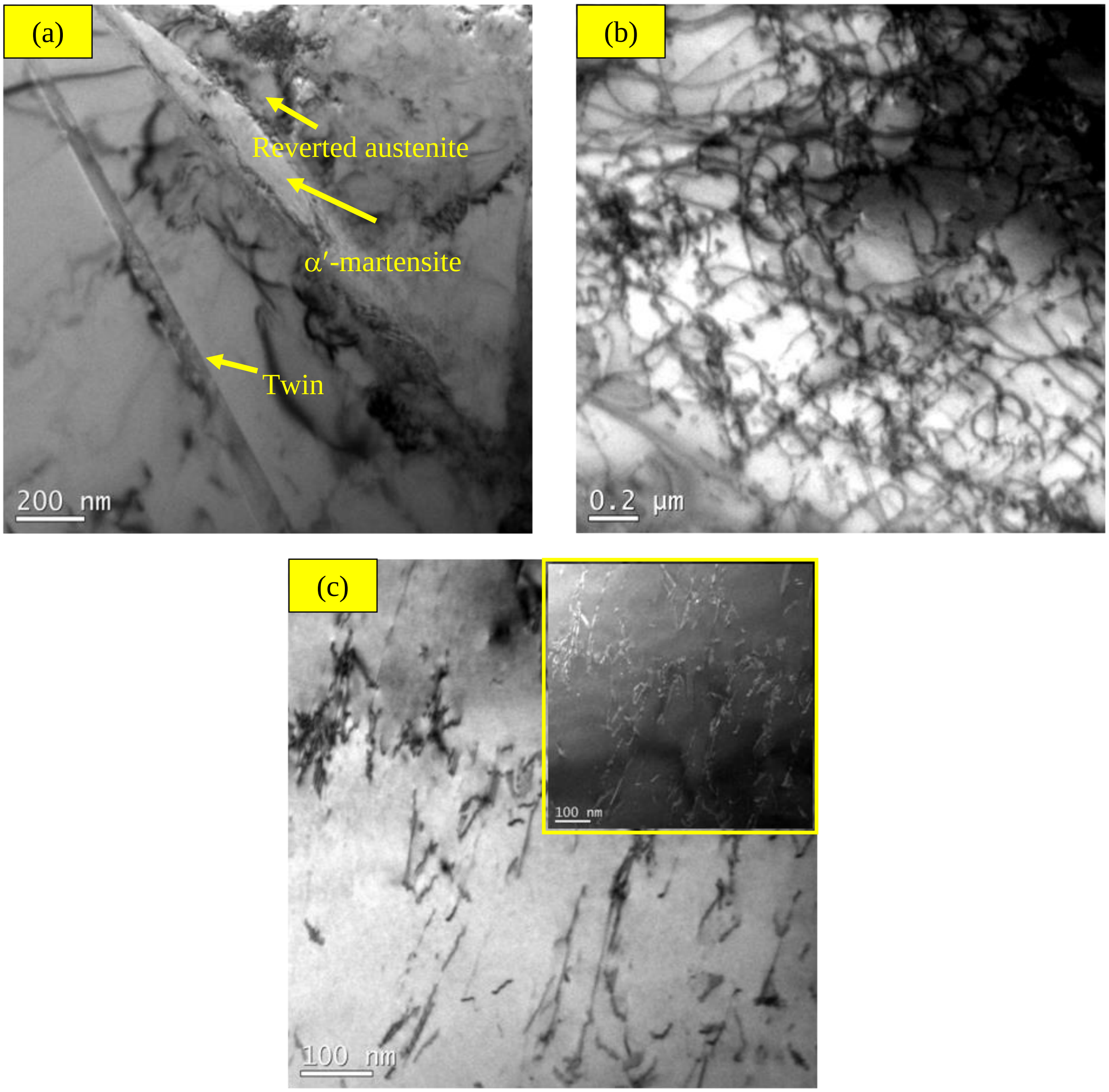

Figure 8.13: (a)-(c) TEM micrographs of 20PS-30LNQ samples followed by reversion annealing at 725°C for 1 h.

Figures 8.12(a) and (b) reveal the lath structure of α′-martensite in 20LND specimen subjected to reversion at 300°C. A few reverted austenite grains are observed in these microstructures. On the other hand, a greater amount of reverted austenite, precipitate and recrystallised austenite grains are evident in Figures 8.12(c) and (d), respectively, after reversion at 725°C for 1 h. The signature of α′-martensite is also observed in this microstructure. Dark field image in the inset of Figure 8.12(c) is helpful to distinguish the reverted austenite structure. However, it may be noted that some deformation induced martensite also coexist with the reverted grains of austenite.

Figures 8.13(a) and (b) reveal the lath structure of α′-martensite and reverted austenite in 20PS-30LNQ specimen subjected to reversion at 725°C for 1 h. The signature of α′-martensite is also observed in these microstructures. Figure 8.13(b) reveals the characteristic feature of dislocation substructures, where dislocations are denser and tangled which is indicative of planar structures and three-dimensional arrangements. Dark field image at the inset of Figure 8.13(c) reveals dislocation nodes indicating that significant recovery has taken place.

8.5 Mechanism of $\alpha' \rightarrow \gamma$ reversion

In the present study, commercially pure 304 stainless steel has been cold rolled at 0°C and cryogenic (-196°C) temperatures with different amount of thickness reduction. Subsequently, the samples were subjected to reversion annealing with an aim to improve the mechanical properties. The deformed structure generally consists of strain-induced martensite (α′), ε-martensite, deformation twin, stacking faults and dislocation-cell type structure along with the retained austenite. Upon annealing, this deformed martensite reverts to austenite through a martensitic shear or diffusional reversion mechanism depending on the chemical composition of the steel.

The reverse transformation from α′ to γ is beneficial for achieving a favourable strength-ductility combination by utilising the plasticity of the defect containing reverted austenite, defect free fine grain and untransformed martensite [182]. Grain refinement is also achieved by the reversion mechanism and thereby influences the mechanical properties of the steel [285]. Earlier, results [24, 45, 166, 286, 287] have shown that the reversion can happen by two mechanisms; one is shear transformation and the other one is the diffusion controlled transformation. Shear transformation during reversion, generally reveals fine γ grains and high dislocation structure through recovery and recrystallisation [288]. Whereas, diffusionally reversed γ is differentiated by the nucleation of equiaxed austenite grains within the α' matrix and such γ grains gradually grow during annealing [164]. It is evident that the reversion mechanism significantly depends on the chemical composition of the steel and also the heating rate of the steel [164]. Transformation of α' to γ occurs through the movements of the α'/γ interfaces and the formation of reverted austenite while keeping the orientation same. The $\alpha' \rightarrow \gamma$ transformation happens through the formation of twinned γ and with the improved recovery process produces the sub-grain structure. To understand the transformation kinetics of $\alpha' \rightarrow \gamma$, the thermodynamic data reported earlier [24, 282, 289] have been used for the ternary Fe-Cr-Ni system steels. Thus, free energy changes during $\alpha' \rightarrow \gamma$ transformation in Fe-Cr-Ni system steels are calculated from the equation below [284]:

$$\Delta G^{\alpha' \rightarrow \gamma}\ (\mathrm{J/mol}) = 10^{-2}\, \Delta G_{Fe}^{\alpha' \rightarrow \gamma}\,(100 - Cr - Ni) - 97.\,5Cr + 2.02\, Cr^2 - 108.8\, Ni + 0.52\, Ni^2 - 0.05CrNi + 10^{-3}\, T\,(73.3Cr - 0.67Cr^2 + 50.2Ni - 0.84Ni^2 - 1.51CrNi) \qquad (8.1)$$

Where T is the selected temperature (in K) and Ni and Cr correspond to the chemical compositions of each element (mass %). $\Delta G_{Fe}^{\alpha' \rightarrow \gamma}$ is the difference in free energy change during $\alpha' \rightarrow \gamma$ transformation in pure iron. The calculated values of $\Delta G^{\alpha' \rightarrow \gamma}$ at 300°C and 725°C are + 555 J/mol and -372 J/mol. respectively. Therefore, at 300°C the reversion is imperceptible, whereas at 725°C reversion can occur significantly. In this context, it is important to note that, when free energy is negative, γ is more stable than α'-martensite. Now the related mechanism of reversion can be inferred from the above thermodynamical approach as well as a microstructural observation as enumerated below.

For a shear (martensitic) transformation of α'-martensite, a certain driving force is required. Tomimura et al. [24] have reported that for a16Cr-10Ni steel, the lowest temperature where deformation induced α' can completely revert to γ through shear transformation is 650°C and the calculated $\Delta G^{\alpha' \rightarrow \gamma}$ at that temperature is about -500 J/mol. In another word, the minimum driving force required for the complete reversion process is 500 J/mol [284]. Earlier [24, 284] results show that this value is constant and independent of Cr, Ni content in Cr-Ni steels. Tomimura et al. [24] have also reported that when the value of $\Delta G^{\alpha' \rightarrow \gamma}$is less than -500 J/mol, the martensitic shear reversion may take place spontaneously. However, in the present study, the value of -372 J/mol is higher than the constant value of -500 J/mol. Therefore, the theoretically shear transformation is not spontaneous here. The shear transformation of α' is also possible during heating to the annealing temperature at a rate of 10°C/s, which has not been followed here. Therefore, under the present schedule, the diffusional transformation plays a dominant role other than the shear mode of transformation during the reversion process. In Fe-Cr-Ni steels, where the Cr content is higher and Ni content is lower, it is expected that the martensitic shear reversion is difficult to occur as the free energy change will be relatively higher than the value of -500 J/mol. It is noteworthy that driving force for the martensitic shear reversion to γ is influenced by the chemical composition and temperature of the steel, and it is barely affected by the stored energy.

In the shear reversion process, the microstructure generally contains high dislocation density lath type deformed austenite, which can be subdivided into sub-grains or dislocation cells by the recovery process [24, 290]. The reverted austenite through diffusion reversion process is differentiated by the equiaxed γ grains within the α'-martensite matrix and such newly formed γ grains may grow with the increase of annealing time by consuming the remaining martensite [291]. If the reversion annealing is done for a prolonged period, the growth of the newly formed equiaxed austenite grains occurs, which results in low dislocation density austenite grains.

In Figures 8.10(a) to (b), 8.11(a) and 8.12(a) to (b), the microstructures contain primarily dislocation cell structures, high dislocation density, reverted lath type austenite and α'-martensite in the case of 40ZCD, 10LND, and 20LND samples subjected to reversion at 300°C, respectively. Such microstructures can form during shear reversion, and it is also important to note here that formation of reverted austenite by shear mechanism is limited at low temperature. X-ray diffraction patterns also substantiate the results, where the amount of reverted austenite is very low at the level of 3-4%. On the other hand, after annealing at a higher temperature (725°C), the microstructures inherit low dislocation density and evolve fine grained austenite where some of the equiaxed austenite grains are surrounded by the remaining untransformed α'-martensite. Therefore, it can be concluded that during reversion at the aforesaid temperatures, the strain induced martensite has transformed to austenite through both shear and diffusional processes. However, the dominating mechanism of reversion is diffusional in nature mainly at a higher temperature.

8.6 Microstructure and mechanical properties correlation

Microstructure evolved after deformation at low temperatures, primarily consists of ε- and α′-martensite along with the untransformed austenite containing defects like deformation twin, SFs, dislocation etc. Evolution of such microstructural features in austenitic stainless steel is strongly governed by the temperature dependent SFE value [129]. In the course of deformation of the present steels during rolling at low (0°C) and cryogenic temperature (-196°C) formation, accumulation and interaction of defects like dislocations, twins, and stacking faults promote the martensitic transformation as the combined effect of SFE, temperature and strain. Deformation twin can form when the stacking fault energy (SFE) of steel lies in the range of 20-40 mJ/m^2. When the SFE value is <20 mJ/m^2, the martensitic transformation is favoured [292]. At -196°C and 0°C, the SFE are ~9 and ~19 mJ/m^2, respectively, where the formation of deformation twin and α′-martensite are favoured. It is noteworthy that at -196°C, the SFE is very low and SFs are formed extensively as the precursor of the deformation twins. 20LND sample shows the maximum tensile strength of 1589 MPa with 9% elongation upon formation of strain induced martensite and deformation twins to the maximum extent. However, the 40ZCD sample reveals 1225 MPa tensile strength and 13% elongation. In 20PS-30LNQ sample, pre-strain has been applied to introduce high dislocation density and slip bands which promotes the reversion process. The 20PS-30LNQ sample has yielded a combination of 786 MPa tensile strength, with 68% of total elongation, which is more attractive for high strength applications as compared to that of as-received samples (675 MPa and 90%).

Reversion at low temperature (300°C) is carried out to reduce the residual stress stored during deformation which helps in recovering the ductility that had been lost after deformation at low temperature. Reversion at 300°C, results in the formation of reverted austenite as low as 3-4%, which is presumably due to the shear mechanism. However, the tensile strength values in 20LND and 40ZCD samples have increased and ductility values are found almost same after reversion at 300°C for 1 h. The increased strength is corroborated by the stress relieving and increase of the martensite tetragonality after reversion, as well as the formation of fine, reverted austenite through shear transformation mechanism at this low temperature. On the other hand, the tensile strength is decreased and elongation is increased for 10LND samples after reversion at 300°C. After reversion at 725°C for 1 h, reverted austenite appears mostly as recovered sub-grain structure or in combination with new defect-free recrystallised austenite grains. The HRTEM micrograph in Figure 8.12(d) also reveals that defect-free nano austenite grains (< 100 nm) which are surrounded by reverted austenite grains. Tensile strength has been found to decrease for all the samples, however, the ductility increases, which is due to the presence of strain free reverted austenite grains [293].

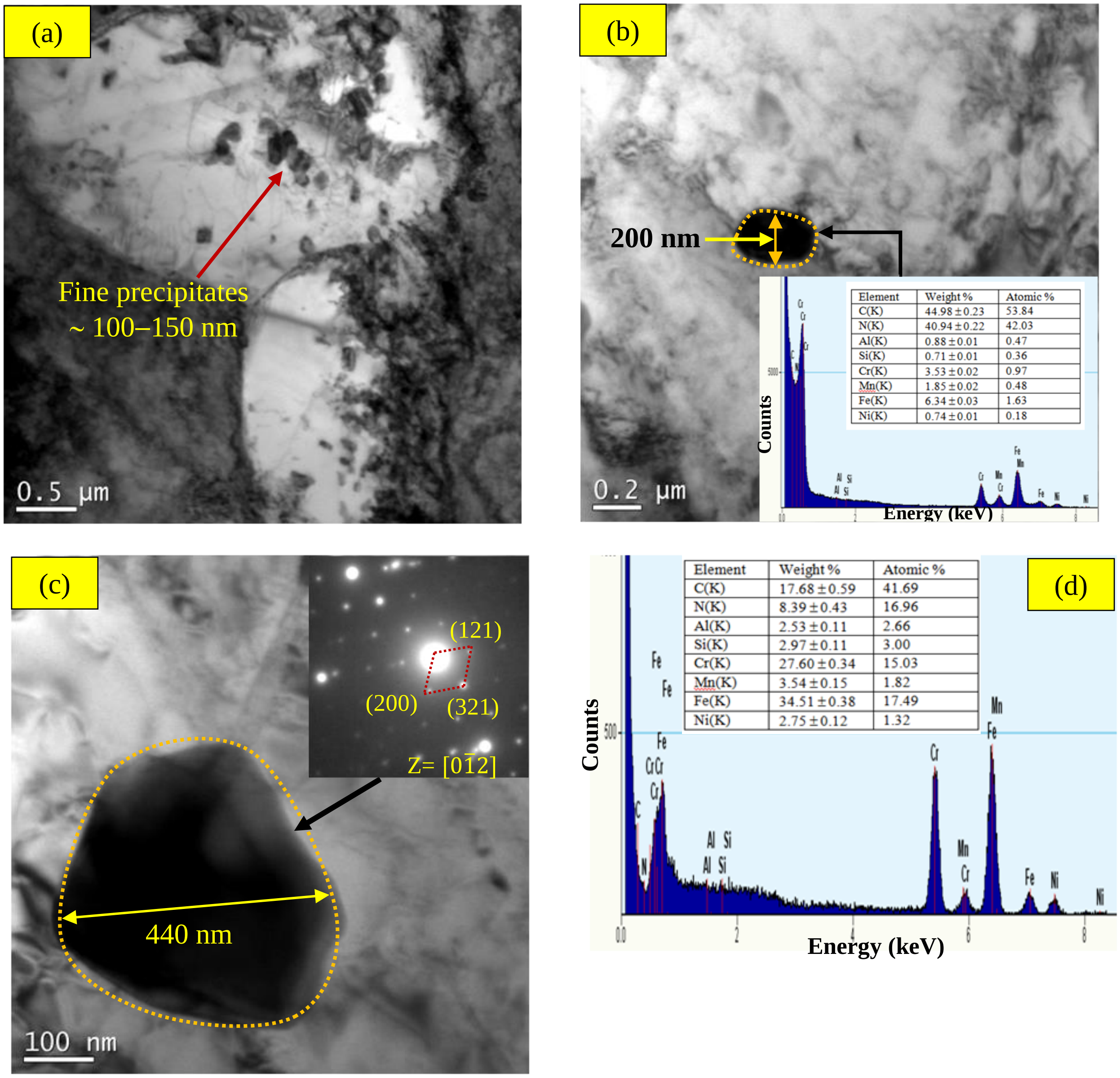

Element	Weight %	Atomic %
C(K)	44.98 ± 0.23	53.84
N(K)	40.94 ± 0.22	42.03
Al(K)	0.88 ± 0.01	0.47
Si(K)	0.71 ± 0.01	0.36
Cr(K)	3.53 ± 0.02	0.97
Mn(K)	1.85 ± 0.02	0.48
Fe(K)	6.34 ± 0.03	1.63
Ni(K)	0.74 ± 0.01	0.18

Element	Weight %	Atomic %
C(K)	17.68 ± 0.59	41.69
N(K)	8.39 ± 0.43	16.96
Al(K)	2.53 ± 0.11	2.66
Si(K)	2.97 ± 0.11	3.00
Cr(K)	27.60 ± 0.34	15.03
Mn(K)	3.54 ± 0.15	1.82
Fe(K)	34.51 ± 0.38	17.49
Ni(K)	2.75 ± 0.12	1.32

Figure 8.14: TEM bright field micrographs of precipitates of different size observed after reversion at 725°C for 1 h of (a) 40ZCD, (b) 10LND with EDS results of precipitate, (c) 20LND with SAED and its analysis at the inset and (d) EDS spectra with the chemical composition of precipitate in (c).

It is important to note that reversion at 725°C for a period of 1 h reveals the different size of precipitates as shown in Figure 8.14. Such precipitates help to increase the tensile strength and also hinder the reversion process. It is also noteworthy that reversion process is incomplete even after annealing of deformed samples at 725°C for 1 h due to the presence of the precipitates [294]. Figure 8.14(a) shows very fine precipitates (100-150 nm) whereas some coarse precipitates (200-440 nm) are found in Figures 8.14(b) and (c). EDS analysis indicates that precipitate in Figure 8.14(b) has a higher amount of C and N and therefore, these precipitates could be carbo-nitride of Fe and Cr. The precipitate and its EDS spectrum as shown in Figures 8.14(c) and (d) confirm that the precipitates are rich in Cr, Fe and C. Such precipitates are reasonably of $M_{23}C_6$ type i.e., $(Cr, Fe)_{23}C_6$ carbide. SAED at the inset of Figure 8.14(c) taken from the precipitate confirms the chromium carbide precipitate with a body centred cubic (BCC) structure. The carbides are generally formed during annealing in austenitic stainless steel because chromium is strong carbide former. These $M_{23}C_6$ carbides are formed in the temperature range 700-900°C, which is accelerated in alloys that are strengthened by cold deformation [167]. These carbides also obstruct the reversion process [25]. Therefore the reversion has not completed after annealing for 1 h at 725°C. During diffusional reversion, the dislocation movement can be hindered by these carbides and also contribute to the strengthening of the reversed austenite [22].

Among all these samples, the 40ZCD and reversion of the same have yielded 1225 MPa to 858 MPa and 13% to 37% elongation. Similarly, 10LND and its reversion have yielded tensile strength of 1306 MPa to 929 MPa, respectively and elongation of 15% to 45%, respectively. On the other hand, 20 LND sample and reversion of the same resulted in the tensile strength of 1676 MPa to 992 MPa, respectively and elongation of 8% to 32%, respectively. Such combinations of tensile properties are well comparable with the modern grades of ultra high strength steels [246, 295-297] and are a promising candidate for diverse applications like biomedical, structural, liquid gas transportation etc. Therefore, the optimal combination of the aforesaid strengthening and softening through cold deformation and reversion process offers the possibility of evolving a wide range of microstructural features and consequently strength-ductility combination in 304 SS.

8.7 Summary

The outcome of above results and discussion are summarised below.

1. Lowering of deformation temperature at cryogenic level results in the higher amount of α′-martensite as compared to that at 0°C, irrespective of deformation amount (% reduction). With the increase in deformation, at 0°C and -196°C, the density of dislocation and stacking fault, respectively is enhanced significantly.
2. 20% deformation at -196°C shows the maximum tensile strength of 1589 MPa with lowest elongation value of 9% due to the presence of high martensite volume fraction (44%) and highly dislocated austenite. In contrast, reversion annealing of the same at 725°C for 1 h resulted in a combination of 992 MPa strength and 32% elongation. The observed improvement in elongation, due to reversion treatment, is attributed to the transformation of the cold deformed microstructure to a configuration consisting of fine reverted austenite.
3. Reversion at 725°C for 1 h shows higher amount (12-35%) of reverted austenite than that (<10%) formed after conducting the annealing at 300°C for 1 h. In the case of the pre-strained sample, reversion annealing at 725°C, the 20PS-30LNQ resulted into highest elongation value of 72% along with tensile strength value of 753 MPa as the formation of α′-martensite is constrained in the pre-strained austenite matrix.
4. The formation of $\gamma \rightarrow \alpha'$ during deformation and $\alpha' \rightarrow \gamma$ during reversion is enhanced by the presence of strain localisation features due to interception among the twin, grain boundary, shear band and stacking fault.
5. The mechanism of the reversion of $\alpha' \rightarrow \gamma$ could occur through shear or diffusion. However, the dominating mechanism of reversion is essentially diffusional at a higher temperature of 725°C.

9

EPILOGUE

Cold deformation and annealing have been established as an attractive route for manufacturing thin gauge ultrafine grain high strength steels. In view of this, an attempt has been made to explore the microstructure evolution and mechanical properties of 304 stainless steels subjected to the different cold deformation and annealing route for exploring the possibility of their thin gauge applications in one hand and to demonstrate the influence of stacking fault energy, deformation and annealing temperature on evolution of microstructure and mechanical properties on the other.

The results of specific interest are summarised below:

9.1 Deformation of austenitic stainless steel

The 304 stainless steels with fully austenitic microstructure are subjected to varying deformation schedule to understand the effect of deformation on the microstructural evolution and, in turn, mechanical properties.

In the case of thermo-mechanical processing, optical and TEM microstructures obtained for the FRT of 700°C, 800°C and 900°C, primarily reveal fully austenitic structure with some amount of annealing twins and the grains are oriented and flattened along the direction of rolling. Fine austenite grains have been observed at a lower finish rolling temperature of 700°C, where the grain sizes lie in a range of 1 μm to 30 μm range. On the other hand, for the FRT of 800°C and 900°C the austenite grains are equiaxed and relatively coarser than those seen in the case of FRT of 700°C.

XRD analysis and TEM micrographs also corroborated the formation of stable austenitic microstructure after TMCP. The TEM micrographs have also shown the formation of deformation twins which generally form during deformation in low SFE materials. The TEM microstructure has also shown the presence of $M_{23}C_6$ type i.e., $(Cr, Fe)_{23}C_6$ precipitate in higher FRT of 900°C samples.

Among all the TMCP samples, the highest hardness of 210 VHN, YS of 460 MPa and UTS of 925 MPa have been achieved in FRT 700°C samples. The highest elongation value of 68% has been attained in FRT 900°C samples.

In the case of room temperature deformation of the fully austenitic sample analysis of X-ray diffraction patterns reveal the formation of 19% - 26% α′-martensite after deformation (30% and 40%) at room temperature and 24% - 32% α′-martensite after deformation at 0°C, for cold deformed samples. The as-received specimen reveals the lowest strength (675 MPa) with maximum total elongation (90%) among all of the specimens. Deformation of the fully austenitic as-received samples, at both the room temperature as well as at 0°C, enhances the hardness, yield strength and tensile strength values along with a drop of percent elongation. Thus, appropriate deformation schedule increases amenability of the steel for use in high strength thin gauge structural and safety applications with and without annealing.

The fracture surface and sub-surface of the as received and the 40% deformed samples indicate a transition from a predominantly ductile fracture in the as-received specimen to the brittle type of fracture in the deformed sample. The sub-surface micrographs provide the potential sites for the initiation of micro-voids and/or micro-cracks. Such fractographic information is supportive of the attempt of designing the microstructural modification of austenitic steel, hence its mechanical properties, by cold deformation.

The present study has also explored the genesis of different deformation induced features and their interactions in austenite, under the given amount of strain and temperature dependent SFE, leading to the strengthening and initiating the mechanical instability. Despite the absence of a quantitative understanding, the microstructural analyses have reliably demonstrated the contribution of the strain induced microstructural features to the encouraging tensile properties conducive to the high strength applications at sub-ambient (0°C) as well as cryogenic (-196°C) temperatures.

Table 9.1: Summary of the process-microstructure-property correlation for the cold deformed samples.

Key parameters	As-received	Cold deformation (40%)	Cold deformation (40%)	Cold deformation (10%)	Cold deformation (20%)
Deformation temperature	-	Room temperature	0°C	-196°C	-196°C
Mode of deformation	-	Rolling	Rolling	Rolling	Rolling
Stacking fault energy (mJ/m^2)	-	20	19	9	9
Constituent phases in microstructure	γ	γ+α′	γ+α′	γ+ε+α′	γ+ε+α′
Other important microstructural features	Twins	Dislocation density, deformation twin, annealing twin, stacking fault, shear band, intergranular crack, slip band		Extensive stacking fault, overlapping stacking faults, deformation twin, shear band, slip band	
Nucleation site	-	Intersection of above features		Interaction between above features	
Transformation pathway	-	γ→α′		γ→ε→α′	
YS (MPa)	259±10	1110±28	936±20	1061±12	1463±16
UTS (MPa)	675±14	1210±21	1225±29	1306±17	1589±15
TEL (%)	90±5	11±2	13±1	15±2	9±1

Lowering of deformation temperature at the cryogenic level results in the higher amount of α′-martensite as compared to that at 0°C, irrespective of the deformation amount (% reduction). With the increase in deformation, at 0°C and -196°C, the density of dislocation is found to be noticeable and stacking fault is enhanced significantly with the lowering of temperature.

Extended stacking faults, ε-martensite (up to 6%) and α′-martensite (28% to 44%) are the dominant strain induced features as compared to the homogeneous dislocation structure along with some amount of α′-martensite (13% to 32%) formed in the case of deformation of austenite at 0°C. Such difference corresponds to the lowering of SFE from 19 mJ/m^2 at 0°C to 9 mJ/m^2 at -196°C.

Twins are found as the common strain induced feature in all the samples rolled at 0°C as well as -196°C. However, the formation of deformation twin is more favourable during deformation at 0°C due to the relatively higher value of SFE. The presence of substantial amount of ε-martensite after 20% deformation at -196°C corroborates the overlapping of stacking faults and lower value of SFE of 9 mJ/m^2. The presence of higher volume percentage of α′-martensite (44%) after 20% deformation at -196°C is attributed to the numerous nucleation sites formed at the locations of intersections among ε-martensite and shear bands. On the contrary, 20% deformation at 0°C leads to the formation of a lower amount of α′-martensite (17%) due to the paucity of nucleation sites. 40% cold deformation at 0°C leads to the high strength (1225 MPa) with appreciable (13%) total elongation, whereas comparatively lower deformation (10-20%) at -196°C leads to higher level of strength (1306-1589 MPa) with 15-9% elongation due to the formation of higher volume fraction of strain induced martensite (ε/α′). Table 9.1 summarises the process-microstructure-property correlation for the cold deformed samples.

9.2 Reversion annealing of the selected deformed samples

Cold deformation followed by reversion annealing treatment is considered to be conducive to manufacturing high strength thin gauge 304 austenitic stainless steel under deformation-reversion route. In this approach, it is important to explore the combined effect of temperature and deformation on the evolution of microstructural features those govern the technological properties of the steel.

In the case of cold deformed samples, the reversion transformation has been found to be enhanced with increasing annealing temperature without significant grain growth up to 800°C in the presence of finer Cr-carbide precipitation at austenite grain boundaries. The residual α′-martensite volume fraction after reversion at 800°C for 1 h has been estimated through X-ray diffraction analysis to 8% for both 30% and 40% cold deformed sample at 0°C.

The activation energy value corresponding to the first and second stage of reversion followed by Cr-carbide precipitation has been estimated to be as 77, 130 and 251 kJ/mol, respectively for 30% cold deformed sample at 0°C. These results are suitably compared with the published results. This allows correlating the occurrence of specific reaction with the different temperature regimes concerning the proposed manufacturing schedule.

Both tensile strength and percent elongation values increase with increasing annealing temperature up to 450°C and beyond that annealing result in a drop of tensile strength value with a consequent rise in percent elongation. 40% cold deformation and annealing at 500°C for 1 h has resulted in an attractive strength-ductility combination (30.25 GPa%). Fractographic features substantiate and corresponding sub-surface examination identifies the micro-mechanism of tensile fracture.

20% deformation at -196°C shows the maximum tensile strength of 1589 MPa with lowest elongation value of 9% due to the presence of high martensite volume fraction (44%) and highly dislocated austenite. In contrast, reversion annealing of the same at 725°C for 1 h resulted in a combination of 992 MPa of strength and 32% of elongation. The observed improvement in elongation, due to reversion treatment, is attributed to the transformation of the cold deformed microstructure to a configuration consisting of fine reverted austenite.

Reversion of cryogenically rolled steel at 725°C for 1 h shows higher amount (12-35%) of reverted austenite than that (<10%) formed after conducting the annealing at 300°C for 1 h. In the case of the pre-strained sample, reversion annealing at 725°C, the 20PS-30LNQ resulted into highest elongation value of 72% along with tensile strength value of 753 MPa as the formation of α'-martensite is constrained in the pre-strained austenite matrix.

The formation of $\gamma \rightarrow \alpha'$ during deformation and $\alpha' \rightarrow \gamma$ during reversion is enhanced by the presence of strain localisation features due to interception among the twin, grain boundary, shear band and stacking fault. The mechanism of the reversion of $\alpha' \rightarrow \gamma$ could occur through shear or diffusion. However, the dominating mechanism of reversion is essentially diffusional at a higher temperature of 725°C.

Table 9.2 summarises the process-microstructure-property correlation for the samples subjected to reversion annealing treatment after cold deformation.

Table 9.2: Summary of process-microstructure-property correlation of the samples subjected to reversion annealing treatment after cold deformation.

Key parameters	Cold deformation (40%)	Cold deformation (40%)	Cold deformation (10%)	Cold deformation (20%)
Deformation temperature	Room temperature	0°C	-196°C	-196°C
Annealing temperature	Not carried out	725°C, 1 h		
Constituent phases in microstructure	γ+ reverted γ + residual α′		γ+ reverted γ + residual α′	
Other important microstructural features	Dislocation substructure deformation twin, annealing twin, recrystallised finer grains, precipitates		Deformation twin, annealing twin, recrystallised finer grains, precipitates, defect free nano γ grains surrounded by reverted γ grains.	
Transformation kinetics	Shear transformation followed by recrystallisation and recovery at low temperature, diffusion controlled transformation and formation of equiaxed grain at higher temperatures.			
Nucleation site	Blocky martensite is a nucleation site for austenite reversion. The austenite-martensite interface is also favoured for nucleation of reverted austenite during annealing.			
YS (MPa)	Not carried out	617±14	628±13	706±9
UTS (MPa)		858±15	929±7	992±15
TEL (%)		37±3	45±2	32±3

In view of the limits and gaps identified in the present study, an attempt has been made here to propose the future scope of work.

It is realised that microstructural evolution and achievable mechanical properties under the cold deformation and reversion annealing route is critically determined by the combination of stacking fault energy, deformation, reversion time and temperature. It is therefore essential to explore the different Ni and Mn content in such steels with an aim to achieve 8% Ni equivalent which is suitable to provide best strength-ductility combination under an industrially viable processing route.

As cold deformation and reversion annealing route are aimed at thin gauge application, it is of interest to study the technological properties viz., bendability, formability, weldability etc., for such thin gauge steels.

An attempt may be made to suitably modify the composition of 304 stainless steel with an aim to achieve the M_d temperature above the room temperature so that sufficient martensite would form during cold deformation at room temperature.

The mechanical properties of the cold deformed and reversion annealed steels involve a wide range of strain hardening behaviour including yield point phenomena, dynamic strain ageing, the formation of stacking fault, twin and different strain induced transformation of austenite. It is essential to establish the combination of stacking fault energy of austenite, amount of cold deformation, reversion annealing parameters which will evolve the microstructure to achieve the desired work hardening behaviour.

A rational approach in process leading to effective application of the present steel can be adopted from above study. The reduction percentage through cold rolling and the selection of process temperature is main parameters during rolling followed by suitable annealing process in annealing furnace with proper control. To maintain desired rolling temperature the rolling stock can be passed through cryogenic or sub-ambient (filled with liquid nitrogen or ice water) chambers in between rolling strands. The cold rolled product can be subjected to off-line reversion annealing either in batches or in continuous process. Thus a material can be engineered with designated microstructure and predictable mechanical property for specific applications. Various components in automotive sector can be proposed from 304 stainless steel with above manufacturing process. Crash worthiness and weight saving are the important criteria to consider for automotive application in addition to excellent corrosion and heat resisting properties, where 304 stainless steel components have an edge over others. To be specific the components such as fuel tank, cylinder head gasket, knuckle suspension arm, pump bodies, heat shields, container for airbag inflation, seat belt springs, resonator, intermediate pipe, silencer, tail pipe, crash box, anti-intrusion bar, vehicle body frame etc. can be proposed for vehicle operated at harsh environments and road conditions like off shore region, mining localities etc. The road barrier is also an important safety item which can be processed from 304 stainless steel. Bullet proof body armour and window mess can also be proposed, where stainless steel finds potential applications.

REFERENCES

[1] L. Xie, Tian-Lin Huang, Yu-Hui Wang, Gui-Lin Wu, Nobuhiro Tsuji, and Xiao-Xu Huang, Deformation Induced Martensitic Transformation and Its Initial Microstructure Dependence in a High Alloyed Duplex Stainless Steel, steel research int. 87 (2017) 1611-3683.

[2] J. Liu, D. Kaoumi, Use of in-situ TEM to characterize the deformation-induced martensitic transformation in 304 stainless steel at cryogenic temperature, Materials Characterization 136 (2018) 331-336.

[3] E. Polatidis, W.-N. Hsu, M. Šmíd, T. Panzner, S. Chakrabarty, P. Pant, H. Van Swygenhoven, Suppressed martensitic transformation under biaxial loading in low stacking fault energy metastable austenitic steels, Scripta Materialia 147 (2018) 27–32.

[4] I. Sapezanskaia, J.J. Roa, G. Fargas, M. Turon-Viñas, T. Trifonov, R. Kouitat Njiwa, A. Redjaïmia, A. Mateo, Deformation mechanisms induced by nano indentation tests on a metastable austenitic stainless steel: A FIB/SIM investigation, Materials Characterization 131 (2017) 253-260.

[5] M. G. Fontana, Corrosion Engineering, Tata McGraw-Hill Pub. Co. Ltd., New Delhi, 3rd edition, (1986) 1-557.

[6] M. A. Streicher, Austenitic and ferritic stainless steels, Uhlig's corrosion handbook, John Wiley & Sons, Nova York, 2nd edition (2000) 601-650.

[7] J. R. Davis, ASM speciality handbook: stainless steels, ASM Int., Materials Park, Ohio, USA, 3rd printing (1999) 3-526.

[8] Z. Z. Yuan, Q. X. Dai, Q Zhang, Effects of temperature cycling and nitrogen on the stability of microstructures in austenitic stainless steels, Mater. Charact., 59(1) (2008) 18-22.

[9] G. L. Huang, D. K. Matlock, G. Krauss, Martensite formation, strain rate sensitivity and deformation behaviour of type 304 stainless steel sheet, Metall. Trans. A, 20(7)

(1989) 1239-1246.

[10] A. Das, S. Sivaprasad, M. Ghosh, P. Chakraborti, S. Tarafder, Morphologies and characteristics of deformation induced martensite during tensile deformation of 304 LN stainless steel, Mater. Sci. Eng. A, 486 (1-2) (2008) 283-286.

[11] Y. Tomota, Y. Morioka, W. Nakagawara, Epsilon martensite to austenite reversion and related phenomenon in Fe-24Mn and Fe-24Mn-6Si alloys, Acta Mater., 46(4) (1998) 1419-1426.

[12] A. K. De, D. C. Murdock, M. Mataya, J. G. Speer, D. Matlock, Quantitative measurement of deformation-induced martensite in 304 stainless steel by X-ray diffraction, Scr. Mater., 50(12) (2004) 1445-1449.

[13] H. M. Otte, The formation of stacking faults in austenite and its relation to martensite, Acta Metall., 5(11) (1957) 614-627.

[14] F. Haeβner, R. L. Plaut, A. F. Padilha, Separation of static recrystallisation and reverse transformation of deformation-induced martensite in an austenitic stainless steel by calorimetric measurements, ISIJ Int., 43(9) (2003) 1472-1474.

[15] P. L. Mangonon, G. Thomas, The martensite phases in 304 stainless steel, Metall. Mater. Trans. B, 1(6) (1970) 1577-1586.

[16] J. A. Venables, The martensitic transformation in stainless steel, Phil. Mag., 7 (73) (1962) 35-44.

[17] R. Lagneborgj, The martensite transformation in 18%Cr-8%Ni steels, Acta Metall., 12 (7) (1964) 823-843.

[18] P. L. Mangonon, G. Thomas, Structure and properties of thermal-mechanically treated 304 stainless steel, Metall. Mater. Trans. B, 1(6) (1970) 1587-1594.

[19] J. Y. Chio, W. Jin, Strain induced martensite formation and its effect on strain hardening behaviour in the cold drawn 304 austenitic stainless steels, Scr. Mater., 36(1) (1997) 99-104.

[20] T. Angel, Formation of martensite in austenitic stainless steels, J. Iron Steel Inst., 177 (1954) 165-174.

[21] F. B. Pickering, Physical metallurgical of stainless steels development, Int. Mater. Rev. (ASM-IOM-Maney), 21 (1976), 1-42.

[22] H. Smith, D. R. F. West, The reversion of martensite to austenite in certain stainless steels, J. Mater. Sci., 8(10) (1973) 1413-1420.

[23] A. D. Schino, M. Barteri, J. M. Kenny, Development of the ultra fine grain structure by martensitic reversion in stainless steel, J. Mater. Sci. Lett., 21 (9) (2002) 751-753.

[24] K. Tomimura, S. Takaki, Y. Tokunaga, Reversion mechanism from deformation induced martensite to austenite in metastable austenitic stainless steels, ISIJ Int., 31(12) (1991) 1431-1437.

[25] D. L. Johannsen, A. Kryolainen, P. J. Ferreira, Influence of annealing treatment on the formation of nano/submicron grain size AISI 301 austenitic stainless steels, Metall. Mater. Trans. A, 37(8) (2006) 2325-2338.

[26] R.D.K. Misra, S. Nayak, S.A. Mali, J.S. Shah, M.C. Somani, and L.P. Karjalainen, Microstructure and Deformation Behavior of Phase-Reversion-Induced Nano-grained/Ultrafine-Grained Austenitic Stainless Steel, Metall. Mater. Trans. A, 40(10) (2009) 2498-2509.

[27] K. Ono, T. J. Koppenaal, The effects of prior deformation and transformations on the microstructure of an iron-nickel alloy, Metall. Mater. Trans. B, 5(3) (1974) 739-746.

[28] M. Tokizane, N. Matsumura, K. Tsuzaki, T. Maki, I. Tamura, Recrystallization and formation of austenite in deformed lath martensitic structure of low carbon steels, Metall. Mater. Trans. A, 13(8) (1982) 1379-1388.

[29] L. Margulies, G. Winther, H. F. Poulsen, In situ measurement of grain rotation during deformation of polycrystals, Science, 291(5512) (2001) 2392-2394.

[30] P. Hedström, Deformation induced martensitic transformation of metastable stainless steel AISI 301, PhD Thesis, Luleå University of Technology, Sweden, (2005).

[31] Design guidelines for the selection and use of stainless steel, Handbook series No 9014. Nickel Development Institute, USA (1993) 1-52.

[32] D. C. Stouffer, L. T. Dame, Inelastic Deformations of metals-models, mechanical properties and metallurgy, John Wiley & Sons, Inc., New York, USA, 1st edition (1996) 1-494.

[33] M. F. McGuire, Stainless steels for design engineers, ASM Int., Materials Park, Ohio, USA, 1st edition, Chapter 6: ASS, (2008) 69-90.

[34] David Maréchal, Linkage between mechanical properties and phase transformation in a 301LN austenitic stainless steel, PhD Thesis, The University of British Columbia, Vancouver, (2011).

[35] Thermo-Calc software, database TCFE 2000, S-version, 2000.

[36] S. Tavares, J. Pardal, M. G. da Silva, H. Abreu, M. da Silva, Deformation induced martensitic transformation in a 201 modified austenitic stainless steel, Mater. Charact., 60(8) (2009) 907-911.

[37] L. Rémy, Twinning and strain induced martensitic transformation (FCC→HCP) in low stacking fault energy Co-Ni-Cr-Mo-Fe-Mn-Cr-C austenitic system, PhD Thesis. University Paris-Sud, Paris, France, (1975).

[38] R. Schramm, R. Reed, Stacking fault energies of seven commercial austenitic stainless steels, Metall. Mater. Trans. A, 6(7) (1975) 1345-1351.

[39] F. Lecroisey, A. Pineau, Martensitic transformations induced by plastic deformation in the Fe-Ni-Cr-C system, Metall. Mater. Trans. B, 3(2) (1972) 391-400.

[40] J. Talonen, Effect of strain-induced α′- martensite transformation on mechanical properties of metastable austenitic stainless steels, PhD thesis, Aalto University School of Science and Technology (TKK), Finland. (2007).

[41] L. Bracke, Deformation behaviour of austenitic Fe-Mn alloys by twinning and martensitic transformation, PhD thesis, Ghent University, Netherlands, (2007).

[42] L. E. Murr, Interfacial phenomena in metals and alloys, Addison-Wesley Pub. Co., USA, 8(1) (1975). 1-387.

[43] E. I. Galindo-Nava, P. E. J. Rivera-Díaz-del-Castillo, Understanding martensite and twin formation in austenitic steels: A model describing TRIP and TWIP effects, Acta Mater., 128 (2017) 120-134.

[44] A. Hedayati, A. Najafizadeh, A. Kermanpur, F. Forouzan, The effect of cold rolling regime on microstructure and mechanical properties of AISI 304L stainless steel, J. Mater. Process. Technol., 210 (2010) 1017-1022.

[45] G. B. Olson, M. A. Cohen, A mechanism for the strain-induced nucleation of martensitic transformations, J. Less-Common Met., 28(1) (1972) 107-118.

[46] G. B. Olson, M. A. Cohen, Kinetics of strain-induced martensitic nucleation, Metall. Mater. Trans. A, 6(4) (1975) 791-795.

[47] M. Milad, N. Zreiba, F. Elhalouani, C. Baradai, The effect of cold work on structure and properties of AISI 304 stainless steel, J. Mater. Process. Technol., 203 (2008) 80-85.

[48] M. Humbert, B. Petit, B. Bolle, N. Gey, Analysis of the γ→ε→α′ variant selection induced by 10% plastic deformation in 304 stainless steel at -60°C, Mater. Sci. Eng. A, 454-455 (2007) 508-517.

[49] M. Linderov, C. Segel, A. Weidner, H. Biermann, A. Vinogradov, Deformation mechanisms in austenitic TRIP/TWIP steels at room and elevated temperature investigated by acoustic emission and scanning electron microscopy, Mater. Sci. Eng. A, 597 (2014) 183-193.

[50] K. Spencer, The Work-hardening of austenitic stainless steel, applied to the fabrication of high-strength conductors, PhD thesis, McMaster University, Canada, (2004).

[51] W. G. Burgers, On the process of transition of the cubic-body-centered modification into the hexagonal-close-packed modification of zirconium, Physica, 1(7-12) (1934) 561-586.

[52] G. Stone, G. Thomas, Deformation induced alpha' and epsilon martensites in Fe-Ni-Cr single crystals, Metall. Mater. Trans. B, 5(9) (1974) 2095-2102.

[53] T. H. Lee, E. Shin, C. S. Oh, H. Y. Ha, S. J. Kim, Correlation between stacking fault energy and deformation microstructure in high interstitial alloyed austenitic steels, Acta Mater., 58(8) (2010) 3173-3186.

[54] H. K. D. H. Bhadeshia, Worked examples in the geometry of crystals, The Institute of Materials, London, 2nd Edition, (2001) 1-89.

[55] L. Rémy, A. Pineau, Twinning and strain-induced fcc → hcp transformation in the Fe-Mn-Cr-C system, Mater. Sci. Eng., 28(1) (1977) 99-107.

[56] H. Idrissi, L. Ryelandt, M. Véron, D. Schryvers, P. Jacques, Is there a relationship between the stacking fault character and the activated mode of plasticity of Fe-Mn-based austenitic steels, Scr. Mater., 60(11) (2009) 941-944.

[57] J. W. Brooks, M. H. Loretto, R. E. Smallman, Direct observations of martensite nuclei in stainless steel, Acta Metall., 27(12) (1979) 1839-1847.

[58] J. L. Putaux, J. P. Chevalier, HREM study of self-accommodated thermal ε-martensite in an Fe-Mn-Si-Cr-Ni shape memory alloy, Acta Mater., 44(4) (1996) 1701-1716.

[59] K. Verbeken, N. V. Caenegem, D. Raabe, Identification of epsilon martensite in a Fe-based shape memory alloy by means of EBSD, Micron, 40(1) (2009) 151-561.

[60] S. Allain, J. P. Chateau, O. Bouaziz, S. Migot, N. Guelton, Correlations between the calculated stacking fault energy and the plasticity mechanisms in Fe-Mn-C alloys, Mater. Sci. Eng. A, 387-389 (2004) 158-162.

[61] S. Kajiwara, Characteristic features of shape memory effect and related transformation behavior in Fe-based alloys, Mater. Sci. Eng. A, 273-275 (1999) 67-88.

[62] H. Fujita, S. Ueda, Stacking faults and f.c.c. (γ) → h.c.p. (ε) transformation in 18/8-type stainless steel, Acta Metall., 20(5) (1972) 759-767.

[63] Z. Nishiyama, Martensitic transformation, Materials science and technology, Academic Press, New York, USA, 2nd edition, (1978) 2-438.

[64] J. W. Brooks, M. H. Loretto, R. E. Smallman, In-situ observations of the formation of martensite in stainless steel, Acta Metall., 27(12) (1979) 1829-1838.

[65] B. Jiang, X. Qi, S. Yang, W. Zhou, T. Y. Hsu, Effect of stacking fault probability on γ→ε martensitic transformation and shape memory effect in Fe-Mn-Si based alloys, Acta Mater., 46(2) (1998) 501-510.

[66] G. B. Olson, M. A. Cohen, A general mechanism of martensitic nucleation. Part I: General concepts and fcc-hcp transformation, Metall. Mater. Trans. A, 7(12) (1976) 1897-1904.

[67] P. Hedström, U. Lienert, J. Almer, M. Odén, Elastic strain evolution and ε-martensite formation in individual austenite grains during in situ loading of a metastable stainless steel, Mater. Lett., 62(2) (2008) 338-340.

[68] S. Allain, Multi-scale thermomechanical characterization and modeling of the deformation and work hardening mechanisms of high manganese austenitic steels: application to the TWIP effect, PhD thesis, INP Lorraine, Metz France, (2004).

[69] G. Blanc, R. Tricot, R. Castro, Martensitic transformations in Fe-Cr-Ni austenitic stainless steels. Relationship between the parameters of the phase and the mechanisms of the transformation, Rev. Métall., 70(7-8) (1973) 527-541.

[70] W. L. Fink, E. D. Campbell, Influence of heat treatment and carbon content on the structure of pure iron-carbon alloys, Trans. Am. Soc. Steel Treating, 9 (1926) 717-752.

[71] J. W. Jr. Morris, J. W. Chan, Z. Mei, The influence of deformation-induced martensite on the cryogenic behaviour of 300-series stainless steels, Fourteenth International Cryogenic Engineering Conference and International Cryogenic Materials Conference, Kiev, Ukraine, (1992) 1-13.

[72] C. S. Roberts, Effect of carbon on the volume fractions and lattice parameters of retained austenite and martensite, Trans. AIME, 197 (1953) 203-204.

[73] G. Krauss, Deformation and fracture in martensitic carbon steels tempered at low temperatures, Metall. Mater. Trans. B, 32(2) (2001) 205-221.

[74] D. T. Llewellyn, Work-hardening effects in austenitic stainless steels, J. Mater. Sci. Technol., 13(5) (1997) 389-400.

[75] L. Xiao, Z. Fan, Z. Jinxiu, Lattice parameter variation with carbon content of martensite (I), Phys. Rev., 52(14) (1995) 9970-9978.

[76] J. Breedis, L. Kaufman, The formation of HCP and BCC phases in austenitic iron alloys, Metall. Mater. Trans. B, 2(9) (1971) 2359-2371.

[77] J. Dash, H. M. Otte, The martensite transformation in stainless steel, Acta Metall., 11(10) (1963) 1169-1178.

[78] L. E. Murr, K. P. Staudhammer, S. S. Hecker, Effects of strain state and strain rate on deformation-induced transformation in 304 stainless steel: Part II. Microstructural study, Metall. Trans. A, 13(4) (1982) 627-635.

[79] H. Fujita, T. Katayama, In-situ observation of strain-induced $\gamma \rightarrow \varepsilon \rightarrow \alpha'$ and $\gamma \rightarrow \alpha'$ martensitic transformations in Fe-Cr-Ni alloys, Mater. Trans. JIM, 33(3) (1992) 243-252.

[80] V. Tsakiris, D. V. Edmonds, Martensite and deformation twinning in austenitic steels, Mater. Sci. Eng. A, 273-275 (1999) 430-436.

[81] T. Inamura, K. Takashima, Y. Higo, Crystallography of nanometre-sized α'-martensite formed at intersections of mechanical twins in an austenitic stainless steel, Philos. Mag., 83(8) (2003) 935-954.

[82] N. Nakada, H. Ito, Y. Matsuoka, T. Tsuchiyama, S. Takaki, Deformation induced martensitic transformation behaviour in cold-rolled and cold-drawn type 316 stainless steels, Acta Mater., 58(3) (2010) 895-903.

[83] S. Curtze, V-T. Kuokkala, A. Oikari, J. Talonen, H. Hänninen, Thermodynamic modeling of the stacking fault energy of austenitic steels, Acta Mater., 59(3) (2011) 1068-1076.

[84] C. Sinclair, A molecular dynamics study of deformation induced phase transformations at fault band intersections, J. Phys. Conf. Ser., 240(1) (2010) 1-4.

[85] N. Gey, B. Petit, M. Humbert, Electron backscattered diffraction study of ε/α′-martensite martensitic variants induced by plastic deformation in 304 stainless steel, Metall. Mater. Trans. A, 36(12) (2005) 3291-3299.

[86] Y. K. Lee, C. S. Choi, Effects of thermal cycling on the kinetics of the γ→ε martensitic transformation in an Fe-17%Mn alloy, Metall. Mater. Trans. A, 31(11) (2000) 2735-2738.

[87] G. B. Olson, M. A. Cohen, A general mechanism of martensitic nucleation. Part II: FCC→BCC and other martensitic transformations, Metall. Mater. Trans. A, 7(11) (1976) 1905-1914.

[88] J. Guimaraes, S. F. De Oliveira, Work-hardening and martensitic transformation in Fe-27% Ni-0.23%C at 263 K, Scr. Metall., 13(7) (1979) 537-542.

[89] Y. Gang; H. Chongxiang, W. Shiding, Z. Zhefeng, Strain-induced martensitic transformation in 304L austenitic stainless steel under ECAP deformation, Acta Metall. Sinica, 45(8) (2009) 906-911.

[90] T. Suzuki, H. Kojima, K. Suzuki, T. Hashimoto, M. Ichihara, An experimental study of the martensite nucleation and growth in 18/8 stainless steel, Acta Metall., 25(10) (1977) 1151-1162.

[91] K. Spencer, J. D. Embury, K. T. Conlon, M. Véron, Y. Bréchet, Strengthening via the formation of strain-induced martensite in stainless steels, Mater. Sci. Eng. A, 387-89 (2004) 873-881.

[92] W. S. Lee, C. F. Lin, The morphologies and characteristics of impact-induced martensite in 304L stainless steel, Scr. Mater., 43(8) (2000) 777-782.

[93] L. Bracke, L. Kestens, J. Penning, Transformation mechanism of α′ martensite in an austenitic Fe-Mn-C-N alloy, Scr. Mater., 57(5) (2007) 385-388.

[94] C. Huang, G. Yang, Y. Gao, S. Wu, S. Li, Investigation on the nucleation mechanism of deformation-induced martensite in an austenitic stainless steel under severe plastic deformation, J. Mater. Res., 22(3) (2007) 724-729.

[95] K. Spencer, M. Véron, K. Yu-Zhang, J. D. Embury, The strain induced martensite transformation in austenitic stainless steels. Part 1: Influence of temperature and strain history, Mater. Sci. Technol., 25(1) (2009) 7-17.

[96] H. S. Yang, H. Bhadeshia, Austenite grain size and the martensite-start temperature, Scr. Mater., 60(7) (2009) 493-495.

[97] M. J. Dickson, The significance of texture parameters in phase analysis by X-ray diffraction, J. Appl. Crystallogr., 2 (1969) 176-180.

[98] H. M. Rietveld, A profile refinement method for nuclear and magnetic structures, J. Appl. Crystallogr., 2(2) (1969) 65-71.

[99] A. Albinati, B. T. M. Willis, The Rietveld method in neutron and X-ray powder diffraction, J. Appl. Crystallogr., 15(4) (1982) 361-374.

[100] R. D. Arnell, Determination of retained austenite in steel by X-ray diffraction, J. Iron Steel Inst., 206 (1968) 1035-1036.

[101] R. W. Cheary, Y. Ma-Sorrell, Quantitative phase analysis by X-ray diffraction of martensite and austenite in strongly oriented orthodontic stainless steel wires, J. Mater. Sci., 35(5) (2000) 1105-1113.

[102] V. Randle, O. Engler, Introduction to texture analysis: macrotexture, microtexture and orientation mapping, CRC Press, 2nd edition, (2010) 3-368.

[103] D. T. Lewis, J. G. Speer, D. K. Matlock, M. C. Mataya, Influence of composition variation on deformation induced martensite formation in type 304 stainless steel, 41st MWSP Conference Proceedings ISS, 37 (1999) 343-351.

[104] A. Das, S. Tarafder, P. C. Chakraborti, Estimation of deformation induced martensite in austenitic stainless steels, Mater. Sci. Eng. A, 529 (2011) 9-20.

[105] M. Umemoto, W. Owen, Effects of austenitizing temperature and austenite grain size on the formation of a thermal martensite in an iron-nickel and an iron-nickel-carbon alloy, Metall. Mater. Trans. B, 5(9) (1974) 2041-2046.

[106] B. H. Jiang, L. Sun, R. Li, T. Y. Hsu, Influence of austenite grain size on γ-ε martensitic transformation temperature in Fe-Mn-Si-Cr alloys, Scr. Metall. Mater., 33(1) (1995) 63-68.

[107] T. Durlu, Effect of austenite grain size on ε martensite formation in an Fe-Mn-Mo alloy, J. Mater. Sci. Lett., 16(4) (1997) 320-321.

[108] Y. Inokuti, B. Cantor, Splat-quenched Fe-Ni alloys, Scr. Metall., 10(7) (1976) 655-659.

[109] Y. Inokuti, B. Cantor, Overview 15: The microstructure and kinetics of martensite transformations in splat-quenched Fe and Fe-Ni alloys - II, Acta Metall., 30(2) (1982) 343-356.

[110] A. Hamada, P. Sahu, S. G. Chowdhury, L. Karjalainen, T. Levoska, J. Oittinen, Kinetics of the α′ martensitic transformation in fine grained Fe-26Mn-0.14C austenitic steel, Metall. Mater. Trans. A, 39 (2008) 462-465.

[111] Y. Matsuoka, T. Iwasaki, N. Nakada, T. Tsuchiyama, S. Takaki, Effect of grain size on thermal and mechanical stability of austenite in metastable austenitic stainless steel, ISIJ Int., 53(7) (2013) 1224-1230.

[112] K. Tao, H. Choo, H. Li, B. Clausen, J. E. Jin, Y. K. Lee, Transformation induced plasticity in an ultrafine grained steel: An in situ neutron diffraction study, Appl. Phys. Lett., 90(10) (2007) 101911.

[113] J. H. Jun, C. S. Choi, Variation of stacking fault energy with austenite grain size and its effect on the M_s temperature of $\gamma \rightarrow \varepsilon$ martensitic transformation in Fe-Mn alloy, Mater. Sci. Eng. A, 257(2) (1998) 353-356.

[114] T. Maki, Y. Tomota, I. Tamura, Effect of grain size on the transformation-induced plasticity in metastable austenitic Fe-Ni-C alloy, J. Jpn. Inst. Met., 38 (1974) 871-876.

[115] E. Jimenez-Melero, N. H. Van Dijk, L. Zhao, J. Sietsma, S. Offerman, J. Wright, S. Van der Zwaag, Martensitic transformation of individual grains in low-alloyed TRIP steels, Scr. Mater., 56(5) (2007) 421-424.

[116] K. Nohara, Y. Ono, N. Ohashi, Composition and grain-size dependencies of strain-induced martensitic transformation in metastable austenitic stainless steels, ISIJ Int., 63 (1997) 212-222.

[117] J. Gonzales, R. Aranda, M. Jonapá, The influence of grain size on the kinetics of strain induced martensite in type 304 stainless steel, Applications of Stainless Steel, 2 (1992) 1009-1016.

[118] W. Jeong, D. Matlock, G. Krauss, Effects of tensile-testing temperature on deformation and transformation behavior of retained austenite in a 0.14C-1.2Si-1.5Mn steel with ferrite-bainite-austenite structure, Mater. Sci. Eng. A, 165(1) (1993) 9-18.

[119] S. K. Varma, J. Kalyanam, L. E. Murr, V. Shrinivas, Effect of grain size on deformation-induced martensite formation in 304 stainless steel and 316 stainless steel during room temperature tensile testing, J. Mater. Sci. Lett., 13(2) (1994) 107-111.

[120] A. Petein, On the interaction between strain-induced phase transformations and mechanical properties in Mn-Si-Al steels and Ni-Cr austenitic stainless steels, PhD thesis, Université Catholique de Louvain, Belgium, 2007.

[121] R. H. Leal, J. Guimaraes, Microstructure evolution during mechanically induced martensitic transformation in Fe-33%Ni-0.1%C, Mater. Sci. Eng., 48(2) (1981) 249-254.

[122] V. Shrinivas, S. K. Varma, L. E. Murr, Deformation-induced martensitic characteristics in 304 and 316 stainless steels during room-temperature rolling, Metall. Mat. Trans. A, 26 (1995) 661-671.

[123] A. K. De, J. Speer, D. Matlock, D. Murdock, M. Mataya, and R. Comstock: Deformation-induced phase transformation and strain-hardening in type 304 austenitic stainless steel, Metall. Mater. Trans. A, 37(6) (2006) 1875-1886.

[124] S. Nanga, A. Pineau, B. Tanguy, L. Nazé, P-O. Santacreu, Plasticity and strain-induced martensitic transformation in two austenitic stainless steels, International Conference on Martensitic Transformations (ICOMAT), 2008.

[125] K. Mumtaz, S. Takahashi, J. Echigoya, L. Zhang, Y. Kamada, M. Sato, Temperature dependence of martensitic transformation in austenitic stainless steel, J. Mater. Sci. Lett., 22(6) (2003) 423-427.

[126] R. Kubler, Study of the behavior of TRIP effect steels: micromechanical and phenomenological approaches. Application to formatting, PhD thesis, Paul Verlaine University of Metz, France, 2004.

[127] J. Talonen, H. Hänninen, P. Nenonen, G. Pape, Formation of shear bands and strain-induced martensite during plastic deformation of metastable austenitic stainless steels, Acta Mater., 55(18) (2007) 6108-6118.

[128] V. Talyan, R. H. Wagoner, J. K. Lee, Formability of stainless steel, Metall. Mater. Trans. A, 29(8) (1998) 2161-2172.

[129] H. N. Han, C. G. Lee, C-S. Oh, T-H. Lee, S. J. Kim, A model for deformation behavior and mechanically induced martensitic transformation of metastable austenitic steel, Acta Mater., 52(17) (2004) 5203-5214.

[130] J. A. Lichtenfeld, C. J. Van Tyne, M. C. Mataya, Effect of strain rate on stress-strain behavior of alloy 309 and 304L austenitic stainless steel, Metall. Mater. Trans. A, 37(1) (2006) 147-161.

[131] S. Hecker, M. Stout, K. Staudhammer, J. Smith, Effects of strain state and strain rate

on deformation-induced transformation in 304 stainless steel. Part I: Magnetic measurements and mechanical behaviour, Metall. Mater. Trans. A, 13(4) (1982) 619-626.

[132] S. G. S. Raman, K. A. Padmanabhan, Tensile deformation-induced martensitic transformation in AISI 304LN austenitic stainless steel, J. Mater. Sci. Lett., 13 (1994) 389-392.

[133] J. Talonen, P. Nenonen, G. Pape, H. Hänninen, Effect of strain rate on the strain-induced γ→α'-martensite transformation and mechanical properties of austenitic stainless steel, Metall. Mater. Trans. A, 36(2) (2005) 421-432.

[134] A. A. Lebedev, V. V. Kosarchuk, Influence of phase transformations on the mechanical properties of austenitic stainless steels, Int. J. Plast., 16(7-8) (2000) 749-767.

[135] G. W. Powell, E. R. Marshall, W. A. Backofen, Strain-hardening of austenitic stainless steel, ASM Trans., 50 (1958) 478-497.

[136] T. Iwamoto, T. Tsuta, Y. Tomita, Investigation on deformation mode dependence of strain-induced martensitic transformation in TRIP steels and modeling of transformation kinetics, Int. J. Mech. Sci., 40(2-3) (1998) 173-182.

[137] M. Kato, T. Mori, Orientation of martensite formed in Fe-23Ni-5Cr crystals under uniaxial stress along [001], Acta Metall., 25(8) (1977) 951-956.

[138] P. Jacques, Q. Furnémont, T. Pardoen, F. Delannay, On the role of martensitic transformation on damage and cracking resistance in TRIP-assisted multiphase steels, Acta Mater., 49(1) (2001) 139-152.

[139] P. Jacques, Q. Furnémont, F. Lani, T. Pardoen, F. Delannay, Multiscale mechanics of TRIP-assisted multiphase steels. Part I: Characterization and mechanical testing, Acta Mater., 55(11) (2007) 3681-3693.

[140] E. Hall, The deformation and ageing of mild steel, Proceedings of the Physical Society. Section B, 64 (1951) 747-753.

[141] N. Petch, Ductile fracture of polycrystalline α-iron, Philos. Mag., 1 (1956) 186-190.

[142] S. Rajasekhara, P. J. Ferreira, L. P. Karjalainen, A. Kyrolainen, Hall-Petch behaviour in ultra-fine grained AISI 301LN stainless steel, Metall. Mater. Trans. A, 38(6) (2007) 1202-1210.

[143] A. Di Schino, M. Barteri, J. M. Kenny, Effects of grain size on the properties of a low nickel austenitic stainless steel, J. Mater. Sci., 38(23) (2003) 4725-4733.

[144] B. P. Kashyap, K. Tangri, On the Hall-Petch relationship and substructural evolution in type 316L stainless steel, Acta Metall. Mater., 43(11) (1995) 3971-3981.

[145] S. M. G. Singh, K. K. Sangal, Hall-Petch behaviour of 316L austenitic stainless steel at room temperature, Mater. Sci. Technol., 18(2) (2002) 165-172.

[146] S. Brochet, Understanding the role of microstructure of austenitic fine grain stainless steels on fatigue behaviour, PhD thesis, University of Science and Technology of Lille, France, 2007.

[147] M. A. Meyers, C. K. Kumar, Mechanical Metallurgy: Principles and applications, Chapter 14: Grain size Strengthening, Prentice-Hall Inc., (1984) 494-514.

[148] A. W. Thompson, Effect of grain size on work hardening in nickel, Acta Metall., 25 (1977) 83-86.

[149] K. Singh, Strain hardening behaviour of 316L austenitic stainless steel, Mater. Sci. Technol., 20(9) (2004) 1134-1142.

[150] B. P. Kashyap, K. Tangri, Hall-Petch relationship and substructural evolution in boron containing type 316L stainless steel, Acta Mater., 45(6) (1997) 2383-2395.

[151] X. Feaugas, H. Haddou, Grain-size effects on tensile behavior of nickel and AISI 316L stainless steel, Metall. Mater. Trans. A, 34(10) (2003) 2329-2340.

[152] F. Ebrahimi, G. R. Bourne, M. S. Kelly, T. E. Matthews, Mechanical properties of nanocrystalline nickel produced by electro deposition, Acta Metall., 11(3) (1999) 343–350.

[153] C. W. Sinclair, H. Proudhon, J. D. Mithieux, Work-hardening in a fine grained austenitic stainless steel, Mater. Sci. Forum, 539-543 (2007) 4714-4719.

[154] U. F. Kocks, Laws for work-hardening and low-temperature creep, J Eng. Mater. Technol., 98(1) (1976) 76-85.

[155] T. Horiuchi, R. P. Reed, Austenitic stainless steels at low temperatures, chapter-factors influencing the low-temperature dependence of yielding in AISI 316 stainless steels. Plenum Press, New York, 1st edition (1983) 135-158.

[156] S. Nanga, École Nationale Supérieure des Mines de Paris, PhD thesis, France, 2008.

[157] S. Allain, O. Bouaziz, J. Chateau, Thermally activated dislocation dynamics in austenitic FeMnC steels at low homologous temperature, Scr. Mater., 62(7) (2010) 500-503.

[158] T. Lebedkina, M. Lebyodkin, J-P. Chateau, A. Jacques, S. Allain, On the mechanism of unstable plastic flow in an austenitic Fe-Mn-C TWIP steel, Mater. Sci. Eng. A,

519(1-2) (2009) 147-154.

[159] K. Renard, S. Ryelandt, P. Jacques, Characterisation of the Portevin-Le Chatelier effect affecting an austenitic TWIP steel based on digital image correlation, Mater. Sci. Eng. A, 527(12) (2010) 2969-2977.

[160] S. Nanga, A. Pineau, B. Tanguy, P-O. Santacreu, Strain-induced martensitic transformations in two austenitic stainless steels: macro-micro behaviour, 17th European Conference on Fracture (ECF 17), Brno, Czech Republic, (2008) 1373-1380.

[161] R. A. Varin, B. Mazurek, D. Himbeault, Discontinuous yielding in ultrafine-grained austenitic stainless steels, Mater. Sci. Eng., 94 (1987) 109-119.

[162] E. PerdahcIoglu, H. Geijselaers, M. Groen, Influence of plastic strain on deformation-induced martensitic transformations, Scr. Mater., 58(11) (2008) 947-950.

[163] De Mania, The influence of martensitic transformation on the formability of 304L stainless steel sheet, Master's thesis, Massachusetts Institute of Technology, USA, 1995.

[164] M. C. Somani, P. Juntunen, L. P. Karjalainen, R. D. K. Misra, A. Kyröläinen, Enhanced mechanical properties through reversion in metastable austenitic stainless steels, Metall. Mater. Trans. A, 40(3) (2009) 729-744.

[165] A. Di Schino, I. Salvatori J. M. Kenny, Effects of martensite formation and austenite reversion on grain refining of AISI 304 stainless steel, J. Mater. Sci., 37 (2002) 4561-4563.

[166] R. D. K. Misra, S. Nayak, P. K. C. Venkatasurya, V. Ramuni, M. C. Somani, L. P. Karjalainen, Nanograined/ultrafine-grained structure and tensile deformation behavior of shear phase reversion-induced 301 austenitic stainless steel, Metall. Mater. Trans. A, 41(8) (2010) 2162-2174.

[167] A. F. Padilha, R. L. Plaut, P. R. Rios, Annealing of cold-worked austenitic stainless steels, ISIJ Int., 43(2) (2003) 135-143.

[168] A. F. Padilha, P. R. Rios, Decomposition of austenite in austenitic stainless steels, ISIJ Int., 42(4) (2002) 325-327.

[169] B. Weiss, R. Stickler, Phase instabilities during high temperature exposure of 316 austenitic stainless steel, Metall. Trans., 3(4) (1972) 851-866.

[170] K. B. Guy, E. P. Butler, D. R. F. West, Reversion of bcc α′ martensite in Fe–Cr–Ni austenitic stainless steels, Met. Sci., 17(4) (1983) 167-176.

[171] L. F. M. Martins, R. L. Plaut, A. F. Padilha, Effect of carbon on the cold-worked state and annealing behavior of two 18wt%Cr–8wt%Ni austenitic stainless steels, ISIJ Int., 38(6) (1998) 572-579.

[172] Y. Ikegami, R. Nemoto, Effect of thermo-mechanical of high-nitrogen containing treatment Cr-Mn-Ni on mechanical properties austenitic stainless steels, ISIJ Int., 36(7) (1996) 855-861.

[173] D. L. Engelberg, R. C. Newman, T. J. Marrow, Effect of thermo-mechanical process history on grain boundary control in an austenitic stainless steel, Scr. Mater., 59 (2008) 554-557.

[174] R. Novotny, P. Hähner, J. Siegl, P. Haušild, S. Ripplinger, S. Penttilä, A. Toivonen, Stress corrosion cracking susceptibility of austenitic stainless steels in supercritical water conditions, J. Nucl. Mater., 409 (2011) 117-123.

[175] C. Leygraf, I. O. Wallinder, J. Tidblad, T. E. Graedel, Atmospheric Corrosion, John Wiley & Sons, New York, USA, 2nd edition (2000) 1-358.

[176] I. O. Wallinder, J. Lu, S. Bertling, C. Leygraf, Release rates of chromium and nickel from 304 and 316 stainless steel during urban atmospheric exposure- a combined field and laboratory study, Corros. Sci., 44 (2002) 2303-2319.

[177] H. Castro, C. Rodriguez, F. J. Belzunce, A. F. Canteli, Mechanical properties and corrosion behaviour of stainless steel reinforcing bars, J. Mater. Process. Technol., 143-144 (2003) 134-137.

[178] A. Bautista, G. Blanco, F. Velasco, Corrosion behaviour of low-nickel austenitic stainless steels reinforcements: A comparative study in simulated pore solutions, Cem. Concr. Res., 36 (2006) 1922-1930.

[179] L. Gardner, The use of stainless steel in structures, Prog. Struct. Eng. Mater. 7(2) (2005) 45-55.

[180] L. Gardner, K.T. Ng, Temperature development in structural stainless steel sections exposed to fire, Fire Saf. J., 41(3) (2006) 185-203.

[181] L. Gardner, N. R. Baddoo, Fire testing and design of stainless steel structures, J. Constr. Steel Res., 62(6) (2006) 532-543.

[182] Y. Sakumoto, T. Nakazato, A. Matsuzaki, High-temperature properties of stainless steel for building structures, J. Struct. Eng., 122(4) (1996) 399-406.

[183] L. Di Sarno, A. S. Elnashai, Special metals for seismic retrofitting of steel buildings, Prog. Struct. Eng. Mater., 5(2) (2003) 60-76.

[184] L. Di Sarno, A. S. Elnashai, D. A. Nethercot, Seismic retrofitting of framed structures with stainless steel, J. Constr. Steel Res., 62(1-2) (2006) 93-104.

[185] S. Sahin, M. Ubeyli, A review on the potential use of austenitic stainless steels in nuclear fusion reactors, J. Fusion Energ., 27(4) (2008) 271-277.

[186] D. N. Wasnik, V. Kain, I. Samajdar, B. Verlinden, P. K. De, Resistance to sensitization and intergranular corrosion through extreme randomization of grain boundaries, Acta Mater., 50 (2002) 4587-4601.

[187] S. H. Lee, J. C. Lee, J. Y. Choi, W. J. Nam, Effects of deformation strain and aging temperature on strain aging behavior in a 304 stainless steel, Met. Mater. Int., (16) (1) (2010) 21-26.

[188] R. J. Hill, C. J. Howard, Quantitative phase analysis from neutron powder diffraction data using the Rietveld method, J. Appl. Crystallogr., 20 (1987) 467-474.

[189] H. E. Kissinger, Reaction kinetics in differential thermal analysis, Anal. Chem., 29 (11) (1957) 1702-1706.

[190] M. W. Bowkett, S. R. Keown, D. R. Harries, Quench-induced and deformation-induced structures in two austenitic stainless steels. J. Mater. Sci., 16(11) (1982) 499-518.

[191] K. Mumtaz, S. Takahashi, J. Echigoya, Magnetic measurements of martensitic transformation in austenitic stainless steel after room temperature rolling, J. Mater. Sci. 39(1) (2004) 85-97.

[192] I. Karaman, H. Sehitoglu, Y. I. Chumlyakov, H. J. Maier, The deformation of low-stacking-fault-energy austenitic steels, JOM, Miner. Metal. Mater. Soc. (TMS), 54(7) (2002) 31-37.

[193] M. Güner, E. Güler, H. Aktas, Effect of homogenization temperature on the martensitic transformation kinetics in a Fe-32%Ni-0.4%Cr alloy, Mater. Charact., 59(4) (2008) 498-502.

[194] H. Nakagawa, T. Miyazaki, H. Yokota, Effects of ageing temperature on the microstructure and mechanical properties of 1.8Cu-7.3Ni-15.9Cr-1.2Mo-low C, N martensitic precipitation hardening stainless steel, J. Mater. Sci., 35(9) (2000) 2245-2253.

[195] M. M. Shea, A. K. Sachdev, Influence of strain rate on the mechanical behavior of a high carbon iron-nickel austenite, Scr. Metall., 18(10) (1984) 1181-1184.

[196] A. K. Sachdev, M. M. Shea, Twinning in metastable Fe-Ni-C austenite during elevated temperature deformation, Mater. Sci. Eng., 95 (1987) 31-36.

[197] A. K. Sachdev, M. M. Shea, Influence of strain rate and temperature on the deformation behavior of a metastable high carbon iron-nickel austenite, Metall. Trans. A, 16(3) (1985) 445-452.

[198] P. J. Brofman, G. S. Ansell, On the effect of carbon on the stacking fault energy of austenitic stainless steels, Metall. Trans. A, 9(6) (1978) 879-880.

[199] R. W. Rathbun, D. K. Matlock, J. Speer, Strain agingbehavior of austenitic stainless steels containing strain induced martensite, Scr. Mater., 42 (2000) 887–891.

[200] R. Montanari, Increase of martensite content in cold rolled AISI 304 steel produced by annealing at 400°C, Mater. Lett., 10(1-2) (1990) 57-61.

[201] H. K. Yeddu, B. A. Shaw, M. A. J. Somers, Effect of thermal cycling on martensitic transformation and mechanical strengthening of stainless steels – A phase-field study, Mater. Sci. Eng. A, 690 (2017) 1-5.

[202] H. N. Nan, C. G. Lee, D. W. Suh, S. J. Kim, A microstructure-based analysis for transformation induced plasticity and mechanically induced martensitic transformation, Mater. Sci. Eng. A, 485(1-2) (2008) 224-233.

[203] H. N. Nan, C. S. Oh, G. Kim, O. Kwon, Design method for TRIP-aided multiphase steel based on a microstructure-based modelling for transformation-induced plasticity and mechanically induced martensitic transformation, Mater. Sci. Eng. A, 499(1-2) (2009) 462-468.

[204] P. V. Morra, A. J. Böttger, E. J. Mittemeijer, Decomposition of iron-based martensite. a kinetic analysis by means of differential scanning calorimetry and dilatometry, J. Therm. Anal. Calorim., 64(3) (2001) 905-914.

[205] H. Kessler, W. Pitsch, On the nature of the martensite to austenite reverse transformation, Acta Metall., 15(2) (1967) 401-405.

[206] R. L. Orr, J. Chipman, Thermodynamic functions of iron, Trans. Am. Inst. Min. Metall. Pet. Eng., 239 (1967) 630-633.

[207] B. Lee, S. Millman, I. L. MacDougall, S. R. Keown, B. B. Argent, Enthalpy of the martensitic transformation in steels containing nickel and chromium, Met. Sci., 11(7) (1977) 261-271.

[208] E. De Moor, S. Lacroix, L. Samek, J. Penning, J. G. Speer, Dilatometric study of the quench and partitioning process, proceedings of the 3rd international advanced structural steels conference, Gyeongju, Korea, (2006) 873-878.

[209] A. K. De, S. Vandeputte, B. C. De Cooman, Kinetics of strain aging in bake hardening ultra low carbon steel—a comparison with low carbon steel, J. Mater. Eng. Perform., 10(5) (2001) 567-575.

[210] M. Fujita, Y. Kaneko, A. Nohara, H. Saka, R. Zauter, H. Mughrabi, Temperature dependence of the dissociation width of dislocations in a commercial 304L stainless steel, ISIJ Int., 34(8) (1994) 697-703.

[211] M. Cohen, Self-diffusion during plastic deformation, Trans. JIM, 11 (3) (1970) 145-151.

[212] W. S. Owen, The effect of silicon on the kinetics of tempering, Trans. Am. Soc. Met., 46 (1954) 812-829.

[213] P. L. Gruzin, V. G. Kostogonov, P. A. Platanov, Use of carbon isotope ^{14}C for investigation of the diffusion of carbon in steel, Doklady Akad. Nauk SSSR, 100 (1955) 1069-1072.

[214] F. S. Buffington, K. Hirano, M. Cohen, Self diffusion in iron, Acta Metall., 9(5) (1961) 434-439.

[215] A. W. Bowen, G. M. Leak, Solute diffusion in alpha-and gamma-iron, Metall. Mater. Trans. B, 1(6) (1970) 1695-1700.

[216] Y. Estrin, H. Mecking, A unified phenomenological description of work hardening and creep based on one-parameter models, Acta Metall., 32 (1984) 57-70.

[217] X. Feaugas, On the origin of the tensile flow stress in the stainless steel AISI 316L at 300 K: Back stress and effective stress, Acta Metall., 47(13) (1999) 3617-3632.

[218] E. I. Samuel E, B. K. Choudhary, K. B. S. Rao, Influence of temperature and strain rate on tensile work hardening behaviour of type 316 LN austenitic stainless steel, Scr. Mater., 46 (7) (2002) 507-512.

[219] S. K. Ray, K. G. Samuel, P. Rodriguez, Anomalies in the tensile work-hardening in type-316 stainless-steel at 300 K, Trans. Indian Inst. Met., 45 (4) (1992) 257-260.

[220] D. J. Michel, J. Moteff, A. J. Lovell, Substructure of type 316 stainless steel deformed in slow tension at temperatures between 21°C and 216°C, Acta Metall., 21 (1973) 1269-1277.

[221] B. P. Kashyap, K. Mc Taggart, K. Tangri, Study on the substructure evolution and flow behaviour in type 316L stainless steel over the temperature range 21–900°C, Philos. Mag., 57 (1) (1988) 97-114.

[222] Chang Ye, A. Telang, A. S. Gill, S. Suslov, Y. Idell, K. Zweiacker, J. M. K. Wiezorek, Z. Zhou, D. Qian, S. R. Mannava, V. K. Vasudevan, Gradient nanostructure and residual stresses induced by ultrasonic nano-crystal surface modification in 304 austenitic stainless steel for high strength and high ductility, Mater. Sci. Eng. A, 613(2014) 274-288.

[223] S Qu, CX Huang, YL Gao, G Yang, SD Wu, QS Zang, ZF Zhang, Tensile and compressive properties of AISI 304L stainless steel subjected to equal channel angular pressing, Mater. Sci. Eng. A, 475 (2008), 207-216.

[224] A. P. Zhilyaev, T. G. Langdon, Using high-pressure torsion for metal processing: Fundamentals and applications, Prog. Mater. Sci. 53(6) (2008) 893-979.

[225] Y. Saito, H. Utsunomiya, N. Tsuji, T. Sakai, Novel ultra-high straining process for bulk materials—development of the accumulative roll-bonding (ARB) process,
Acta Mater. 47(2) (1999), 579-583.

[226] A. Momeni, S. M. Abbasi, Repetitive thermo mechanical processing towards ultra fine grain structure in 301, 304 and 304L stainless steels, J. Mater. Sci. Technol., 2011, 27(4), 338-343.

[227] M. Naghizadeh, H. Mirzadeh, Microstructural Evolutions During Annealing of Plastically Deformed AISI 304 Austenitic Stainless Steel: Martensite Reversion, Grain Refinement, Recrystallization, and Grain Growth, Metal. Mater. Trans. A, 47(8) (2016), 4210-4216.

[228] M. Shirdel, H. Mirzadeh, M. H. Parsa, Nano/ultrafine grained austenitic stainless steel through the formation and reversion of deformation-induced martensite: Mechanisms, microstructures, mechanical properties, and TRIP effect, Mater. Charact. 103 (2015) 150-161.

[229] B. R. Kumar, S. Sharma, B. P. Kashyap, N. Prabhu, Ultrafine grained microstructure tailoring in austenitic stainless steel for enhanced plasticity, Mater. Des. 68 (2015) 63-71.

[230] S. Fréchard, A. Redjäımia, E. Lach, A. Lichtenberger, Mechanical behaviour of nitrogen-alloyed austenitic stainless steel hardened by warm rolling, Mater. Sci. Eng. A, 415 (2006) 219-224.

[231] A. K. Panda, P. K. Ray, R. I. Ganguly, Effect of thermomechanical treatment parameters on mechanical properties of duplex ferrite–martensite structure in dual phase steel, Mater. Sci. Technol. 16(6) (2000) 648-656.

[232] X. Li, T. Li, K. H. Lo, C. T. Kwok, F. Chen, Influences of thermomechanical treatments on the cryogenic treatability of a slightly unstable austenitic stainless steel, Mater. Manufact. Proc. 32(11) (2017) 1239-1247.

[233] S. K. Pradhan, T. S. Prithiv, S. Mandal, Through-thickness microstructural evolution during grain boundary engineering type thermomechanical processing and its implication on sensitization behavior in austenitic stainless steel, Mater. Charac. 134 (2017) 134-142.

[234] H. Mirzadeh, A Simplified Approach for Developing Constitutive Equations for Modeling and Prediction of Hot Deformation Flow Stress, Metal. Mater. Trans. A, 46(9) (2015) 4027–4037.

[235] H. Mirzadeh, M. H. Parsa, D. Ohadi, Hot deformation behavior of austenitic stainless steel for a wide range of initial grain size, Mater. Sci. Eng. A, 569 (2013) 54-60.

[236] D. Samantaray, S. Mandal, C. Phaniraj, A. K. Bhaduri, Flow behaviour and microstructural evolution during hot deformation of AISI type 316 L(N) austenitic stainless steel, Mater. Sci. Eng. A, 528 (2011) 8565-8572.

[237] S. Sankaran, V. S. Sarma,V. Kaushik, K. A. Padmanabhan, Thermomechanical processing and characterisation of multi-phase microstructures in a V-bearing medium carbon micro-alloyed steel, J. Mater. Proc. Technol. 139(1-3) (2003) 642-647.

[238] A. Ghosh, S. Das, S. Chatterjee, B. Mishra, P. R. Rao, Influence of thermo-mechanical processing and different post-cooling techniques on structure and properties of an ultra low carbon Cu bearing HSLA forging, Mater. Sci. Eng. A, 348(1-2) (2003) 299-308.

[239] H. W. Zhang, Z. K. Hei, G. Liu, J. Lu, K. Lu, Formation of nanostructured surface layer on AISI 304 stainless steel by means of surface mechanical attrition treatment, Acta Mater., 51 (2003) 1871-1881.

[240] R. Mohammed, G. M. Reddy, K. S. Rao, Microstructure and pitting corrosion of shielded metal arc welded high nitrogen stainless steel, Defence Technol. 11(3) (2015) 237-243.

[241] X. Tao, C. Li, L. Han, J. Gu, Microstructure evolution and mechanical properties of X12CrMoWVNbN10-1-1 steel during quenching and tempering process J. Mater. Res. Technol., 5(1) (2016), 45-57.

[242] S. Sadeghpour, A. Kermanpur, A. Najafizadeh, Influence of Ti microalloying on the formation of nanocrystalline structure in the 201L austenitic stainless steel during martensite thermomechanical treatment, Mater. Sci. Eng. A, 584 (2013) 177-183.

[243] Y. Tian, O. I. Gorbatov, A. Borgenstam, A.V. Ruban, P. Hedstrő̃m, Deformation microstructure and deformation-induced martensite in austenitic Fe-Cr-Ni alloys depending on stacking fault energy, Metall. Mater. Trans. A, 48(1) (2017) 1-7.

[244] K. Barat, H. N. Bar, D. Mandal, H. Roy, S. Sivaprasad , S. Tarafder, Low temperature tensile deformation and acoustic emission signal characteristics of AISI 304LN stainless steel, Mater. Sci. Eng. A, 527 (2010) 7334-7339.

[245] D. Witkin, Z. Lee, R. Rodriguez, S. Nutt, E. Lavernia, Al–Mg alloy engineered with bimodal grain size for high strength and increased ductility, Scr. Mater., 49 (2003) 297-302.

[246] N. K. Tewary, S. K. Ghosh, S. Bera, D. Chakrabarti, S. Chatterjee, Influence of cold rolling on microstructure, texture and mechanical properties of low carbon high Mn TWIP steel, Mater. Sci. Eng. A, 615 (2014) 405-415.

[247] Z. Xu, Z. Ding, L. Dong, B. Liang, Characterization of $M_{23}C_6$ carbides precipitating at grain boundaries in 100Mn13 Steel, Metall. Mater. Trans. A, 47 (2016) 4862-4868.

[248] K. M. Rahman, V. A. Vorontsov, D. Dye, The effect of grain size on the twin initiation stress in a TWIP steel, Acta Mater., 89 (2015) 247-257.

[249] Y. F. Shen, X. X. Li, X. Sun, Y. D. Wang, L. Zuo, Twinning and martensite in a 304 austenitic stainless steel, Mater. Sci. Eng. A, 552 (2012) 514-522.

[250] K. J. Lee, M. S. Chun, M. H. Kim, J. M. Lee, A new constitutive model of austenitic stainless steel for cryogenic applications, Comput. Mater. Sci., 46 (2009) 1152-1162.

[251] Y. F. Shen, X. X. Li, X. Sun, Y. D. Wang, L. Zuo, Twinning and martensite in a 304 austenitic stainless steel, Mater. Sci. Eng. A, 552 (2012) 514-522.

[252] C. Gauss, I. R. Souza Filho, M. J. R. Sandim, P. A. Suzuki, A. J. Ramirez, H. R. Z. Sandim, In situ synchrotron X-ray evaluation of strain-induced martensite in AISI 201 austenitic stainless steel during tensile testing, Mater. Sci. Eng. A, 651 (2016) 507-516.

[253] H. Mirzadeh, J. M. Cabrera, A. Najafizadeh, P. R. Calvillo, EBSD study of a hot deformed austenitic stainless steel, Mater. Sci. Eng. A, 538 (2012) 236 - 245.

[254] J. Lu, L. Hultman, E. Holmström, K. H. Antonsson, M. Grehk, W. Li, L. Vitos, A. Golpayegani, Stacking fault energies in austenitic stainless steels, Acta Mater., 111 (2016) 39-46.

[255] S. S. F. de Dafé, F. L. Sicupira, F. C. S. Matos, N. S. Cruz, D. R. Moreira, D. B. Santos, Effect of cooling rate on (ε, α′) martensite formation in twinning/transformation-induced plasticity Fe–17Mn–0.06C Steel, Mater. Res., 16(6) (2013) 1229-1236.

[256] A. Viswanath, B. P. C. Rao, S. Mahadevan, P. Parameswaran, T. Jayakumar, B. Raj, Nondestructive assessment of tensile properties of cold worked AISI type 304 stainless steel using nonlinear ultrasonic technique, J. Mater. Process. Technol., 211 (2011) 538–544.

[257] J. Talonen, H. Hänninen, Formation of shear bands and strain-induced martensite during plastic deformation of metastable austenitic stainless steels, Acta Mater., 55 (2007) 6108-6118.

[258] G. Kurdjumov, G. Sachs, Over the mechanisms of steel hardening, Z. Phys., 64 (1930) 325-343.

[259] S. Mandal, N. K. Tewary, S. K. Ghosh, D. Chakrabarti, S. Chatterjee, Thermo-mechanically controlled processed ultrahigh strength steel: microstructure, texture and mechanical properties, Mater. Sci. Eng. A, 663 (2016) 126-140.

[260] P. M. Kelly, The martensite transformation in steels with low stacking fault energy, Acta Metall., 13(6) (1965) 635-646.

[261] F. J. Humphreys, Quantitative metallography by electron backscattered diffraction, J. Microsc., 195(3) (1999) 170-185.

[262] H. Jazaeri, F. J. Humphreys, Quantifying recrystallization by electron backscatter diffraction, J. Microsc., 213 (2004) 241-246.

[263] L. Jiang, X. Ye, C. Cui, H. Huang, B. Leng, Z. Li, X. Zhou, Intermediate temperature embrittlement of one new Ni-26W-6Cr based superalloy for molten salt reactors,

Mater. Sci. Eng. A, 668 (2016) 137-145.

[264] A. W. Wilson, J. D. Madison, G. Spanos, Determining phase volume fraction in steels by electron back scattered diffraction: Scr. Mater. 45 (2001) 1335-1340.

[265] E. Cakmak, H. Choo, Jun-Yun Kang, Y. Ren, Relationships between the phase transformation kinetics, texture evolution, and microstructure development in a 304L stainless steel under biaxial loading conditions: synchrotron X-ray and electron backscatter diffraction studies, Metall. Mater. Trans. A, 46(A) (2015) 1860-1877.

[266] J. Zheng, C. Li, S. He, B. Ma, Y. Song, Deformation twin and martensite in the Fe–36%Ni alloy during cryorolling, Mater. Sci. Technol., (2017) 1-7.

[267] Jin-tao Shi, Long-gang Hou, Jin-rongZuo, Lin-zhongZhuang, Ji-shan Zhang, Effect of cryogenic rolling and annealing on the microstructure evolution and mechanical properties of 304 stainless steel, Int. J. Miner. Metall. Mater., 24 (2017) 638-644.

[268] B. Roy, R. Kumar, J. Das, Effect of cryorolling on the microstructure and tensile properties of bulk nano-austenitic stainless steel, Mater. Sci. Eng. A, 631 (2015) 241-247.

[269] M. Odnobokova, A. Belyakov, N. Enikeev, D. A. Molodov, R. Kaibyshev, Annealing behavior of a 304L stainless steel processed by large strain cold and warm rolling, Mater. Sci. Eng. A, 689 (2017) 370-383.

[270] R. D. K. Misra, J. Hu, I. V. S. Yashwanth, V. S. A. Challa, L.-X. Du, G.-S. Sun, H. Xie, Phase reverted transformation-induced nanograined microalloyed steel: Low temperature superplasticity and fracture, Mater. Sci. Eng. A, 668 (2016) 105-111.

[271] R. D. K. Misra, S. Nayak, S. A. Mali, J. S. Shah, M. C. Somani, L. P. Karjalainen, On the significance of nature of strain-induced martensite on phase-reversion-induced nanograined/ultrafine-grained austenitic stainless steel, Metall. Mater. Trans. A, 41(A) (2010) 3-12.

[272] M. C. Somani, L. P. Karjalainen, R. D. K. Misra, P. Juntunen, A. Kyröläinen, In Proc. 6th Eur. Stainless Steel Conf. Science and Market, Helsinki, The Swedish Steel Producers’ Association, Stockholm, Sweden, (2008) 519-524.

[273] K. Tomimura, S. Takaki, S. Tanimoto, Y. Tokunaga, Optimal refining chemical composition in Fe-Cr-Ni alloys for ultra grain by reversion from deformation induced martensite, ISIJ Int., 31 (1991) 721-727.

[274] M. Eskandari, A. Najafizadeh, A. Kermanpur, Effect of strain-induced martensite on the formation of nanocrystalline 316L stainless steel after cold rolling and annealing, Mater. Sci. Eng. A, 519 (2009) 46-50.

[275] X. H. Chen, J. Lu, L. Lu, K. Lu, Tensile properties of a nanocrystalline 316L austenitic stainless steel, Scr. Mater., 52 (2005) 1039-1044.

[276] R. D. K. Misra, B. R. Kumar, M. Somani, P. Karjalainen, Deformation processes during tensile straining of ultrafine/nanograined structures formed by reversion in metastable austenitic steels, Scr. Mater., 59 (2008) 79-82.

[277] M. Karimi, A. Najafizadeh, A. Kermanpur, M. Eskandari, Effect of martensite to austenite reversion on the formation of nano/submicron grained AISI 301 stainless steel, Mater. Charact., 60 (2009) 1220-1223.

[278] R. Fu, L. Qiu, T. Wang, C. Wang, Y. Zheng, Cryogenic deformation microstructures of 32Mn–7Cr–1Mo–0.3N austenitic steels, Mater. Charact., 55 (2005) 355-361.

[279] N. Stepanov, M. Tikhonovsky, N. Yurchenko, D. Zyabkin, M. Klimova, S. Zherebtsov, A. Efimov, G. Salishchev, Effect of cryo-deformation on structure and properties of CoCrFeNiMn high-entropy alloy, Intermetallics, 59 (2015) 8-17.

[280] T. S. Wang, J. G. Peng, Y. W. Gao, F. C. Zhang, T. F. Jing, Microstructure of 1Cr18Ni9Ti stainless steel by cryogenic compression deformation and annealing, Mater. Sci. Eng. A, 407 (2005) 84-88.

[281] F. Forouzan, A. Najafizadeh, A. Kermanpur, A. Hedayati, R. Surkialiabad, Production of nano/submicron grained AISI 304L stainless steel through the martensite reversion process, Mater. Sci. Eng. A, 527 (2010) 7334-7339.

[282] P. Dastur, A. Zarei-Hanzaki, M. H. Pishbin, M. Moallemi, H. R. Abedi, Transformation and twinning induced plasticity in an advanced high Mn austenitic steel processed by martensite reversion treatment, Mater. Sci. Eng. A, 696 (2017) 511-519.

[283] G. S. Sun, L. X. Du, J. Hu, H. Xie, H. Y. Wu, R. D. K. Misra, Ultrahigh strength nano/ultrafine-grained 304 stainless steel through three-stage cold rolling and annealing treatment, Mater. Charact., 110 (2015) 228-235.

[284] R. D. K. Misra, Z. Zhang, P. K. C. Venkatasurya, M. C. Somani, L. P. Karjalainen, Martensite shear phase reversion-induced nanograined/ultrafine-grained Fe–16Cr–10Ni alloy: The effect of interstitial alloying elements and degree of austenite stability on phase reversion, Mater. Sci. Eng. A, 527 (2010) 7779-7792.

[285] S-J. Lee, Y-M. Park, Y-K. Lee, Reverse transformation mechanism of martensite to austenite in a metastable austenitic alloy, Mater. Sci. Eng. A, 515 (2009) 32-37.

[286] T. Maki, T. Hazama, S. Shimookaand, I. Tamura, Effect of pre treatment on the temperature of the reverse transformation from martensite to austenite in an Fe-33per cent Ni alloy, J. Soc. Mater. Sci., Japan, 24 (1975) 296-300.

[287] D-S. Leem, Y-D. Lee, J-H. Jun, C-S. Choi, Amount of retained austenite at room temperature after reverse transformation of martensite to austenite in an Fe–13%Cr–7%Ni–3%Si martensitic stainless steel, Scr. Mater., 45(7) (2001) 767-772.

[288] Y. Zhang, X. T. Jing, B. Z. Lou, F. S. Shen, F. Z. Cui, Mechanism and reversible behaviour of the $\alpha' \rightarrow \gamma$ transformation in 1Cr18Ni9Ti stainless steel, J. Mater. Sci., 34 (1999) 3291-3296.

[289] L. Kaufman, E.V. Clougherty, R. J. Weiss, The lattice stability of metals-III. Iron, Acta Metall., 11 (1963) 303-335.

[290] A. Rezaee, A. Najafizadeh, A. Kermanpur, M. Moallemi, The influence of reversion annealing behavior on the formation of nanograined structure in AISI 201L austenitic stainless steel through martensite treatment, Mater. Des., 32 (2011) 4437-4442.

[291] E. Dryzek, M. Sarnek, M. Wróbel, Reverse transformation of deformation-induced martensite in austenitic stainless steel studied by positron annihilation, J. Mater. Sci., 49 (2014) 8449-8458.

[292] M. Moallemi, A. Kermanpur, A. Najafizadeh, A. Rezaee, H. S. Baghbadorani, P. D. Nezhadfar, Deformation-induced martensitic transformation in a 201 austenitic steel: The synergy of stacking fault energy and chemical driving force, Mater. Sci. Eng. A, 653 (2016) 147-152.

[293] H. Springer, M. Belde, D. Raabe, Bulk combinatorial design of ductile martensitic stainless steels through confined martensite-to-austenite reversion, Mater. Sci. Eng. A, 582 (2013) 235–244.

[294] H. S. Baghbadorani, A. Kermanpur, A. Najafizadeh, P. Behjati, M. Moallemi, A. Rezaee, Influence of Nb-microalloying on the formation of nano/ultrafine-grained microstructure and mechanical properties during martensite reversion process in a 201-type austenitic stainless steel, Metall. Mater. Trans. A, 46 (2015) 3406-3413.

[295] L. G. Garza-Martinez, G. A. Thomas, A. S. Gill, High manganese 3rd generation advanced high strength steels, Patent US20160340763, 2016.

[296] C. Haase, O. Kremer, W. Hu, T. Ingendahl, R. Lapovok, D. A. Molodov, Equal-channel angular pressing and annealing of a twinning-induced plasticity steel: Microstructure, texture, and mechanical properties, Acta Mater., 107 (2016) 239-253.

[297] J. Hu, L-X. Du, G-S. Sun, H. Xie, R. D. K. Misra, The determining role of reversed austenite in enhancing toughness of a novel ultra-low carbon medium manganese high strength steel, Scr. Mater., 104 (2015) 87–90.

LIST OF PUBLICATIONS

1. S. K. Ghosh, **P. Mallick** and P. P. Chattopadhyay: Effect of reversion of strain induced martensite on microstructure and mechanical properties in an austenitic stainless steel, Journal of Materials Science, 46 (2011) 3480-3487.

2. S. K. Ghosh, **P. Mallick** and P. P. Chattopadhyay: Effect of cold deformation on phase evolution and mechanical properties in an austenitic stainless steel for structural and safety applications, Journal of Iron and Steel Research, International, 19 (4) (2012) 63-68.

3. S. K. Ghosh, Shikhar Jha, **P. Mallick** and P. P. Chattopadhyay: Influence of mechanical deformation and annealing on kinetics of martensite in a stainless steel, Materials and Manufacturing Processes, 28 (3) (2013) 249-255.

4. **P. Mallick**, N. K. Tewary, S. K. Ghosh and P. P. Chattopadhyay: Effect of cryogenic deformation on microstructure and mechanical properties of 304 austenitic stainless steel, Materials Characterization, 133 (2017) 77-86.

5. **P. Mallick**, N. K. Tewary, S. K. Ghosh, and P. P. Chattopadhyay: Microstructure-tensile property correlation in 304 stainless steel after cold deformation and austenite reversion, Materials Science & Engineering A, 707 (2017) 488-500.

6. **P. Mallick**, N. K. Tewary, S. K. Ghosh, and P. P. Chattopadhyay: Effect of TMCP on Microstructure and Mechanical Properties of 304 Stainless Steel; Steel Research International, 89 (8) (2018) 1-7.

J Mater Sci (2011) 46:3480–3487
DOI 10.1007/s10853-011-5253-x

Effect of reversion of strain induced martensite on microstructure and mechanical properties in an austenitic stainless steel

S. K. Ghosh · P. Mallick · P. P. Chattopadhyay

Received: 27 November 2010 / Accepted: 6 January 2011 / Published online: 19 January 2011

Abstract Effect of reversion of strain induced α' martensite on mechanical properties of an austenitic stainless steel has been examined. The α' martensite formed by cold rolling (40%) at 0 °C has been reverted to austenite by carrying out annealing in the temperature range of 300–800 °C for 1 h. Microstructural investigation has demonstrated the enhanced reversion with increasing annealing temperature without any perceptible grain growth up to 800 °C. X-ray diffraction (XRD) analysis has revealed that 40% cold rolling has resulted in the formation of 32% martensite. The residual martensite content has been found to be about 8% after reversion at 800 °C. Different stages of reversion behavior has been examined by differential scanning calorimetric measurement. The variation of $d\sigma/d\varepsilon$ with ε is examined to identify different stages of work hardening of the investigated steel. Both tensile strength and percent elongation values increase with increasing annealing temperature up to 500 °C. Beyond that annealing treatment results in the drop of tensile strength value with the consequent increase in percent elongation. Attractive strength–ductility combination (22.80 GPa%) has been achieved after annealing of the 40% cold deformed specimen at 800 °C for 1 h. The fractographic observation corroborates the tensile results.

Introduction

Austenite in steel exhibits deformation induced transformation into martensite within the temperature range marked by M_S and M_{d30} as the lower and upper limits, respectively, following the sequence of γ(FCC) → ε (HCP) → α'(BCC) transformation [1, 2]. The amount of α' martensite depends on the deformation methods, amount of plastic strain, strain rate, and temperature [3–5]. Stacking fault energy (SFE) of austenite which is a function of temperature and composition governs the dominant deformation mechanism. For higher SFE (>20 mJ/m^2) the deformation mode is shifted from ε martensite formation to deformation twining and then slip [6]. Plastic deformation of the austenite creates the proper defect structure which acts as the embryo for the transformation product. In austenitic stainless steels, embryos are formed at the intersections of shear bands, e.g., stacking faults, twins, etc. [4, 7, 8]. Usually ε martensite is formed at the low deformation level (i.e., 5–10%) and at the higher strain levels, the α' martensite increases at the expense of ε martensite [9]. The morphology of the transformation product is typically lath-like [1, 4]. In respect of the effect of composition, at considerably lower temperatures, δ-ferrite forming elements like, Cr, Si, Mo act as strong austenite stabilizer in the same way as Ni, Mn, C, N, etc. The upper limit of the transformation temperature is obtained as [3]:

$$\begin{aligned} M_{d30}(^\circ C) = 413 - 462(C + N) - 9.2(Si) - 8.1(Mn) \\ - 13.7(Cr) - 9.5(Ni) - 18.5(Mo) \end{aligned} \quad (1)$$

where elements are in wt%.

Reversion of strain induced martensite to austenite (e.g., $\alpha' \rightarrow \gamma$) improves mechanical properties by grain refinement [10, 11] which is known to improve the both strength and toughness of structural steels. Grain refinement

S. K. Ghosh (✉) · P. Mallick · P. P. Chattopadhyay
Department of Metallurgy and Materials Engineering,
Bengal Engineering and Science University, Shibpur,
Howrah 711103, India
e-mail: skghosh@metal.becs.ac.in

JOURNAL OF IRON AND STEEL RESEARCH, INTERNATIONAL. 2012, 19(4): 63-68

Effect of Cold Deformation on Phase Evolution and Mechanical Properties in an Austenitic Stainless Steel for Structural and Safety Applications

S K Ghosh, P Mallick, P P Chattopadhyay

(Department of Metallurgy and Materials Engineering, Bengal Engineering and Science University,
Shibpur, Howrah 711 103, India)

Abstract: The effects of cold deformation on the formation of strain induced α' martensite and mechanical properties of an austenitic stainless steel have been examined. X-ray diffraction analysis has revealed that 30% and 40% cold rolling have resulted in the formation of 24% and 31.5% martensite respectively. Microstructural investigation has demonstrated that the formation of martensite is enhanced with increase in the percent deformation at 0 ℃. Investigation of mechanical properties reveals that hardness, yield strength and tensile strength values increase where as percent elongation drops with increasing deformation. The fractographic observation corroborates the tensile results. Examination of sub-surface at the fractured end of the tensile sample manifests that void/microcrack nucleation occurs in the interfacial regions of the martensite phase as well as at the austenite-martensite interface.

Key words: austenitic stainless steel; cold deformation; martensite; mechanical property

Nearly 70% of the entire production of stainless steel is austenitic stainless steel which possesses excellent cryogenic properties, formability, anticorrosion and biocompatibility. This grade of steel has been found extensive application in low temperature technology, chemical industry, ocean technology, food processing industry, biomedicine, petrochemical processing etc[1]. 304 category of austenitic stainless steel has been slotted for the specific applications for achieving architectural excellence, e. g. Gateway to the West Arch in St. Louis, Missouri, Cleveland Federal Office Building, dome of the Chrysler Building in New York City, etc because of its excellent corrosion resistance property, low maintenance and superior surface finish[2].

As received austenitic stainless steel (hot rolled sheets and plates) exhibits low yield strength and ultimate tensile strength with excellent total elongation. Lower level of achievable strength often limits their application for structural and other safety purposes. Judicious plastic deformation has been found to be effective in improving the strength of austenitic stainless steel[3]. The austenitic phase transforms into martensite upon deformation. Martensite so produced offers higher strength as well as toughness owing to the presence of retained austenite. This process of cold working does not necessitate additional heat treatment (hardening and tempering). Thus, the approach enhances the versatility and usefulness of the steel for structural and safety applications by the way of improvement of strength with admissible sacrifice in ductility.

Formation of deformation induced martensite (DIM) depends on various parameters such as chemistry of material, temperature, rate of deformation (strain rate), strain, stress state, stacking fault energy (SFE), pre-strain etc[4-9]. Stacking fault energy of austenite which is a function of temperature and composition governs the dominant deformation mechanism. For higher stacking fault energy (>20 mJ/m^2) the deformation mode is shifted from ε martensite formation to deformation twining and then slip[10]. Plastic deformation of the austenite creates the proper defect structure which acts as the embryo for the transformation product. In austenitic stainless steels, embryos are formed at the intersections of shear bands, e. g. stacking faults, twins etc[11-13]. Usually ε martensite is formed at the low deformation level (i. e., 5%−10%) and at the higher strain levels, the α' martensite increases at the expense of

---

Biography: S K Ghosh(1970—), Male, Doctor, Associate Professor; **E-mail**: skghosh@metal. becs. ac. in; **Received Date**: January 5, 2011

Materials and Manufacturing Processes, 28: 249–255, 2013
Copyright © Taylor & Francis Group, LLC
ISSN: 1042-6914 print/1532-2475 online
DOI: 10.1080/10426914.2012.667893

Influence of Mechanical Deformation and Annealing on Kinetics of Martensite in a Stainless Steel

S. K. Ghosh, Shikhar Jha, P. Mallick, and P. P. Chattopadhyay

Department of Metallurgy and Materials Engineering, Bengal Engineering and Science University, Shibpur, Howrah, India

An attempt has been made to understand the kinetics concerning the manufacturing schedule of high strength 304 stainless steel comprising formation of strain-induced α' martensite in the course of cold rolling (25%) at 0°C and its reversion during annealing in the temperature range of 300–800°C for 1 h. Increase in reversion with increasing annealing temperature without any perceptible grain growth up to 800°C has been demonstrated by the microstructural investigation. X-ray diffraction analysis has revealed that the 25% cold rolling has resulted in the formation of 20% deformation induced martensite which after annealing at 800°C has been reduced to 8%. Different stages of reversion behaviour have been envisaged by carrying out differential scanning calorimetry. Activation energies of the reactions involved during reversion have been determined by Kissinger method. Results are compared and found to be in good agreement with the published data.

Keywords Activation energy; Austenitic stainless steel; Differential scanning calorimetry; Reversion.

INTRODUCTION

304 and 304(L) austenitic stainless steels, processed under various manufacturing schedules, have been found to be amenable to advanced fabrication and machining techniques [1–3]. High-strain hardening property of the steels extends its application in the areas like high-strength structural and safety applications. The commercially available forms of the steels *viz.*, blooms, billets, slabs, etc., are subjected to further processing steps like rolling, heat treatment, descaling, and polishing for production of the finished products.

Deformation processing, under the manufacturing schedule of the austenitic stainless steel, results in strain-induced transformation following the sequence of γ (FCC)$\rightarrow$$\varepsilon$(HCP)$\rightarrow$$\alpha'$(BCC) transformation [4, 5]. Formation of deformation-induced martensite exerts significant influence on the manufacturing process and, in turn, the target properties of the product [6–8]. The amount of α' martensite depends on the deformation methods, amount of plastic strain, strain rate and temperature [9–11]. For higher stacking fault energy ($>20\,\mathrm{mJ/m^2}$), the deformation mode is shifted from ϵ martensite formation to deformation twining and then slip [12]. Plastic deformation of the austenite creates the embryo which forms at the intersections of shear bands, e.g., stacking faults, twins, etc. [10, 13, 14]. Usually, ε martensite is formed at the low deformation level (i.e., 5–10%) and at higher strain levels, the α' martensite increases at the expense of ε martensite [15]. In respect of the effect of composition, at considerably lower temperatures, δ-ferrite forming elements like chromium, silicon, and molybdenum act as strong austenite stabilizer in the same way as nickel, manganese, carbon, nitrogen, etc. The upper limit of the transformation temperature is obtained as [9]:

$$M_{d30}(^\circ C) = 413 - 462(C + N) - 9.2(Si) - 8.1(Mn) - 13.7(Cr) - 9.5(Ni) - 18.5(Mo)(wt\%) \quad (1)$$

Appropriate annealing treatment of the deformed steel results in reversion of the strain-induced martensite to austenite leading to microstructural refinement. In general, studies on reversion of deformation induced martensite during heating are limited [16]. Reversion of deformation induced martensite is essentially governed by the two mechanisms, namely (a) diffusion controlled and (b) shear type. It has been found that increase in nickel/chromium ratio lowers the martensitic shear reversion temperature by increasing the Gibbs free energy change between FCC and BCC structure [17]. Steels with high nickel/chromium ratio (0.625) easily undergo the martensitic reversion in a low temperature range [17]. Thermodynamically, for the shear mechanism to be operative; a minimum driving force is required and lowest possible temperature is 650°C [17]. During annealing, the heavily deformed regions of austenite undergo recovery and recrystallization, whereas deformation-induced martensite transforms to austenite. During annealing, the grains of the reverted austenite are refined through the recovery process of the matrix: formation of dislocation cell and sub-grain, similar to the process in cold worked austenite.

The attractive manufacturing potential of the 304 and 304(L) steels warrants serious endeavour to understand

---

Received August 26, 2011; Accepted October 6, 2011

Address correspondence to S. K. Ghosh, Department of Metallurgy and Materials Engineering, Bengal Engineering and Science University, Shibpur, Howrah - 711 103, India; E-mail: skghosh@metal.becs.ac.in

Materials Characterization 133 (2017) 77–86

Contents lists available at ScienceDirect

Materials Characterization

journal homepage: www.elsevier.com/locate/matchar

Effect of cryogenic deformation on microstructure and mechanical properties of 304 austenitic stainless steel

P. Mallick[a], N.K. Tewary[a], S.K. Ghosh[a,*], P.P. Chattopadhyay[b]

[a] *Department of Metallurgy & Materials Engineering, Indian Institute of Engineering Science and Technology, Shibpur, Howrah 711103, India*
[b] *National Institute of Foundry & Forge Technology (NIFFT), Hatia 834003, Ranchi, India*

ARTICLE INFO

Keywords:
304 austenitic stainless steel
Cryogenic rolling
Deformation induced martensite
Stacking fault energy

ABSTRACT

304 austenitic stainless steel plates have been deformed (10 to 40%) by multi-pass cold rolling incorporating soaking at 0 °C and − 196 °C after each pass with an aim to correlate the microstructure and mechanical properties under cold/cryogenically deformed conditions. Characterisation of phase constituents, microstructure and mechanical properties of such steel specimens has been conducted after processing under different schedules. Rolling of the investigated steel at near cryogenic temperature results into the formation of extended stacking faults, ε-martensite and α′-martensite in contrast to the formation of homogeneous dislocation structure along with α′-martensite in the samples rolled at 0 °C, which can be correlated with temperature dependent stacking fault energy. EBSD phase analysis reveals 46.3% and 69.2% α′-martensite in the austenitic matrix for 10% and 20% deformation at − 196 °C, respectively. Deformation twins are evident in all the samples rolled at 0 °C as well as − 196 °C. 40% cold deformation at 0 °C leads to high strength (1225 MPa) and 13% total elongation, whereas comparatively lower 10–20% deformation at − 196 °C leads to higher level of strength (1306–1589 MPa) with 15–9% elongation due to the formation of the higher volume fraction of strain induced martensite (ε/α′).

1. Introduction

Austenitic stainless steel (ASS) finds extensive applications in low-temperature technology, chemical industry, ocean technology, food processing industry, petrochemical processing etc. [1]. Despite their superior corrosion resistance and good formability, ASS exhibits low yield strength [2]. Therefore, strengthening of such steels by suitable mechanisms is desired to enhance their technological merit for structural application. Recently, transportation of the cryogenic material like LNG (Liquefied Natural Gas) is increasing rapidly. For this purpose, 304 SS has been slotted as a potential material due to its attractive mechanical properties at cryogenic temperature [3]. It is known that austenitic stainless steels are not amenable to the conventional hardening and tempering method. Imparting appropriate plastic deformation has been found to be effective in improving the strength of this material, through the formation of α′-martensite in austenite matrix during deformation [4]. The extent of such transformation depends upon several factors like stress and strain rate, deformation temperature, alloy composition etc. [5–10]. Proper defect structures created through plastic deformation in austenite perform as embryos for the transformation product. For example, stacking fault or HCP band intersection region, twins, shear intersection, isolated shear band, intersection between shear band and grain boundary and grain boundary triple points act as the favourable nucleation site for martensite formation in austenitic stainless steels [11–12]. Overlapping of stacking faults usually forms ε-martensite [13]. At higher strain regime, α′-martensite forms at the expense of ε-martensite [14]. The amount of plastic strain (tension) also increases the amount of α′-martensite. While biaxial tension enhances the volume fraction of α′-martensite through the formation of a large number of shear bands, compressive strain decreases the amount of α′-martensite [11]. The transformation product reveals distinctive lath-like morphology [11,15]. Strain energy accumulated by about 60% plastic deformation is consumed for the formation of deformation induced martensite and martensite deformation takes place at higher reductions [16]. The achievable strength-ductility combination of such steel is governed by the work hardening of the microstructure, which is significantly influenced by the composition and/or temperature dependant variation of stacking fault energy (SFE) [17].

Due to the limited opportunity of compositional modification, judicious microstructural design in cold deformed austenitic stainless steel is a favourable option for achieving the desired strength-ductility

---

[*] Corresponding author.
E-mail address: skghosh@metal.iiests.ac.in (S.K. Ghosh).

http://dx.doi.org/10.1016/j.matchar.2017.09.027
Received 24 June 2017; Received in revised form 21 September 2017; Accepted 21 September 2017

Materials Science & Engineering A 707 (2017) 488–500

Contents lists available at ScienceDirect

Materials Science & Engineering A

journal homepage: www.elsevier.com/locate/msea

Microstructure-tensile property correlation in 304 stainless steel after cold deformation and austenite reversion

P. Mallick[a], N.K. Tewary[a], S.K. Ghosh[a,*], P.P. Chattopadhyay[b]

[a] Department of Metallurgy & Materials Engineering, Indian Institute of Engineering Science and Technology, Shibpur, Howrah 711103, India
[b] National Institute of Foundry & Forge Technology (NIFFT), Hatia 834003, Ranchi, India

ARTICLE INFO

Keywords:
Austenitic stainless steel
Cryogenic deformation
Reversion
Microstructure
Mechanical properties

ABSTRACT

The present study aims to investigate the evolution of microstructure of 304 austenitic stainless steel (SS) due to reversion annealing of cold deformed samples under different schedules. Evolution of phases in selected samples was identified and quantified by X-ray diffraction analysis along with corresponding microstructural characterisation through optical, scanning and transmission electron microscopy. Mechanical properties of the samples were determined by carrying out tensile test. Electron microscopy of selected samples has revealed that, while strain induced martensite, deformation twins, ε-martensite and high dislocated structures are the dominant microstructural features of the cold deformed samples, reversion annealing of the same results into ultrafine-grained reverted austenite, cell type dislocation sub-structures with some amount of untransformed martensite. The maximum tensile strength of 1589 MPa with an elongation of 9% has been obtained after 20% deformation at −196 °C (20LND), whereas 40% deformation at 0 °C (40ZCD) results into a tensile strength of 1225 MPa with 13% elongation. Annealing of 40ZCD and 20LND specimens at 300 °C results in significant improvement in tensile strength, while annealing at 725 °C increases the elongation with a decrease in tensile strength. During reversion annealing, strain induced martensite transforms to austenite through shear and diffusional processes. However, the reversion is essentially diffusional in nature at a higher temperature.

1. Introduction

304 austenitic stainless steel is one of the important engineering alloys characterised by its high ductility and excellent corrosion resistance offered by the high Cr content [1]. However, the low value of strength restricts its application in several structural purposes. 304 stainless steels exhibit austenitic structure at room temperature, particularly due to the presence of Cr and Ni, which results in a high value of ductility. However, the onset of deformation results into the improvement of strength due to martensite formation and increase in defects structures [2]. Cryogenic and low temperature deformation of 304 stainless steel has recently drawn the significant interest of the industries engaged in the transportation of the cryogenic material, liquefied natural gas, low temperature technology, ocean technology, food processing, petrochemical processing etc. [3]. Cryogenically or low temperature deformation of austenitic stainless steels exhibits high strength and toughness due to the presence of strain induced martensite, deformation twins, ε-martensite and high dislocated structures.

On the other hand, reversion annealing treatment of the cryogenically deformed steel is important from the viewpoint of restoring the loss in ductility during cryogenic or room temperature deformation [4]. Due to deformation at zero and cryogenic temperature, the microstructure inherits strain induced martensite, twins, stacking faults and high dislocation density within the austenite grains, leading to increase in tensile strength with low ductility in the case of austenitic stainless steels having low stacking fault energy (SFE) [5]. Whereas, the purpose of reversion annealing is to increase the ductility without significant loss in strength. The favourable amount of strength-ductility combination which can be achieved by the reversion of strain induced martensite is an important way out [6].

After reversion annealing of stainless steel, the microstructure exhibits primarily ultrafine-grained reverted austenite, formed predominantly on the dislocation cell type structure with some amount of untransformed martensite [7]. Such microstructure has been found to play a significant role in altering the mechanical properties of 304 SS. Misra et al. [8] reported that transformation of lath type martensite to dislocation cell type martensite during deformation involves refinement of laths which causes high strength in austenitic stainless steel. However, the deformation process limits the ductility. Earlier, several studies have demonstrated that in the course of reversion annealing

---

* Corresponding author.
E-mail address: skghosh@metal.iiests.ac.in (S.K. Ghosh).

http://dx.doi.org/10.1016/j.msea.2017.09.070
Received 28 July 2017; Received in revised form 15 September 2017; Accepted 16 September 2017

steel research international

www.steel-research.d

Effect of TMCP on Microstructure and Mechanical Properties of 304 Stainless Steel

Pratik Mallick, Nisith Kumar Tewary, Swarup Kumar Ghosh, and Partha Protim Chattopadhyay*

The present study investigates the evolution of microstructure and mechanical properties of 304 stainless steel after thermo-mechanical controlled processing (TMCP). Three different FRTs (finish rolling temperatures) have been adopted and the micro-constituents are identified as austenite grains, stacking faults, annealing, and deformation twins. Fine austenite grains in the range of 1–30 µm are obtained at lower FRT (700 °C) whereas at higher FRT, coarse grains are formed. TEM and X-ray analyses indicate the formation of $M_{23}C_6$ ($(Cr, Fe)_{23}C_6$) precipitates for higher FRT (900 °C). Specimen processed with 700 °C FRT results into 37% enhancement in UTS compared to the base metal which is attributed to fine partially recrystallized grain, extensive deformation twinning and high dislocation density. Maximum elongation (68%) is obtained due to the formation of strain-free equiaxed grains (≈40 µm) at 900 °C FRT.

1. Introduction

Grain refinement is one of the effective methods employed for enhancing the strength with a favorable ductility of steel.[1] There are several methods which produce fine grain structure like equal channel angular pressing (ECAP),[2] high-pressure torsion (HPT),[3] accumulative roll bonding (ARB)[4] reversion annealing of martensitic structure etc. However, the main problem in these methods is the formation of stain induced martensite, which lowers the ductility.[5] In this connection, it is important to note that reversion of strain induced martensite improves the ductility in the steels processed under aforesaid routes.[6,7] During reversion, the formation of fine grains and inhomogeneous distribution of these fine grains lead to strain localization causing improvement in the ductility value.[8,9] Cold rolling, as well as hot rolling, has been employed for achieving grain size refinement. Cold working improves the strength of the material and lowers the ductility by higher forming forces, while hot rolling allows simultaneous recrystallization, which controls the grain refinement. To avoid high working temperatures and forces, warm rolling ($0.35T_m < T < 0.55T_m$) is commonly used as the intermediate process,[10] which allows recovery but not recrystallization to get a favorable combination of strength and ductility. Among the available methods, grain refinement by thermo-mechanical treatment has drawn great attention in steel research, because it improves both corrosion and mechanical properties of the stainless steel.[11–13] During thermo-mechanical processes (TMCP), the steel undergoes various metallurgical phenomena such as work hardening, dynamic recovery and dynamic recrystallization. Among these processes, dynamic recrystallization[14,15] is the most important mechanism during thermo-mechanical controlled processing (TMCP) of low stacking fault energy FCC alloys, because it influences the final microstructures and thereby the mechanical properties of the materials.[16] Thermo-mechanical controlled processing (TMCP) and its influence on the microstructure and mechanical properties are well established in low and ultralow carbon steels.[17,18] However, limited studies have been carried out on this aspect in austenitic stainless steels.

In view of the above, in the present study, 304 austenitic stainless steel has been thermo-mechanically processed with three different finish rolling temperatures (FRT) of 700, 800, and 900 °C to study the effect of FRT on microstructure and mechanical properties of the steel. Recrystallization and grain growth which strongly influence the mechanical properties of steel are known to occur during TMCP. The purpose of the present work is to vary the grain size with altering the finish rolling temperature during TMCP and the presence of different types of microstructural features generally form in austenitic stainless steel which strongly affects the strength-ductility combination of the steel.

2. Experimental Section

The material used for this study is commercially available 304 stainless steel. Its chemical composition has been analyzed in an optical emission spectrometer (ARL 4460) and the values are listed in **Table 1**. The hot rolled steel with a thickness of 25 mm was cut down to a cross-section of 12 × 12 mm and 100 mm length. The

Prof. S.K. Ghosh, P. Mallick, N. K. Tewary
Department of Metallurgy & Materials Engineering
Indian Institute of Engineering Science and Technology
Shibpur, Howrah 711103, India
E-mail: skghosh@metal.iiests.ac.in

Prof. P.P. Chattopadhyay
National Institute of Foundry & Forge Technology (NIFFT)
Hatia 834003, Ranchi, India

DOI: 10.1002/srin.201800103